UNIVERSITY OF LIVERPOOL

Discovery and Functionalisation of Microporous Materials

Jamie Liam Culshaw

Department of Chemistry, University of Liverpool

Thesis submitted in accordance with the requirements of the University of Liverpool for the degree of Doctor in Philosophy

2012

Acknowledgements

I first would like to express my sincere thanks towards Prof. Andrew Cooper for giving me the opportunity to complete both a Masters project and now a PhD within such a prestigious and forward-thinking research group.

Secondly, I owe a very deep level of gratitude to Dr. Dave Adams, whose guidance and many thought provoking conversations have helped me to where I am today. I also owe Dave many thanks for the hours he spent reading over my work and insightful comments which he provided so that I could construct this thesis.

I would also like to thank my fellow group members past and present who have all contributed toward my work in one form or another. Thank you to Rob D, Stephen, Lyndsey, Donocadh, Tom, Marc, James H, James J, Mike, Tamoghna, Xiaofeng, Shan, Ben, Dan, Kim, Mike, Sam, Shijie, George, Ming, Jia-Xing, Ev, Erol, Paul, Adam and Ed.

I am also thankful toward the technical and support staff within the Centre for Materials Discovery and department who have aided me in solving both scientific problems and generic troubles I have faced. Rob C, Sean, Neil, Jean, Moya, Sandra, Nadeen, Paul, and Anne – thank you.

To my friends across other research groups who have helped me overcome the lows and enjoyed the highs my PhD has brought: Jaclyn, Rob, Mike, Marco and Tom, thank you.

Finally I would like to thank my family who have supported me unwaveringly and made me the man I am today. To my mother Anita and father Ian, thank you for giving me such unbelievable support and for being the best parents I could ever have wished for. To my three brothers, Ian, Darren and Liam, you are all a constant source of drive and inspiration for me. To Liam, I both love and miss you.

Index

Abstract

This thesis describes the preparation of a new [4+6] porous organic cage, CC12. The new cage has a N_2 SA_{BET} of up to 946 m^2/g, as well as inherent selectivity of gases based on polymorphism. This new porous organic cage has also been reduced and catenated as seen with previous cages. Cages have also been formed from aliphatic diamines, highlighting importance of diamine length in formation of either [2+3] or [4+6] cages (Chapter 3).

CC1 has been prepared and reduced in situ to yield RC1, while CC5 was also reduced to produce RC5. These reduced cages have provided a route towards decorated cages *via* nucleophilic addition/elimination with various acid halides. While no porous materials were observed by addition of bulky or aliphatic groups, this new class of decorated cages presented an excellent basis for further reactions on a 12-armed core, higher than that of POSS alternatives (Chapter 4).

Finally, RC1 has been polymerised with bis-acid halides to yield networks with modest N_2 SA_{BET} of up to 106 m^2/g. Decorated cages were also successfully homo-coupled by Yamamoto and polymerised with Sonogashira methods to yield polymers with N_2 SA_{BET} of up to 150 m^2/g. Decorated cages were lastly hyper cross-linked to yield H_2 selective polymers and co-polymerised with benzene to yield N_2 SA_{BET} of up to 954 m^2/g (Chapter 5).

Abbreviations

BET	Brunauer Emmett Teller
BPDC	Biphenyl-4,4'-dicarboxylate
BTE	4,4',4''-[benzene-1,3,5-triyl-tris-(ethyne-2,1-diyl)]tribenzoate
CAF	Cage Aromatic Framework
CC	Covalent Cage
CCAD	Covalent Cage Aliphatic Diamine
CMP	Conjugated Microporous Polymer
COF	Covalent Organic Framework
CSA	Connolly Surface Area
CTF	Covalent Triazine Framework
DCM	Dichloromethane
DMF	N,N-dimethylformamide
DSC	Differential Scanning Calorimetry
EDX	Energy-dispersive X-ray Spectroscopy
FDA	Formaldehyde dimethyl acetal
FTIR	Fourier Transform Infrared Spectroscopy
HCP	Hyper Cross-linked Polymer
HPLC	High Performance Liquid Chromatography
HT	High-Throughput
IPA	Isopropyl Alcohol
MALDI	Matrix-assisted laser desorption/ionization
MeCN	Acetonitrile

MOF	Metal Organic Framework
MOP	Metal-organic Polyhedra
MS	Mass Spectrometry
NMR	Nuclear Magnetic Resonance Spectroscopy
OCF	Organic Cage Framework
PAF	Porous Aromatic Framework
PIM	Polymers of Intrinsic Microporosity
PPN	Porous Polymer Network
POSS	Polyhedral Oligomeric Silsesquioxane
PSD	Pore Size Distribution
pXRD	Powder X-ray Diffraction
RC	Reduced Cage
RT	Room Temperature
SA	Surface Area
SA_{BET}	BET Surface Area
$SA_{Langmuir}$	Langmuir Surface Area
SEM	Scanning Electron Microscope
TFA	Trifluoroacetic acid
TFB	1,3,5-Triformylbenzene
TGA	Thermogravimetric Analysis
THF	Tetrahydrofuran
TMS	Tetramethylsilane
4TMSEBP	3,3’,4,4’-Tetra(trimethylsilylethynyl)biphenyl

TPP	Tris(*o*-phenylenedioxy)cyclotriphosphazene
TTBI	Triptycenetrisbenzimidazolone
ZIF	Zeolitic Imidazolate Frameworks

Chapter 1

Introduction

Table of Contents

1.1 Aims and Objectives

This thesis aims to describe the synthesis, functionalisation and properties of new members of a rare class of discrete 'porous molecules' known as porous organic cages.[1] These materials are prepared by simple imine condensation reactions toward the thermodynamic product, as shown in the example in Figure 1 below.[2]

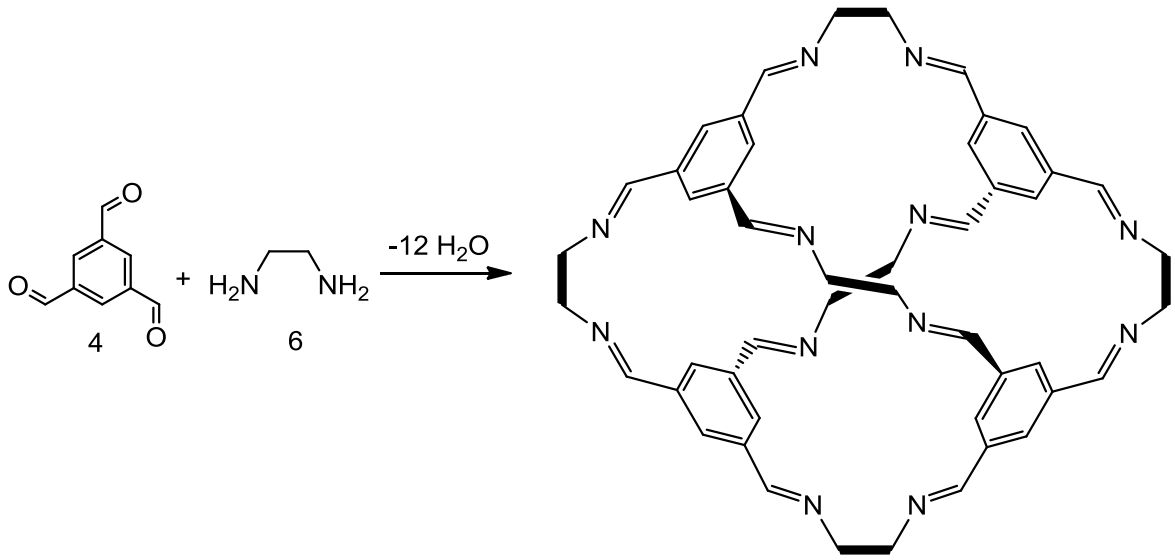

Figure 1: Formation of CC1.

A range of new porous organic cages were produced and evaluated for use in gas storage and separation (Chapter 3). Cages were also reduced and functionalised by simple addition/elimination reactions with acid halides, with the goal of increasing porosity and functionality (Chapter 4). Reduced cages were also polymerised with bi-functional acid halides and through other techniques to yield cage-containing porous networks (Chapter 5).

There is a plethora of microporous materials in existence today. We hope that porous organic cages add value into this field, be it for use in gas storage, gas separation, CO_2 capture, or catalysis.[3]

1.2 Microporous Materials

1.2.1 Definition

Nanoporous materials can consist of extended frameworks (either organic, inorganic or hybrid), or of discrete molecules, either with internal cavities (giving rise to intrinsic porosity) and/or packing inefficiently to create voids and channels (extrinsic porosity). The pore diameter in such materials are within the nanometre range, between $1x10^{-7}$ and $0.2x10^{-9}$ m. There are three different IUPAC (Table 1) subdivisions of nanoporous materials.[4] Pores larger than 50 nm are classified as macropores, 2-50 nm as mesopores, and smaller than 2 nm as micropores.

Subdivision	**Pore Size ($x10^{-9}$ m)**
Microporous	0.2–2.0
Mesoporous	2.0–50
Macroporous	50–1000

Table 1: IUPAC porous materials subdivisions.[4]

High surface areas (e.g., those greater than 1000 m^2/g) are usually derived from microporous materials[5] which give rise to adsorption of gases at lower pressures.[6] Thermodynamics disfavour the formation of voids in solids and the surfaces that surround them. During the preparation of porous materials, such voids are filled with solvent or other small molecules; meaning that, often, a promising structure collapses when the molecules stabilizing the nascent 'pores' are removed.[7]

In terms of porous molecular solids, many new systems have been reported,[8] but the porosity in molecular solids is often not permanent in the sense that it remains intact upon evacuation of the pores.[7] Issues with defining porosity in molecular solids were also highlighted by Barbour, who defined three different kinds of porosity (conventional porosity, virtual porosity and porosity without pores).[7] Conventional porosity occurs when materials retain repeating, interconnected empty channels with

diameters >3 Å at their most narrow points after guest/solvent removal. Virtual porosity describes situations where a material can appear to be porous by removing guests (such as solvent or counter ions) *in silico* from a crystal structure but where in reality, these nascent 'pores' collapse upon guest removal. Representation is also important: displaying a molecule in a ball-and-stick plot, rather than space-filling model may give the impression of a larger void. Porosity 'without pores' was defined as the ability of a solid to adsorb guests without formally interconnected pores. Molecular solids with disconnected void volume nonetheless have been shown to adsorb considerable quantities of guests by cooperative diffusion mechanisms.[9,10]

Holst *et al.* described porosity in molecular solids as either intrinsic or extrinsic.[3] Intrinsic porosity arises from pre-defined pores or cavities in molecules such as calixarenes[11] or porous organic cages.[1] Extrinsic porosity occurs when molecules pack inefficiently in such a way as to create voids and channels between the molecules, with examples including Dianin's compound[12] and *tris-o*-phenylenedioxycyclotriphosphazene (TPP).[13] In the case of extrinsic porosity, the resulting porosity is usually not obvious from the molecule viewed in isolation. Attempts were also made by the same group to enhance both of these types of porosity in a single crystal, with a molecule that comprised a pre-defined pores and a bulky structure.[14]

Microporous materials have applications in a wide variety of areas such as molecular separations, heterogeneous catalysis, and gas storage. For gas storage, hydrogen storage targets for vehicular transport were originally set as high as 9 wt. % by the US Department of Energy just a few years ago.[15] These targets were cited as unreachable by some.[16] In 2009, hydrogen storage targets were revised to 5.5 wt. % at room temperature by 2015, with an ultimate target of 7.5 wt. %.[17] At the time of writing, hydrogen storage materials are still short of this room temperature targe.[18]

1.2.2 Types of Microporous Materials

Microporous materials can be separated into six categories (Table 2); as defined by their inherent nature (e.g., be it a repeating networks or discrete molecules) and by

the elements from which they are made up (inorganic, organic, or a hybrid of the two). This thesis focuses on synthetic microporous materials; however, there are examples of naturally occurring or naturally derived microporous materials such as some zeolites[19] and activated carbons[20] respectively. There are many examples of porous networks in the literature and this area was extensively researched over the past few decades. Discrete porous molecules (such as cages) are rarer because molecules tend to pack efficiently in the solid state, (leaving as little empty space as possible) thus leading to non-porous solids.

	Inorganic	**Hybrid**	**Organic**
Networks	Zeolites[19]	MOFs[21,22] ZIFs[23]	COFs[24,25] CMPs[26-28] PIMs*[29,30] HCPs[31,32] Covalent Triazine Frameworks[33]
Molecules	No examples to date?	Metal Coordinated Cages[34,35]	Porous Organic Cages[1] Calixarenes[9,10] Cucurbiturils[36] Tris(*o*-phenylenedioxy)cyclotriphosphazene (TPP)[37] 3,3',4,4'-Tetra(trimethylsilylethynyl)biphenyl (4TMSEBP)[38] Dianin's Compound[39]

Table 2: Categories of microporous materials. *PIMs may be either soluble oligomeric chains or networks.

1.3 Microporous Extended Networks

1.3.1 Extended Inorganic Networks

Zeolites are naturally occurring or synthetic crystalline aluminosilicates with a repeating pore network.[19] They have well-defined network structures made up of silicon and aluminium atoms linked *via* oxygen atoms.[40] Windows and cages within the zeolite framework allow small molecules to access high internal surface areas. Some types of zeolite are found naturally, but many more have been synthesised in the laboratory using templates of varying sizes to dictate pore size, which can then be removed by pyrolysis. Zeolites are extremely important materials in heterogeneous catalysis.

1.3.2 Extended Hybrid Networks

Metal-organic frameworks (MOFs)

Metal-organic frameworks (MOFs) have been the subject of intense research since they were first prepared as a permanently porous framework by Yaghi and co-workers,[21] building on the work of Robson and colleagues.[41-43] MOFs can be prepared from a variety of metal centres and organic connecting struts, often similar to those seen in discrete organometallic complexes. Unlike those organometallic complexes, MOF ligands (the organic molecular struts) contain at least two functional bonding groups in order to create a repeating crystalline network. Ligands can also be mixed in one material. In MOF-210 for example (Figure 2)[22], a zinc (Zn_4O) centre is linked by both bidentate (BPDC) and tridentate (BTE) ligand yielding a N_2 BET surface area (SA_{BET}) of 6240 m^2/g. This is the highest N_2 SA_{BET} for MOFs discovered at time of writing, although slightly lower than some amorphous polymer networks (see discussion on CMPs, below).

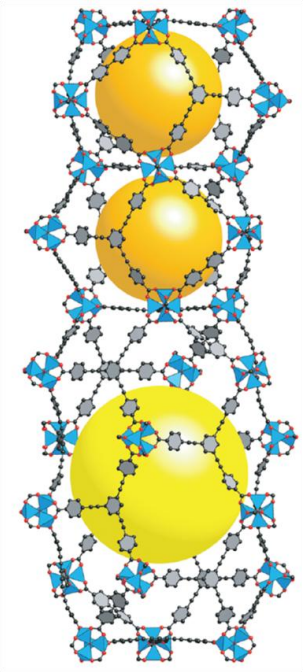

Figure 2: Crystal structure of MOF-210 showing pore volume (yellow and orange), carbon (black), oxygen (red) and zinc tetrahedrons (blue) (image taken from reference).[22]

Zeolitic Imidazolate Frameworks (ZIFs)

Zeolitic imidazolate frameworks (ZIFs) are a sub-class of MOFs which use tetrahedral metal clusters (as seen with MOFs), but using imidazolate linkers to yield structures based on zeolites topologies.[23] While ZIFs do not possess the same high surface area as MOFs (ZIF-8 showed N_2 SA_{BET} of 1630 m^2/g), they are both chemically and physically stable. ZIFs can also exhibit exceptional selectivity of CO_2 through their imidazolate linkers, especially when containing polar groups.[44,45]

1.3.3 Extended Organic Networks

Covalent organic frameworks

Covalent organic frameworks (COFs) are crystalline networks consisting of organic monomers linked together through strong covalent bonds. Originally discovered in 2005 by Yaghi and co-workers, COF-1 and COF-5 (Figure **3**) were found to exhibit

N_2 SA_{BET} of 711 m^2/g and 1590 m^2/g, respectively.[24] COFs are prepared by reversible self-condensation of boronic acids or boronic acids and alcohols, producing water as a by-product to produce strong B-O bonds.[46] These boroxine rings can be viewed as the organic analogues of metal clusters seen in MOFs. More recently, COFs were reported with surface areas of up to N_2 SA_{BET} 3600 m^2/g.[25] COF-102 for example consisted of 2,3,6,7,10,11-hexahydroxytriphenylene (HHTP) and a 3D tetrahedral monomers (shown in below in Figure 3).

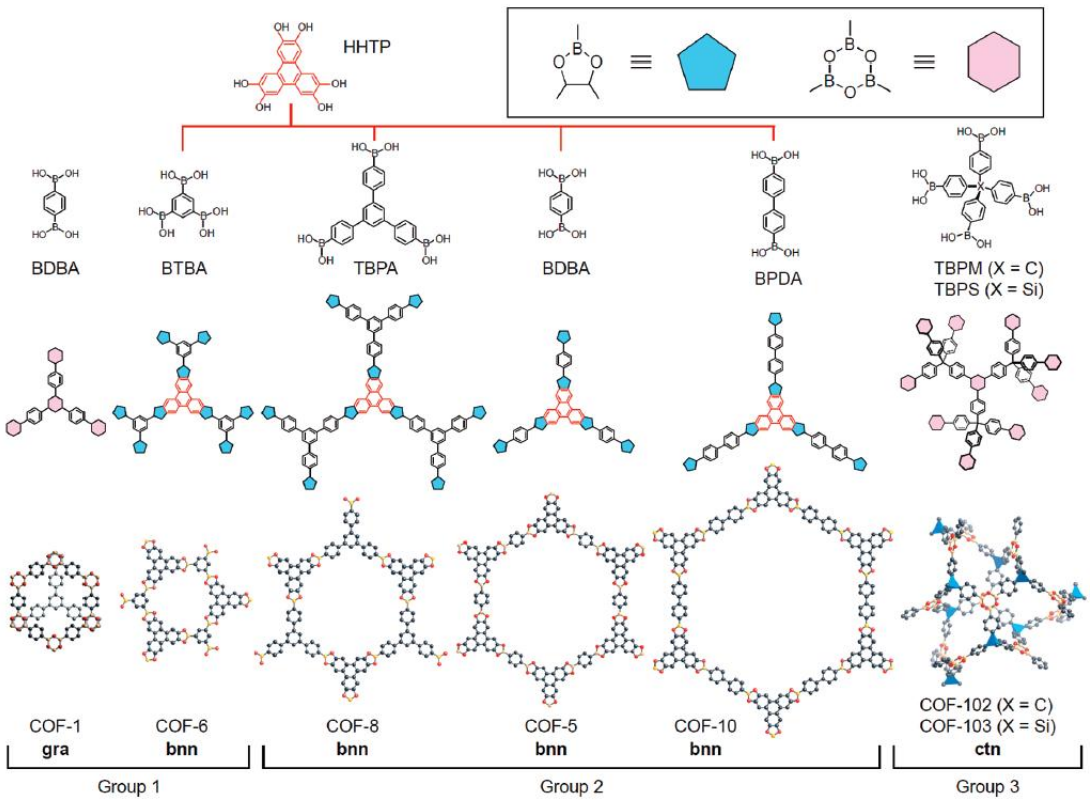

Figure 3: Condensation of various boronic acids and HHTP used to produce COFs (taken from reference).[25]

Covalent Triazine Frameworks

Formed by the condensation of nitriles in the presence of $ZnCl_2$, the first Covalent Triazine Frameworks (CTFs) were formed from the condensation of 4,4'-dicyanobiphenyl and displayed a N_2 SA_{BET} up to 2475 m^2/g at 77 K.[33] From this work, it was noted that a lower equivalence of monomer to catalyst returned higher N_2 SA_{BET} than the same reaction with an equivalent amount of monomer/catalyst. Condensation of 1,4-dicyanobenzene with an equivalent amount of catalyst (1:1) yielded a material with a N_2 SA_{BET} of 791 m^2/g, while the same reaction with 0.1

equivalence of catalyst improved N_2 SA_{BET} to 1123 m^2/g (Figure 4). Focusing on the 1,4-dicyanobenzene monomer, further investigations from the same group into the effects of reaction temperature showed an increased N_2 SA_{BET} up to 3270 m^2/g when utilising a two step heating method where the reaction was started at 400 °C, held for 24 hours and then increased to 600 °C for a further four days, highlighting the importance of preparation of COF properties.[47] The degree of crystalline order in CTFs is much lower than COFs and MOFs, probably because the nitrile trimerization reaction is much less reversible. Recently, Ren *et al.* have shown a route to prepare CTFs at room temperature, with N_2 SA_{BET} exceeding 1100 m^2/g and exceptional CO_2 capacities (up to 4.17 mmol/g).[48]

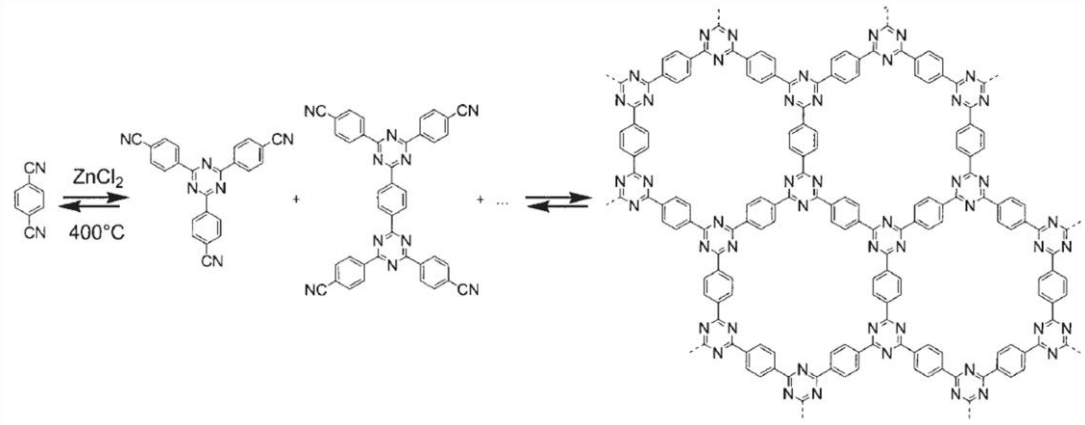

Figure 4: Preparation of a CTF from 1,4-dicyanobenzene (taken from reference).[33]

Polymers of Intrinsic Microporosity

Polymers of Intrinsic Microporosity (PIMs) were among the first completely microporous organic polymers reported.[29,30] PIMs have since been widely studied due to their range of applications including gas storage,[49,50] separation[51] and catalysis[51]. The microporosity in PIMs is the result of rigid bent monomers containing a tetrahedral carbon atom known as the site of contortion. Unlike most extended porous networks, there are examples of soluble PIMs (i.e., PIM-1 and PIM-7). PIM-1 exhibited N_2 SA_{BET} = 750 m^2/g and H_2 Langmuir surface area ($SA_{Langmuir}$) of 540 m^2/g.[50] The most important advantage of PIMs is that, uniquely for porous polymers, they are soluble in organic solvents and can be cast as membranes.

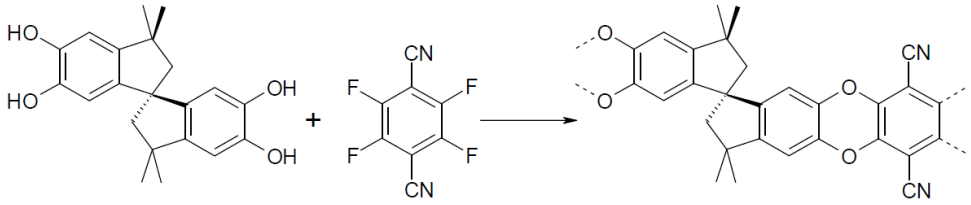

Figure 5: Preparation of PIM-1 from 5,5',6,6'-tetrahydroxy-3,3,3',3'-tetramethyl-1,1'-spirobisindane and 2,3,5,6-tetrafluorophthalonitrile.[29,30]

Recently Du *et al*. were able to utilise 'click' addition of an azide to PIM-1 nitrile groups in order to create a PIM functionalized with pendant tetrazole groups (TZPIM). This modified TZPIM showed increased uptake of CO_2 in the lower pressure ranges compared with PIM-1while greatly inhibiting uptake of N_2, as a result of CO_2-philic nature of tetrazoles. This functionalisation of PIM-1 to TZPIMs resulted in excellent selectivity of CO_2 over N_2.[52]

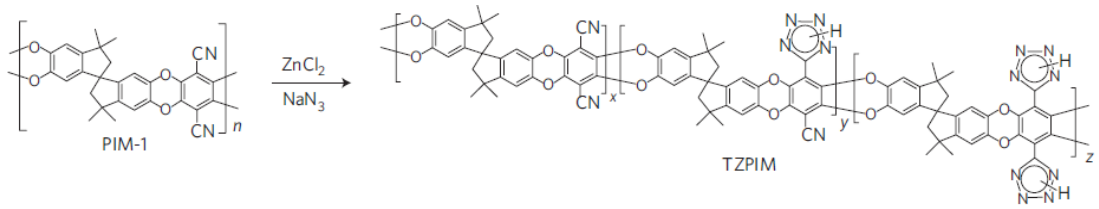

Figure 6: Click addition of sodium azide to PIM-1 to form a TZPIM (taken from reference).[52]

Conjugated Microporous Polymers (CMPs)

Unlike other organic networks discussed so far, conjugated microporous polymers (CMPs) consist of multiple bonds and aromatic rings connected in a conjugated manner. The first CMPs reported were produced *via* a Sonogashira-Hagihara coupling reaction, producing polymers with N_2 SA_{BET} surface area up to 834 m^2/g at 77 K (CMP-1).[26] Since these initial CMPs, the methodology has improved significantly with solvent effects being found to influence the reaction of 1,3,5-triethynylbenzene and various dibromo monomers.[27] This latter report showed that, on average, an increase in surface areas was observed for CMPs when utilising different solvents in the order DMF>THF>dioxane>toluene, highlighting that toluene, the initial solvent choice, was not optimal. The highest N_2 SA_{BET} observed

was 1260 m^2/g at 77 K, from the coupling of 1,3,5-triethynylbenzene and 1,4-dibromo-2,5-difluorobenzene (shown in Figure 7).

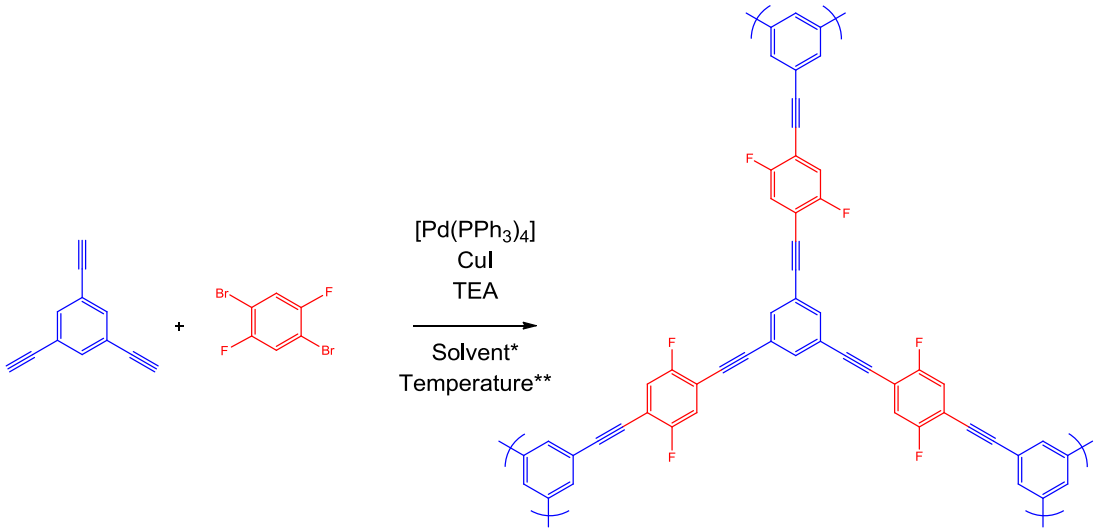

Figure 7: 1,3,5-Triethynylbenzene and 1,4-dibromo-2,5-difluorobenzne. *Reactions were screened in THF, DMF, dioxane and toluene. **Reactions in THF were carried out under reflux, while those in DMF, dioxane and toluene were performed at 100 °C (based on reference).[27]

CMP-like materials have also been reported *via* two other methods; Suzuki and Yamamoto coupling. Yamamoto-style CMPs (Figure 8) have produced the highest surface area materials to date in any class, with PAF-1 and PPN-4 (Figure **8**) exhibiting N_2 SA_{BET} of 5640 m^2/g and 6461 m^2/g at 77 K respectively.[28,53]

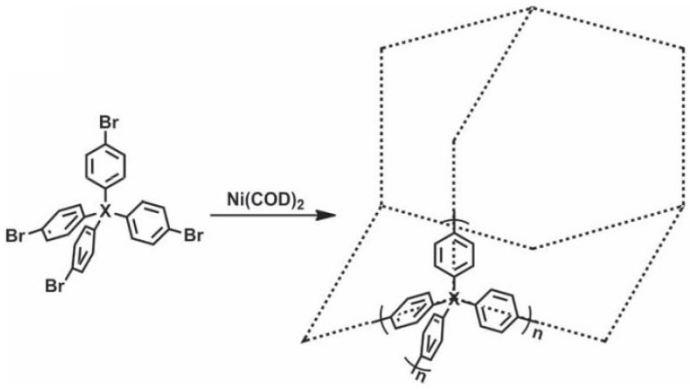

Figure 8: Yamamoto synthesis of PAF-1 and PPN-4 (X = C and Si respectively, taken from reference).[28]

Hyper cross-linked Polymers (HCPs)

One of the oldest types of microporous organic networks are hyper cross-linked polymers (HCPs). As with CMPs and PIMs, HCPs are formed by non-reversible reactions, with porosity arising from poor packing created by the rigid struts. Some of the earliest HCPs were based on cross-linking of polystyrene (containing functional chloromethyl groups, Figure 9).[31,54] This gave rise to a hyper cross-linked polymer *via* a Friedel-Crafts alkylation reaction with the use of a Lewis acid such as iron(III) chloride.[55-58]

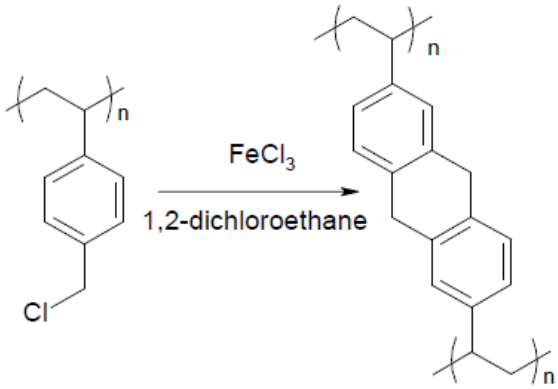

Figure 9: Hyper cross-linking of poly(chloromethyl)styrene using iron(III) chloride as in references.[55-58]

This method has been employed to produce polymers directly with high surface areas without a lightly cross-linked precursor such as poly(chloromethyl)styrene, as seen above. For example, bischloromethyl monomers such as dichloroxylene (DCX), 4,4'- bis(chloromethyl) -1,1'- biphenyl (BCMBP), and 9,10-bis(chloromethyl)anthracene (BCMA) were mixed in various ratios of copolymers and Lewis Acids. This gave rise to N_2 SA_{BET} up to 1904 m^2/g at 77 K (BCMP:DCX in 3:1 ratio) and H_2 uptake of 1.69 wt. % at 1.13 bar and 77 K (pDCX).[59]

Li *et al.*[32] slightly modified the Friedel-Crafts alkylation to polymerise seemingly non-functional monomers (including benzene, biphenyl and 1,3,4-triphenylbenzene). In this example of modified Friedel-Crafts alkylation,[32] all of the functionality arises from the cross-linker formaldehyde dimethyl acetal (FDA), producing HCPs with N_2 SA_{BET} up to 1391 m^2/g at 77 K (benzene with a three equivalence of FDA). The authors referred to this process as "knitting".

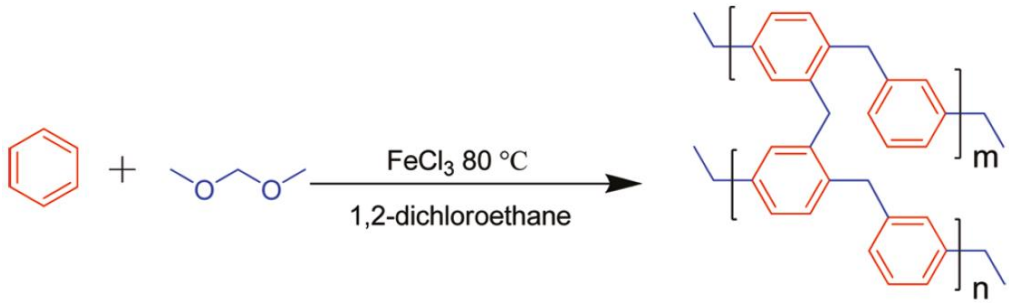

Figure 10: Hyper cross-linking of benzene with FDA using iron (III) chloride.[32]

1.3.4 Overview of Microporous Networks

Networks as a medium for gas storage have been extensively studied over the previous 10-15 years, as highlighted in recent reviews[8,60,61] and shown in Figure 11. Extremely high surface areas have been achieved, as in MOF-210, PAF-1 and PPN-4[22,28,53]. Molecular crystals are a much less studied class of materials, but they are gaining interest in recent years due to potential processing advantages owing to their solubility[3] (see section 1.4 for more details).

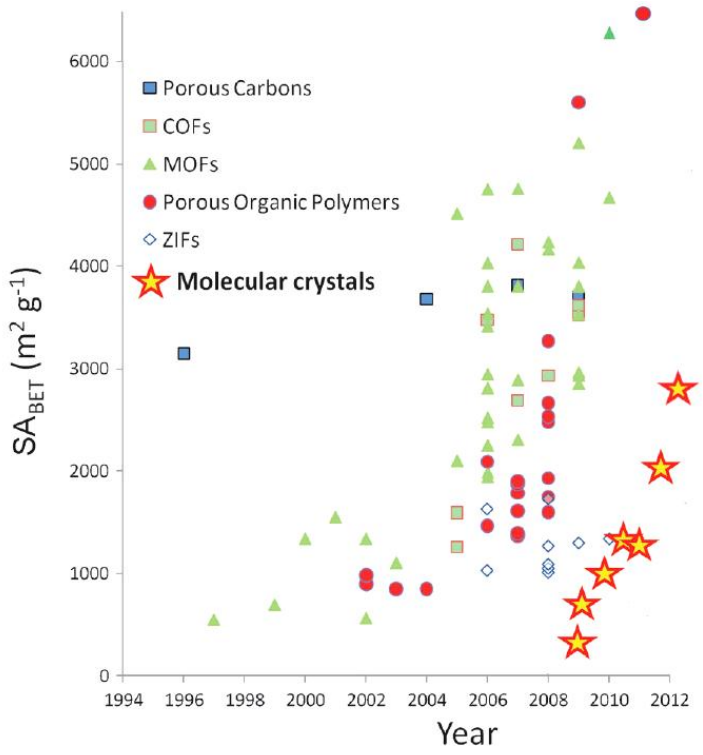

Figure 11: Plot of SA_{BET} versus publication year for examples of materials with exceptional surface areas in their class (figure adapted from reference).[61]

However, none of these materials has yet reached the target set by the DOE of 5.5 wt% of H_2 at room temperature,[17] highlighting the need for chemical 'added value' in future porous materials. One further additional issue facing porous networks is that activated carbon also shows high surface areas of around 3000 m^2/g, and is comparatively cheap and chemically/physically stable. In terms of cost considerations, the palladium[62] and nickel[53] catalysts used in cross-coupling catalysis used in production of CMPs are a concern when contemplating scale up. Tetrakis(triphenylphosphine)palladium(0) is £42.90/g and Bis(1,5-cyclooctadiene)-nickel(0) is £34.65/g at time of writing based on Sigma-Aldrich prices.

With the exception of PIMs,[63] molecular organic polymers are generally insoluble, making processing into functional materials a potentially difficult challenge. There have, however, been examples of networks with added value, such as the CTF produced by Palkovits *et al.*[64] with inclusion of the Periana Catalyst, which showed low temperature oxidation of methane to methanol. Another example would be the 'CMP supercapacitors' described by Jiang *et al*.[65]

1.4 Microporous Discrete Molecules

Porous molecules consisting of only discrete molecules were de-emphasized for some time because surface areas, stability and functionality could not compete with those shown by 3D polymeric materials like MOFs,[22] COFs[25] and CMPs[28]. Microporosity in networks is stabilised by strong directional covalent or coordination bonding, a feature which is absent in molecular solids.[8] Permanent porosity in molecules is much rarer as they tend to pack more efficiently in the solid state with minimal void volume.[7] As such, surface areas and pore volumes, if present at all, are often low for these solids.

However, discrete porous molecules possess many possible advantages over their network counterparts. The incorporation of 'chemical added value' has already been predicted for such materials.[3] Unlike extended frameworks, discrete molecules are soluble and, as such, have processing advantages. They can be recrystallised to give different polymorphs, therefore greatly altering their characteristics[66] (as discussed in Chapter 3) or cast as thin films.[63] Solubility also allows mixing of different discrete

molecules within one compound to alter properties,[67,68] or in principle to allow the mixing of apparently incompatible chemical functionalities (*e.g.*, separate molecules containing acid or base groups, imitating the spatial isolation of functionality in enzymes). Discrete molecules may also be more readily modified to create a wider array of diverse molecules than in frameworks (again owing to their solubility). Finally, because discrete porous molecules are not interconnected by covalent bonds, they have potential for host-guest interactions which could allow the trapping of specific molecules.[35]

1.4.1 Discrete Inorganic Molecules

There are currently are no examples of inorganic microporous molecules to my knowledge. In principle, however, this could be achieved with materials such as polyoxometallates.

1.4.2 Discrete Hybrid Molecules

Porous nanocrystals were prepared from derivatives of iron phthalocyanine. When connected by bidentate ligands (1,4-phenylene diisocyanide) *via* a "wall-tie" motif in the axial plane, PUNC[*v*N_2-Fe-*c*pdic-Fe*v*N_2] exhibited a N_2 SA_{BET} of 1002 m^2/g at 77 K (Figure **12**).[69]

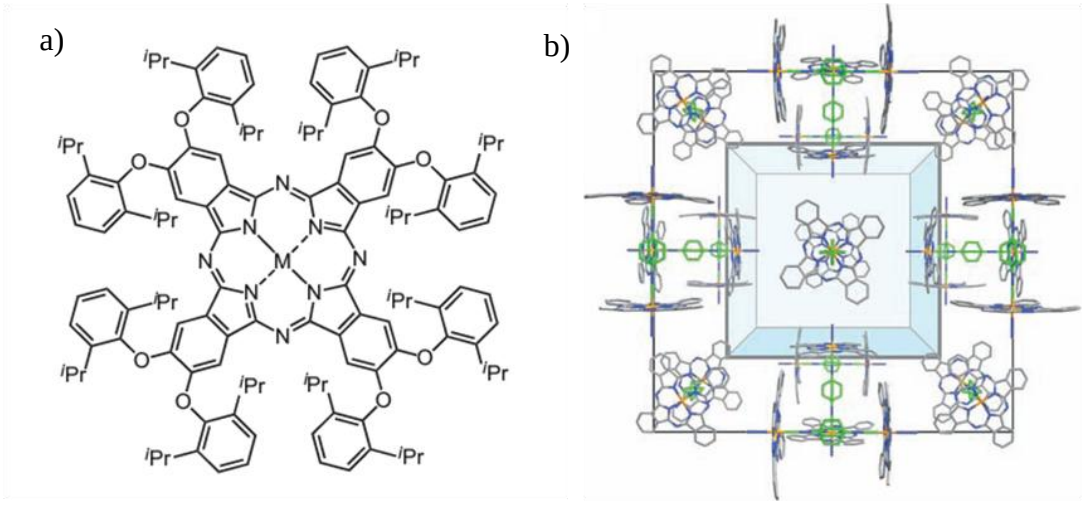

Figure 12: a) Phthalocyanine where M is Fe and b) Perspective representation of the crystal structure of PUNC[*v*N_2-Fe-*c*pdic-Fe*v*N_2] with wall ties in green (phenoxyl substituents removed for clarity) (taken from reference).[69]

Hybrid discrete porous molecules have also been shown to possess added chemical value in the literature. While not inherently porous to gas uptake, Mal *et al.* have prepared iron-containing hybrid cages shown to stabilise highly pyrophoric white phosphorous (P_4) in air and allow dissolution in water.[35] By encapsulation of the P_4 in the tetrahedral cage, addition of oxygen is prevented due to size constraints of the intermediate. P_4 can also be released under controlled instances by introducing benzene as a second guest molecule (Figure 13).

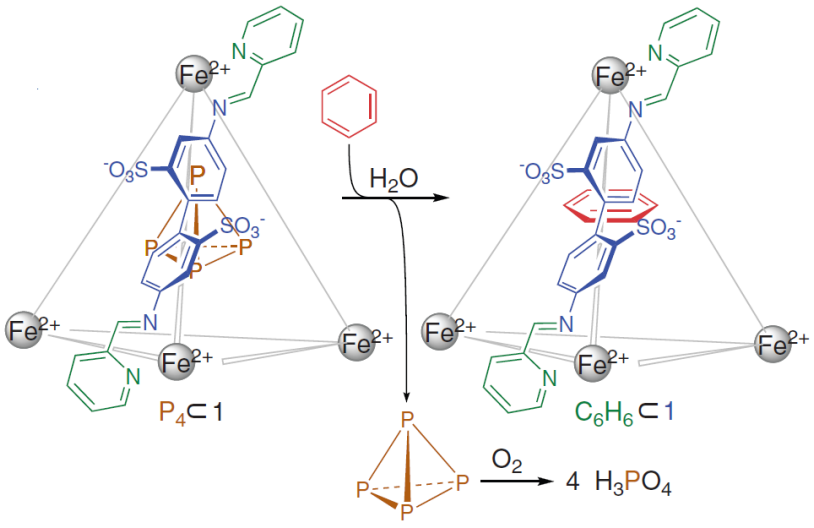

Figure 13: Tetrahedral cage with encapsulated P_4 and removal of P_4 by substitution with benzene (taken from reference).[35]

Yaghi and co-workers reviewed the synthesis of several metal-organic polyhedra (MOPs) and described the design principles for polyhedra most likely to result from the assembly of secondary building units.[70] More recently, water-soluble ruthenium organometallic cages ([porphin⊂1]$^{6+}$ and [porphin⊂2]$^{8+}$, Figure 14) were utilised in drug delivery of porphyrins to cancer cells.[71] The photosensitizer remains non-reactive to light until entering the cancer cells, at which point it was photoactivated: thus increasing cytotoxicity in cancer cells.

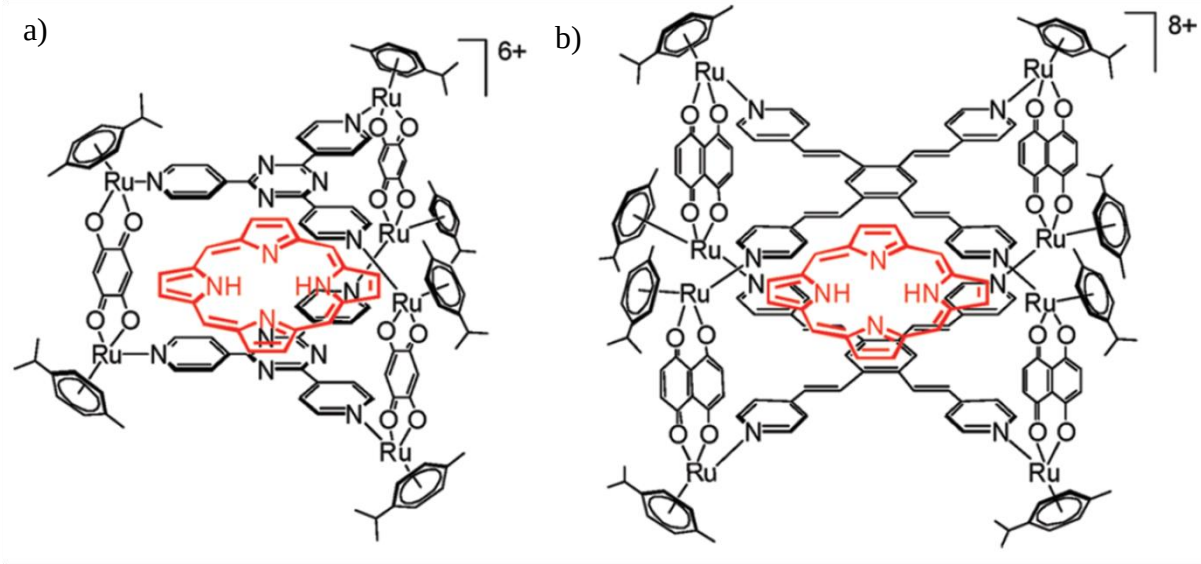

Figure 14: Molecular structures of a) [porphin⊂1]$^{6+}$ and b) [porphin⊂2]$^{8+}$ (taken from reference).[71]

1.4.3 Discrete Organic Molecules

Dianin's Compound

In 1914, while performing the condensation of phenol with mesityl oxide, Dianin found that solvents were trapped and firmly held by the reaction product.[72] 'Dianin's Compound' was first shown to adsorb a number of gas molecules, including Ar, Kr, Xe, CO_2, CH_4, C_2H_6, C_3H_8 and n-C_4H_{12} by Barrer and Shanson in 1976, and as such is the first report of a discrete porous molecular solid.[39] This material is the archetypal 'organic zeolite', although it is not, in fact, very porous. Dianin's Compound possesses interconnecting channels of only 2.5 Å minimum diameter, hence appearing to exhibit "porosity without pores".[7] It forms hourglass-shaped one-

dimensional channels within the crystals, created by six host molecules held in place by hydrogen bonding (shown in Figure 15).[12]

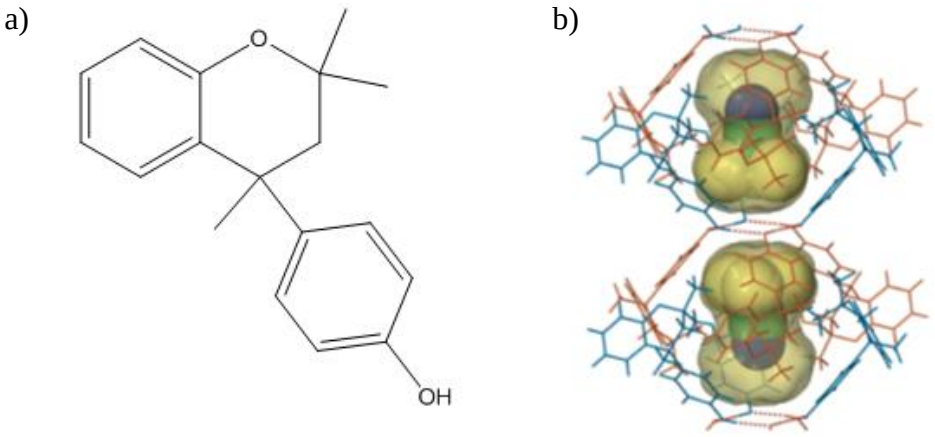

Figure 15: a) Chemical structure of Dianin's Compound, the archetypal 'organic zeolite', and b) Dianin's Compound shown as a trichloroacetonitrile clathrate with hourglass-shaped solvent accessible void.[73]

Tris(*o*-phenylenedioxy)cyclotriphosphazene (TPP)

Another of the earliest permanently porous discrete organic crystalline materials is tris(*o*-phenylenedioxy)cyclotriphosphazene (TPP). Originally discovered by Allcock and Siegel in 1964[74], TPP was more recently reinvestigated by Sozzani *et al.*[37] and again by several other groups[13,75-77]. Their combined studies show that the encapsulated solvent molecules can be removed without loss of the porous structure, and that gases can then be adsorbed in the hexagonal channels of the permanent porous crystals. The measured N_2 SA_{BET} for TPP was 240 m^2/g; and CO_2 uptake was determined to be 4 wt% at 800 mbar and 298 K. TPP contains no internal pore and hence no intrinsic porosity, with surface area arising extrinsically from hexagonal channels found in the crystal structure. This is a good example of a molecule where crystalline porosity cannot simply be inferred from the molecular structure in isolation.

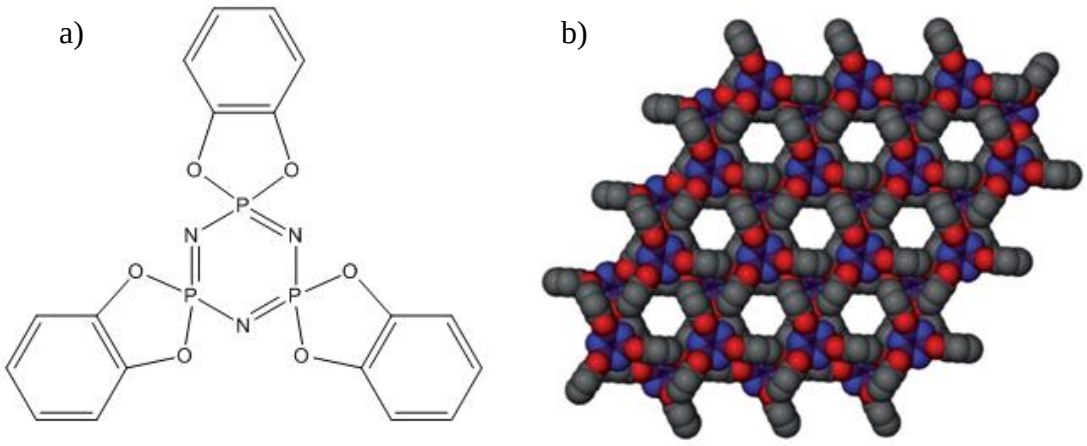

Figure 16: a) TPP and b) Crystal structure in the nanoporous hexagonal modification viewed along the channel axis (taken from reference).[77]

Calixarenes

Calix[*n*]arenes are a class of macrocyclic compounds based on a hydroxyalkylation product of a phenol and an aldehyde to create a bowl-shaped structure, where n = 4–9 repeat units.[78] Four-membered calix[4]arenes in particular possess a permanent cone-shaped molecular cavity, and are an important cornerstone for this research area.[11] Originally, Atwood and co-workers focused on formally non-porous *p*-tert-butylcalix[4]arene, which was nonetheless shown to adsorb various guests through cooperative diffusion mechanisms.[9-11] More recently, *p-tert*-butylcalix[4]dihydroquinone has been shown to have a more conventional nanoporous supramolecular architechture.[79,80] In these examples, the crystal structure of *p-tert*-butylcalix[4]dihydroquinone exhibits interconnected cavities and unoccupied lattice voids, while structural integrity is retained on desolvation to yield a N_2 SA_{BET} of 230 m^2/g at 77 K with selective uptake of CO_2 of 0.5 wt % at ambient conditions (increasing to 6.9 wt % at 550 Psi).[79] Further studies (again by Tedesco *et al.*) showed CH_4 uptake of 0.29 wt % at ambient conditions (increasing to 5 wt % at 203 K and 3 atm).[80] Calixarenes can be considered to be 'intrisically' porous because of their bowl-like shape.

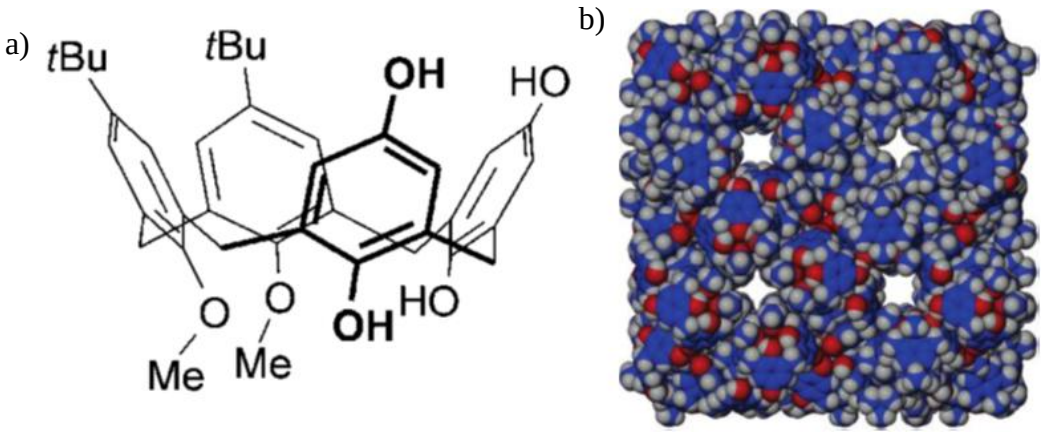

Figure 17: a) *p-tert*-butylcalix[4]dihydroquinone b) and space-filling model showing polar open channels and two hydrophobic cavities (water molecules removed for clarity).[79,80]

Cucurbiturils

Cucurbit[n]urils (where n = 5-8, 10 and denoted CB[n]) are another class of discrete, porous organic molecules. Wheel-shaped and consisting of methylene-bridged glycouril units, CB[6] in particular showed a SA_{BET} = 210 m^2/g at 77 K.[36] On recrystallisation from HCl the same molecule exhibited high selectivity of CO_2 over CO and CH_4, with uptake of CO_2 shown to be 2.2 mmol/g at 298 K, 1 bar.[81] More recently, prepared CB[7] was shown to have selectivity of CO_2 over both N_2 and CH_4, with SA_{BET} from CO_2 measured to be 293 m^2/g at 196 K.[82]

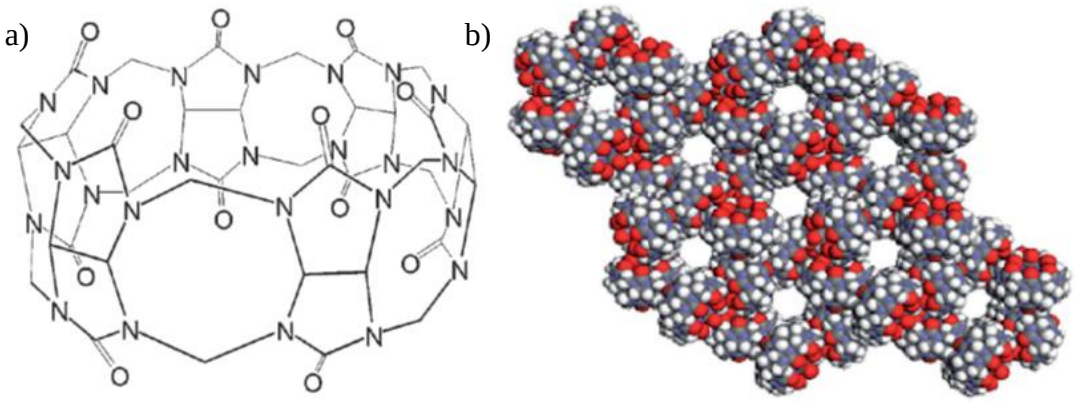

Figure 18: a) Cucurbit[6]uril and b) space-filling reperesentation.[36]

3,3',4,4'-Tetra(trimethylsilylethynyl)biphenyl

3,3',4,4'-Tetra(trimethylsilylethynyl)biphenyl (4TMSEBP) was initially discovered in 1983 by K. Larsson.[83] Msayib *et al*. reinvestigated 4TMSEBP after searching the Cambridge Structural Database (CSD) for previously discovered organic molecules with low crystalline densities which might have been overlooked as discrete porous organic molecules.[38] By exploring the CSD for known molecules with diameters < 0.9 Å, rigid aromatic rings to induce stability, and prospective porosity in the micropore range (diameter < 10 Å), 4TMSEBP was selected for its striking resemblance to that of a typical zeolite. The molecule exhibited a N_2 SA_{BET} of 278 m^2/g and had an hydrogen uptake of 3.9 mmol/g at 10 bar (both at 77 K); arising from extrinsic porosity. This is a promising approach for discovering other new porous systems.

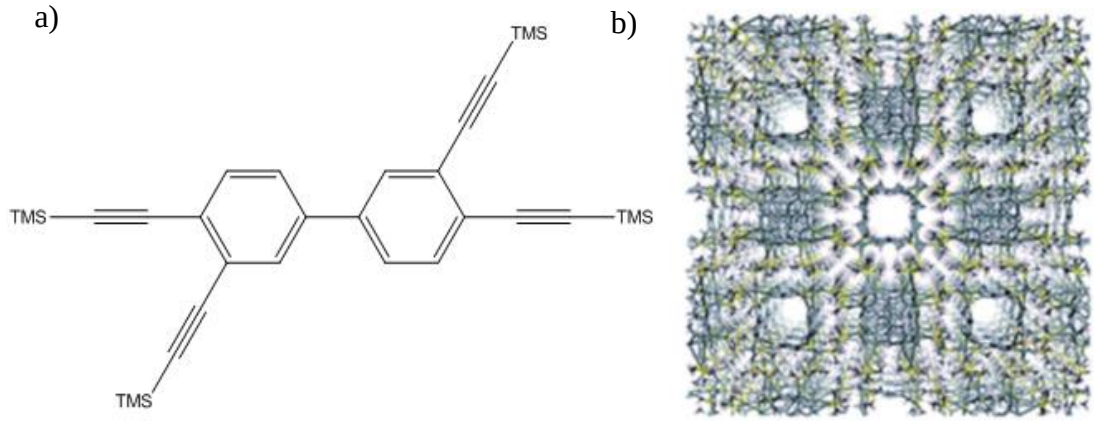

Figure 19: a) 4TMSEBP and b) Crystal structure of 4TMSEBP extended lattice.[38]

Dipeptides

Porosity is also found in certain crystalline dipeptides (including L-alanyl-L-valine, L-valyl-L-alanine, L-isoleucyl-L-valine and L-valyl-L-isoleucine). A 1D channel motif in dipeptides has been known since studies in 1996 by Gorbitz and Gundersen,[84] but more recently, dipeptide crystals containing nanochannels of various sizes show remarkable and selective adsorption of CH_4, CO_2 and H_2.[85] It was also demonstrated that L-isoleucyl-L-valine could show efficient selectivity of CO_2 over CH_4 at pressures of less than 0.07 bar. All of these materials are extrinsically

porous and it would again be difficult to infer the porous properties of the crystals by simple examination of the isolated molecular structures. More recently, Afonso *et al.* have shown L-alanyl-L-alanine crystals with narrow 1D channels, exhibiting high O_2/N_2 selectivity >124 based on size exclusion.[86] Moure *et al.* have also shown the synthesis of a series of [2+3] pseudopeptidic cages, with one shown to encapsulate tris(tetrabutyl)-ammonium salt.[87]

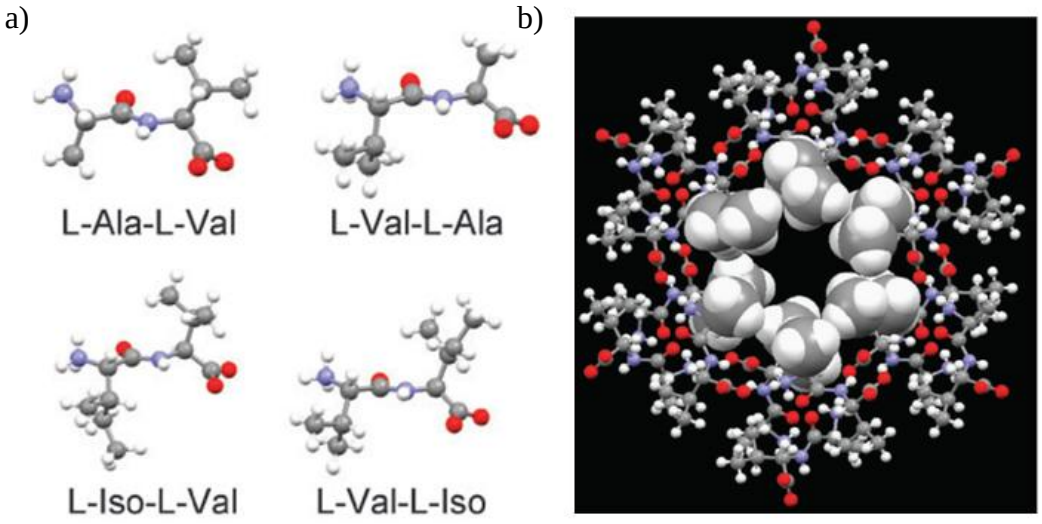

Figure 20: a) Various dipeptides and b) Crystal structure of L-alanyl-L-valine showing the open hydrophobic channel of 5 Å.[85]

Noria Waterwheel

Atwood *et al*. showed that a cyclic waterwheel-like oligomer, Noria (Latin for waterwheel),[88] exhibits porosity and gas adsorption properties in the amorphous state.[89] Low N_2 SA_{BET} of only 40 m^2/g was reported at 77 K; however, when CO_2 was used as an adsorbate a surface area of 280-350 m^2/g was calculated. Along with selectivity favouring CO_2 over N_2, when calculating the internal cavity volume for the Noria molecule, it was discovered that there was not enough space for the entire volume of CO_2. This indicated that only a fraction of adsorbed CO_2 was adsorbed internally, implying extrinsic porosity was also available from inefficient molecular packing. The Noria molecule exhibits a hydrophobic internal cavity with volume of 160 $Å^3$ and a window of 5 Å (Figure 21). To our knowledge, Noria was the first *amorphous* porous organic molecular solid to be reported.

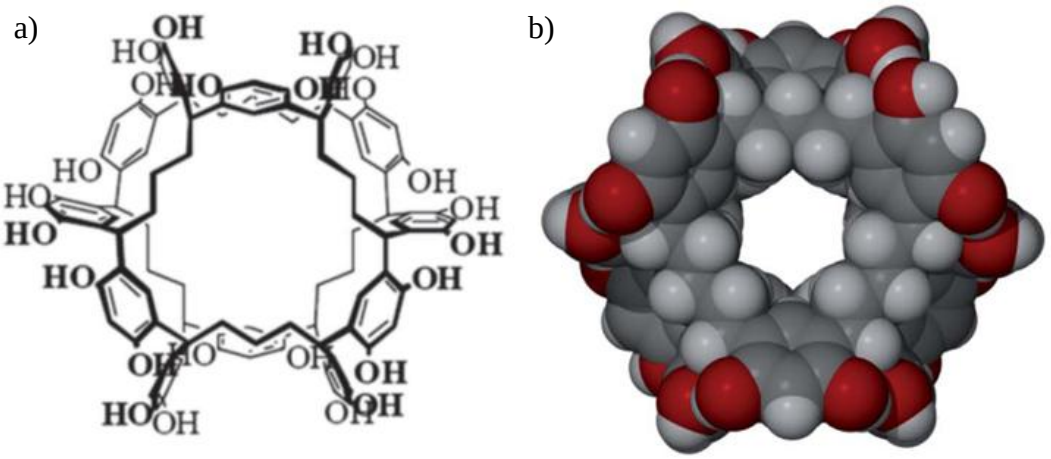

Figure 21: Noria Waterwheel shown by a) schematic and b) space filling representation.[88,90] Unusually, Noria is also porous in the amorphous state.

Porous Organic Cages

Cage-like macrocyclic organic molecules are well known, but until recently they had not been shown to possess permanent porosity. Covalent cage 3 (CC3) was shown through a reversible imine-forming condensation reaction,[91] thermodynamically driven to give a [4+6] imine cage in 2008 by Skawronek *et al.*[92] The molecule was investigated concurrently by Tozawa *et al.* in 2009 alongside two other analogues (denoted CC1 and CC2, also [4+6] imine cages).[1] The covalently-bonded imine CC3 was shown to crystallise in such a fashion that each window in the cage was directly facing a neighbouring cage window.[1] This gave rise to an extended 3D diamondoid network of voids and exhibited N_2 SA_{BET} of 624 m^2/g. CC1, meanwhile, was formally non porous, packing in a window-to-arene conformation so that there was no extended connection between internal pores. CC2 packed in a similar window-to-arene fashion, but with frustrated packing of stacks created by methyl groups from the diamine vertices. This created 1D pore channels between the cages and subsequent N_2 SA_{BET} of 533 m^2/g. More recent publications by our group have shown this original CC3 material to be between 75-80 % crystalline; in the completely amorphous state, N_2 SA_{BET} increases to 859 m^2/g, while a 100 % crystalline sample showed a reduction of N_2 SA_{BET} to 409 m^2/g.[68] CC3 was also recently shown to reversibly adsorb up to 20.1 % water, while also being remarkably

stable to hydrolysis, maintaining structural integrity after boiling in water for 4 hours.[93]

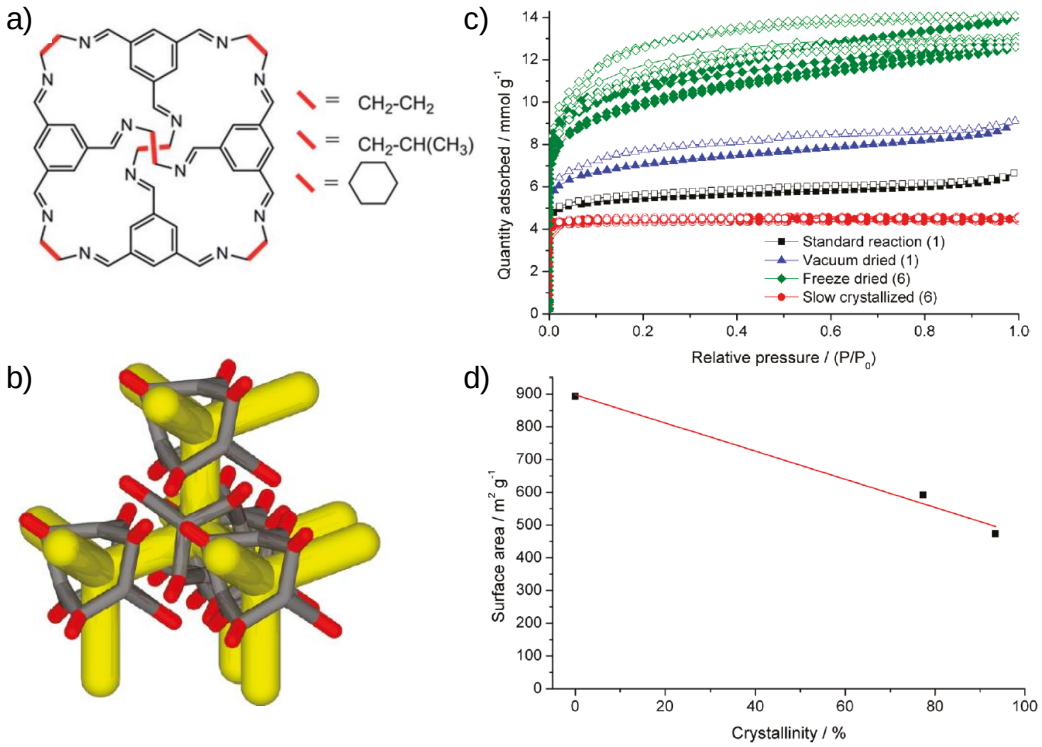

Figure 22: a) Schematic illustration of CC1, CC2 and CC3; b) 3D interconnected diamondoid network of voids (yellow) in crystal structure of CC3; c) N_2 uptake for CC3 when slowly crystallised (red), as formed by standard reaction (black), as vacuum dried (blue) and as freeze-dried and amorphous (green); d) Comparison between surface area and percentage crystallinity for highly crystalline, intermediately crystalline, and amorphous samples of CC3 (images taken from reference).[68]

Originally non-porous upon its discovery in 2009, CC1 was subsequently inter-converted between three separate polymorphs, drastically altering its gas sorption properties (Figure 23).[66] In its original $P2_1/c$ polymorph (1α'), CC1 was nonporous to both N_2 and H_2. When recrystallised from DCM to create a new R3 polymorph (1β'), however, sufficient connected voids were available such that the material became porous to H_2 but still not to N_2. The $P2_1/c$ polymorph (1α') could also be recrystallised from DCM and *o*-xylene to create a third $P2_1$ polymorph (1γ') which showed interconnected voids and was consequently porous to both N_2 and H_2 (N_2

SA_{BET} = 550 m^2/g). CC1 has also been prepared and reduced *in situ* before being successfully employed as a MOF linker.[94]

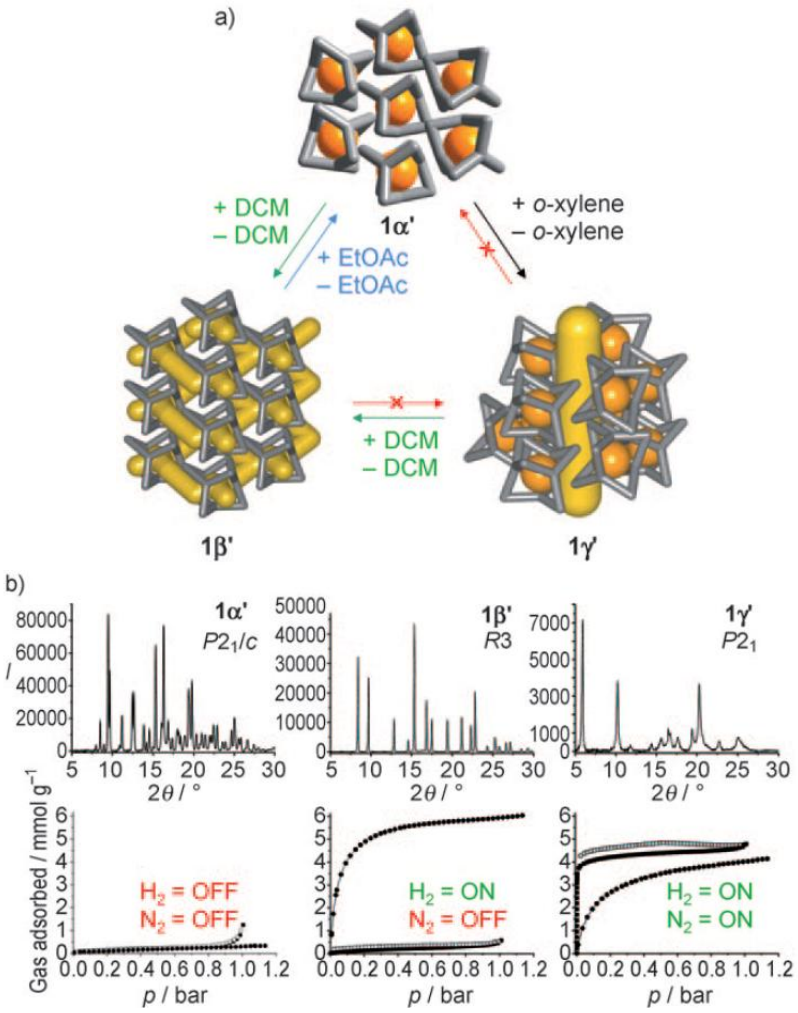

Figure 23: On-Off porosity switching in CC1 showing a) voids and their connectivity (non-connected are orange, connected are yellow) and b) polymorphism of materials as characterised by X-Ray diffraction and their N_2 and H_2 sorption properties.[66]

Attempts were made towards the formation of cages using bulky 1,2-diamines, with the ultimate goal of creating a cage which would contain high levels of both intrinsic and extrinsic porosity.[14] These cages (CC9 and CC10, Figure **24**) consisted of two phenyl rings on the diamine vertices and exhibited N_2 SA_{BET} of 854 m^2/g in a P3 polymorph, which is far higher than CC1 which consists of the same internal dimensions. Unlike previous cages, these cages required harsher synthetic conditions including heating, the use of acid catalyst, and molecular sieves to sequester water in

order to prevent Diaza-Cope side-reactions while also overcoming the steric hindrance encountered using such bulky diamines.

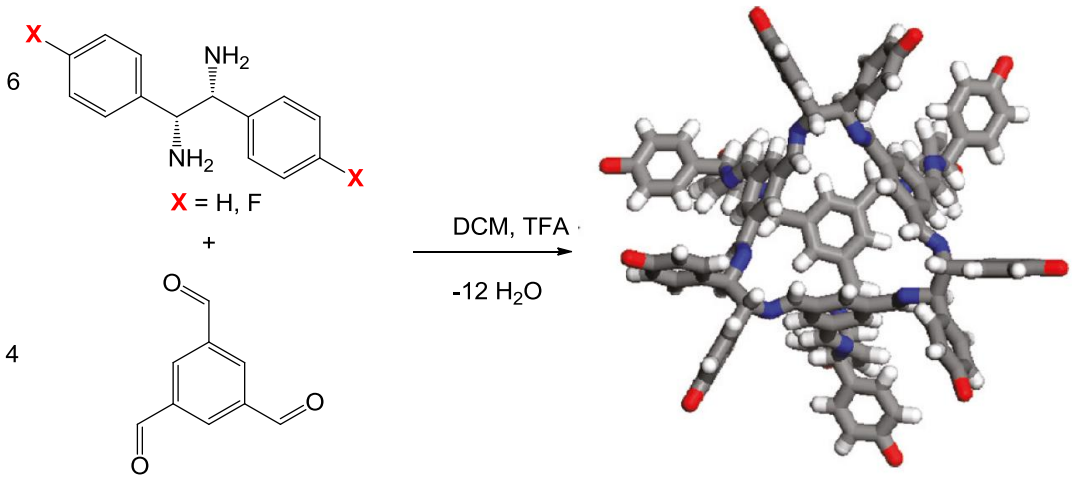

Figure 24: Synthesis of CC9 (X=H) and CC10 (X=F). C, N and H are coloured grey, white and blue respectively.[14]

Jiang *et al.* have also produced a smaller [2+3] "propeller" cage from the reaction of 1,3,5-tri(4-formylphenyl)benzene with 1,5-pentanediamine, which exhibits selective adsorption of H_2 and CO_2 over N_2.[95] H_2/N_2 selectivity was measured as 2.4 at 77 K (total uptake of H_2 was 3.76 mmol/g). CO_2/N_2 selectivity was measured to be 11/1 for at 300 K and 1 bar (total uptake of CO_2 was 0.9 mmol/g). N_2 SA_{BET} is modest at 99 m^2/g when compared to other porous organic cages,[1] although this can be attributed to the smaller propeller cage exhibiting only extrinsic porosity.[3] Jin *et al.* also prepared an organic cage molecule with high CO_2/N_2 adsorption selectivity of 73 at 20 °C and 1 bar. [96] The same group have reported a series of related cage compounds which exhibited CO_2/N_2 selectivity in the range from 36 to 138 at 20 °C and 1 bar, although absolute amounts of gas adsorbed were low (0.1–0.25 mmol/g).[97]

Some of these porous organic cages have also been catenated, and joined together by 'mechanical' bonds, *i.e.*, they are interlocked and not covalently bonded to one another.[98] Catenanes of CC1, CC2 and CC4 (CC4 being the combination of 1,3,5-triformylbenzene and 1,2-cyclopentanediamine hydrochloride)[99] were achieved by synthesis in the presence of trifluoroacetic acid (Figure **25**). However, steric bulk of 1,2-cyclohexanediamine prevents the formation of a catenane for CC3. While these materials did not possess microporosity, they did contain two well-defined cavities per catenated dimer. It was suggested by Hasell *et al*. that such mechanically

interlocked species could prove useful for the modular construction of complex porous materials from preformed 'porous' building blocks,[98] or as hydrophobic direceptors for the self-assembly of supramolecular polymers. [100,101]

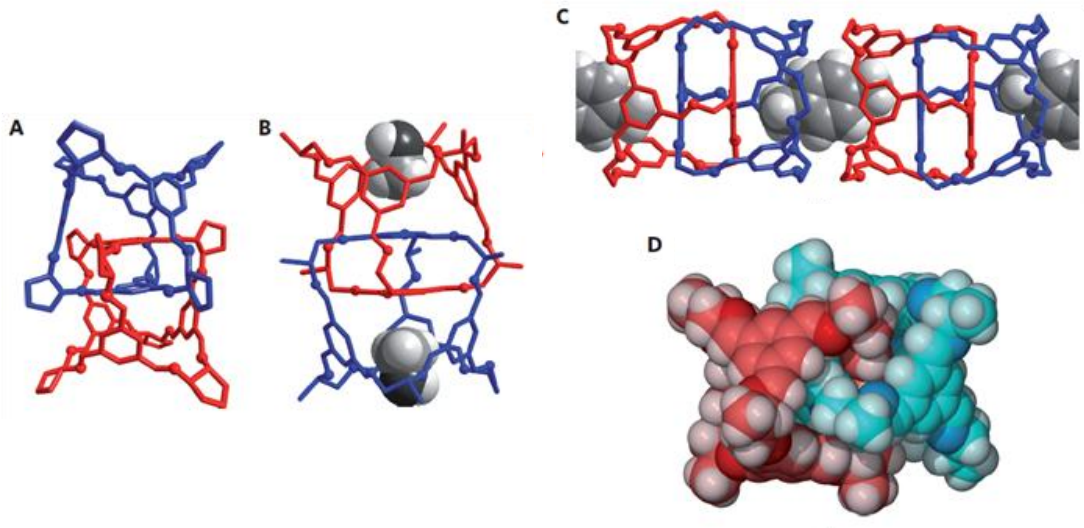

Figure 25: Crystal structures of catenated CC4 (A), CC2 (B) and CC1 (C). Space-filling representation of catenated CC2 (D).[98]

Mastalerz also produced similar cages *via* imine-forming condensation reactions through utilising dialdehyde and triamine reactants, which contained a much larger internal cavity than other organic cages and possessed bulky *t*-butyl groups on the peripheral of the material.[102] When subsequently re-investigated, the same cage exhibited N_2 SA_{BET} of 1375 m^2/g as synthesised from THF.[103] Recent recrystallisation of this cage from DMSO as part of a larger study has offered an alternate polymorph with N_2 SA_{BET} of 2071 m^2/g, the highest value to date for a discrete wholly organic cage.[104] The same group have also published smaller [2+3] cages with N_2 SA_{BET} of 744 m^2/g through condensation of the same triamine and 4,4'dihydroxy-[1,1'biphenyl]-3,3'-dicarbaldehyde, which is the highest surface area for a [2+3] cage to date.[105]

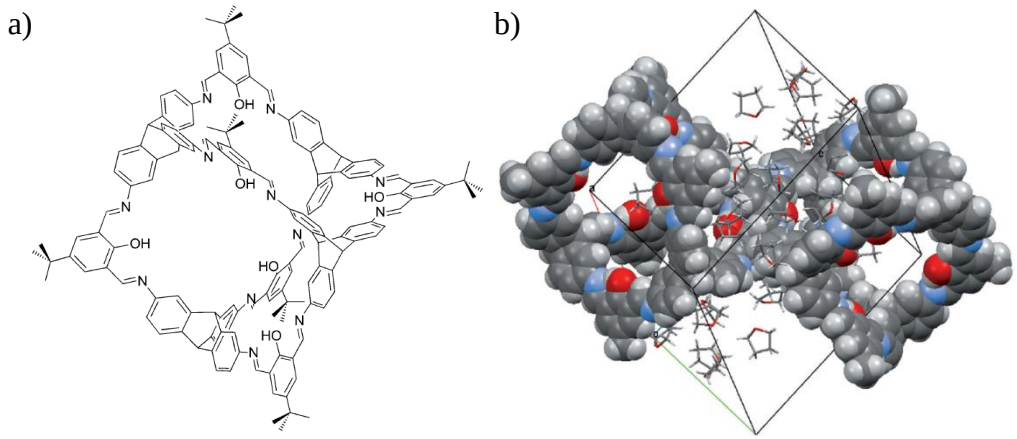

Figure 26: a) Mastalerz cage compound and b) unit cell of the X-Ray crystal structure of compound with cage in space-filling representation and THF in stick motif.[104]

Mastalerz and Oppel have since described the preparation of an entirely extrinsically porous molecular crystal with impressive N_2 SA_{BET} of up to 2796 m^2/g.[106] This rigid triptycene derivative (triptycenetrisbenzimidazolone, denoted TTBI) self-assembles by hydrogen bonds to a porous crystal with one-dimensional channels of about 14 Å diameter. This is by some margin the highest surface area reported so far for a porous organic molecular solid.

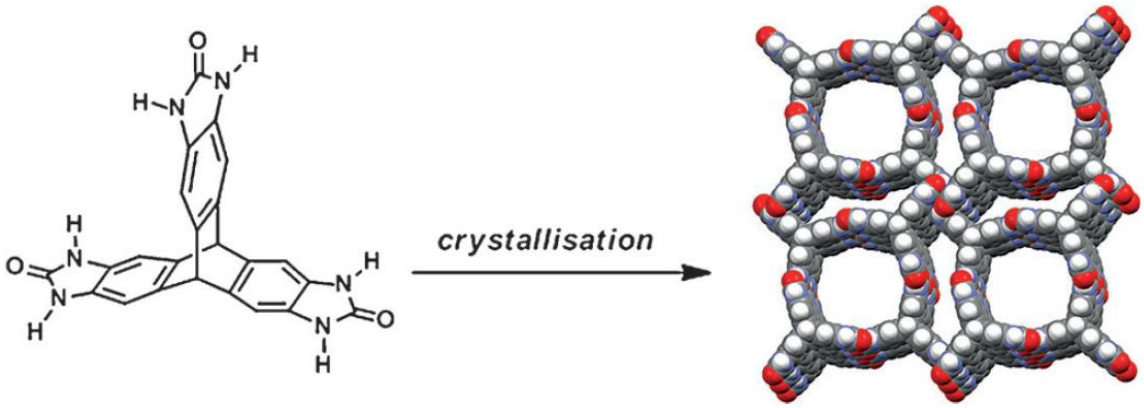

Figure 27: Crystallisation of TTBI to prepare an extrinsically porous molecular crystal[106] – the current 'record holder' for porosity in a molecular crystal.

Lia *et al*. introduced imine bonded nanocapsules on the basis of a one-pot synthesis of resorcinarene derivatives with diamines in high yields. By extensive studies of the reaction conditions they were able to reach high product selectivity.[107-109] More

recently Sun *et al*. have shown these nanocapsules to encapsulate four $CHCl_3$ and three CH_3OH guests in the solid state as determined by X-Ray crystallography.[110,111]

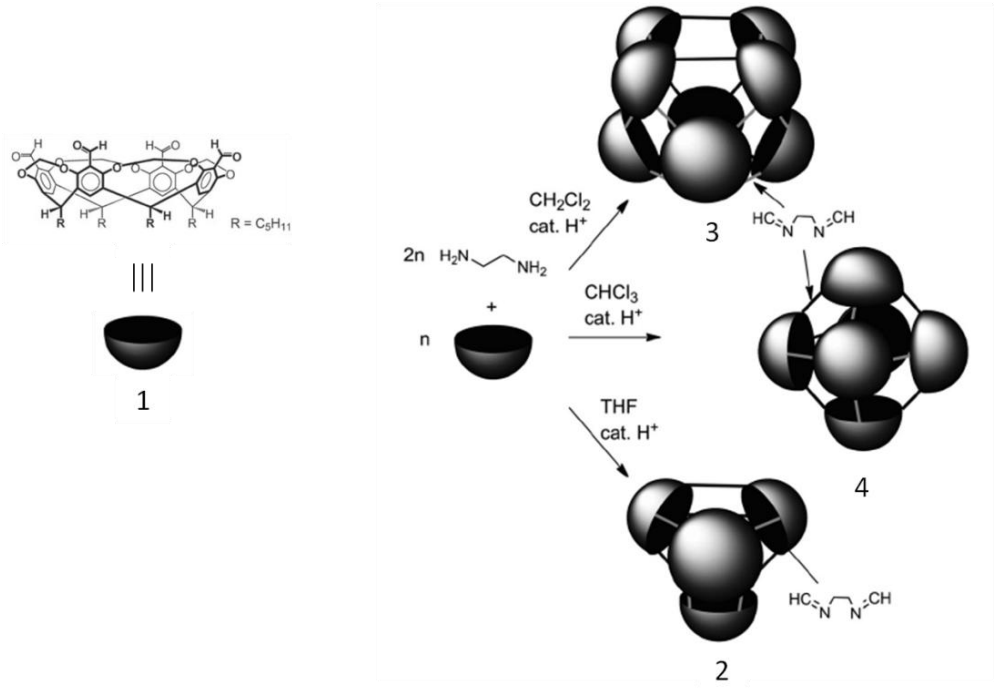

Figure 28: Solvent-dependent condensation of a cavitand (1) with two equivalents of ethylene-1,2-diamine yielding tetrahedral capsule (2) in THF, octahedral capsule (4) in $CHCl_3$ and the square antiprism (3) in CH_2Cl_2.[107,108,112]

Xu and co-workers also designed the synthesis of a [8+12] chiral nanocube by first preparing a trialdehyde corner unit (P)-2 with a cone angle of ~82 °. When reacted with 1,4-phenylenediamine in the presence of a catalytic amount of trifluoroacetic acid (as seen in previous examples of imine cage preparation) the chiral nanocube was afforded. [113] This structure was prepared in mind as a possible nanocapsule as with previous materials prepared by Liu *et al.*, but may yet display porosity like the imine cages prepares by Cooper[1] and Mastalerz groups[103] due to its more rigid nature.

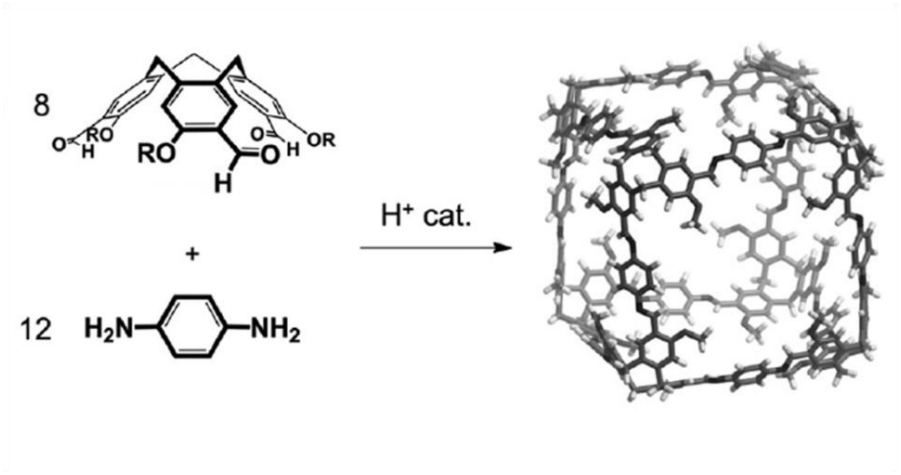

Figure 29: Preparation of a chiral nanocube. R = hexadecyl. Bulky stabilizing R-Groups are not shown, and image is a model, not a crystal structure (image taken from reference).[113]

1.5 Overview

This thesis will describe the preparation of new porous organic cages, their chemical reduction and functionalisation, and the subsequent polymerisation of reduced and functionalised organic cages.

We have aimed to prepare new porous organic cages to demonstrate the importance of solubility and the processing advantages that this brings, while also highlighting the importance of choice of reagents which make up the cage materials. Chapter 3 explores the preparation of a new porous organic cage and its polymorphism, and also looks at the effect of diamine choice in preparation of an organic cage.

Chemical reduction and functionalisation was carried out in the attempt to alter properties of organic cages, including gas sorption and melting points. Chapter 4 looks at the synthetic diversification of the previously-discovered porous organic cages CC1 and CC5 by reduction and subsequent functionalisation.

Finally, in Chapter 5 we explore the polymerisation possibilities of these new class of functionalised organic cages through reaction of the reduced cage itself with bi-functional acid halides, and also by more conventional polymerisation techniques

such as hyper cross-linking, Sonogashira cross-coupling, and Yamamoto homo-coupling.

1.6 References

(1) Tozawa, T.; Jones, J. T. A.; Swamy, S. I.; Jiang, S.; Adams, D. J.; Shakespeare, S.; Clowes, R.; Bradshaw, D.; Hasell, T.; Chong, S. Y.; Tang, C.; Thompson, S.; Parker, J.; Trewin, A.; Bacsa, J.; Slawin, A. M. Z.; Steiner, A.; Cooper, A. I. *Nat. Mater.* **2009**, *8*, 973.

(2) Lydon, D. P.; Campbell, N. L.; Adams, D. J.; Cooper, A. I. *Synth. Commun.* **2011**, *41*, 2146.

(3) Holst, J. R.; Trewin, A.; Cooper, A. I. *Nat. Chem.* **2010**, *2*, 915.

(4) Sing, K. S. W.; Everett, D. H.; Haul, R. A. W.; Moscou, L.; Pierotti, R. A.; Rouquerol, J.; Siemieniewska, T. *Pure Appl. Chem.* **1985**, *57*, 603.

(5) Galarneau, A.; Cambon, H.; Di Renzo, F.; Fajula, F. *Langmuir* **2001**, *17*, 8328.

(6) Hernández, M. A.; Rojas, F.; Lara, V. H. *J. Porous Mater.* **2000**, *7*, 443.

(7) Barbour, L. J. *Chem. Commun.* **2006**, 1163.

(8) Holst, J. R.; Cooper, A. I. *Adv. Mater.* **2010**, *22*, 5212.

(9) Atwood, J. L.; Barbour, L. J.; Jerga, A. *Science* **2002**, *296*, 2367.

(10) Atwood, J. L.; Barbour, L. J.; Jerga, A.; Schottel, B. L. *Science* **2002**, *298*, 1000.

(11) Dalgarno, S. J.; Thallapally, P. K.; Barbour, L. J.; Atwood, J. L. *Chem. Soc. Rev.* **2007**, *36*.

(12) Imashiro, F.; Yoshimura, M.; Fujiwara, T. *Acta Crystallogr. Sect. C.* **1998**, *54*, 1357.

(13) Sozzani, P.; Bracco, S.; Comotti, A.; Ferretti, L.; Simonutti, R. *Angew. Chem. Int. Ed.* **2005**, *44*, 1816.

(14) Bojdys, M. J.; Briggs, M. E.; Jones, J. T. A.; Adams, D. J.; Chong, S. Y.; Schmidtmann, M.; Cooper, A. I. *J. Am. Chem. Soc.* **2011**, *133*, 16566.

(15) http://www1.eere.energy.gov/hydrogenandfuelcells/storage/pdfs/targets_onboard_hydro_storage_explanation.pdf accessed Feb 2012.

(16) http://novell.ftj.agh.edu.pl/doc/pl/seminarium/chapelle.pdf accessed Mar 2012.

(17) http://www1.eere.energy.gov/hydrogenandfuelcells/storage/current_technology.html accessed Feb 2012.

(18) http://www1.eere.energy.gov/hydrogenandfuelcells/storage/tech_status.html accessed Feb 2012.

(19) Schüth, F.; Sing, K. S. W.; Weitkamp, J. *Handbook of porous solids*; Wiley-VCH, 2002.

(20) Kitagawa, H.; Yuki, N. *Carbon* **1981**, *19*, 470.

(21) Li, H.; Eddaoudi, M.; O'Keeffe, M.; Yaghi, O. M. *Nature* **1999**, *402*, 276.

(22) Furukawa, H.; Ko, N.; Go, Y. B.; Aratani, N.; Choi, S. B.; Choi, E.; Yazaydin, A. Ö.; Snurr, R. Q.; O'Keeffe, M.; Kim, J.; Yaghi, O. M. *Science* **2010**, *329*, 424.

(23) Park, K. S.; Ni, Z.; Côté, A. P.; Choi, J. Y.; Huang, R.; Uribe-Romo, F. J.; Chae, H. K.; O'Keeffe, M.; Yaghi, O. M. *Proc. Natl. Acad. Sci* **2006**, *103*, 10186.

(24) Côté, A. P.; Benin, A. I.; Ockwig, N. W.; O'Keeffe, M.; Matzger, A. J.; Yaghi, O. M. *Science* **2005**, *310*, 1166.

(25) Furukawa, H.; Yaghi, O. M. *J. Am. Chem. Soc.* **2009**, *131*, 8875.

(26) Jiang, J.-X.; Su, F.; Trewin, A.; Wood, C. D.; Campbell, N. L.; Niu, H.; Dickinson, C.; Ganin, A. Y.; Rosseinsky, M. J.; Khimyak, Y. Z.; Cooper, A. I. *Angew. Chem. Int. Ed.* **2007**, *46*, 8574.

(27) Dawson, R.; Laybourn, A.; Khimyak, Y. Z.; Adams, D. J.; Cooper, A. I. *Macromolecules* **2010**, *43*, 8524.

(28) Yuan, D.; Lu, W.; Zhao, D.; Zhou, H.-C. *Adv. Mater.* **2011**, 3723.

(29) McKeown, N. B.; Hanif, S.; Msayib, K.; Tattershall, C. E.; Budd, P. M. *Chem. Commun.* **2002**, 2782.

(30) McKeown, N. B.; Makhseed, S.; Budd, P. M. *Chem. Commun.* **2002**, 2780.

(31) Davankov, V. A.; Tsyurupa, M. P. *React. Polym.* **1990**, *13*, 27.

(32) Li, B.; Gong, R.; Wang, W.; Huang, X.; Zhang, W.; Li, H.; Hu, C.; Tan, B. *Macromolecules* **2011**, *44*, 2410.

(33) Kuhn, P.; Antonietti, M.; Thomas, A. *Angew. Chem. Int. Ed.* **2008**, *47*, 3450.

(34) Mastalerz, M.; Hauswald, H.-J. S.; Stoll, R. *Chem. Commun.* **2012**.

(35) Mal, P.; Breiner, B.; Rissanen, K.; Nitschke, J. R. *Science* **2009**, *324*, 1697.

(36) Lim, S.; Kim, H.; Selvapalam, N.; Kim, K.-J.; Cho, S. J.; Seo, G.; Kim, K. *Angew. Chem. Int. Ed.* **2008**, *47*, 3352.

(37) Sozzani, P.; Comotti, A.; Simonutti, R.; Meersmann, T.; Logan, J. W.; Pines, A. *Angew. Chem. Int. Ed.* **2000**, *39*, 2695.

(38) Msayib, K. J.; Book, D.; Budd, P. M.; Chaukura, N.; Harris, K. D. M.; Helliwell, M.; Tedds, S.; Walton, A.; Warren, J. E.; Xu, M.; McKeown, N. B. *Angew. Chem.* **2009**, *121*, 3323.

(39) Barrer, R. M.; Shanson, V. H. *J. Chem. Soc., Chem. Commun.* **1976**, 333.

(40) Meier, W. M.; Moeck, H. J. *J. Solid State Chem.* **1979**, *27*, 349.

(41) Hoskins, B. F.; Robson, R. *J. Am. Chem. Soc.* **1990**, *112*, 1546.

(42) Gable, R. W.; Hoskins, B. F.; Robson, R. *J. Chem. Soc., Chem. Commun.* **1990**, 1677.

(43) Abrahams, B. F.; Hoskins, B. F.; Robson, R. *J. Am. Chem. Soc.* **1991**, *113*, 3606.

(44) Banerjee, R.; Phan, A.; Wang, B.; Knobler, C.; Furukawa, H.; O'Keeffe, M.; Yaghi, O. M. *Science* **2008**, *319*, 939.

(45) Banerjee, R.; Furukawa, H.; Britt, D.; Knobler, C.; O'Keeffe, M.; Yaghi, O. M. *J. Am. Chem. Soc.* **2009**, *131*, 3875.

(46) Severin, K. *Dalton Trans.* **2009**, 5254.

(47) Kuhn, P.; Forget, A. l.; Su, D.; Thomas, A.; Antonietti, M. *J. Am. Chem. Soc.* **2008**, *130*, 13333.

(48) Ren, S.; Bojdys, M. J.; Dawson, R.; Laybourn, A.; Khimyak, Y. Z.; Adams, D. J.; Cooper, A. I. *Adv. Mater.* **2012**, *24*, 2357.

(49) McKeown, N. B.; Budd, P. M.; Book, D. *Macromol. Rapid Commun.* **2007**, *28*, 995.

(50) Budd, P. M.; Butler, A.; Selbie, J.; Mahmood, K.; McKeown, N. B.; Ghanem, B.; Msayib, K.; Book, D.; Walton, A. *PCCP* **2007**, *9*, 1802.

(51) Budd, P. M.; McKeown, N. B.; Fritsch, D. *J. Mater. Chem.* **2005**, *15*, 1977.

(52) Du, N.; Park, H. B.; Robertson, G. P.; Dal-Cin, M. M.; Visser, T.; Scoles, L.; Guiver, M. D. *Nat. Mater.* **2011**, *10*, 372.

(53) Ben, T.; Ren, H.; Ma, S.; Cao, D.; Lan, J.; Jing, X.; Wang, W.; Xu, J.; Deng, F.; Simmons, J. M.; Qiu, S.; Zhu, G. *Angew. Chem. Int. Ed.* **2009**, *48*, 9457.

(54) Tsyurupa, M. P.; Davankov, V. A. *React. Funct. Polym.* **2002**, *53*, 193.

(55) Lee, J.-Y.; Wood, C. D.; Bradshaw, D.; Rosseinsky, M. J.; Cooper, A. I. *Chem. Commun.* **2006**, 2670.

(56) Germain, J.; Hradil, J.; Fréchet, J. M. J.; Svec, F. *Chem. Mater.* **2006**, *18*, 4430.

(57) Ahn, J.-H.; Jang, J.-E.; Oh, C.-G.; Ihm, S.-K.; Cortez, J.; Sherrington, D. C. *Macromolecules* **2005**, *39*, 627.

(58) Fontanals, N.; Manesiotis, P.; Sherrington, D. C.; Cormack, P. A. G. *Adv. Mater.* **2008**, *20*, 1298.

(59) Wood, C. D.; Tan, B.; Trewin, A.; Niu, H.; Bradshaw, D.; Rosseinsky, M. J.; Khimyak, Y. Z.; Campbell, N. L.; Kirk, R.; Stöckel, E.; Cooper, A. I. *Chem. Mater.* **2007**, *19*, 2034.

(60) Dawson, R.; Cooper, A. I.; Adams, D. J. *Prog. Polym. Sci.* **2012**, *37*, 530.

(61) Cooper, A. I. *Angew. Chem. Int. Ed.* **2012**.

(62) Chinchilla, R.; Nájera, C. *Chem. Rev.* **2007**, *107*, 874.

(63) Budd, P. M.; Ghanem, B. S.; Makhseed, S.; McKeown, N. B.; Msayib, K. J.; Tattershall, C. E. *Chem. Commun.* **2004**, 230.

(64) Palkovits, R.; Antonietti, M.; Kuhn, P.; Thomas, A.; Schüth, F. *Angew. Chem. Int. Ed.* **2009**, *48*, 6909.

(65) Jiang, J.-X.; Wang, C.; Laybourn, A.; Hasell, T.; Clowes, R.; Khimyak, Y. Z.; Xiao, J.; Higgins, S. J.; Adams, D. J.; Cooper, A. I. *Angew. Chem. Int. Ed.* **2011**, *50*, 1072.

(66) Jones, J. T. A.; Holden, D.; Mitra, T.; Hasell, T.; Adams, D. J.; Jelfs, K. E.; Trewin, A.; Willock, D. J.; Day, G. M.; Bacsa, J.; Steiner, A.; Cooper, A. I. *Angew. Chem. Int. Ed.* **2011**, *50*, 749.

(67) Jones, J. T. A.; Hasell, T.; Wu, X.; Bacsa, J.; Jelfs, K. E.; Schmidtmann, M.; Chong, S. Y.; Adams, D. J.; Trewin, A.; Schiffman, F.; Cora, F.; Slater, B.; Steiner, A.; Day, G. M.; Cooper, A. I. *Nature* **2011**, *474*, 367.

(68) Hasell, T.; Chong, S. Y.; Jelfs, K. E.; Adams, D. J.; Cooper, A. I. *J. Am. Chem. Soc.* **2011**, *134*, 588.

(69) Bezzu, C. G.; Helliwell, M.; Warren, J. E.; Allan, D. R.; McKeown, N. B. *Science* **2010**, *327*, 1627.

(70) Tranchemontagne, D. J.; Ni, Z.; O'Keeffe, M.; Yaghi, O. M. *Angew. Chem. Int. Ed.* **2008**, *47*, 5136.

(71) Schmitt, F.; Freudenreich, J.; Barry, N. P. E.; Juillerat-Jeanneret, L.; Süss-Fink, G.; Therrien, B. *J. Am. Chem. Soc.* **2011**.

(72) Dianin, A. P. *Russ. Phys. Chem. Soc.* **1914**, *46*, 1.

(73) Jacobs, T.; Bredenkamp, M. W.; Lloyd, G. O. *Acta Crystallogr. Sect. E.* **2006**, *62*, 4400.

(74) Allcock, H. R.; Siegel, L. A. *J. Am. Chem. Soc.* **1964**, *86*, 5140.

(75) Couderc, G.; Hertzsch, T.; Behrnd, N. R.; Krämer, K.; Hulliger, J. *Microporous Mesoporous Mater.* **2006**, *88*, 170.

(76) Hertzsch, T.; Gervais, C.; Hulliger, J.; Jaeckel, B.; Guentay, S.; Bruchertseifer, H.; Neels, A. *Adv. Funct. Mater.* **2006**, *16*, 268.

(77) Tian, J.; Thallapally, P.; Liu, J.; Exarhos, G. J.; Atwood, J. L. *Chem. Commun.* **2011**, *47*, 701.

(78) Gutsche, C. D. *Calixarenes: An Introduction* 2008.

(79) Thallapally, P. K.; McGrail, B. P.; Atwood, J. L.; Gaeta, C.; Tedesco, C.; Neri, P. *Chem. Mater.* **2007**, *19*, 3355.

(80) Tedesco, C.; Erra, L.; Brunelli, M.; Cipolletti, V.; Gaeta, C.; Fitch, A. N.; Atwood, J. L.; Neri, P. *Chem. Eur. J.* **2010**, *16*, 2371.

(81) Kim, H.; Kim, Y.; Yoon, M.; Lim, S.; Park, S. M.; Seo, G.; Kim, K. *J. Am. Chem. Soc.* **2010**, *132*, 12200.

(82) Tian, J.; Ma, S.; Thallapally, P. K.; Fowler, D.; McGrail, B. P.; Atwood, J. L. *Chem. Commun.* **2011**, *47*, 7626.

(83) Larsson, K. *Nature* **1983**, *304*, 664.

(84) Görbitz, C. H.; Gundersen, E. *Acta Crystallogr. Sect. C.* **1996**, *52*, 1764.

(85) Comotti, A.; Bracco, S.; Distefano, G.; Sozzani, P. *Chem. Commun.* **2009**, 284.

(86) Afonso, R. V.; Durão, J.; Mendes, A.; Damas, A. M.; Gales, L. *Angew. Chem. Int. Ed.* **2010**, *49*, 3034.

(87) Moure, A.; Luis, S. V.; Alfonso, I. *Chem. Eur. J.* **2012**, n/a.

(88) Kudo, H.; Hayashi, R.; Mitani, K.; Yokozawa, T.; Kasuga, N. C.; Nishikubo, T. *Angew. Chem. Int. Ed.* **2006**, *45*, 7948.

(89) Tian, J.; Thallapally, P. K.; Dalgarno, S. J.; McGrail, P. B.; Atwood, J. L. *Angew. Chem. Int. Ed.* **2009**, *48*, 5492.

(90) Tian, J.; Thallapally, P. K.; McGrail, B. P. *Cryst. Eng. Comm*, **2012**.

(91) Belowich, M. E.; Stoddart, J. F. *Chem. Soc. Rev.* **2012**.

(92) Skowronek, P.; Gawronski, J. *Org. Lett.* **2008**, *10*, 4755.

(93) Hasell, T.; Schmidtmann, M.; Smith, M.; Stone, C.; Cooper, A. I. *Chem. Commun.* **2012**.

(94) Swamy, S. I.; Bacsa, J.; Jones, J. T. A.; Stylianou, K. C.; Steiner, A.; Ritchie, L. K.; Hasell, T.; Gould, J. A.; Laybourn, A.; Khimyak, Y. Z.; Adams, D. J.; Rosseinsky, M. J.; Cooper, A. I. *J. Am. Chem. Soc.* **2010**, *132*, 12773.

(95) Jiang, S.; Bacsa, J.; Wu, X.; Jones, J. T. A.; Dawson, R.; Trewin, A.; Adams, D. J.; Cooper, A. I. *Chem. Commun.* **2011**.

(96) Jin, Y.; Voss, B. A.; Noble, R. D.; Zhang, W. *Angew. Chem. Int. Ed.* **2010**, *49*, 6348.

(97) Jin, Y.; Voss, B. A.; Jin, A.; Long, H.; Noble, R. D.; Zhang, W. *J. Am. Chem. Soc.* **2011**, *133*, 6650.

(98) Hasell, T.; Wu, X.; Jones, J. T. A.; Bacsa, J.; Steiner, A.; Mitra, T.; Trewin, A.; Adams, D. J.; Cooper, A. I. *Nat. Chem.* **2010**, *2*, 750.

(99) Mitra, T.; Wu, X.; Clowes, R.; Jones, J. T. A.; Jelfs, K. E.; Adams, D. J.; Trewin, A.; Bacsa, J.; Steiner, A.; Cooper, A. I. *Chem. Eur. J.* **2011**, *17*, 10235.

(100) Roosma, J.; Mes, T.; Leclère, P.; Palmans, A. R. A.; Meijer, E. W. *J. Am. Chem. Soc.* **2008**, *130*, 1120.

(101) Brunsveld, L.; Folmer, B. J. B.; Meijer, E. W.; Sijbesma, R. P. *Chem. Rev.* **2001**, *101*, 4071.

(102) Mastalerz, M. *Chem. Commun.* **2008**, 4756.

(103) Mastalerz, M.; Schneider, M. W.; Oppel, I. M.; Presly, O. *Angew. Chem. Int. Ed.* **2011**, *50*, 1046.

(104) Schneider, M. W.; Oppel, I. M.; Ott, H.; Lechner, L. G.; Hauswald, H.-J. S.; Stoll, R.; Mastalerz, M. *Chem. Eur. J.* **2012**, *18*, 836.

(105) Schneider, M. W.; Oppel, I. M.; Mastalerz, M. *Chem. Eur. J.* **2012**, *18*, 4156.

(106) Mastalerz, M.; Oppel, I. M. *Angew. Chem. Int. Ed.* **2012**, *51*, 5252.

(107) Liu, X.; Liu, Y.; Li, G.; Warmuth, R. *Angew. Chem. Int. Ed.* **2006**, *45*, 901.

(108) Liu, X.; Warmuth, R. *J. Am. Chem. Soc.* **2006**, *128*, 14120.

(109) Liu, Y.; Liu, X.; Warmuth, R. *Chem. Eur. J.* **2007**, *13*, 8953.

(110) Sun, J.; Bennett, J. L.; Emge, T. J.; Warmuth, R. *J. Am. Chem. Soc.* **2011**, *133*, 3268.

(111) Sun, J.; Warmuth, R. *Chem. Commun.* **2011**.

(112) Rue, N. M.; Sun, J.; Warmuth, R. *Isr. J. Chem.* **2011**, *51*, 743.

(113) Xu, D.; Warmuth, R. *J. Am. Chem. Soc.* **2008**, *130*, 7520.

Chapter 2

Characterisation Methods

Table of Contents

2.1 Gas Sorption

Gas sorption isotherms for cages and polymers were collected by Dr. R. Dawson (Micromeritics) or the author (Quantachrome). Approximately 100 mg of sample was used for sorption analysis, weighed accurately by difference to four decimal places before analysis and after rigorous degas. All samples were degassed at 120 °C for at least 15 hours under a vacuum of 10^{-5} bar.

Surface areas and pore size distributions of materials were measured by nitrogen adsorption and desorption at 77.3 K using either a Micromeritics ASAP 2420, ASAP 2020 volumetric adsorption analyzer, or Quantachrome Nova 4200 (Figure 1). Pore size distributions and pore volumes were derived from the adsorption branches of the isotherms using the non-local density functional theory model (NL-DFT) for pillared clay with cylindrical pore geometries found within the Micromeritics ASAP software.

Hydrogen isotherms up to 1.1 bar were measured at 77.3 K and 87.3 K using a Micromeritics ASAP 2420 volumetric adsorption analyzer.

Figure 1: Micromeritics ASAP 2020 (left), 2420 (centre) and Quantachrome Nova 4200 (right) gas sorption analyzers.

2.1.1 Gas Sorption Theory

The most common method for characterising a porous solid is to measure the sorption of gases to the solid surface. Gases (sorbate) can interact with a solid surface (sorbent) in two distinct ways; chemisorption and physisorption. Chemisorption occurs when interactions between a gas and a solid surface are strong, with chemical bonds formed between the sorbent and sorbate. Physisorption describes the formation of weaker van der Waals interactions between the sorbent and sorbate.

Langmuir Theory

There are two major models used to determine adsorption of gases to a solid surface, with the first being the Langmuir model.[1-4] The Langmuir model accounts only for monolayer formation.

The Langmuir model, however, relies on a number of assumptions which may not always be satisfied by real materials:

a) The solid surface is uniform and contains a number of equivalent sites, each of which may be occupied by only one molecule of adsorbate
b) A dynamic equilibrium exists between the gas and the adsorbed layer at constant temperature
c) Adsorbate molecules from the gas phase are continually colliding with the surface. If they impact on a vacant adsorption site, they form a bond with the surface and stick. If they strike a filled site, they are reflected back into the gas phase
d) Once adsorbed, the molecules are localised (they cannot migrate to an adjacent site) and enthalpy of adsorption per site remains constant irrespective of coverage

The Langmuir model assumes that (at constant temperatures and pressure) the rate of molecules (M) sticking to the surface (adsorption) (S) and the rate of molecules leaving the surface (desorption) are in dynamic equilibrium:

$$M_{(g)} + S_{(surface\ site)} \rightleftharpoons M\text{–}S$$

Consequently, the rate constant for adsorption/desorption (K) can be defined as follows where k_{ads} and k_{des} are the rate constants for adsorption and desorption steps:

$$K = k_{ads} / k_{des}$$

The coverage of the surface is the fractional surface coverage θ. This can be defined as the total number of occupied sites ($N_{occupied}$) divided by the total number of sites (N_{total}), which is:

$$\theta = N_{occupied} / N_{total}$$

The rate of adsorption is proportional to the pressure of the gas (P) and the number of sites unoccupied, whereas the rate of desorption is proportional to the number of occupied sites.

$$\text{rate of adsorption} = k_{ads}P(1 - \theta)$$
$$\text{rate of desorption} = k_{des}\theta$$

According to the above, rate of desorption is independent of the pressure, P, but will depend on θ. However, P does determine θ so there is an 'indirect' influence on the rate of adsorption. At equilibrium rate of adsorption and desorption are equal:

$$k_{ads}P(1 - \theta) = k_{des}\theta$$

Which when rearranged equates to:

$$K = \theta / P(1 - \theta)$$
or
$$\theta = KP / 1+KP$$

This is known as the Langmuir equation for associative adsorption and predicts how the fractional monolayer coverage θ of adsorbate changes with P.

Coverage θ can also be defined in terms of relative masses and volumes. In terms of volumes, this is the volume of gas adsorbed (V_{ads}) divided by the volume of gas corresponding to monolayer coverage (V_{mono}).

$$\theta = V_{ads}/V_{mono}$$

The Langmuir equation can then be arranged to form a linear equation

$$P/V_{ads} = (1/KV_{mono}) + (P/V_{mono})$$

A plot of P / V_{ads} against P will give a linear graph from which the surface area can be determined by multiplying V_{mono} by the area of one molecule A

$$SA_{Langmuir} = V_{mono}\, A$$

Brunauer-Emmett-Teller Theory

The second model for determination of the adsorption of gases to a solid surface is the BET theory. [2-5] An extension of the Langmuir model, BET theory accounts for the formation of multilayers of adsorbed gas molecules. As with the Langmuir model it is assumed that the surface is uniform in nature. The BET theory also makes a number of new assumptions:

a) Adsorption of the first adsorbate layer is assumed to take place on an array of surface sites of uniform energy.
b) Second layer adsorption can only take place on top of first, third on top of second, fourth on top of third, etc. When $P = P_0$ (the saturated vapour pressure of the adsorbate), an infinite number of layers will form.
c) At equilibrium, the rates of condensation and evaporation are the same for each individual layer.
d) When the number of adsorbed layers is greater than or equal to two, equilibrium constants K^0 are equal and the corresponding value of ΔH_{ads} = -

ΔH_{des}. For the first adsorbed layer, the enthalpy of adsorption is ΔH_{ads} as in the Langmuir case.

As with the Langmuir theory, fractional coverage is given by θ and the Langmuir isotherm can be applied to each layer of adsorption. This leads to the BET equation:

$$\theta = \frac{c\left(\frac{P}{P_0}\right)}{\left(1-\frac{P}{P_0}\right)\left(1+\frac{(c-1)\,P}{P_0}\right)}$$

Where:

$$c = e^{(\Delta H_{ads} - \Delta H_{liq})/\mathrm{RT}}$$

This can be rearranged to give a linear equation:

$$\frac{P}{V_{ads}\left(\frac{P_0}{P}\right)} = \frac{1}{cV_\infty} + \frac{(c-1)P}{cV_\infty}\frac{P}{P_0}$$

Where a plot of $P/V_{ads}(P_0/P)$ against P/P_0 will give a linear plot when the BET equation is valid. From this plot, c and V_∞ can be obtained and hence the surface area.

Isotherm Classification

The majority of sorption isotherms may be grouped in to six categories (Figure 2a).[6] Type I isotherms indicate a microporous solid, where large uptakes occur at low pressures. Here, uptake is limited by accessible pore volume rather than surface area. A Type II isotherm indicates macroporosity where unrestricted layers of adsorbates form. Point B is used to indicate the point at which monolayer adsorption is complete, and multilayers begin to form. Type III isotherms are less common, with monolayer formation absent and absorbate-absorbate interactions playing a much more important role. Type IV isotherms are indicative of a mesoporous material and are similar to Type I and II isotherms at lower pressures due to monolayer formation. At higher pressures, larger volumes of gas are adsorbed due to condensation in mesopores, which shows hysteresis on desorption. Type V isotherms are also rare,

and related to Type III isotherms in that adsorbate-adsorbate interactions are weak. Type VI isotherms possess steps in adsorption, related to stepwise filling of pores with discrete sizes. Step-height represents monolayer capacity for each adsorbed layer.

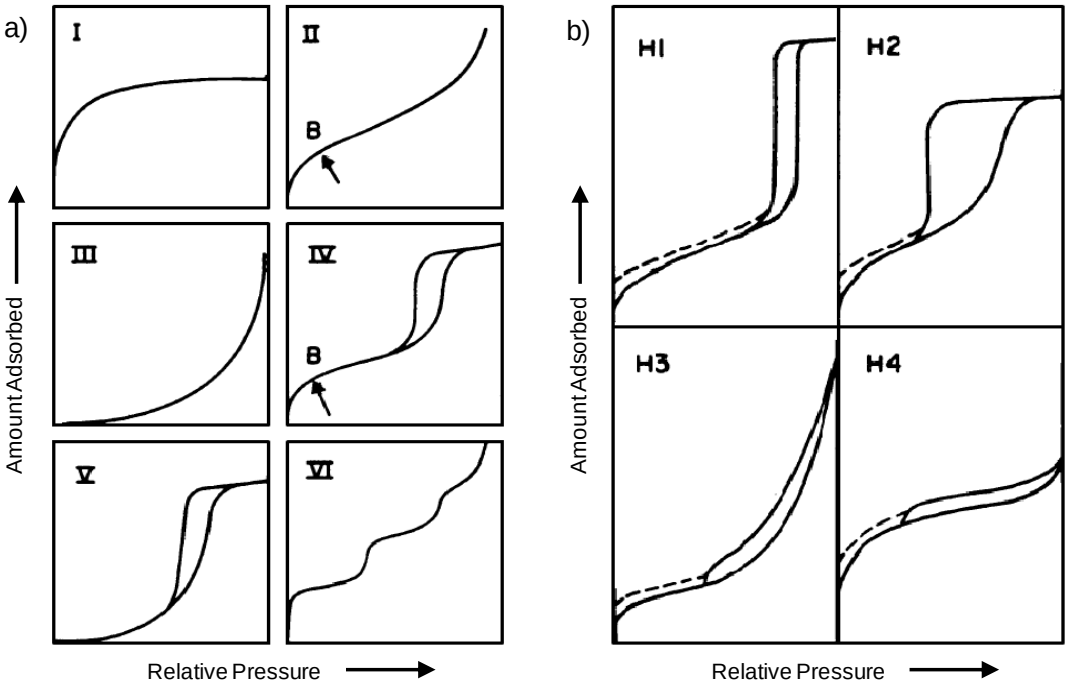

Figure 2: a) Six main physisorption isotherms b) Four types of hysteresis (adapted from reference).[6]

Hystereses appear as a 'loop' in an isotherm created by different adsorption and desorption patterns, and are often a result of capillary condensation in mesoporous structures (Figure 2b). The most extreme examples of hysteresis loops are H1 and H4. In H1, the adsorption and desorption branches are near-vertical and parallel to one another whereas in H4 they are horizontal. H2 and H3 can be described as intermediates of H1 and H4.[6] A common feature of hysteresis loops is closing of the loop at ~ 0.42 P/P_0 when nitrogen gas is used at 77 K. H1 hysteresis is usually found in materials where pores have a narrow distribution in size, while H2 are more common in materials where pore size distribution is less uniform. H3 and H4 are often associated with narrow slit-like pores, with H3 associated with microporosity due to its Type I isotherm shape.

2.2 X-Ray Diffraction

Powder X-ray (pXRD) analysis was run by either Dr. J. T. A. Jones using a Panalytical X'Pert PRO HTS X-Ray Diffractometer or by Dr. S. Chong using a Bruker Advance D8 diffractometer with Ge-monochromated Cu Kα1 radiation and a LynxEye PSD in transmission mode on spinning samples held in 1 mm diameter special glass capillaries. High-resolution synchrotron pXRD data were collected on the I11 beamline at Diamond Light Source ($\lambda = 0.826141$ Å) in transmission geometry using a capillary spinner.

Single crystal X-ray analysis was performed by Dr. M. Schmidtmann while all single crystals were grown by the author. Data was collected either in the department on a Rigaku VariMax rotating anode diffractometer with a Saturn724+ CCD detector and graphite monochromated Mo radiation at 93K or on the small molecule single crystal beamline I19, Diamond Light Source, Didcot, UK ($\lambda = 0.6889$ Å, CrystalLogic Kappa 3 circle goniometer, Rigaku Saturn724+ detector).

2.2.1 X-Ray Diffraction Theory

X-rays are a form of electromagnetic radiation with wavelengths in the range of 10 to 0.01 nm. [7] They are highly penetrating rays which are produced when high energy electrons strike a metal target, normally copper or tungsten, and the metal atom loses an electron. When the resulting vacancy is filled with a higher energy level electron, characteristic X-rays are emitted.

Diffraction is caused by the interference in the path of the wave by regular objects, resulting in a diffraction pattern. It was first suggested by Max von Laue[8] that X-rays may be diffracted when interacting with a crystal. This is due to the wavelength of X-rays being in the same range as crystal lattice spacing. X-ray diffraction (XRD) has become a vital and widely used technique and led to W.H Bragg and son, W.L Bragg, designing a spectrometer to measure diffraction patterns and also producing a law of diffraction, known as Bragg's law.[9]

Atoms within an X-ray beam scatter the X-rays coherently in all directions. These interfere constructively in certain directions if the sample is crystalline, giving Bragg peaks, or reflections which can be determined using the Bragg equation:

$$n\lambda = 2d \sin\theta$$

Bragg diffraction by a crystal occurs as seen in Figure 3.

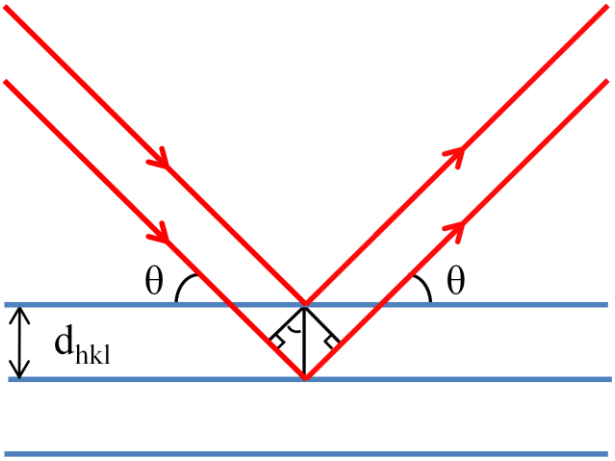

Figure 3: Bragg diffraction by a crystal.

Typically, pXRD patterns are presented as diffracted intensity as a function of the diffraction angle, 2θ. The pattern results from the sum of diffraction from crystallites in all possible orientations and therefore all possible *hkl* planes. It is possible to use Miller indices (*hkl*) to index the lattice planes present. The d-spacings of observed reflections, as calculated from 2θ values, are characteristic of its unit cell parameters and the symmetry of the material. Unit cell dimensions are calculated from the interplanar spacings, d *via* appropriate equations.

2.3 Solution Nuclear Magentic Resonance Spectroscopy

^{1}H NMR spectra were recorded at 400.13 MHz using a Bruker Avance 400 NMR spectrometer fitted with a Samplejet autosampling robot. Low temperature ^{1}H NMR spectra were recorded at -50 °C or -70 °C. ^{13}C NMR spectra were recorded at 100.6

MHz. Deuterated solvents as specified were used and obtained from Sigma-Aldrich. Spectra are referenced to tetramethylsilane (TMS).

2.4 Infrared Spectroscopy

IR spectra were collected on a Bruker Tensor 27 spectrometer. Samples were analyzed as KBr disks for 16 scans with a resolution of 4 cm^{-1}. Spectra were recorded in transmission mode.

2.5 Mass Spectrometry

Accurate Mass Spectrometry was collected by the University of Liverpool's Chemistry Department Service by Ms. M. McCarron and Mrs. J. Ellis using a Micromass LCT Mass Spectrometer, with cone voltage of 100 V in methanol.

Matrix-assisted laser desorption/ionization time-of-flight (MALDI-TOF) mass spectrometry was carried out by Dr. M. Prescott within the Univeristy of Liverpool Biosciences Department using a Waters Micromass M@LDI benchtop mass spectrometer with a-cyano-4-hydroxy-cinnamic acid matrix. A saturated solution of the matrix was prepared in 50 % acetonitrile, before applying 2 mL to the target followed by a 2 mL of sample followed by a further 2 mL of matrix. The voltages used are Pulse Voltage 3400 V and Source Voltage 16,000 V. MALDI was also collected by Dr. J. Behrendt using a Shimadzu Biotech AXIMA Confidence MALDI mass spectrometer in reflectron mode or linear (positive) mode with *trans*-2-[3-(4-*tert*-butylphenyl)-2-methyl-2-propenylidene]malononitrile (DCTB) as matrix in the University of Manchester.

2.6 Scanning Electron Microscopy/ Energy-dispersive X-ray Spectroscopy

Images were collected by Dr. Tom Hasell or Dr. Robert Dawson. High resolution imaging of the materials morphology was achieved using a Hitachi S-4800 cold Field Emission Scanning Electron Microscope (FE-SEM). The dry samples were

prepared on 15 mm Hitachi M4 aluminium stubs using either silver dag or an adhesive high purity carbon tab. The samples were then coated with a 2 nm layer of gold using an Emitech K550X automated sputter coater. The FE-SEM measurement scale bar was calibrated using certified SIRA calibration standards. Imaging was conducted at a working distance of 8 mm and a working voltage of 3 kV using a mix of upper and lower secondary electron detectors. Energy-dispersive X-ray Spectroscopy (EDX) analysis was conducted at a working distance of 15 mm and a working voltage of 30 kV, using an Oxford Instruments 7200 EDX detector.

2.7 Thermogravimetric Analysis

Thermogravimetric Analysis (TGA) analysis was carried out using a Q5000IR TGA (TA instruments) with an automated vertical overhead thermobalance. The samples were heated at a rate of 5 °C /min under a flow of nitrogen to 1000 °C.

2.8 High Performance Liquid Chromatography

High Performance Liquid Chromatography (HPLC) was collected using a Thermo Scientific Accela U-HPLC System. Dual columns were used (Hypersil GOLD Phenyl, 150 x 4.6 mm, 5 µm (SN 0591330K, Lot 9193) linked to Hypersil GOLD, 150 x 4.6 mm, 5 µm, (SN 1284371N, Lot 9231)). The mobile Phase used for separation was MeOH, at a flow rate was 0.5 mL/min. The injection volume was 10 µL and the sample concentration was 0.1 mg/mL in MeOH. The column oven temperature was set to 30 °C.

2.9 Differential Scanning Calorimetry

Differential Scanning Calorimetry (DSC) analysis was carried out using a TA Instruments Q2000 DSC. Samples were heated/cooled at a rate of 5 °C /min over three cycles between -20 °C and 300 °C.

2.10 Elemental Analysis

Elemental (CHN) analysis was carried out by Mrs. Jean Ellis within the departmental service at the University of Liverpool.

2.11 High-Throughput Screening

High-throughput screening for polymorphism studies were carried out using a ChemSpeed ASW 2000 synthesis platform. Experiments were designed using AutoSuite Workflow Management software. Upon completion of sample preparation and after subsequent slow evaporation, high-throughput drying was carried out using a Combidancer infrared vortex evaporator.

2.12 Atomistic Simulations

Molecular models were generated from X-ray crystallographic data structure using Materials Studio 5.0 (Accelrys). Connolly surfaces were calculated by rolling a probe molecule (nitrogen, radius 1.82 Å), across the substrate, the interface taken from the contact point of the probe molecule.[10]

2.13 References

(1) Langmuir, I. *J. Am. Chem. Soc.* **1916**, *38*, 2221.

(2) Lowell, S.; Shields, J. E. T., M. A.; Thommes, M. *Characterization of porous solids and powders: surface area, pore size, and density*; Kluwer Academic Publishers, 2004.

(3) Webb, P. A.; Orr, C.; Micromeritics Instrument, C. *Analytical methods in fine particle technology*; Micromeritics Instrument Corporation, 1997.

(4) Attard, G.; Barnes, C. *Surfaces*; Oxford University Press, 1998.

(5) Brunauer, S.; Emmett, P. H.; Teller, E. *J. Am. Chem. Soc.* **1938**, *60*, 309.

(6) Sing, K. S. W.; Everett, D. H.; Haul, R. A. W.; Moscou, L.; Pierotti, R. A.; Rouquerol, J.; Siemieniewska, T. *Pure Appl. Chem.* **1985**, *57*, 603.

(7) West, A. R. *Basic solid state chemistry*; John Wiley & Sons, 1999.

(8) Ewald, P. *Acta Crystallographica* **1960**, *13*, 513.

(9) Bragg, W. L. *Proceedings of the Cambridge Philosophical Society* **1913**, *17*, 43.

(10) Connolly, M. L. *Science* **1983**, *221*, 709.

Chapter 3

New Porous Organic Cages

Table of Contents

3.0 Porous Organic Cages

The syntheses of imine-based porous organic cages were carried out initially by Tozawa *et al*. (see Chapter 1 for more details) using various diamines and 1,3,5-triformylbenzene (TFB),[1] although other research groups such as Mastalerz and co-workers have also shown the preparation of imine cages from 2,7,14-triaminotriptycene[2] and salicylic dialdehydes.[3-6] The most porous of this first batch of cages by Tozawa *et al*., CC3 (also prepared by Skowronek and Gawronski but with no details of porosity[7]), exhibited N_2 SA_{BET} up to 624 m^2/g. This value was improved by the formation of a scrambled cage with a mixture of CC1 and CC3 constituent diamines (ethylenediamine and cyclohexanediamine), producing an amorphous cage scramble with N_2 SA_{BET} of 818 m^2/g.[8] More recently, a study has estimated that CC3 was originally only around 75-80 % crystalline, while purely amorphous CC3 was shown to have a N_2 SA_{BET} of 859 m^2/g. Conversely, completely crystalline CC3 had a decreased N_2 SA_{BET} of 409 m^2/g, suggesting that (for CC3 at least) enhanced surface areas arose from a reduction in long range order and induction of an amorphous state.[9] CC3 has also recently been shown to be stable to boiling in water, contrary to expectation of degradation of the imine bonds in the cage.[10]

Imines are formed by the addition of an amine to an aldehyde or ketone, with imine formation often occurring in the presence of an acid catalyst to speed up the rate of imine formation (and cleavage; the reaction is in equilibrium).[11] Initially, the amine acts as a nucleophile and undergoes addition with the carbonyl group on the aldehdye or ketone. The intermediate formed then undergoes a proton transfer to form a hemiaminal. Finally, the hydroxyl group is protonated again (usually by an acid catalyst) before water is eliminated to form the imine and regenerate H^+ (Figure 1). The acid catalyst is not always necessary, however, with a prime example being that different cages can be produced both in the presence and absence of acid catalysts. For example, an optimised and non acid-catalysed method for preparation of CC1 utilising slow addition, cooling and dilution was devised for almost quantitative yields by Lydon *et al*.[12] In the presence of trifluoroacetic acid (TFA), CC1 instead forms a catenane (two interlocked cages, which are interconnected by mechanical and not chemical bonds, detailed in Chapter 1).[13] CC3 however cannot

undergo this catenation, and TFA was used to speed up formation of this cage material.[10]

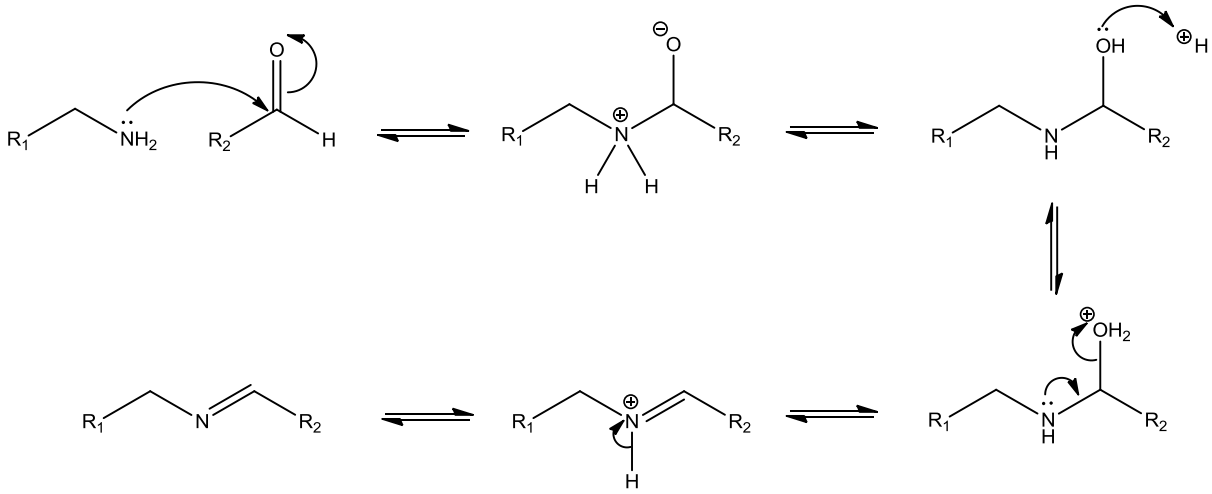

Figure 1: Imine formation in the presence of an acid catalyst.

3.1 Preparation of a New Porous Organic Cage

In this Chapter, the synthetic method for preparation of cages devised by Lydon *et al.*[12] was modified and applied to the production of a new cage, again deploying 1,3,5-triformylbenzene (TFB) as the aldehyde (as used in previous cage synthesis) and 1,2-diamino-2-methyl-propane as a new 1,2-vicinal diamine. This new diamine was selected due to its ease of availability (readily available from TCI Europe) and similarity with previous diamines (namely 1,2-propanediamine, used in production of CC2). By selecting this new diamine, we aimed to prepare a new porous organic cage and to attempt to make a comparison between the new cage and previously prepared cages (especially CC2, which it resembles most closely in structure). Due to structural similarity with CC2, the reaction was expected to afford a [4+6] porous organic cage (Figure 2).

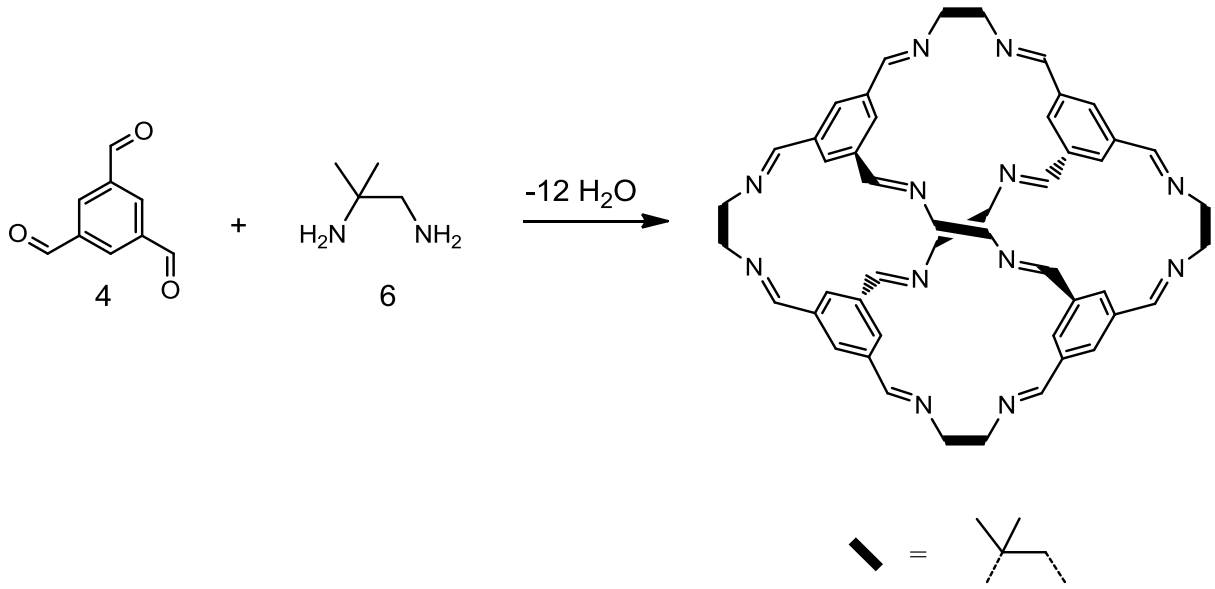

Figure 2: Preparation of a new porous organic cage. Note that the methyl groups are positionally disordered on the cage vertices.

The reaction was monitored by periodically taking aliquots and collecting ^{1}H NMR data, before using a solvent suppression experiment (for the DCM reaction solvent, seen as a peak at 5.33 ppm with two satellite peaks at 5.55 and 5.11 ppm). Using this method, we were able to measure the disappearance of the aldehyde protons at around ~10 ppm, with the emergence of imine protons at around ~8 ppm and CH_2 protons adjacent to the aryl ring at ~3.8 ppm. The shift of the methyl protons of the diamine from ~1 ppm to ~1.5 ppm was also apparent on completion of reaction (Figure 3). Integration of these signals was consistent with previous cage synthesis (1 H for imine protons, 1 H for aryl protons, 1 H for CH_2 protons and 3 H for CH_3 protons; more detail below and in Figure 5) indicating that cage formation had indeed occurred, although this could not confirm if the material was a [2+3] cage, [4+6] cage or [8+12] cage, since the integrations would be identical. The cage was confirmed as a [4+6] cage by accurate mass spectrometry, with a molecular ion with m/z = 961.6 for $C_{60}H_{72}N_{12}$ $[M]^{+}$ observed (Figure 4). This synthesis appeared to be relatively sluggish compared to the production of CC1, where reaction was complete 24 hours after complete reagent addition (as determined by disappearance of aldehyde signals and emergence of imine signals in ^{1}H NMR).[12]. Aliquots taken immediately, after 24 hours, and after 48 hours after complete reagent addition all showed presence of aldehyde protons. There were also multiple aldehyde proton

environments, suggesting partial cage formation. Disappearance of aldehyde protons and subsequent reaction completion was not observed until 72 hours after complete slow addition.

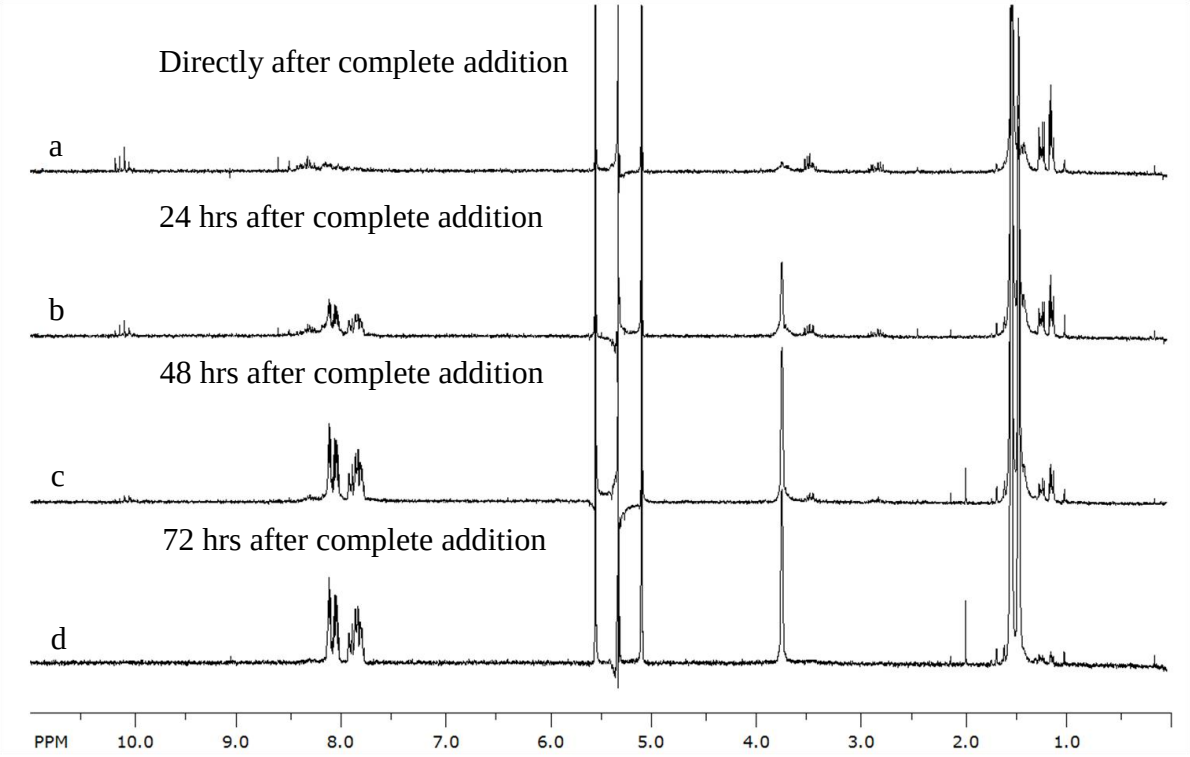

Figure 3: ^{1}H NMR monitoring the formation of a new cage; a) directly after complete addition of TFB, b) 24 hrs after complete addition of TFB, c) 48 hrs after complete addition of TFB and, d) 72 hrs after complete addition of TFB.

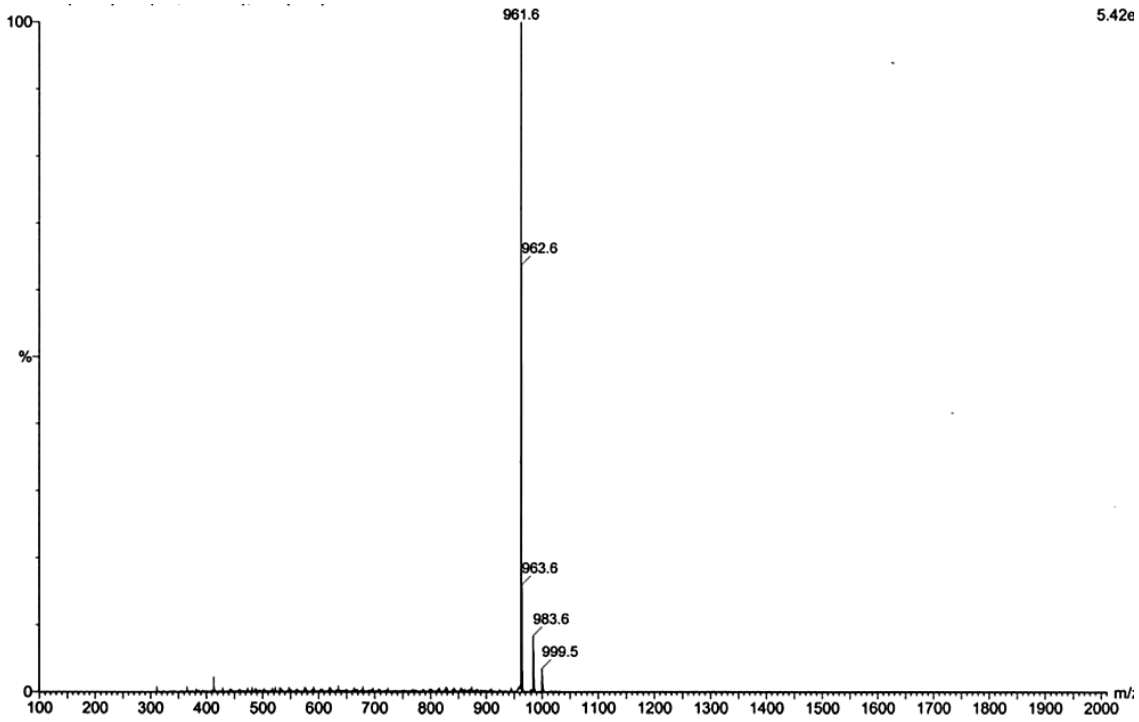

Figure 4: Accurate mass spectrum for CC12.

The new organic cage was denoted as **CC12**, because it was the twelfth cage prepared within the Cooper research group. After work-up from the reaction mixture by filtration and evaporation, ^{1}H NMR of reprecipitated **CC12** was repeated in $CDCl_3$ (apparent at 7.27 ppm) and the spectrum appeared to be much cleaner (Figure 5).The imine CH=N protons appear to be splitting into two separate multiplets at 8.21 and 8.11 ppm (integrated to relative 1 H) caused by alternating dimethyl group disorder throughout the cage. A similar effect is observed for –ArH protons on the benzene ring, with a multiplet observed at 7.94 ppm (integrated to relative 1 H). The CH_2 protons on the diamine vertices can be found at 3.80 ppm (integrated to relative 1 H) and finally the $–C(CH_3)_2$ protons are at 1.51 ppm (integrated to relative 3 H). The ^{13}C NMR could also be assigned by comparison with previous cages (Figure 6). The imine CH=N carbons appear to be greatly affected by stereoisomerism of the cage, with peaks appearing at 160.9 and 155.4 ppm. Aromatic carbons were visible at 137.1-136.6 and 129.3 ppm while the CH_2 carbon and neighbouring carbon from the diamine vertices were at 72.4 ppm and 61.3 ppm, respectively. Finally, $–C(CH_3)_2$ methyl groups are observed at 25.9 ppm.

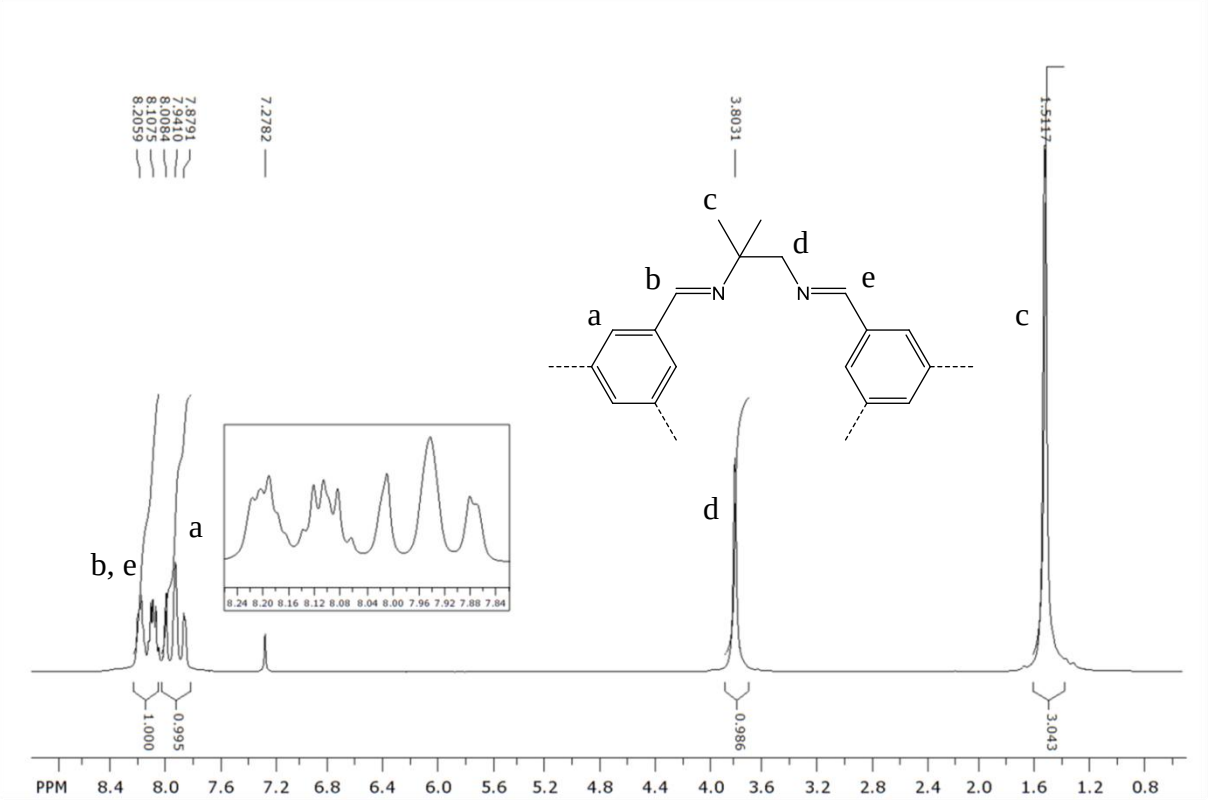

Figure 5: ^{1}H NMR of **CC12**.

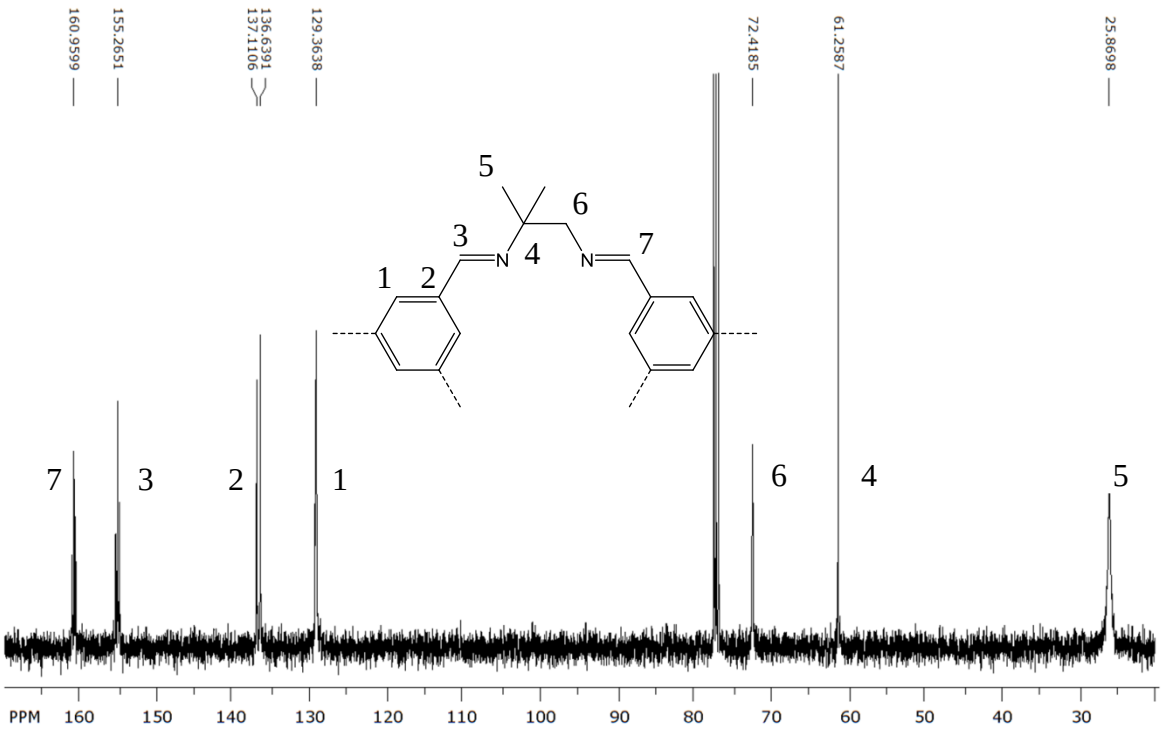

Figure 6: ^{13}C NMR of **CC12**.

3.2 Polymorphism of the New Porous Organic Cage, CC12

Careful work-up is key in the preparation of these porous organic cages, because cages can convert to polymers if heated over-zealously on removal of solvent, as highlighted in the recent paper by Lydon *et al*.[12]

When directly evaporated from chloroform after complete reaction, **CC12** was isolated as a white, amorphous precipitate (deemed so from lack of peaks in pXRD data, denoted **CC12**$^{\alpha}$). Choice of solvent itself also appeared to have an impact on the resulting solid form. If acetone was added as an anti-solvent after complete cage reaction and the mixture concentrated, (thereby solvent swapping, forcing cage out of solution into acetone), a crystalline precipitate was afforded (**CC12**$^{\beta}$). Interestingly, when **CC12** was dissolved in DCM and acetonitrile carefully layered on top to induce a much slower crystallisation process, crystals with the same morphology as **CC12**$^{\beta}$ were obtained (**CC12**$^{\beta 2}$). **CC12** was also recrystallised by vial-in-vial diffusion methods. The sample was dissolved in DCM in a small vial, before placing this in a larger vial containing dioxane, and the system was capped. This yielded another pXRD pattern labelled **CC12**$^{\gamma}$. The stacked pXRD data (offset for clarity) are shown in Figure 7. The differences in these pXRD data as a result of using different crystallisation solvents suggests polymorphism.

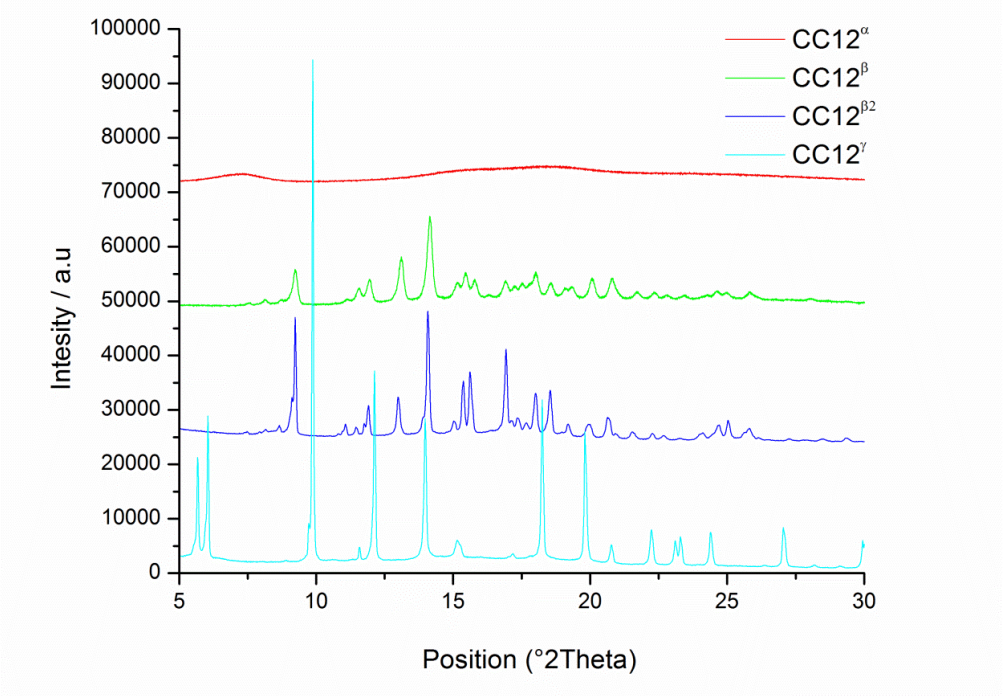

Figure 7: pXRD data for **CC12$^{\alpha}$** (red), **CC12$^{\beta}$** (green), **CC12$^{\beta 2}$** (blue) and **CC12$^{\gamma}$** (cyan).

These amorphous and crystalline variations of **CC12** also displayed different gas sorption properties (Table 1).

Polymorph	**N_2 Uptake (mmol/g)**	**N_2 SA_{BET} (m^2/g)**	**H_2 Uptake (mmol/g)**	**H_2 $SA_{Langmuir}$ (m^2/g)**
CC12$^{\alpha}$	0.04	0	4.89	326
CC12$^{\beta}$	8.22	405	4.70**	359
CC12$^{\beta 2}$	9.58*	549	5.84	399
CC12$^{\gamma}$	13.53	946	7.73	479

Table 1: N_2 and H_2 uptake and surface areas for **CC12** polymorphs. N_2 uptakes at a maximum of 1 P/P0, H_2 uptakes at a maximum of 1.13 bar. *Maximum uptake at 0.89 P/P0. **Maximum uptake at 1.2 bar.

The amorphous sample **CC12$^{\alpha}$** was non-porous to N_2 but porous to H_2 ($SA_{Langmuir}$ = 326 m²/g). The crystalline analogue **CC12$^{\beta}$** (precipitated from acetone), however, was porous to both N_2 (SA_{BET} = 405 m²/g, $SA_{Langmuir}$ = 537 m²/g) and H_2 ($SA_{Langmuir}$ = 359 m²/g). The crystalline **CC12$^{\beta}$** sample appeared to show a type I isotherm with large hysteresis, while also containing a small step in its isotherm at lower pressures (Figure 8 and Figure 9, respectively). This finding of increased surface area in an ordered crystalline state is the opposite trend observed for CC3, which tends to become more porous on induction of an amorphous state.[9] We hypothesise that this is due to the difference in bulk of the diamine vertices in **CC12** and CC3, as **CC12** contains only 2 methyl groups on its diamine vertices while CC3 contains bulky cyclohexane vertices. We hypothesise that upon amorphisation, the bulky cyclohexane groups in CC3 cannot interpenetrate with a neighbouring cages window as easily as the smaller diamine vertices of **CC12**. This would result in **CC12** consisting of a much more tightly packed arrangement of cages, and consequently reduced pore volume, because the methyl groups can penetrate the cage windows while cyclohexane cannot.

When crystallised much more slowly by layering MeCN on top of **CC12** dissolved in DCM (**CC12$^{\beta 2}$**), the isotherm differed greatly. A stepped, type IV isotherm (similar to that previously observed for the crystals produced for CC4)[14] was apparent with an improved N_2 uptake (SA_{BET} = 549 m^2/g) and H_2 uptake ($SA_{Langmuir}$ = 399 m²/g) (Figure 8 and Figure 9 respectively). We hypothesise that, as with CC4, the irregular isotherm shape is the result of a kinetic effect. In CC4, this is attributed to an increase in unit cell size of the cage upon saturation at lower pressures, inducing a sharp increase in gas uptake and creating a stepped isotherm. Due to a slower recrystallisation and higher relative intensity to **CC12$^{\beta}$** in the pXRD pattern (of which it is very similar), we could hypothesise that **CC12$^{\beta 2}$** is more crystalline, whereas the original **CC12$^{\beta}$** sample was not entirely crystalline as a result of its rapid precipitation process.[9]

Finally, **CC12** precipitated by dissolution in DCM and slow diffusion of dioxane yielded **CC12$^{\gamma}$**. This gave the highest N_2 (SA_{BET} = 946 m^2/g) and H_2 uptakes ($SA_{Langmuir}$ = 479 m²/g) observed for any of the **CC12** polymorphs (Figure 8 and Figure 9 respectively).

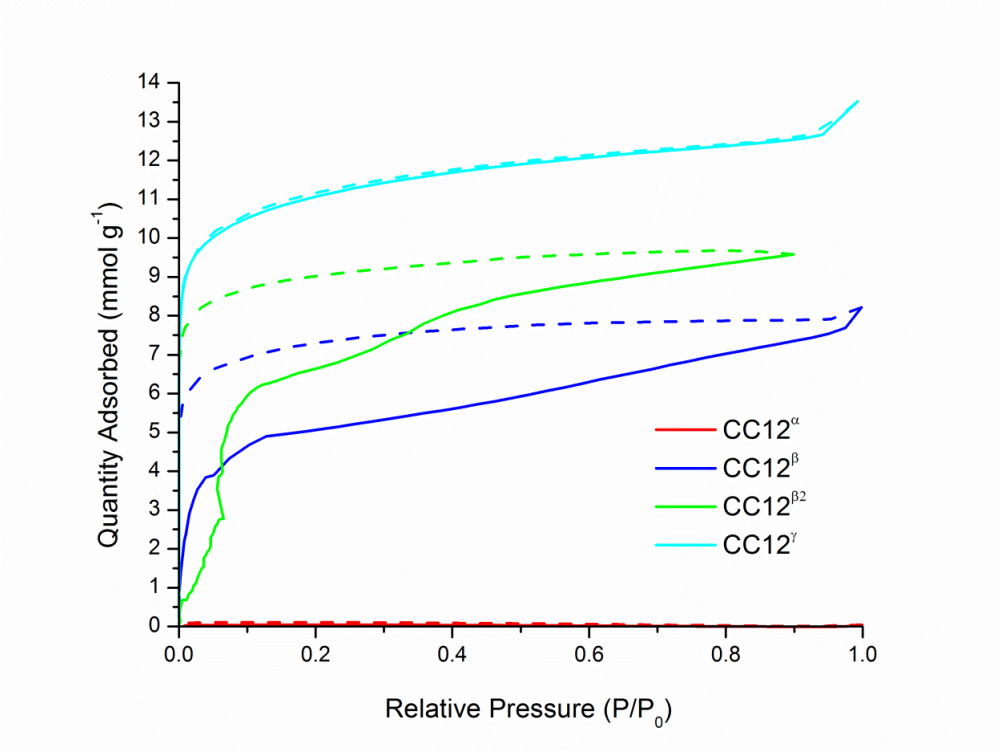

Figure 8: N_2 uptake of **CC12$^{\alpha}$** (red), **CC12$^{\beta}$** (blue), **CC12$^{\beta2}$** (green) and **CC12$^{\gamma}$** (cyan).

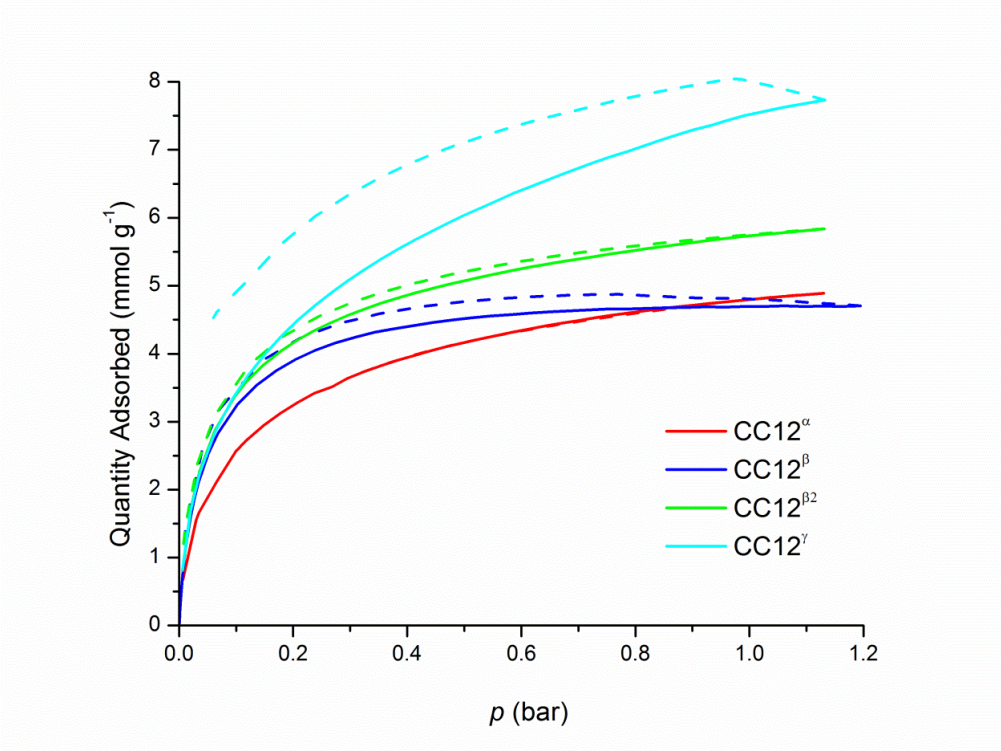

Figure 9: H_2 uptake of **CC12$^{\alpha}$** (red), **CC12$^{\beta}$** (blue), **CC12$^{\beta2}$** (green) and **CC12$^{\gamma}$** (cyan).

Pore size distribution (PSD) was calculated using a pillared clay model (measuring the differential pore volume against the pore width), with **CC12$^{\beta}$** exhibiting a pore size distribution of around ~18 Å, thus confirming microporosity. PSD of **CC12$^{\beta2}$** was increased to ~20 Å and borders on mesoporosity, while **CC12$^{\gamma}$** had the smallest PSD of around ~10 Å (Figure 10).

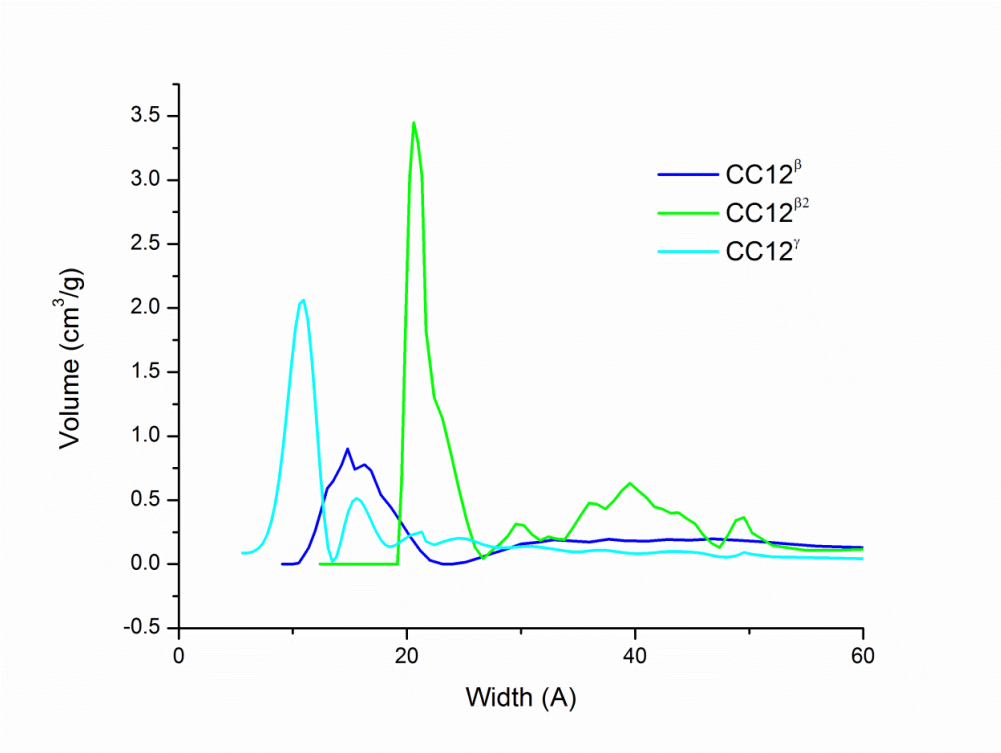

Figure 10: PSD of **CC12$^{\beta}$** (blue), **CC12$^{\beta2}$** (green) and **CC12$^{\gamma}$** (cyan) using pillared clay model. The PSD for **CC12$^{\alpha}$** could not be calculated due to lack of a N_2 isotherm.

SEM for the **CC12** polymorphs was carried out by Dr. T. Hasell or Dr. R. Dawson **CC12$^{\alpha}$** (pXRD amorphous cage directly removed from chloroform, Figure 11) clearly showing irregular chunks of material with no defined surface morphology.

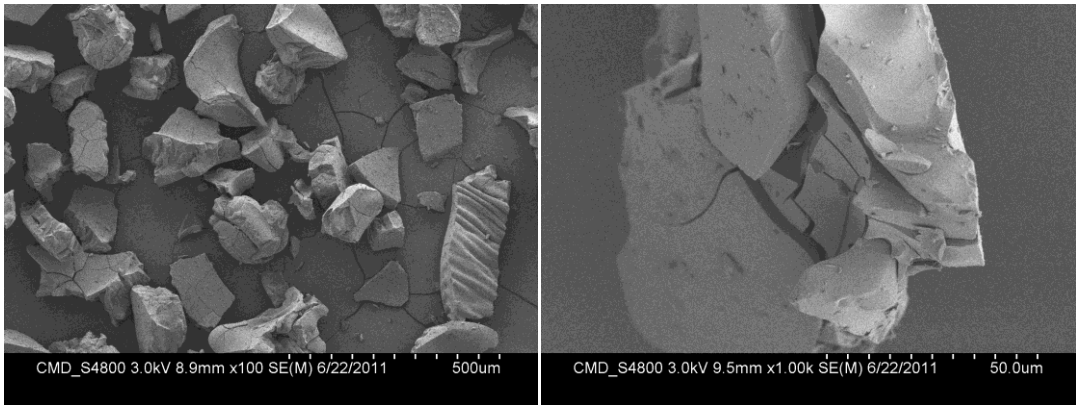

Figure 11: SEM of amorphous **CC12$^{\alpha}$** at 100x magnification (left) and 1000x magnification (right).

CC12$^{\beta}$ (crystalline cage, precipitated by addition of acetone and concentration to force fast precipitation, Figure 12) displayed hexagonal tube morphology with crystal diameters of around 15 μm, and an open channel through them.

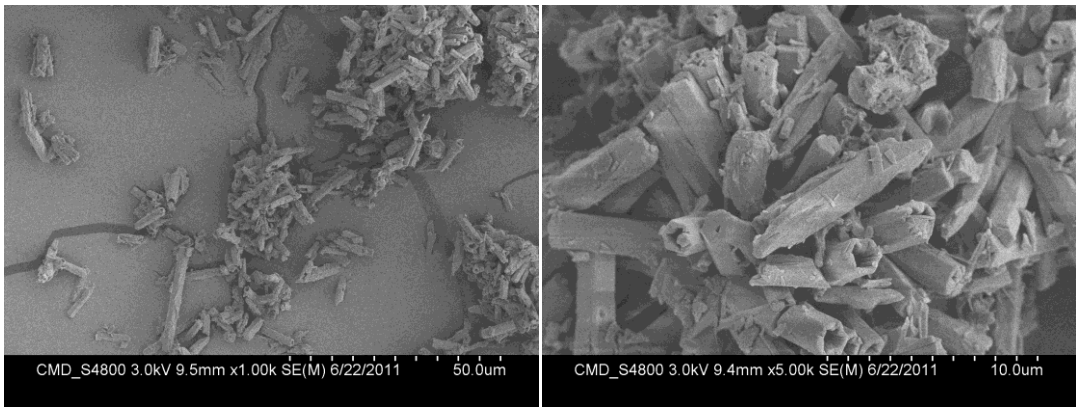

Figure 12: SEM of crystalline **CC12$^{\beta}$** at 1000x magnification (left) and 5000x magnification (right).

CC12$^{\beta 2}$, (crystalline cage, prepared by slow crystallisation through layering acetonitrile onto a solution of the cage in DCM and allowing slow evaporation), again gave hexagonal tubes, although in this instance the open channels were absent. The majority of these hexaganol tubes were larger than seen in **CC12$^{\beta}$** with diameters between 400-600 μm, likely due to the much slower recrystallisation process.

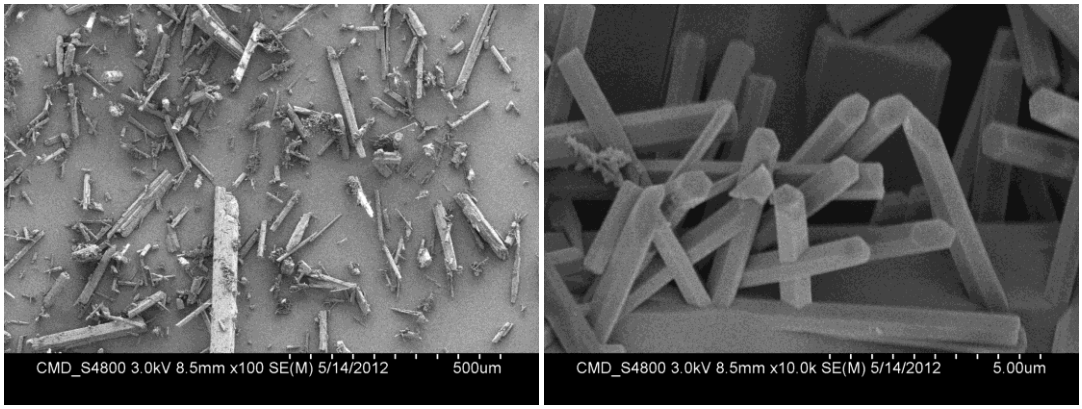

Figure 13: SEM of crystalline **CC12$^{\beta 2}$** at 100x magnification (left) and 10000x magnification (right).

Finally, SEM of **CC12$^{\gamma}$** (crystalline cage, prepared by slow diffusion of dioxane) was collected. As with the amorphous **CC12$^{\alpha}$**, this sample appeared to show no defined surface morphology and again comprised of irregularly shaped clumps of material, even though the pXRD data suggests long range order.

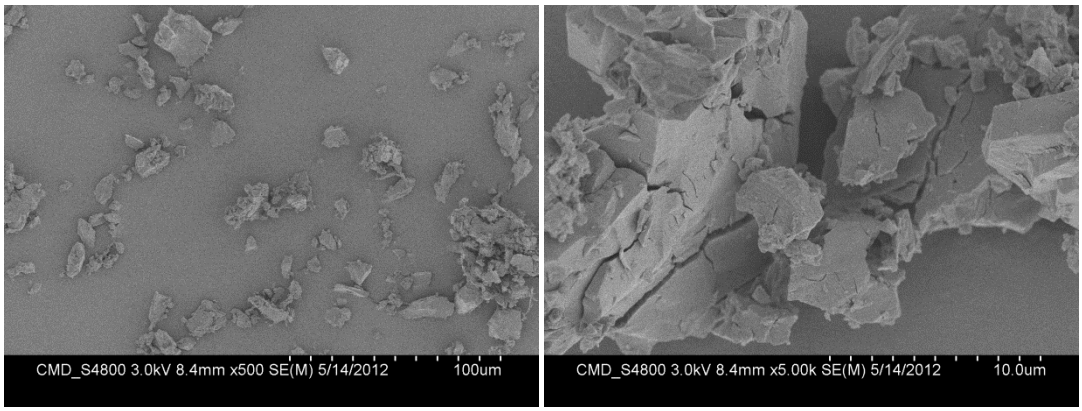

Figure 14: SEM of crystalline **CC12$^{\gamma}$** at 500x magnification (left) and 5000x magnification (right).

CC12 samples were also analysed by FTIR (Figure 15). Characteristic C-H (2966-2833 cm^{-1}), imine C=N (1651 cm^{-1}), CH_3 and CH_2 (1433-1364 cm^{-1}) bands are all present in all samples.

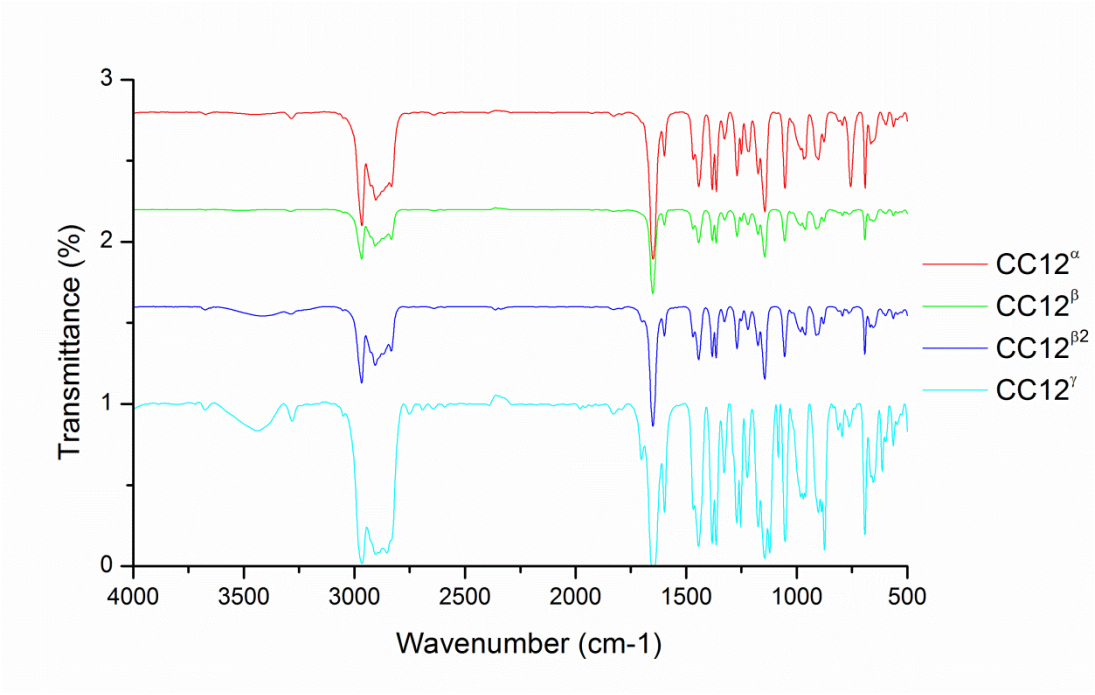

Figure 15: FTIR for **CC12$^{\alpha}$** (red), **CC12$^{\beta}$** (blue), **CC12$^{\beta 2}$** (green) and **CC12$^{\gamma}$** (cyan).

A single crystal of **CC12** was initially grown from DCM and acetonitrile by layering (the same solvent mix as used for **CC12$^{\beta 2}$**). The cage displayed a P3 space group with 3 cages per cell, although the single crystal structure was very poor with a high level of disorder. Two cages were ordered per unit cell (ignoring CH_3 group disorder, which themselves displayed 0.75:0.25 partial occupancy) and one disordered cage which showed complete rotation (0.50:0.50 partial occupancy). As a result of high levels of disorder, attempts to grow another single crystal were made.

Eventually, a single crystal was later grown from DCM and acetone through layering (the same solvent mix as used for **CC12$^{\beta}$**). This sample also exhibited the same P3 space group, however disorder was much less pronounced. In this sample, there were again 3 cages per unit cell, with disorder limited to the methyl groups on the diamine vertices on one half of the cages (0.50:0.50 partial occupancy). Solvent was removed computationally and a Connolly surface area (CSA) was calculated using a nitrogen probe molecule, with 1D (as seen for CC2[1]) propeller shaped cavities present throughout the structure (Figure 16).

Finally, a cubic form of **CC12** in Fd3 space group was grown from DCM/dioxane by vial-in-vial solvent diffusion (**CC12$^{\gamma}$**). Disorder was this time limited to the diamine vertices with two possible arrangements (0.50:0.50 partial occupancy). One molecule

of dioxane sat inside each cage molecule with another four molecules of dioxane positioned in each cage window. The CSA this time showed much larger, better connected 3D cavities similar to those observed in CC3[1] (Figure 17).

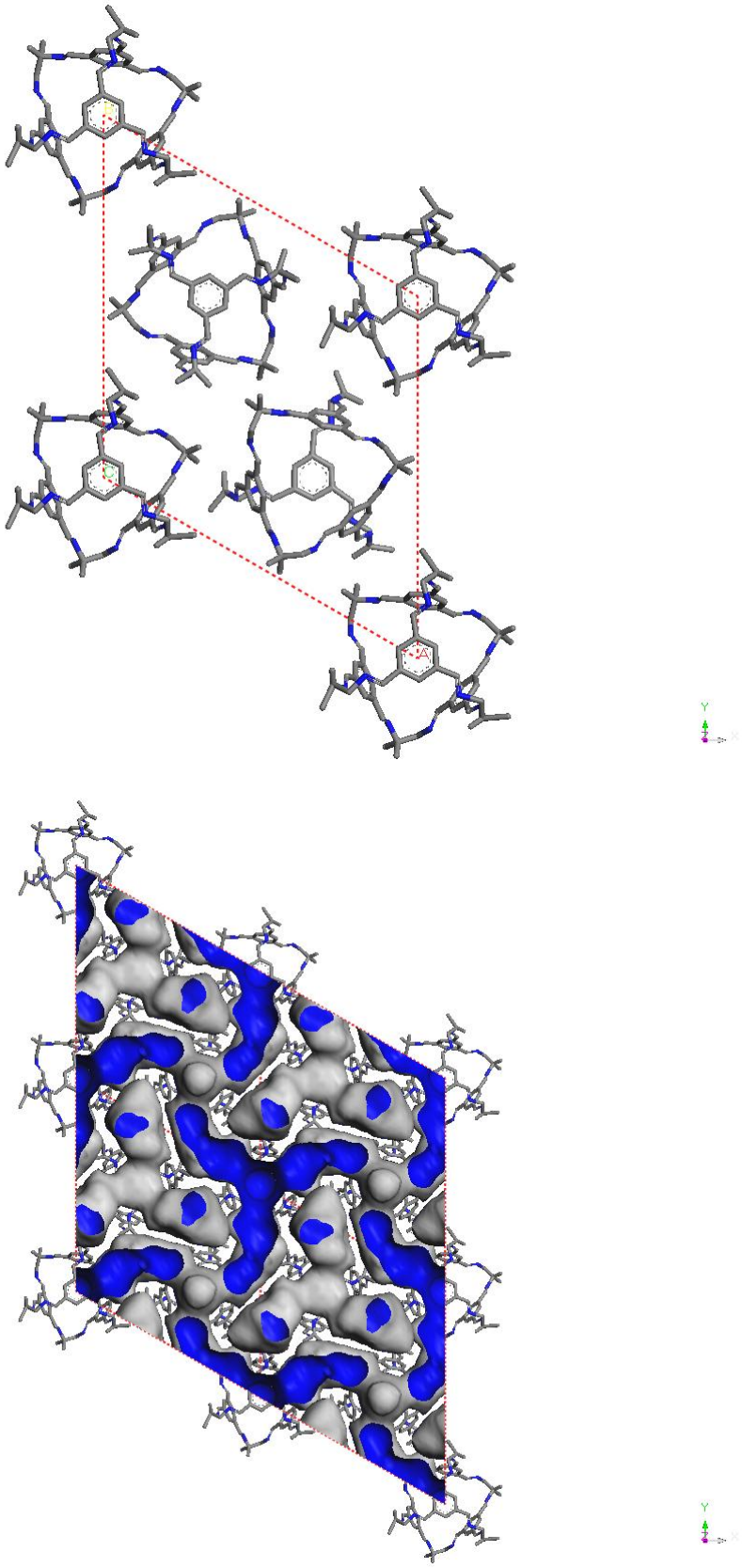

Figure 16: P3 unit cell of **CC12$^{\beta}$** crystal grown from DCM/acteone (top) and N_2 CSA for crystal structure (bottom). H atoms omitted for clarity.

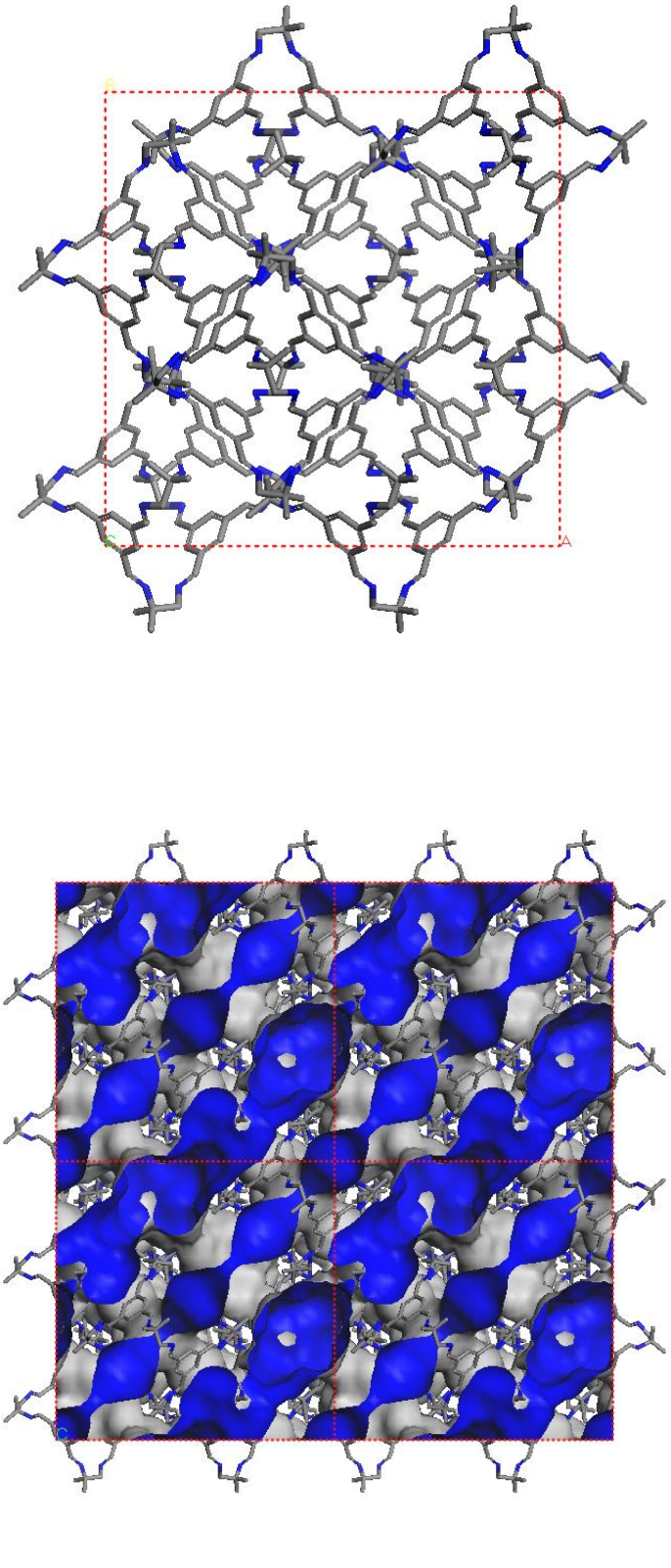

Figure 17: Fd3 unit cell of **CC12**$^{\gamma}$ crystal grown from DCM/dioxane (top) and N_2 CSA for crystal structure (bottom). H atoms omitted for clarity.

3.3 High-Throughput Screening for Further CC12 Polymorphs

Conditions for the work up of **CC12** clearly had a large impact on porosity properties of the cage and, as with CC1, **CC12** appeared to display 'on-off porosity' behaviour dependant on solvent choice.[15] To further investigate the effect of polymorphism on sorption properties of this new porous organic cage, a high-throughput (HT) polymorphism study was carried out by creating a stock solution of **CC12** in dichloromethane (5 mg/mL concentration, 6 mL total solution) and layering one of thirty different 'directing' solvents on top (1 mL) with use of a Chemspeed ASW robot (Table 2).

Sample	Directing Solvent	Boiling Point (°C)	Sample	Directing Solvent	Boiling Point (°C)
0	Dichloromethane	40	15	*n*-Hexane	69
1	Chloroform	62	16	*n*-Heptane	98
2	1,2-Dichloroethane	84	17	Butanol	117
3	Toluene	111	18	Octanol	195
4	Ethanol	79	19	Mesitylene	165
5	IPA	82	20	Acetonitrile	82
6	Dimethylsulfoxide	189	21	Ethanediol	196
7	Tetrahydrofuran	66	22	Cyclohexane	81
8	Dioxane	101	23	Dimethylacetamide	164
9	DMF	153	24	Propanol	97
10	Diethyl ether	34	25	Methanol	65
11	Acetone	56	26	Di-isopropyl-ether	68
12	*o*-Xylene	140	27	Methyl acetate	57
13	*m*-Xylene	140	28	Ethyl acetate	77
14	*p*-Xylene	140	29	Pentane	36

Table 2: Directing solvents and respective boiling points used in HT polymorphism study.

After preparation of all 30 samples, nitrogen was gently flowed over the samples to aid slow evaporation of solvents. All samples were then further dried using a

Combidancer (necessary due to the use of some higher boiling point solvents) and the resulting solids tested with high-throughput pXRD, from which we were able to discover a variety of **CC12** polymorphs. pXRD data was separated into three categories; amorphous, semi-crystalline and crystalline before stacking each subset together with an offset for ease of comparison.

Eight samples were judged to be X-ray amorphous by their lack of peaks in measured pXRD patterns, as shown in Figure 18. Intriguingly, sample 8 (which included dioxane as a directing solvent) was deemed to be amorphous by pXRD when recrystallised *via* this layering method. This highlights that the precise method of recrystallisation is extremely important, as slow diffusion of **CC12** in DCM with dioxane yielded crystalline (and porous) **CC12**$^{\gamma}$ previously.

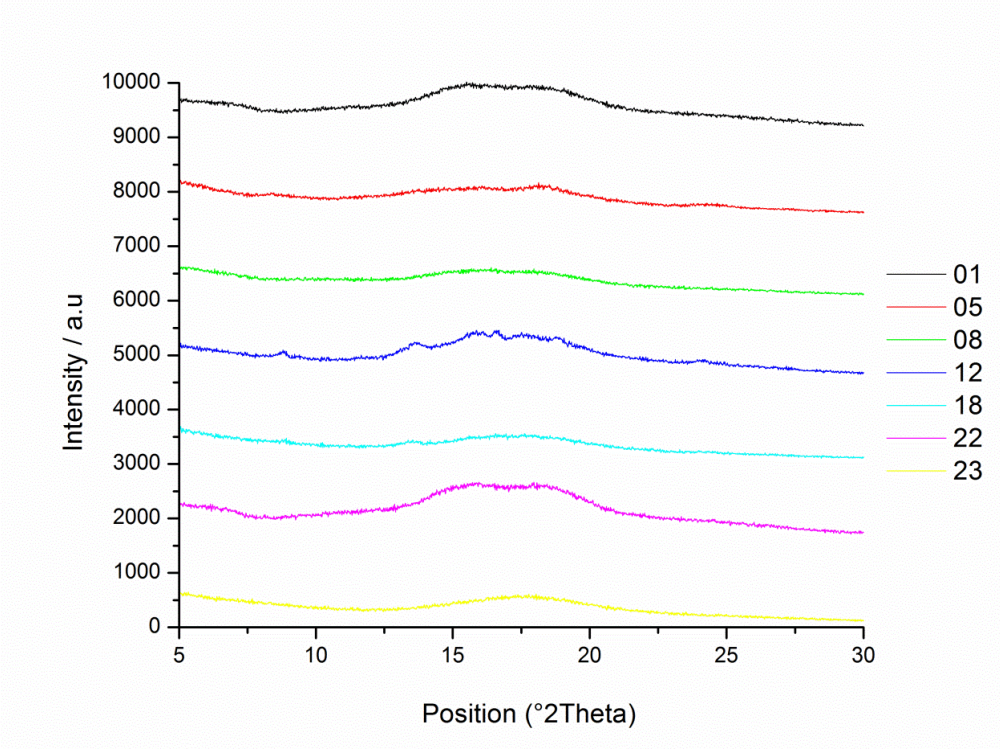

Figure 18: X-Ray amorphous **CC12** samples from HT polymorphism study.

Samples which contained low intensity, broad peaks in their pXRD patterns were classed as "semi-crystalline" (SC) and are highlighted in Figure 19. These materials included samples 0, 2, 3, 16, 17, 19, 24 and 26.

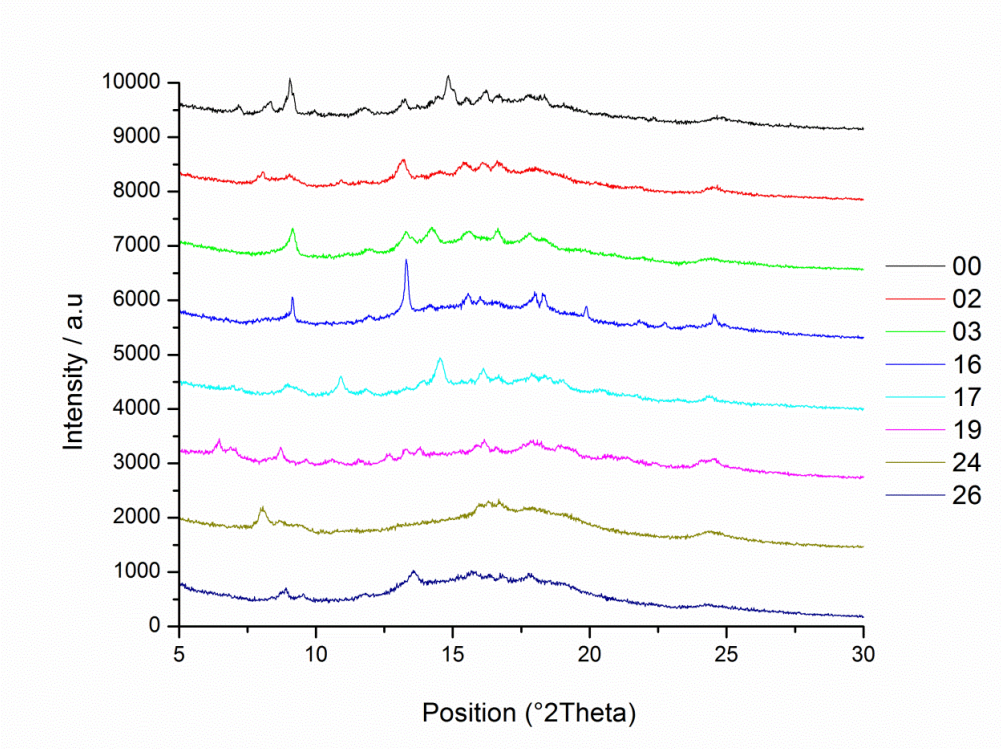

Figure 19: X-Ray semi-crystalline **CC12** samples from HT polymorphism study.

All remaining samples were classed as crystalline (or containing significant crystalline content, Figure 20). The most dominant pXRD pattern in crystalline samples was very similar to that already measured for **CC12**$^{\beta}$ and **CC12**$^{\beta 2}$ (samples 6, 11, 13, 14, 15, 20 and 28). For the other crystalline samples, however, pXRD patterns were far more diverse, with peaks at different 2θ positions being apparent (samples 7, 9, 10, 21, 25, 27 and 29).

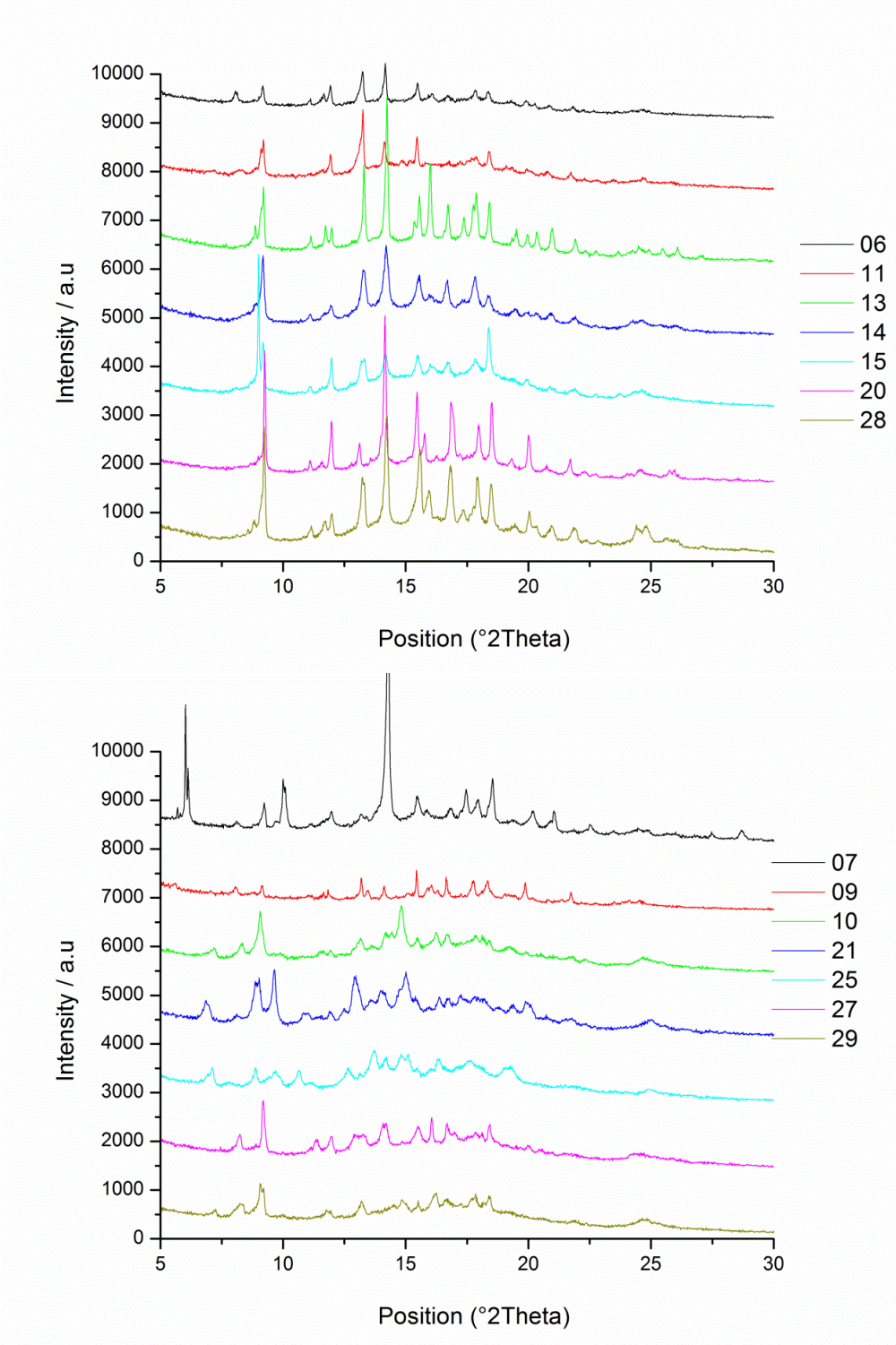

Figure 20: X-Ray crystalline **CC12** samples from HT polymorphism study.

Next, nitrogen gas sorption was collected for all 30 samples by collecting a 7 point BET isotherm. Data was taken as received, although some isotherms returned a negative c constant. In these cases, a single point BET was taken at the highest pressure point so that a reasonable N_2 SA_{BET} could be calculated. In previous cases,

cages had been made more porous by inducing an amorphous state.[8] In this polymorphism study, however, amorphous samples appeared mainly non-porous with the exception of sample 5, which still appeared to exhibit lower porosity than crystalline analogues (as seen previously with **CC12**).

Indeed, the highest N_2 surface areas observed were from crystalline samples. In this polymorphism study, only samples with crystallinity (highlighted in green and blue in Table 3 displayed N_2 SA_{BET} above 200 m^2/g. The highest N_2 SA_{BET} observed in the polymorph study were samples 6 (dimethylsulfoxide, N_2 SA_{BET} = 484 m^2/g) and 25 (methanol, N_2 SA_{BET} = 487 m^2/g).

Sample	Directing Solvent	N_2 SA_{BET} (m^2/g)	Crystallinity
0	Dichloromethane	390	SC
1	Chloroform	0	N
2	1,2-Dichloroethane	329	SC
3	Toluene	268	SC
4	Ethanol	41	Y
5	IPA	159	N
6	Dimethylsulfoxide	484	Y
7	Tetrahydrofuran	385	Y
8	Dioxane	40	N
9	Dimethylforamide	254	Y
10	Diethyl ether	372	Y
11	Acetone	213	Y
12	*o*-Xylene	27	N
13	m-Xylene	107	Y
14	p-Xylene	490	Y
15	n-Hexane	100	Y
16	Heptane	103	SC
17	Butanol	403	SC
18	Octanol	123	Y
19	Mesitylene	117	SC
20	Acetonitrile	185	Y
21	Ethanediol	473	Y

22	Cyclohexane	31	N
23	Dimethylacetamide	10	N
24	Propanol	125	SC
25	Methanol	487	Y
26	Di-isopropyl-ether	101	SC
27	Methyl acetate	228	Y
28	Ethyl acetate	168	Y
29	Pentane	354	Y

Table 3: Directing solvent with measured SA_{BET} from polymorphism study. Amorphous samples are denoted (N), semi-crystalline (SC) and crystalline (Y).

3.4 Reduction of CC12

CC12 was also successfully chemically reduced to "lock" the cage structure, using a modified method to that described in Chapter 4. This involved dissolution of **CC12** in DCM and addition of an equivalent amount of methanol, before slow addition of a slight excess (1:13) of sodium borohydride. As with previous reduced cages, reduced **CC12** (**CC12R**) was X-ray amorphous. The material was characterised by NMR spectroscopy and mass spectrometry.

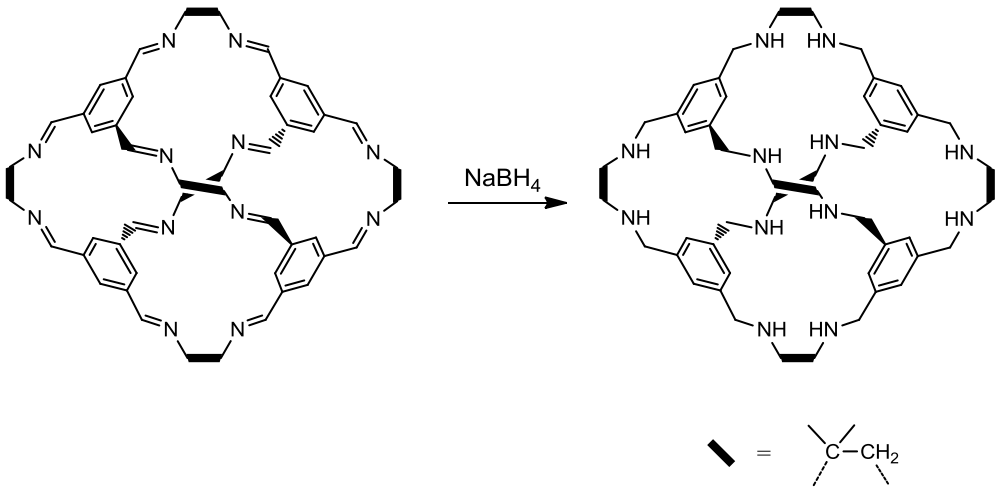

Figure 21: Preparation of **CC12R**.

The reduction was left overnight and the reaction was monitored by ^{1}H NMR. Reaction progress was determined by disappearance of imine protons in order to

confirm complete reduction. The ^{1}H NMR for **CC12R** was relatively poor, displaying multiplets for all proton signals originally. As with **CC12**, this could be attributed to multiple proton environments created by alternating dimethyl group disorder throughout the cage. Low temperature NMR was carried out at -70 °C as a result, improving the spectrum somewhat (Figure 22). As the imine is reduced down to an amine there is less of a shielding effect and the signal appears much lower as a multiplet at around 3.59 ppm (integrated to 2 H). Aryl protons on the benzene ring were observed as a multiplet around 7.14 ppm (integrated to 1 H). The CH_2 protons on the diamine vertices can be found again as a multiplet at 2.47 ppm (integrated to 1 H) and finally the $-C(CH_3)_2$ protons are at 1.11 ppm (integrated to 3 H). Solvent signals for $CDCl_3$ (7.26 ppm), DCM (5.30 ppm), MeOH (3.46 ppm) and acetone (2.17 ppm) were also all apparent.

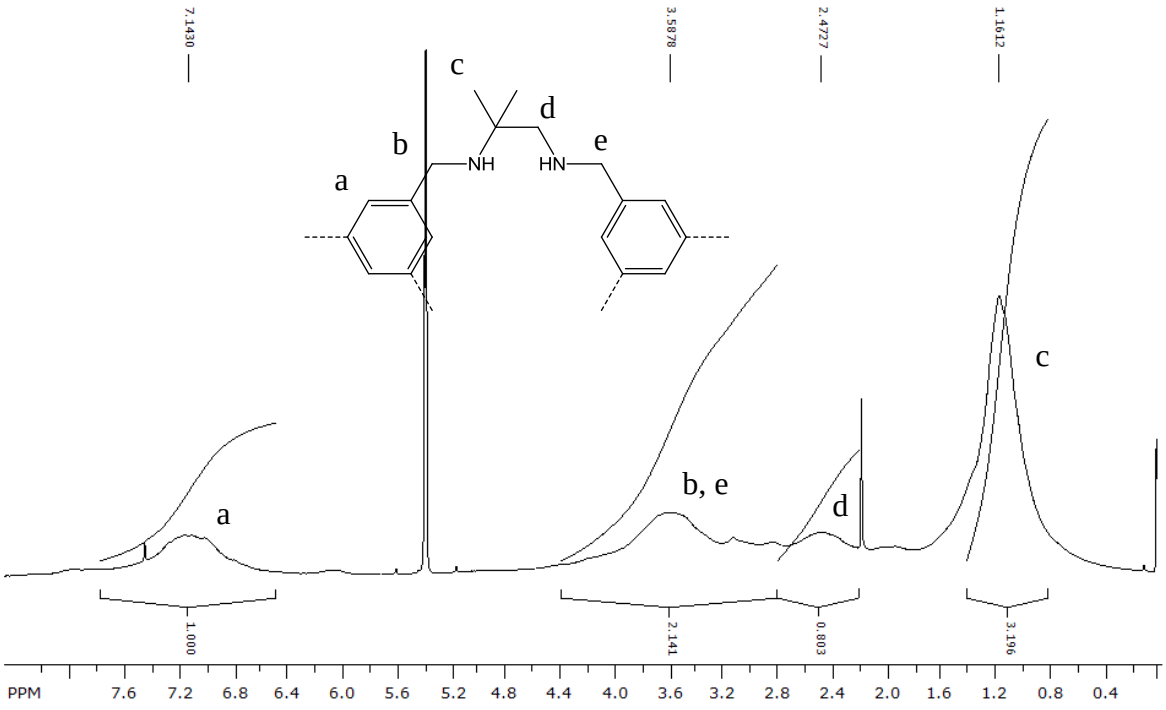

Figure 22: ^{1}H NMR of **CC12R**.

^{13}C NMR was also collected and assigned, shown below in Figure 23.

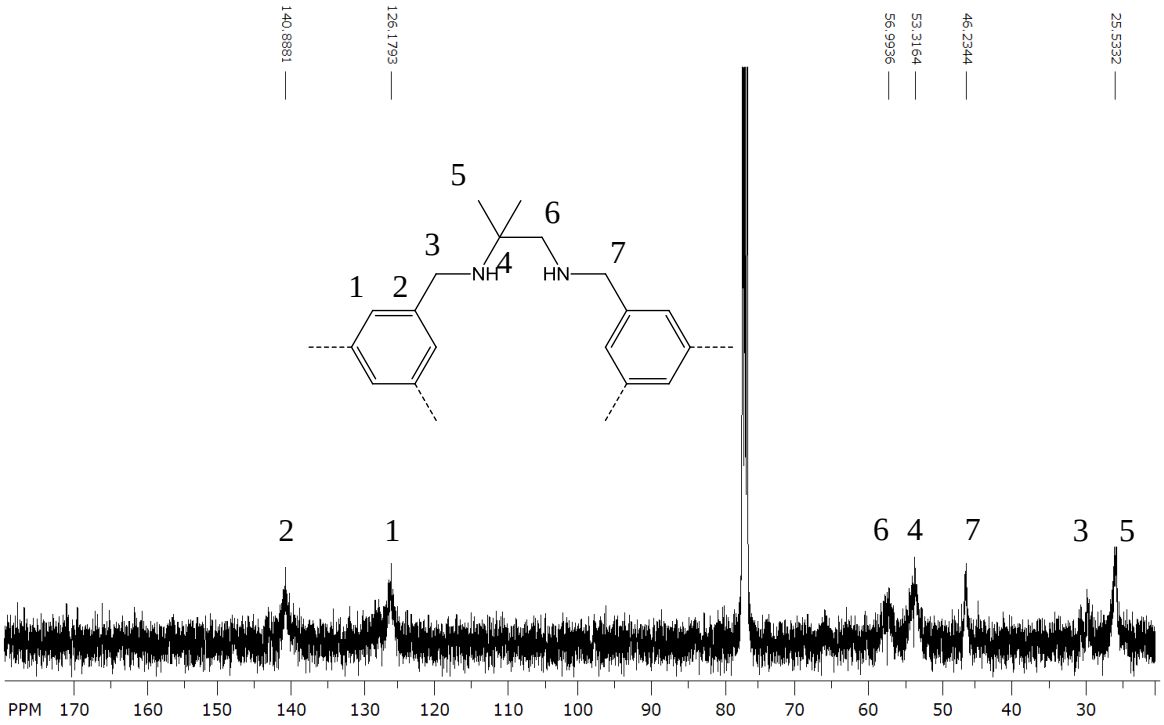

Figure 23: ^{13}C NMR of **CC12R**.

Accurate mass spectrometry of **CC12R** was also obtained (Figure **24**). **CC12R** is at 985.8 Mr, while partially reduced cage is also visible at 979.8, 981.8 and 938.8 Mr.

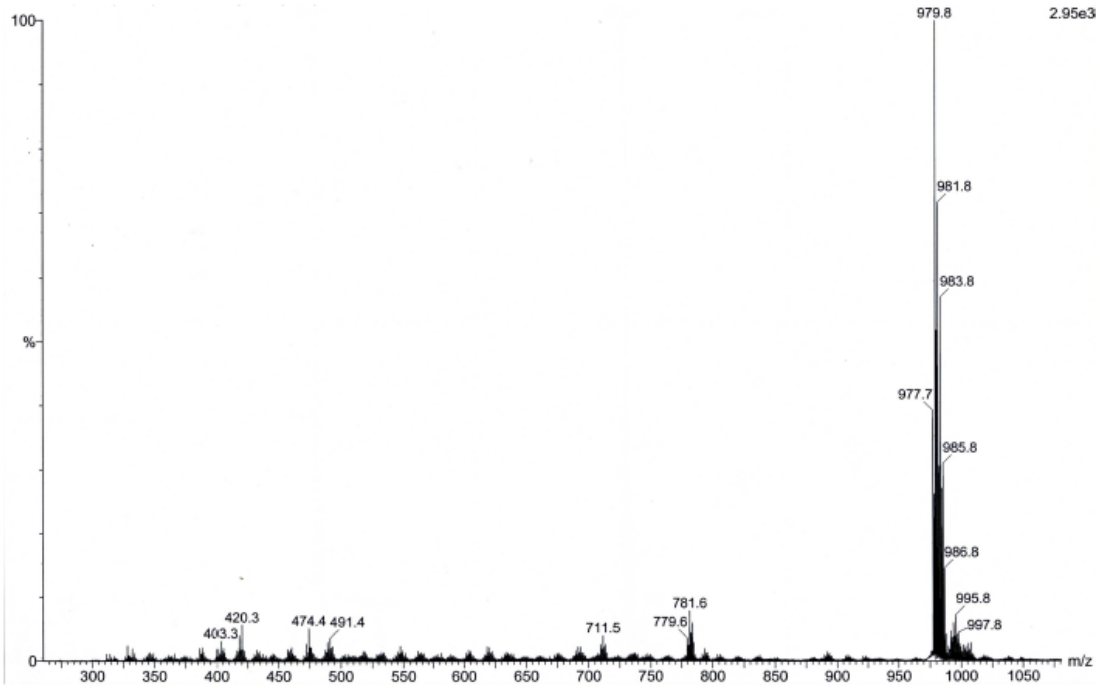

Figure 24: Accurate mass spectrum of **CC12R**.

Reduction of **CC12** was further verified by FTIR and offset for clarity (Figure 25). Characteristic C-H (2966-2833 cm^{-1}), CH_3 and CH_2 (1433-1364 cm^{-1}) bands are all still present in FTIR. On reduction however, the imine band (C=N, 1651 cm^{-1}) has greatly diminished with clear addition of a strong, broad N-H band (3291 cm^{-1}).

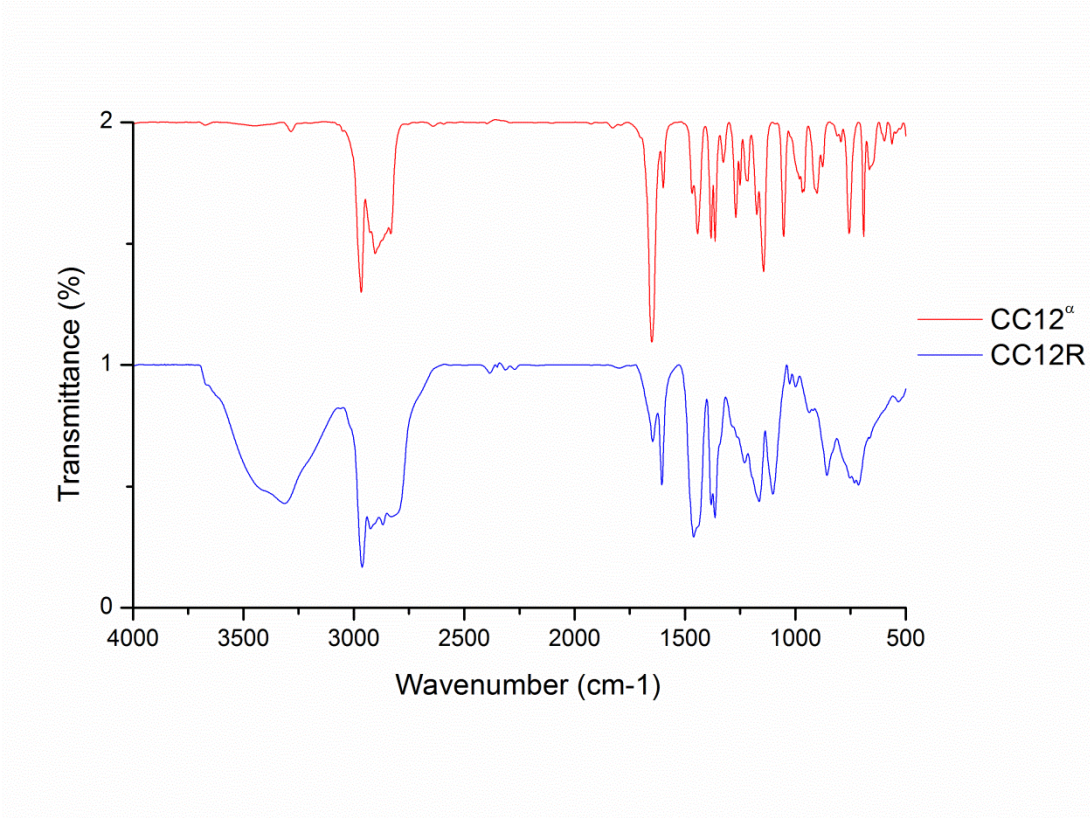

Figure 25: FTIR of **CC12$^{\alpha}$** (red) and **CC12R** (blue).

3.5 CC12 Catenane

Attempts were made to catenate **CC12** with itself, as previously achieved in CC1, CC2 and CC4. [13] Using trifluoroacetic acid to speed up the formation (and degradation) of the imine bonds, formation of the catenane is driven by thermodynamics of the energetically favoured catenane and the precipitation of the catenane from solution upon formation (Figure 26).

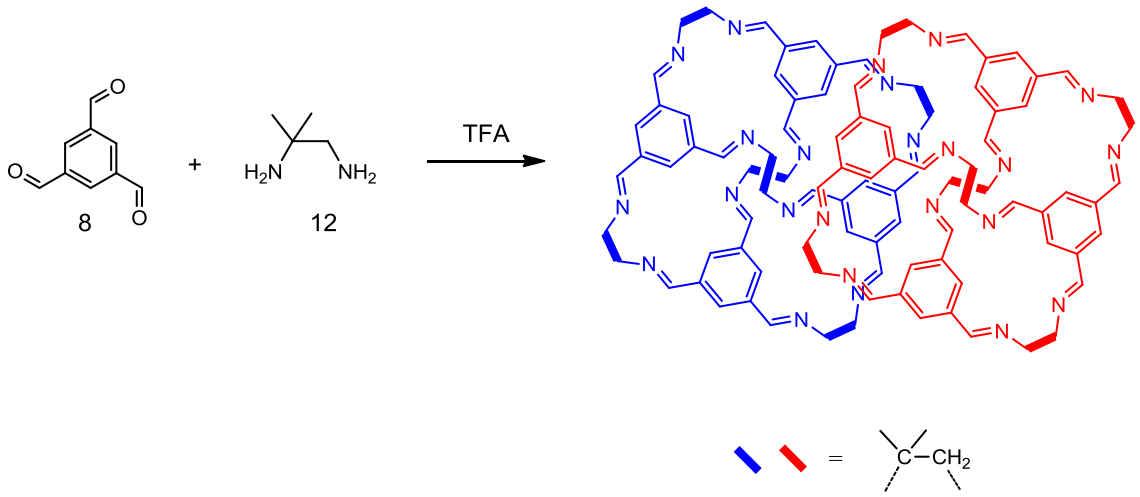

Figure 26: Preparation of catenated **CC12**.

A mixture of needles (majority) and cubic (minority) crystals were formed after 7 days of standing. Cubic single crystals of catenated **CC12** were taken directly from the reaction mixture (acetonitrile) and structure solved as R-3 space group with 3 catenanes per unit cell. The reaction was repeated using dichloromethane (aldehyde) and methanol (amine) layering, producing a larger quantity of cubic crystals and greater yield of catenated **CC12** as a result. These crystals provided a much better, less disordered structure (also R-3 with 3 catenanes per unit cell), in a similar fashion to that previously shown for **CC12** (Figure 27, top). In the crystal structure, two tetrahedral **CC12** molecules can be seen to triply interlock so that three of the four windows in each cage are penetrated by the bis-imine linkers of the partner cage, with one aryl ring from each cage π-π stacking with another from said partner cage (Figure 27, bottom).

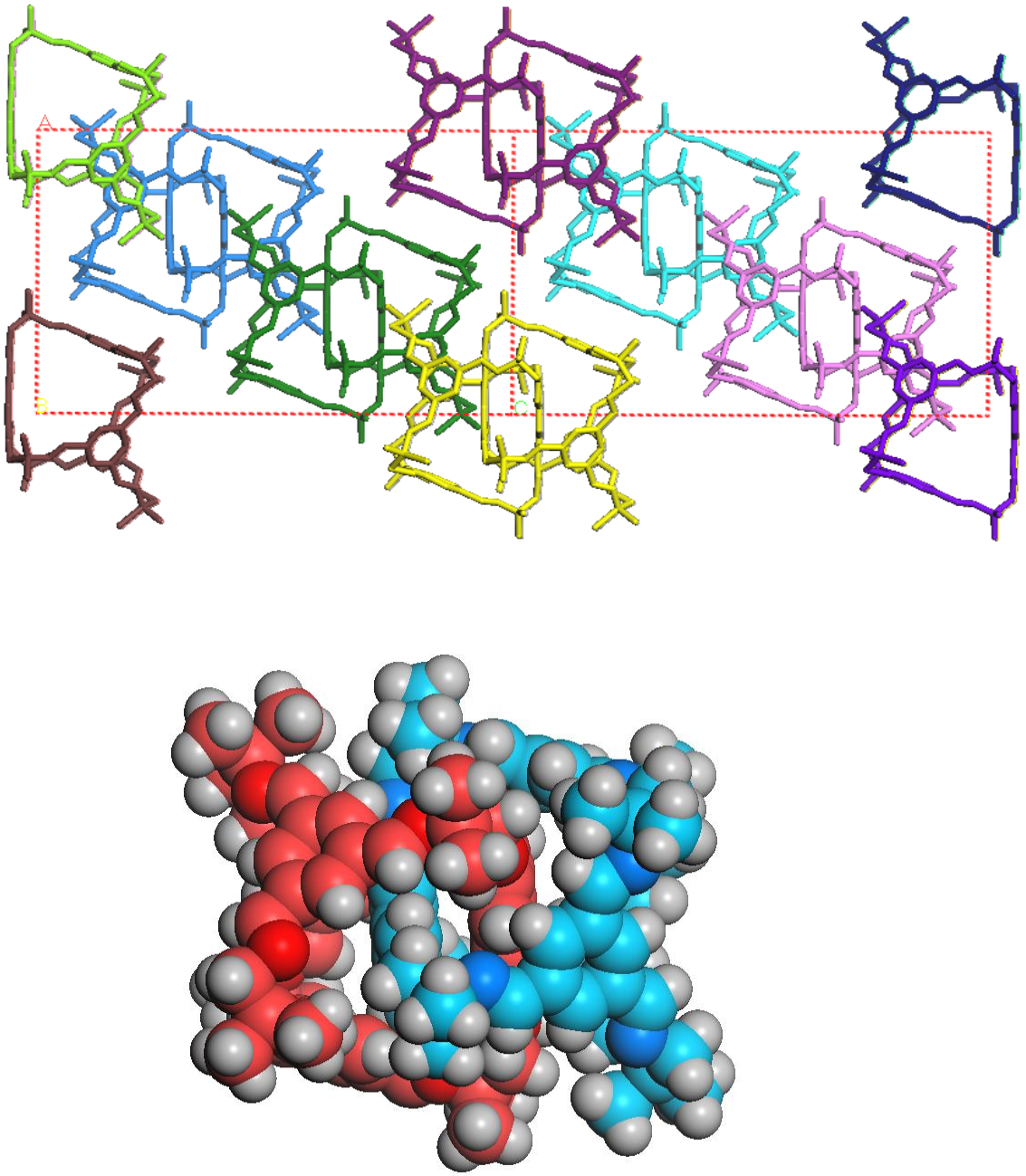

Figure 27: Lattice of **CC12** catenane (top) and single catenated pair of **CC12** (bottom).

As seen with the catenane of CC2, ^{1}H NMR of the catenane of **CC12** differed greatly compared to that of a single cage, and was far more complex.[13] From comparison of CC2 and its catenane, we have attempted to assign ^{1}H NMR. When comparing the ^{1}H NMR of **CC12** to catenated **CC12**, we can see the imine signal splitting to 7.7, 8.2 and 8.5 ppm. Aryl hydrogens split to 5.8, 7.1 and 8.0 ppm, while methyl protons

also broaden to 1.2, 1.4, 1.5 and 1.6 ppm. δDCM is apparent at 5.3 ppm in both spectra, while MeCN is visible at 2.1 ppm (Figure 28).

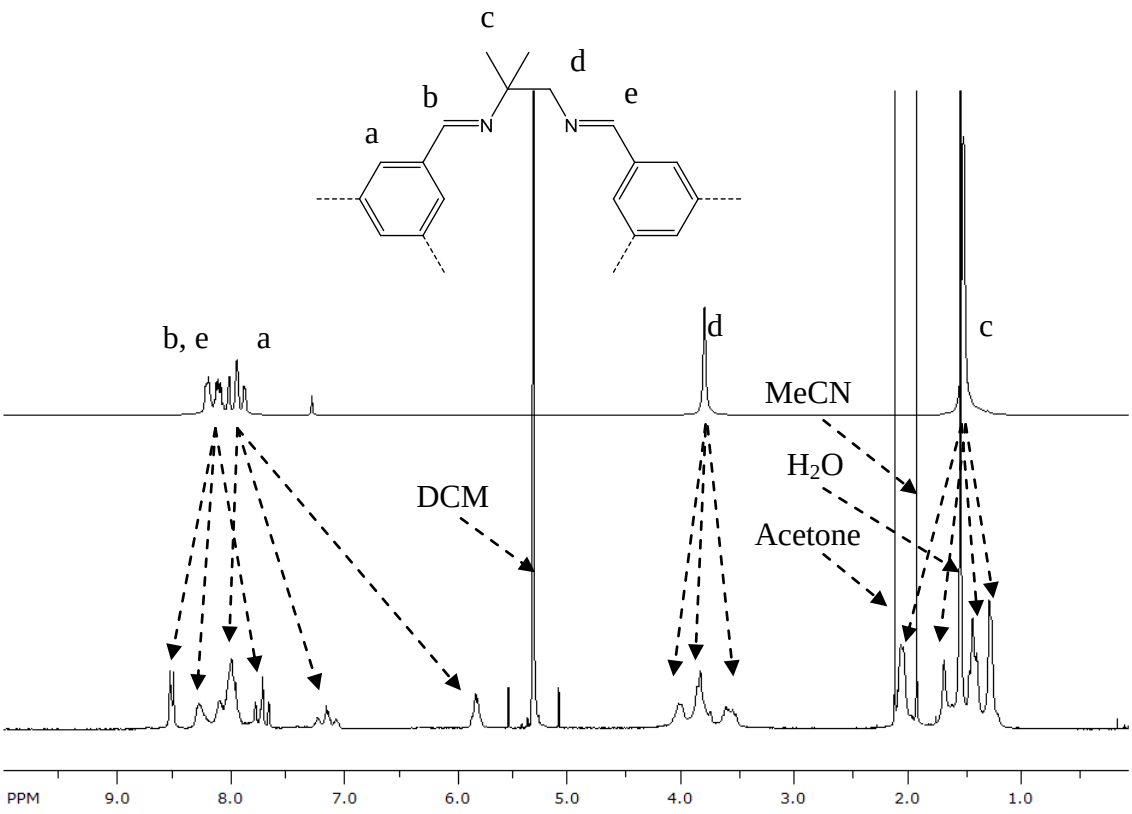

Figure 28: ^{1}H NMR of **CC12** (top) and catenated **CC12** (bottom).

Mass spectrometry of the catenane showed the expected molecular ion at 1923.2 ($C_{120}H_{144}N_{24}$) molecular ion plus Na at 1946.2 ($C_{120}H_{144}N_{24}Na$) (Figure 29). Single cages can also be seen at 961.6 ($C_{60}H_{72}N_{12}$), possibly resulting from fragmentation products of single cages.

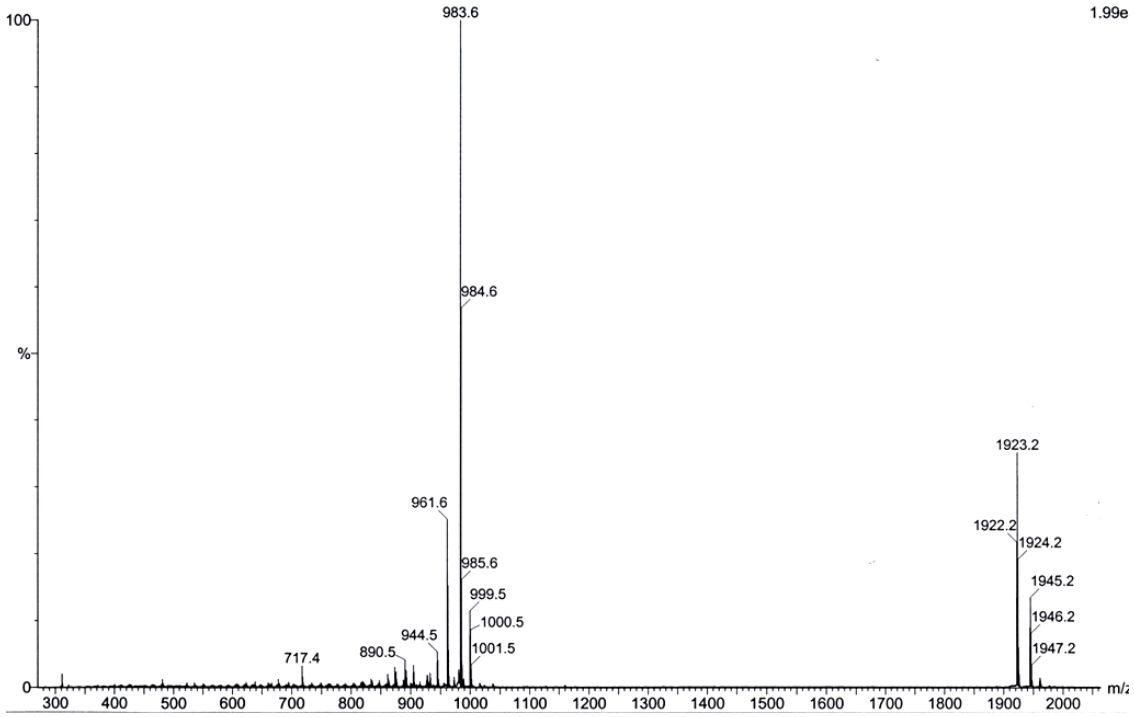

Figure 29: Accurate mass spectrum of **CC12** catenane.

The **CC12** catenane was analysed by FTIR, compared to **CC12$^{\beta}$**, and offset for clarity in Figure 30. Characteristic C-H (2966-2833 cm^{-1}), imine C=N (1651 cm^{-1}), CH_3 and CH_2 (1433-1364 cm^{-1}) bands are all present for both samples with no major differences.

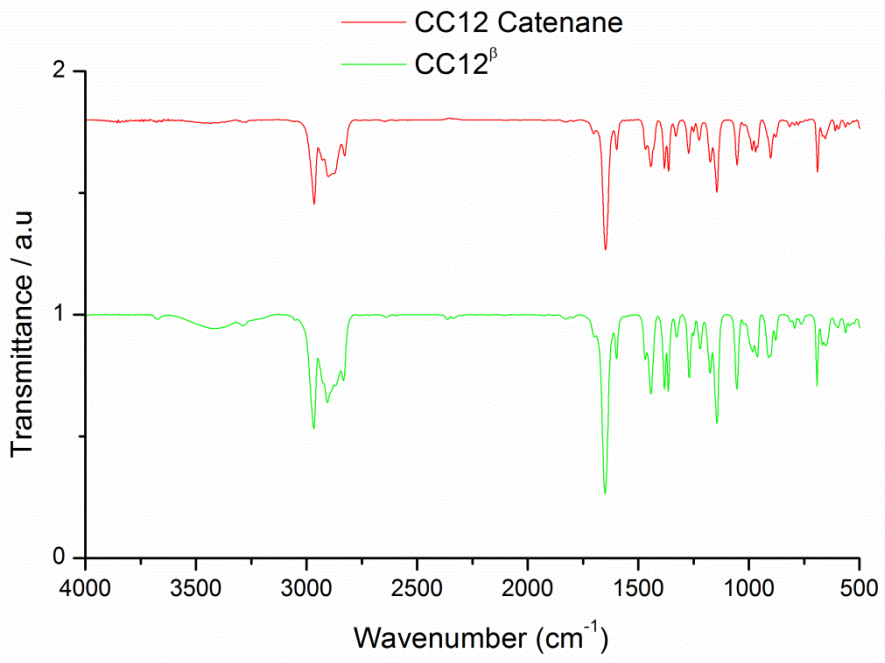

Figure 30: FTIR of **CC12** catenane (red) and **CC12$^{\beta}$** (green).

This catenated **CC12**, as with other prepared mechanically interlocked species,[13] can be cited as being potentially useful for the modular construction of complex porous materials from preformed 'porous' building blocks,[1] or as hydrophobic direceptors for the self-assembly of supramolecular polymers.[16,17]

3.6 Aliphatic Diamines

There have already been multiple reports in imine-forming cage chemistry demonstrating the different effects caused from precursor topology. Tozawa *et al.*[1] exemplified how steric bulk on the diamine vertices affected gas sorption properties, while Schneider *et al.*[6] have monitored the effect on their own set of imine-based organic cages by altering the topology of their dialdehyde. Using TFB as with previous cages, various aliphatic diamines (Figure 31) were experimented with to test effect of diamine length on cage formation.

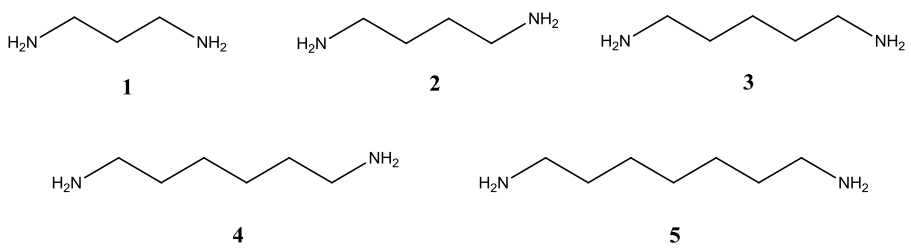

Figure 31: Aliphatic diamines reacted with TFB.

The same synthetic method as used previously for CC1 was employed,[12] with slow addition of aldehyde to diamine to create cages consisting of longer, aliphatic diamines (**CCAD1-5**, Figure 32). From a previous publication by Jiang *et al*. employing a larger trialdehyde and longer aliphatic diamine (1,5-pentanediamine), it was expected that formation of a [2+3] cage would also be possible.[18]

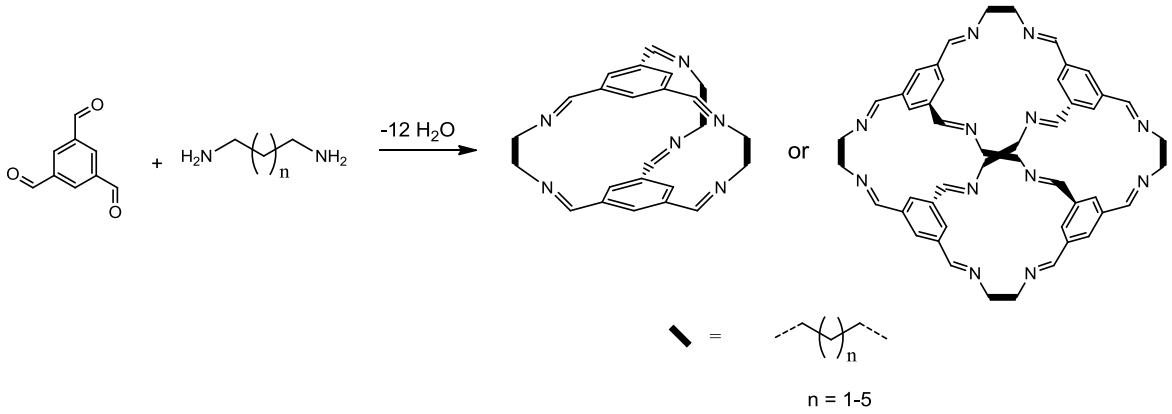

Figure 32: Reaction of TFB with aliphatic diamines to create either [2+3] or [4+6] cages.

Cages were worked up exactly as before,[12] with some of the cages formed proving to be highly unstable. Only the 1,5-diamine and 1,7-diamine cages could be isolated in imine form, while other samples formed thin, insoluble films on removal from solution (likely network formation). As each reaction mixture was clear and contained no precipitate before this work up (suggesting no network formation), the reactions were repeated with ^{1}H NMR and mass spectrometry measured by taking an *in situ* aliquot of the reaction mixture before work up to monitor reaction progress (Figure 33). 48 hours after complete addition, the reaction mixture was divided in to two halves. One half was worked up as before while the other was reduced *in situ* as seen for other preparations in the literature[19] and in this thesis (section 3.4 in this Chapter, and later on in Chapter 4).

Solvent suppression (DCM) ^{1}H NMR of the samples showed clear imine formation in each cage, with imine protons apparent between 8.0 and 8.2 ppm. Aryl hydrogens meanwhile were obvious between 7.6 and 7.8 ppm. Only the 1,6-hexanediamine analogue did not appear to give a clean ^{1}H NMR, with multiple imine and aryl proton environments observed. Integration of the imine and aryl protons for each spectrum indicated an approximate ratio of 1:1 as would be expected, though aliphatic protons from the diamine chain could not all be assigned due to incomplete reaction or overlapping with solvent signals (particularly so with diamine **4**).

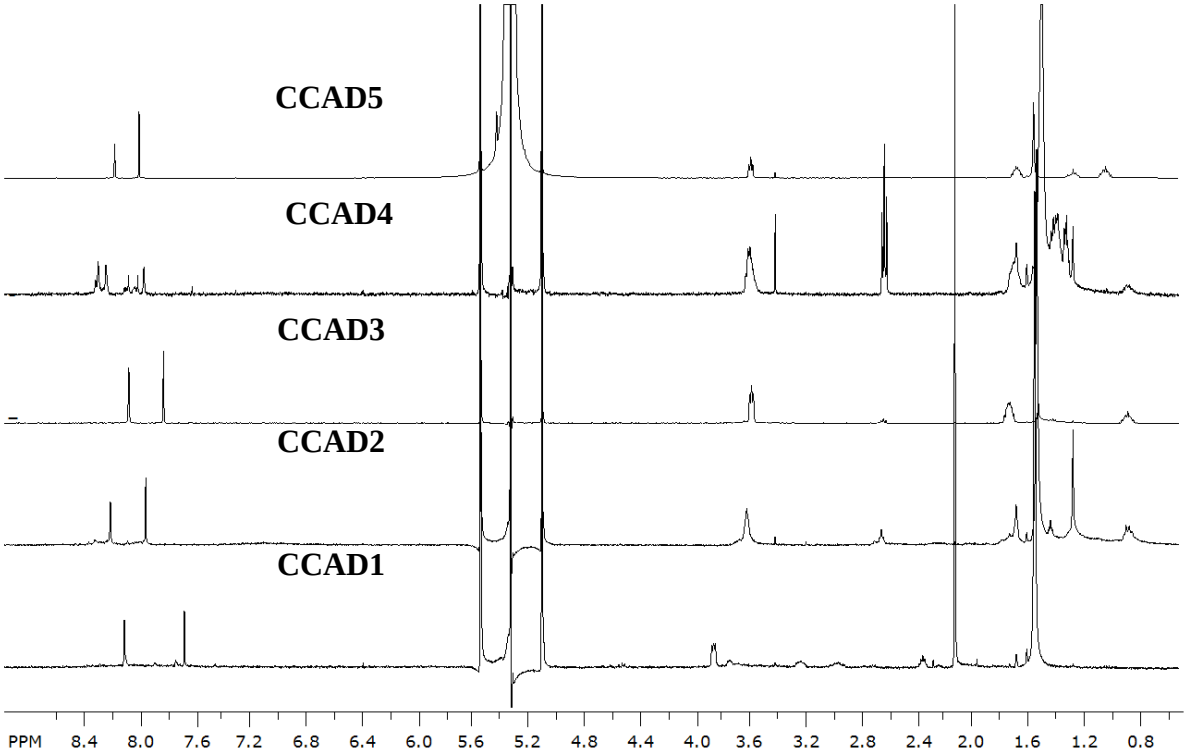

Figure 33: ^{1}H NMR of cages formed from TFB and aliphatic diamines.

Mass spectrometry indicated formation of both regular [4+6] and smaller [2+3] cages (Table 4).[1,18] An intriguing trend can be noted, where cages alternate between the smaller [2+3] and larger [4+6] conformations from **0-3**, with diamines of even carbon numbers producing [4+6] cages and diamines with odd carbon numbers giving rise to smaller [2+3] cages. On the step up to the larger diamine **4**, however, this observation is no longer observed with apparent interchange between [2+3] and [4+6] cages. The trend is then resumed with diamine **5**, with a return to almost exclusive [2+3] cages.

Sample	Diamine	m/z	Cage
0*	1,2-ethanediamine	793	[4+6]
CCAD1	1,3-propanediamine	439.3	[2+3]
CCAD2	1,4-butanediamine	961	[4+6]
CCAD3	1,5-pentanediamine	524	[2+3]
CCAD4	1,6-hexanediamine	565/1130	[2+3]/[4+6]
CCAD5	1,7-heptanediamine	607	[2+3]

Table 4: Mass spectrometry of cages formed from TFB and aliphatic diamines. *Shown previously in the literature.[1]

The other half of the reaction mixtures were reduced *in situ*.[19] Upon work up after reduction, ^{1}H NMR for each could be collected. All samples were successfully reduced, as determined by complete lack of an imine signal in the ^{1}H NMR spectrum which had shifted to a signal at around 3.6 ppm for the new CH_2 proton environment (Figure 34).

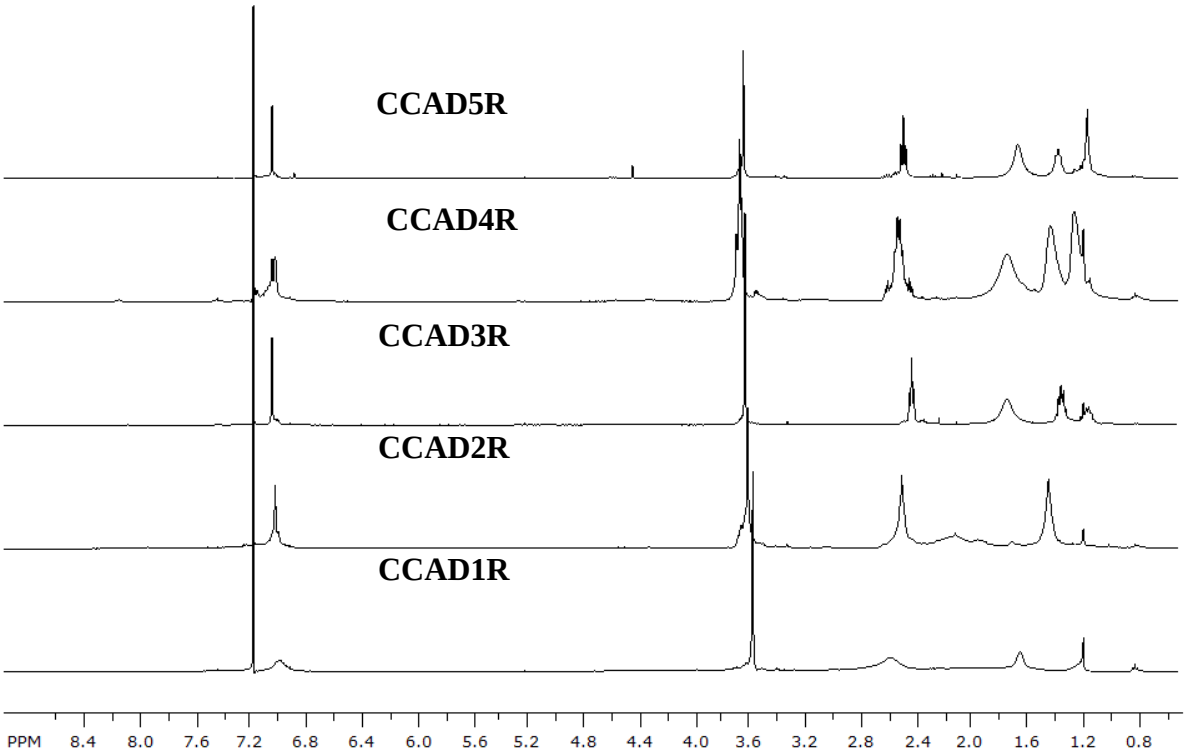

Figure 34: ^{1}H NMR of reduced cages formed from TFB and aliphatic diamines.

Mass spectrometry of the reduced cages again showed a mix of [2+3] and [4+6] cages upon reduction (Table 5).

Sample	Diamine	m/z	Cage
0*	1,2-ethanediamine	817.7	[4+6]
CCAD1R	1,3-propanediamine	451.4	[2+3]
CCAD2R	1,4-butanediamine	985.8	[4+6]
CCAD3R	1,5-pentanediamine	535.4	[2+3]
CCAD4R	1,6-hexanediamine	577.5/1154	[2+3]/[4+6]
CCAD5R	1,7-heptanediamine	619.5	[2+3]

Table 5: Mass spectrometry of cages formed from TFB and aliphatic diamines. *Shown previously in the literature.[19]

We hypothesise that this alternation in cage stoichiometry with odd/even carbon lengths is connected to strain of resulting imine bonds, and calculations are in progress to prove this. The appearance of [2+3] cages is somewhat complimented by the publication by Jiang *et al.* whereby 1,5-pentanediamine also formed a [2+3] propeller shaped cage (although in this instance 1,3,5-tri(4-formylphenyl)benzene was used and not TFB).[18]

3.7 Conclusions

A new porous organic cage has been prepared exhibiting intriguing gas sorption properties, further highlighting the importance of solvent choice in work-up of cages. Unlike previous porous organic cages such as CC3 where surface area increases on amorphisation,[9] **CC12** appeared to become more porous when crystalline and non-porous when amorphous (at least to nitrogen). This observation of porosity switching was made for CC1 previously[15] and exemplified here for **CC12** through a polymorphism study employing thirty directing solvents, with only crystalline samples showing any semblance of nitrogen uptake.

Speed of recrystallisation also impacts heavily on the sorption properties of the cage material, as seen with previous porous organic cages.[9] When forced out of solution quickly by solvent swapping DCM with acetone, a crystalline porous polymorph with N_2 SA_{BET} = 405 m²/g was afforded. However, by slow evaporation of DCM with acetonitrile layered on top, although an identical pXRD pattern was afforded, higher porosity of N_2 SA_{BET} = 517 m²/g was observed. The method of recrystallisation was also extremely important. For example, when dioxane was originally layered on top of a solution of **CC12** in DCM before evaporation in the polymorphism study, an amorphous material was afforded. When repeated by means of slow diffusion of a sealed solution of **CC12** in DCM surrounded by an excess of dioxane however, cubic crystals were afforded which were used to solve the material's structure by single crystal X-ray analysis. This sample was also much more porous with a N_2 SA_{BET} = 946 m²/g.

We can try to rationalise this behaviour by comparing the bulk in the diamine vertices between CC3 and **CC12**. While **CC12** has relatively little steric bulk on its diamine (two hydrogen atoms and two methyl groups), CC3 possesses bulky

cyclohexane vertices. We expect that on loss of long range order in CC3, this bulky cyclohexane group cannot interpenetrate with a neighbouring cages window as easily as the smaller diamine vertices of **CC12** could with another cage. This would result in **CC12** consisting of a much more tightly packed arrangement of cages and consequently reduced pore volume on induction of an amorphous state.

CC12 itself also required significantly longer reaction times compared to CC1 and CC2. We hypothesise this is likely due to the presence of an extra methyl group on the diamine vertices, decreasing the likelihood of the two amine groups preferring an antiperiplanar conformation in comparison to a synperiplanar (reactive) state, with cage formation driven by thermodynamics.

The cage could also be catenated as with previous samples, likely due to relatively low steric bulk on the diamine compared to other cages which cannot catenate (e.g., CC3, cannot undergo catenation due to its bulky cyclohexane groups preventing interpenetration of cages).[13]

Experimentation with length of diamine also showed an influence on the size of cage produced, with an even number of carbons in the diamine (**2**, **4**) resulting in [4+6] cages and an odd number of carbons in the diamine (**3**, **5**, **7**) resulting in [2+3] cages. Diamine **6** was the exception to this rule, resulting in formation of both [2+3] and [4+6] cages.

3.8 Experimental

Materials. 1,3,5-Triformylbenzene was purchased from Manchester Organics, UK. 2-Dimethyl-1,2-propanediamine was purchased from TCI Europe. All other chemicals were purchased from Sigma-Aldrich and used as received.

CC12. 1,2-diamino-2methyl-propane (1.529 g, 0.0173 mol) was dissolved in dichloromethane (450 mL) in 2 L round-bottomed flask cooled in an ice bath equipped with a stirrer bar. Solution was stirred at 270 RPM under N_2 for approximately 15 minutes. 1,3,5-Triformylbenzene (1.875 g, 0.0116 mol) was dissolved in dichloromethane (575 mL) in a pressure equalised dropping funnel and added dropwise over 24 hours to the 2-dimethyl-1,2-propanediamine solution. The reaction mixture was allowed to stir for a further 72 hours at room temperature upon

complete addition (monitored by NMR). The solution was then evaporated to dryness (using a rotary evaporator with bath at 20 °C) to yield the crude product. The crude was re-dissolved in chloroform (100 mL) and filtered. The filter paper was washed over with chloroform (2x 50 mL) and the combined organics evaporated to dryness once more (using a rotary evaporator with bath at 20 °C) to give the product as a white powder. The product was vacuum dried overnight to yield **CC12$^{\alpha}$** as a white amorphous powder in 81 % yield (2.257 g). For production of **CC12$^{\beta}$**, **CC12$^{\alpha}$** was redissolved in DCM (~100 mL) and acetone (200 mL) added before concentrating the solution (~100 mL). This initiated a 'solvent swap' with the cage being forced into acetone (in which the cage is only sparingly soluble) forcing precipitation. Cage was then filtered off under reduced pressure and vacuum dried to yield **CC12$^{\beta}$**. **CC12$^{\beta 2}$** on the other hand was prepared by dissolution of **CC12$^{\alpha/\beta}$** in DCM and layering of MeCN on top, allowing slow evaporation to yield large crystals of **CC12$^{\beta 2}$** over a period of 3-4 days. Finally, **CC12$^{\gamma}$** was prepared by dissolving CC12 in DCM in a small vial and placing in a larger vial containing dioxane to allow slow diffusion. ^{1}H NMR ($CDCl_3$, 400 MHz) δ 8.21-8.11(m, 1 H, -CH=N), 8.01-7.88 (m, 1 H, -ArH), 3.80 (s, 1 H, N-CH_2-C), 1.51 (s, 3 H, -C(CH_3)$_2$). ^{13}C NMR ($CDCl_3$, 100 MHz) δ 161.2-160.7, 155.5-155.0, 137.1-136.6, 129.3, 72.4, 61.3, 25.9 ppm. Acc. Mass MS m/z = 961.6 for $C_{60}H_{72}N_{12}$ $[M]^+$. CHN Calc. C: 74.97, H: 7.55, N: 17.48; found C: 74.04, H: 7.35, N: 17.55.

CC12R. **CC12** (87 mg, 0.09047 mmol) was dissolved in methanol (60 mL) and filtered through fluted filter paper into a 250 mL round-bottomed flask equipped with a stirrer bar. Sodium borohydride (45 mg, 1.1762 mmol) was added over a 5 minute period and solution left stirring at 300 RPM for 14 hours. Extra sodium borohydride (5 mg) added and solution left for a further 5 hours to ensure complete reduction. Water (2 mL) was added and the solution was left to stir for 4 hours. Solution evaporated to dryness to give a white precipitate. Chloroform (50 mL) was added and the mixture was stirred for 1 hour before filtering. Remaining precipitate washed with chloroform (50 mL) and filtered before combining organics and evaporating to dryness to yield **CC12R** as a white foamy precipitate in 82 % yield (73 mg). ^{1}H NMR ($CDCl_3$, 400 MHz) δ 7.23-6.98 (m, 1 H, -ArH), 3.76-3.51 (m, 2H, -ArCH_2), 2.52-2.36 (m, 1 H, N-CH_2-C), 1.17-1.03 (m, 3 H -C(CH_3)$_2$). ^{13}C NMR ($CDCl_3$, 100 MHz) δ 140.9, 126.1, 57.2, 53.5, 46.4, 29.3, 25.4 ppm. Acc. Mass MS

m/z = 985.8 for $C_{60}H_{96}N_{12}$ $[M]^+$. CHN Calc. C: 73.13, H: 9.82, N: 17.06; found C: 69.40, H: 9.20, N: 16.23.

CC12 Catenane. Acetonitrile (150 mL) was added slowly to 1,3,5-triformylbenzene (500 mg, 3.08 mmol) in a 250 mL round-bottom flask at room temperature. After 5 minutes, trifluoroacetic acid (100 μL, 1.35 mmol) was added, followed by a solution of 1,2-diamino-2methly-propane (408 mg, 4.63 mmol) in acetonitrile (50 mL). The resulting mixture was left covered for seven days without stirring. After 5 days, a clear pale yellow solution was observed which contained some crystals with cubic morphology as well as a thin layer of amorphous precipitate at the bottom of the reaction flask. The solids were removed by filtration and re-dissolved in DCM, and filtered to remove the insoluble precipitate (yield ~60 %). Single crystal data was obtained from a crystal grown by evaporation of dichloromethane (DCM) with a layer of methanol added to the surface. ^{1}H NMR (CD_2Cl_2, 400 MHz) δ 8.53-8.50, 8.28, 7.78-7.96 (m, -CH=N), 8.10-7.95, 7.22-7.06, 5.82 (m, -ArH), 4.03-3.58 (m, N-CH_2-C), 2.04, 1.68, 1.43, 1.28 (m, -C(CH_3)$_2$). Acc. Mass MS m/z = 1923.2 for $C_{120}H_{144}N_{24}$ $[M]^+$ and 1924.2 for $[M+Na^+]$ = 1946.2. CHN Calc. C: 74.97, H: 7.55, N: 17.48; found C: 61.13, H: 6.08, N: 13.72.

Polymorphism Study. **CC12** was dissolved in DCM (5 mg/mL concentration) and 6 mL of CC12/DCM solution dispensed in to 40 mL vials using a Chemspeed ASW robot. Various directing solvents (1 mL, 30 different solvents in total) were then added to each solution of cage and N_2 gas passed over for 1 week. Samples containing higher boiling point solvents (6, 9 , 18, 19, 21 and 23) did not completely dry from this process and were gently vacuum dried (800 mbar, 40 °C) for 24 hours to remove remaining solvent. All samples were then thoroughly vacuum dried (0 mbar, 50 °C) for 24 hours before submission for nitrogen gas sorption using a Quantachrome surface area and pore size analyser to collect a 7 point isotherm using N_2. Powder patterns were measured using a Panalytical XRD machine with high-throughput plate.

CCAD1 (representative procedure). 1,3-Propanediamine (129 mg, 1.7346 mmol) was added to dichloromethane (45 mL) in a 200 mL round-bottomed flask cooled in an ice bath equipped with a stirrer bar. Solution was stirred at 270 RPM under N_2 for

approximately 15 minutes. 1,3,5-Triformylbenzene (187.5 mg, 1.1564 mmol) was dissolved in dichloromethane (60 mL) in a pressure equalised dropping funnel and added drop wise over 4 hours to the 1,3-propanediamine solution. 48 hours after slow addition, no more aldehyde was present and the reaction appeared complete by ^{1}H NMR. The reaction mixture was divided into two halves, with one half evaporated to dryness (using a rotary evaporator with bath at 20 °C) to yield an insoluble polymeric film (95.8 mg, 75 % yield). ^{1}H NMR (CD_2Cl_2, 400 MHz) 8.13 (s, 1 H, -CH=N), 7.69 (s, 1 H, -ArH), 3.86 (m, 2 H, N-CH_2-C), 2.35 (m, 1 H, CH_2-CH_2-CH_2). MS m/z = 439.3 for $C_{27}H_{30}N_6$ $[M+H]^+$.**CCAD1R (representative procedure).** Methanol (30 mL) was added to the other half of the reaction mixture followed by sodium borohydride (76 mg, 2.0087 mmol) and allowed to stir overnight. Water (5 mL) was then added and the reaction stirred for a further 12 hours. The solvent was then removed under vacuum. The resulting white solid was extracted with chloroform (2 x 50 mL) and the remaining white solid removed by filtration. The solvent was then removed under vacuum and CCAD1 obtained as white solid in 9 % yield (11.4 mg). ^{1}H NMR ($CDCl_3$, 400 MHz) δ 7.00 (s, 1 H, -ArH), 3.59 (s, 2 H, -ArCH_2), 2.57 (s, 2H, N-CH_2-C), 1.17 (m, 1 H , CH_2-CH_2-CH_2). MS m/z = 451.4 for $C_{27}H_{42}N_6$ $[M+H]^+$.

CCAD2

Insoluble thin film, 58.4 mg (42 % yield). ^{1}H NMR (CD_2Cl_2, 400 MHz) δ 8.23 (s, 1 H, -CH=N), 7.98 (s, 1H, -ArH), 3.62 (m, 2 H, N-CH_2-C), 2.65 (m, 2 H, CH_2-CH_2CH_2-CH_2). MS m/z = 961 for $C_{60}H_{72}N_{12}$ $[M]^+$ and 984 for $C_{60}H_{72}N_{12}Na$ $[M+Na]^+$.

CCAD2R

White precipitate, 32 mg (23 % yield). ^{1}H NMR ($CDCl_3$, 400 MHz) δ 7.04 (s, 1H, -ArH), 3.62 (s, 1H, -ArCH_2), 2.50 (m, 2 H, N-CH_2-C), 1.44 (m, 2 H, CH_2-CH_2CH_2-CH_2). MS m/z = 985.8 for $C_{60}H_{96}N_{12}$ $[M]^+$.

CCAD3

Off-white powder, 138.8 mg (92 % yield). ^{1}H NMR (CD_2Cl_2, 400 MHz) δ 8.10 (s, 1 H, -CH=N), 7.85 (s, 1H, -ArH), 3.59 (m, 2 H, N-CH_2-C), 1.72 (m, 2 H, NCH_2-CH_2-CH_2), 0.87 (m, 1 H, $CH_2(CH_2CH_2)_2$). MS m/z = 523 for $C_{33}H_{42}N_6$ $[M]^+$ and 546 for $C_{33}H_{42}N_6$ [M+Na].

CCAD3R

White precipitate, 73.6 mg (48 % yield). ^{1}H NMR ($CDCl_3$, 400 MHz) δ 7.06 (s, 1H, -ArH), 3.64 (s, 2 H, -ArCH_2), 2.43 (m, 2 H, N-CH_2-C), 1.34 (m, 2 H, NCH_2-CH_2-CH_2), 1.16 (m, 1 H, $CH_2(CH_2CH_2)_2$). MS m/z = 535.4 for $C_{33}H_{54}N_6$ $[M+H]^+$.

CCAD4

Yellow/off-white thin film, 39.7 mg (24 %). ^{1}H NMR (CD_2Cl_2, 400 MHz) δ 8.34-8.26 (m, 1 H, -CH=N), 8.12-7.99 (m, 1H, -ArH), 3.60 (m, N-CH_2-C), 2.63 (m, NCH_2-CH_2-CH_2CH_2), 1.67 (m, N$CH_2CH_2CH_2$-CH_2). MS m/z = 565 for $C_{36}H_{48}N_6$ $[M]^+$ and 588 for $C_{36}H_{48}N_6$ $[M+Na]^+$. MS m/z = 1130 for $C_{72}H_{96}N_{12}$ $[M]^+$ and 1153 for $C_{72}H_{96}N_{12}$ $[M+Na]^+$.

CCAD4R

White precipitate, film, 47.9 mg (29 %). ^{1}H NMR ($CDCl_3$, 400 MHz) δ 7.06 (m, 1H, -ArH), 3.67 (s, 1 H, -ArCH_2), 2.53 (m, 2 H, N-CH_2-C), 1.41 (m, 2 H, NCH_2-CH_2-CH_2CH_2), 1.25 (m, 2 H, N$CH_2CH_2CH_2$-CH_2). MS m/z = 577.5 for $C_{36}H_{54}N_6$ $[M+H]^+$. MS m/z = 1154 for $C_{72}H_{96}N_{12}$ $[M]^+$.

CCAD5

White powder, 166 mg (95 % yield). ^{1}H NMR (CD_2Cl_2, 400 MHz) δ 8.20 (s, 1 H, -CH=N), 8.02 (s, 1 H, -ArH), 3.59 (m, 2 H, N-CH_2-C), 1.67 (m, 2 H, NCH_2-CH_2-CH_2CH_2), 1.26 (m, 1 H, $CH_2(CH_2CH_2CH_2)_2$). MS m/z = 607 for $C_{39}H_{66}N_6$ $[M]^+$ and 630 for $C_{39}H_{66}N_6$ $[M+Na]^+$.

CCAD5

White powder, 105.3 mg (59 % yield). ^{1}H NMR ($CDCl_3$, 400 MHz) δ 7.06 (s, 1 H, -ArH), 3.65 (s, 2 H, -ArCH_2), 2.49 (m, 2 H, N-CH_2-C), 1.37 (m, 2 H, NCH_2-CH_2-CH_2CH_2), 1.16 (m, 1 H, $CH_2(CH_2CH_2CH_2)_2$. MS m/z = 619.5 for $C_{39}H_{66}N_6$ $[M+H]^+$.

Single Crystal Data for CC12$^{\beta}$ and CC12$^{\gamma}$

Single crystal X-ray data were measured on a Rigaku MicroMax-007 HF rotating anode diffractometer (Mo-Kα radiation, λ = 0.71073 Å, Kappa 4-circle goniometer, Rigaku Saturn724+ detector). An empirical absorption correction using equivalent reflections was performed with the program SADABS; the structure was solved with the program SHELXD and refined with SHELXL using the OLEX2 GUI. All non H atoms were refined anisotropically, H atoms were fixed to geometric positions using the riding model, solvent H atoms were omitted from the refinement model.

Crystal data for **CC12$^{\beta}$**: Formula $C_{60}H_{72}N_{12}$, M = 961.30 g·mol^{-1}, trigonal space group $P3$, a = 24.075(2), c = 10.7146(12) Å, V = 5378.3(9) Å^3, Z = 3, ρ = 0.890 g·cm^{-3}, μ = 0.054 mm^{-3}, F (000) = 1548, crystal size = 0.32 x 0.07 x 0.06 mm^3, T = 100(2) K. 3759 reflections measured (1.69 < Θ < 20.81°), 3759 unique (R_{int} = 0.0000), 2576 observed ($I > 2\sigma(I)$), R_1 = 0.0546 for the observed and R_1 = 0.0714 for all reflections, max/min residual electron density = 0.123 and -0.108 e·Å^{-3}, data / restraints / parameters = 3759 / 190 / 711, GOF = 1.112.

Crystal data for **CC12$^{\gamma}$** $C_{60}H_{72}N_{12} \cdot 3C_4H_8O_2 \cdot 6H_2O$, formula $C_{72}H_{108}N_{12}O_{12}$, M = 1333.70 g·mol^{-1}, cubic space group Fd-3, a = 25.8504(9) Å, V = 17274.4(10) Å^3, Z = 8, ρ = 1.026 g·cm^{-3}, μ = 0.070 mm^{-3}, F (000) = 5760, crystal size = 0.18 x 0.18 x 0.10 mm^3, T = 100(2) K. 41367 reflections measured (2.61 < Θ < 20.80°), 765 unique (R_{int} = 0.0375), 618 observed ($I > 2\sigma(I)$), R_1 = 0.0973 for the observed and R_1 = 0.1080 for all reflections, max/min residual electron density = 0.164 and -0.170 e·Å^{-3}, data / restraints / parameters = 765 / 0 / 108, GOF = 2.668.

Single Crystal Data for CC12 Catenane

Single crystal X-ray data were measured on a Rigaku MicroMax-007 HF rotating anode diffractometer (Mo-Kα radiation, λ = 0.71073 Å, Kappa 4-circle goniometer, Rigaku Saturn724+ detector). An empirical absorption correction using equivalent reflections was performed with the program SADABS; the structure was solved with the program SHELXD and refined with SHELXL using the OLEX2 GUI. All non H atoms were refined anisotropically, H atoms were fixed to geometric positions using the riding model, most solvent H atoms were omitted from the refinement model. Atomic displacement parameters (ADPs) of the catenated cage molecules are large, in particular of atoms not involved in π-π stacking, and racemic *R*/*S* disorder as well as disorder in the isobutyl linkers cannot be ruled out. In the current refinement model any such disorder (static or dynamic) is covered by aforementioned large ADPs. Rigid bond restraints (DELU instruction in SHELXL) were applied to all anisotropically refined atoms.

Crystal data for **CC12** Catenane: $(C_{60}H_{72}N_{12})_2 \cdot 7CH_3OH \cdot 3H_2O$, formula $C_{127}H_{178}N_{24}O_{10}$, M = 2200.93 g·mol^{-1}, rhombohedral space group R-3, a = 19.8544(13), b = 19.8544(13), c = 28.849(3) Å, V = 9848.6(13) Å^3, Z = 3, ρ = 1.113

g·cm^{-3}, μ = 0.072 mm^{-3}, F (000) = 3564, crystal size = 0.12 x 0.10 x 0.08 mm^3, T = 90(2) K. 19676 reflections measured (1.84 < Θ < 18.88°), 1739 unique (R_{int} = 0.0415), 1256 observed ($I > 2\sigma(I)$), R_1 = 0.1065 for the observed and R_1 = 0.1304 for all reflections, max/min residual electron density = 0.198 and -0.166 e·Å^{-3}, data / restraints / parameters = 1739 / 57 / 245, GOF = 2.364.

3.9 References

(1) Tozawa, T.; Jones, J. T. A.; Swamy, S. I.; Jiang, S.; Adams, D. J.; Shakespeare, S.; Clowes, R.; Bradshaw, D.; Hasell, T.; Chong, S. Y.; Tang, C.; Thompson, S.; Parker, J.; Trewin, A.; Bacsa, J.; Slawin, A. M. Z.; Steiner, A.; Cooper, A. I. *Nat. Mater.* **2009**, *8*, 973.

(2) Zhang, C.; Chen, C.-F. *J. Org. Chem.* **2006**, *71*, 6626.

(3) Mastalerz, M. *Chem. Commun.* **2008**, 4756.

(4) Mastalerz, M. *Angew. Chem. Int. Ed.* **2010**, *49*, 5042.

(5) Mastalerz, M.; Schneider, M. W.; Oppel, I. M.; Presly, O. *Angew. Chem. Int. Ed.* **2011**, *50*, 1046.

(6) Schneider, M. W.; Oppel, I. M.; Ott, H.; Lechner, L. G.; Hauswald, H.-J. S.; Stoll, R.; Mastalerz, M. *Chem. Eur. J.* **2012**, *18*, 836.

(7) Skowronek, P.; Gawronski, J. *Org. Lett.* **2008**, *10*, 4755.

(8) Jiang, S.; Jones, J. T. A.; Hasell, T.; Blythe, C. E.; Adams, D. J.; Trewin, A.; Cooper, A. I. *Nat. Commun.* **2011**, *2*, 207.

(9) Hasell, T.; Chong, S. Y.; Jelfs, K. E.; Adams, D. J.; Cooper, A. I. *J. Am. Chem. Soc.* **2011**, *134*, 588.

(10) Hasell, T.; Schmidtmann, M.; Smith, M.; Stone, C.; Cooper, A. I. *Chem. Commun.* **2012**, *48*, 4689.

(11) Clayden, J.; Greeves, N.; Warren, S.; Wothers, P. *Organic Chemistry*; Oxford University Press, 2001, 14, 348.

(12) Lydon, D. P.; Campbell, N. L.; Adams, D. J.; Cooper, A. I. *Synth. Commun.* **2011**, *41*, 2146.

(13) Hasell, T.; Wu, X.; Jones, J. T. A.; Bacsa, J.; Steiner, A.; Mitra, T.; Trewin, A.; Adams, D. J.; Cooper, A. I. *Nat. Chem.* **2010**, *2*, 750.

(14) Mitra, T.; Wu, X.; Clowes, R.; Jones, J. T. A.; Jelfs, K. E.; Adams, D. J.; Trewin, A.; Bacsa, J.; Steiner, A.; Cooper, A. I. *Chem. Eur. J.* **2011**, *17*, 10235.

(15) Jones, J. T. A.; Holden, D.; Mitra, T.; Hasell, T.; Adams, D. J.; Jelfs, K. E.; Trewin, A.; Willock, D. J.; Day, G. M.; Bacsa, J.; Steiner, A.; Cooper, A. I. *Angew. Chem. Int. Ed.* **2011**, *50*, 749.

(16) Roosma, J.; Mes, T.; Leclère, P.; Palmans, A. R. A.; Meijer, E. W. *J. Am. Chem. Soc.* **2008**, *130*, 1120.

(17) Brunsveld, L.; Folmer, B. J. B.; Meijer, E. W.; Sijbesma, R. P. *Chem. Rev.* **2001**, *101*, 4071.

(18) Jiang, S.; Bacsa, J.; Wu, X.; Jones, J. T. A.; Dawson, R.; Trewin, A.; Adams, D. J.; Cooper, A. I. *Chem. Commun.* **2011**, *47*, 8919.

(19) Swamy, S. I.; Bacsa, J.; Jones, J. T. A.; Stylianou, K. C.; Steiner, A.; Ritchie, L. K.; Hasell, T.; Gould, J. A.; Laybourn, A.; Khimyak, Y. Z.; Adams, D. J.; Rosseinsky, M. J.; Cooper, A. I. *J. Am. Chem. Soc.* **2010**, *132*, 12773.

Chapter 4
Preparation and Functionalisation of Reduced Organic Cages

Table of Contents

4.0 The Preparation of Reduced Cages 1 and 5

Previously, the syntheses of imine-based porous organic cages have been carried out (see Chapter 1 and 3 for more details) using various diamines and trialdehydes.[1] In such porous organic cages, porosity arises from internal cavities (intrinsic porosity) along with poor packing of cages with one another creating interstitial channels (extrinsic porosity). These cage molecules are created by reversible formation of an imine bond and as such, are susceptible to hydrolysis and consequent degradation of the cage molecule. However, there has been a recent publication by Hasell *et al.*[2] which shows that CC3 can be boiled in water and maintain its structural integrity. By reducing the cage molecule, we can further 'lock' the molecule in its cage form. Upon chemical reduction, however, the cages become much more flexible and collapse in upon themselves, thus becoming impenetrable to gases at low temperature (as seen in other examples in the literature[3]). These reduced cages have been prepared and reduced *in situ* for use as an organic MOF-linker,[4] which itself provides an intriguing secondary amine-based molecule, and the basis for this work. Reduced CC1 (RC1) was produced over two steps *in situ* in good yields (Figure 1). CC1 is first prepared by slow addition of 1,3,5-triformylbenzene to ethylenediamine in cooled methanol (reaction monitored by ^{1}H NMR), before addition of sodium borohydride to reduce to RC1.

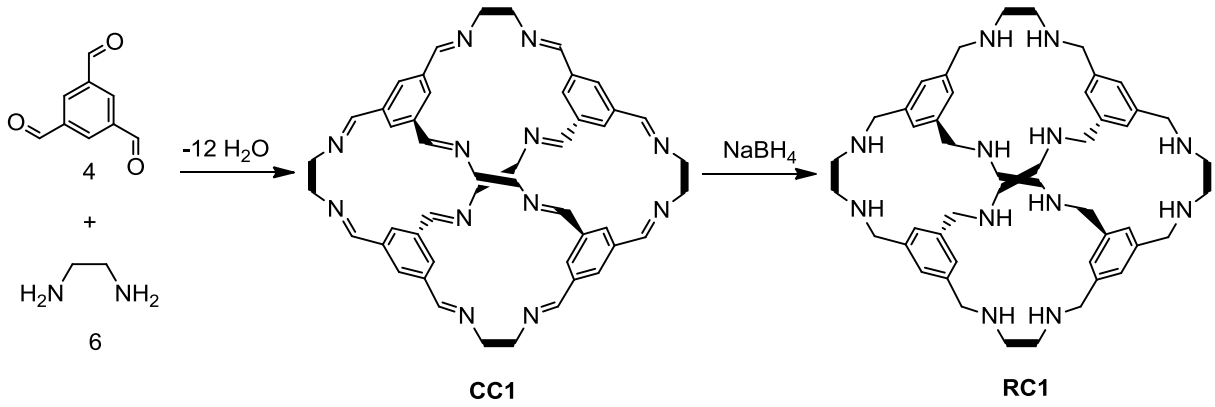

Figure 1: *In situ* preparation of **RC1**, a reduced amine cage.

Cage 5 (CC5)[5] was also selected for functionalisation, in the hope that the cage structure would not collapse because it contains more rigid diamine vertices while also possessing a larger internal pore. Reduced CC5 (RC5) was produced over two separate steps. The imine CC5 was produced by layering (1*S*, 2*S*)-1,2-cyclopentanediamine dihydrocholoride in methanol on top of a solution of tris(4-formylphenyl)amine in dichloromethane as previously reported,[5] before being reduced to the secondary amine afterwards with a large excess of sodium borohydride (Figure 2). This difference in procedure was attributed to CC5 having poor solubility in comparison to CC1. As observed with other reduced cages,[3] RC5 was non-porous to nitrogen and hydrogen.

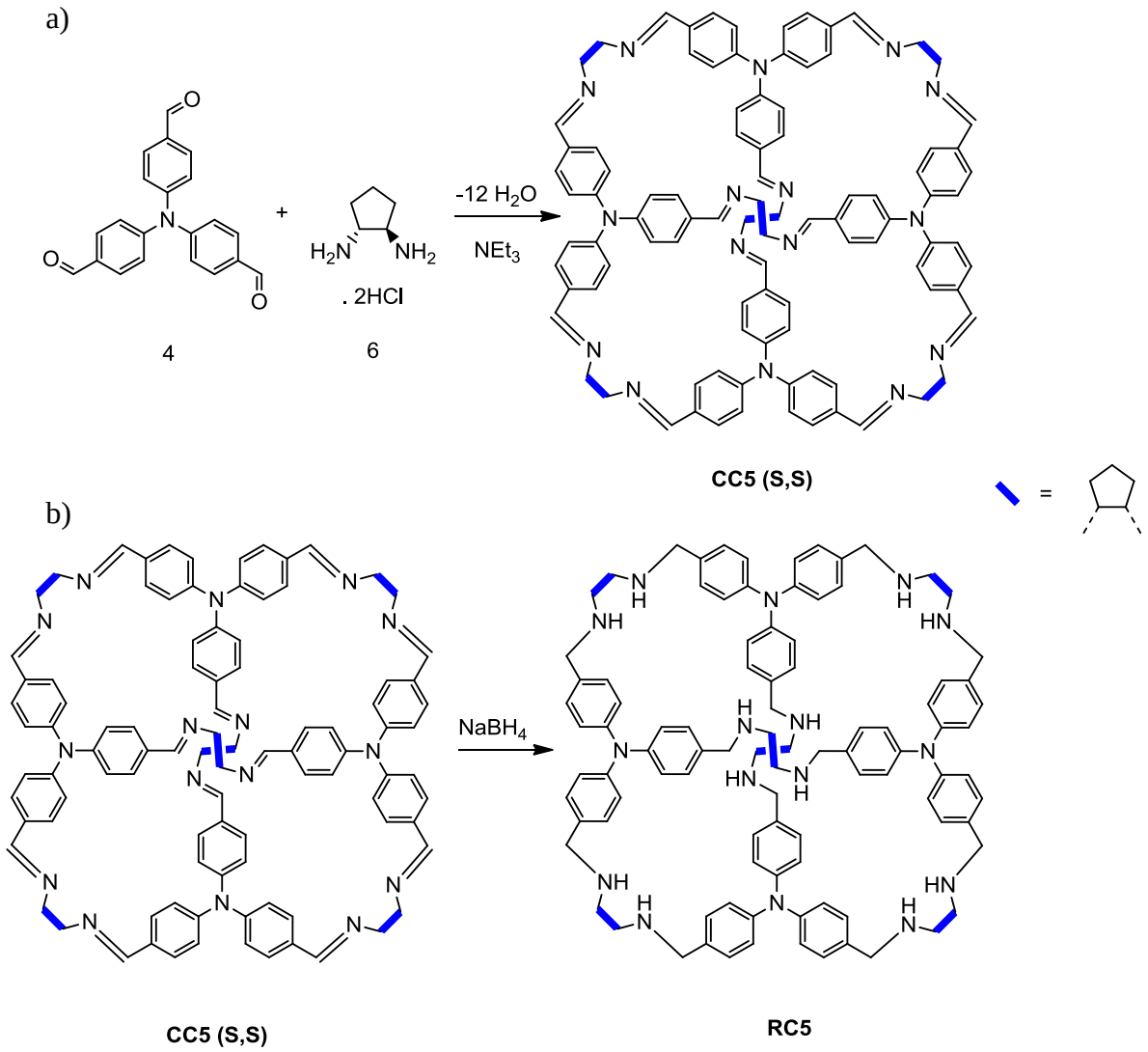

Figure 2: a) Preparation of **CC5 (S,S)** and b) subsequent reduction to **RC5**.

4.1 Nucleophilic Addition/Elimination Between Amines and Acid Halides

In an attempt to rigidify the reduced cages and to restore porosity/increase functionality, reduced cages were modified by simple addition of acid halides to yield various amide-functionalised organic cages.[6] The addition/elimination mechanism is detailed below in Figure 3. Initially, the amine acts as a nucleophile (addition stage), with the nitrogen lone pair attacking the acid halide carbonyl carbon. This is followed by reformation of the carbon-oxygen double bond releasing a halide ion, before removal of hydrogen (elimination stage). Triethlyamine (pK_a = 10.65) is used to remove this eliminated hydrogen atom preferentially over unreacted amine (assuming $pK_a \approx 9.68$, that of benzylethamine).[7]

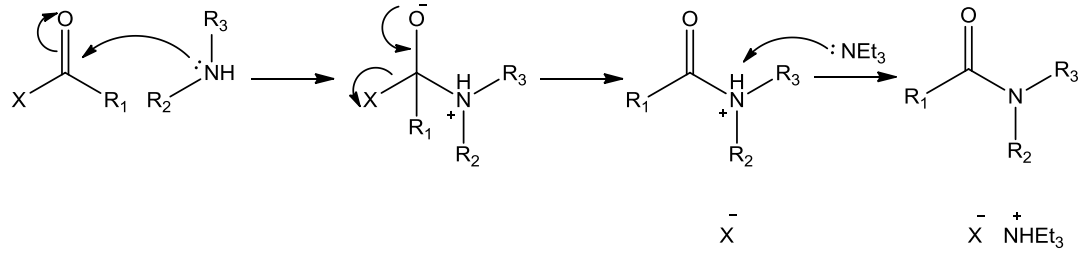

Figure 3: Mechanism of reaction between a secondary amine and an acid halide.

Acid halides were selected due to their abundance and high reactivity. A slight excess of acid chloride was used in the reaction with triethylamine to react with hydrochloric acid that is formed (Figure 4)

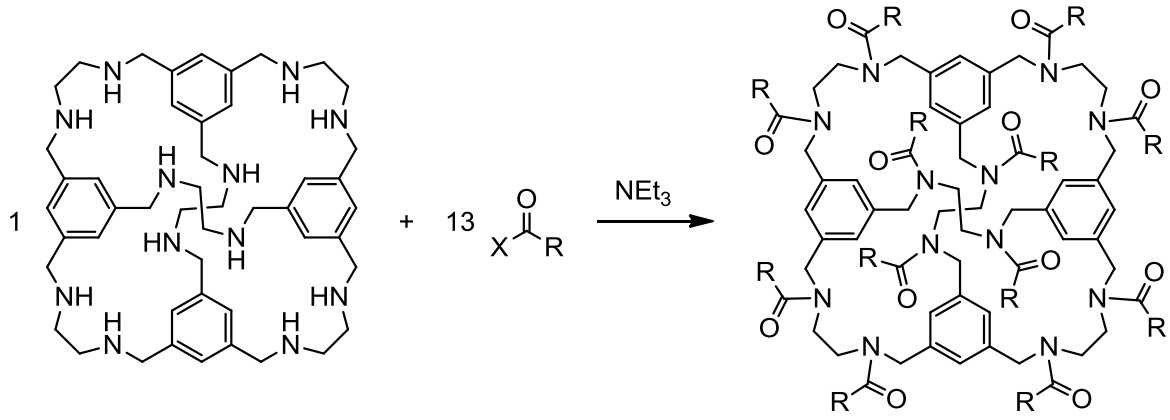

Figure 4: Functionalisation of **RC1** with an acid halide (X = Cl, Br).

4.2 Functional Groups: Toward Increased Porosity

As porosity in these systems is derived through both intrinsic and extrinsic factors (with extrinsic porosity arising from inefficient packing in porous organic cages),[8] pendant groups **a**–**e** (Figure 5) were added with the aim of exaggerating extrinsic porosity by increasing inefficient molecular packing. Groups with the potential for further functionalisation were also selected, with the prospect of opening up opportunities for further reactions on a decorated cage (**a**, **d**, **e** and even **b** – some of which are highlighted in Chapter 5).

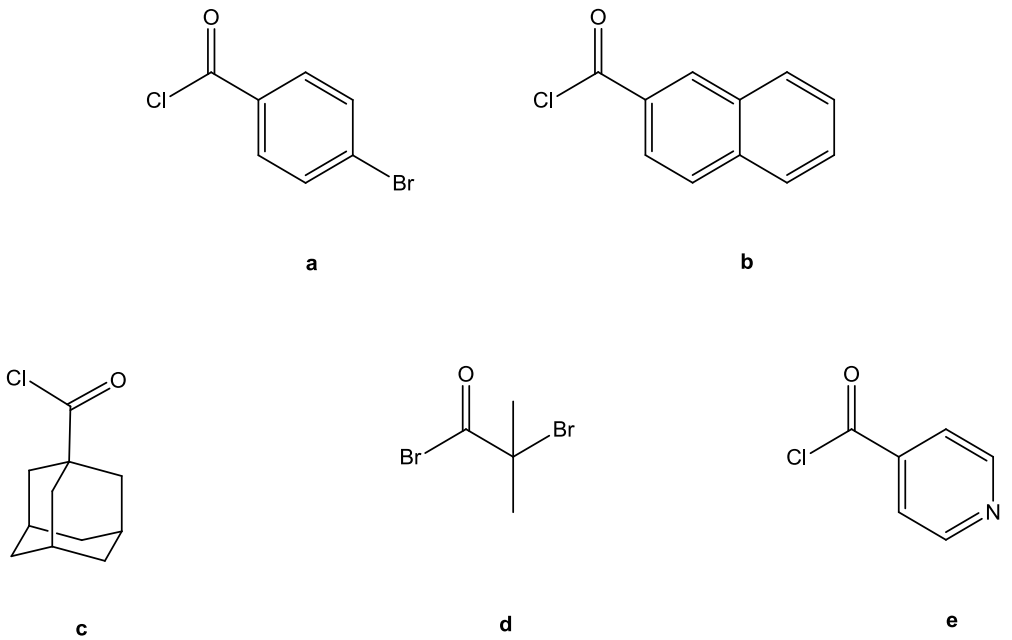

Figure 5: Bulky and/or functional acid chlorides.

Acid halides **a**–**e** were all successfully reacted with **RC1**, and **a**–**c** were also attached to **RC5**. The structures of the functionalised cages were verified by ^{1}H and ^{13}C NMR, FT-IR, MALDI-TOF, and in some cases single crystal x-ray diffraction.

^{1}H and ^{13}C NMR collected for **RC1a**–**e** and **RC5a**–**c** were all relatively poor compared to NMR collected for previous cages,[1] with spectra presenting large, broad signals and making them difficult to interpret. We have rationalised this on the basis of the many rotamers present in each amide-decorated cage (with the amide bond not allowing free rotation), resulting in a series of positional isomers. Attempts were made to minimize this effect by low temperature NMR and, while some spectral data was improved (**RC1a**), other decorated cages became insoluble and hence no improvement in data was observed (such as **RC1b**, as shown later in Figure 23). From the NMR data collected, we were able to assign proton and carbon spectra, with integrals matching well (see Figure 6 and Figure 7 for ^{1}H and ^{13}C NMR of **RC1a** respectively).

^{1}H NMR (Figure 6) was carried out in DCM (solvent peak at 5.27 ppm) at -50 °C, with –BrArH doublets at 7.55-7.54 ppm and 7.32-7.31 ppm. ArH of the internal cage core was apparent at 6.97 ppm while –ArCH_2 appeared at 4.68 ppm and –NCH_2 was at 3.54 ppm.^{13}C NMR (Figure 7) was carried out in $CDCl_3$ (seen as a triplet at 77.3 ppm). 172.1 ppm is assigned to the –CO from the amide bond while 134.3, 132.2, 128.3 and 124.4 ppm corresponded to the –ArBr pendant groups. 138.1 and 126.0 ppm represented –Ar from the internal cage core and finally 52.0 and 39.5 ppm showed the –CH_2 groups also from the cage core.

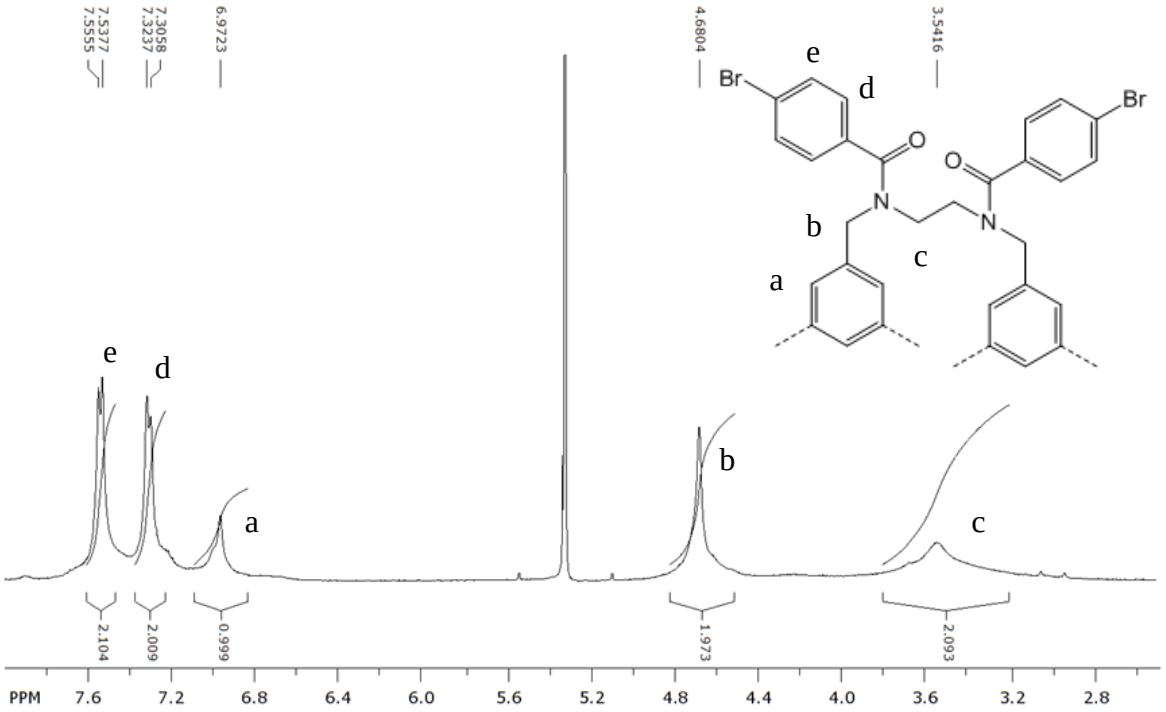

Figure 6: ^{1}H NMR of **RC1a** in DCM.

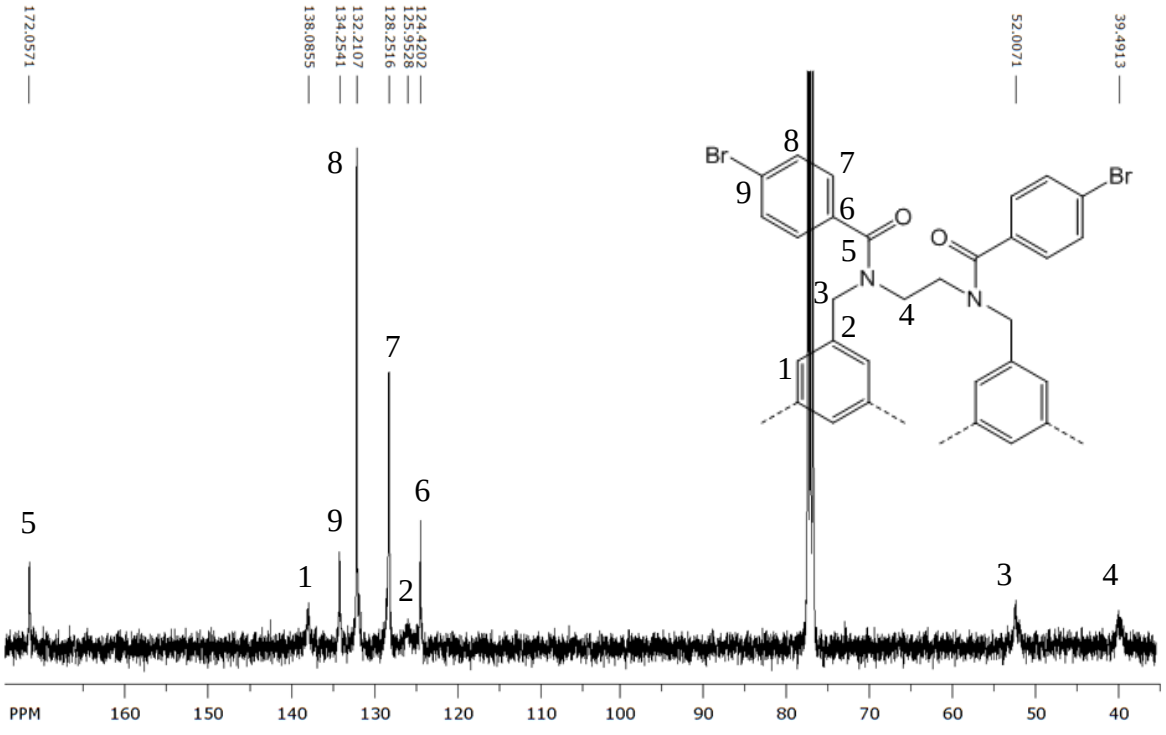

Figure 7: ^{13}C NMR of **RC1a** in $CDCl_3$.

The ^{1}H NMR of **RC1a** shown in Figure 6 was slightly improved due to running at lower temperature (-50 °C). Although broad signals were observed throughout the NMR spectra, broadening of signals was most apparent in –NCH_2 groups on the diamine vertices.

The amide-decorated cages were all worked up directly from solution by evaporation after purification by aqueous extraction and column chromatography. pXRD showed absence of peaks, indicating the products were amorphous (Figure 8, offset for clarity).

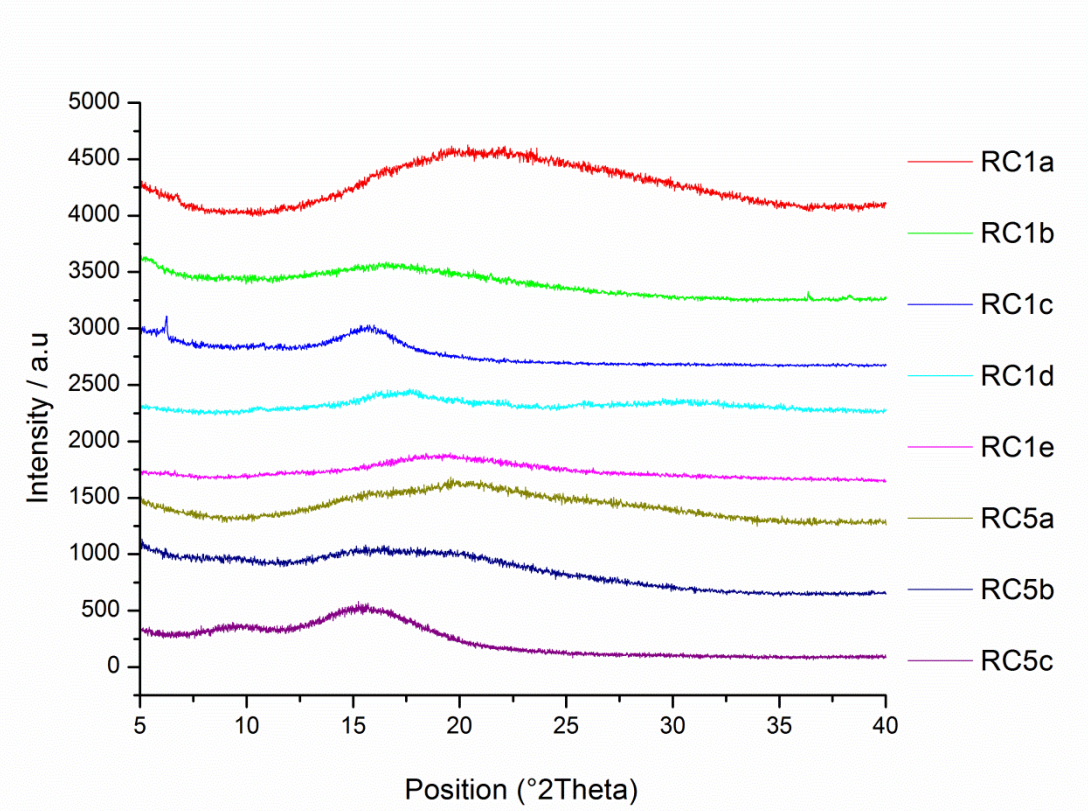

Figure 8: pXRD of functionalised **RC1** and **RC5**. **RC1a** (red), **RC1b** (green), **RC1c** (blue), **RC1d** (cyan), **RC1e** (magenta), **RC5a** (olive), **RC5b** (navy) and **RC5c** (purple).

FTIR of the samples all contained a very strong characteristic amide C=O band at ~1650 cm^{-1}. Reduced cages decorated with aromatic groups (a and b) contained more prominent aromatic C-H bands at ~3000 cm^{-1} (bending) and ~750 cm^{-1} (stretching). Alkyl C-H stretches were apparent in all samples at ~2950 cm^{-1},

although they are more prominent in cages decorated with alkyl carbons (c and d, particularly c). RC5 samples were similar, but with the addition of a tertiary C-N band at ~1300 cm^{-1} (Figure 9, samples offset for clarity).

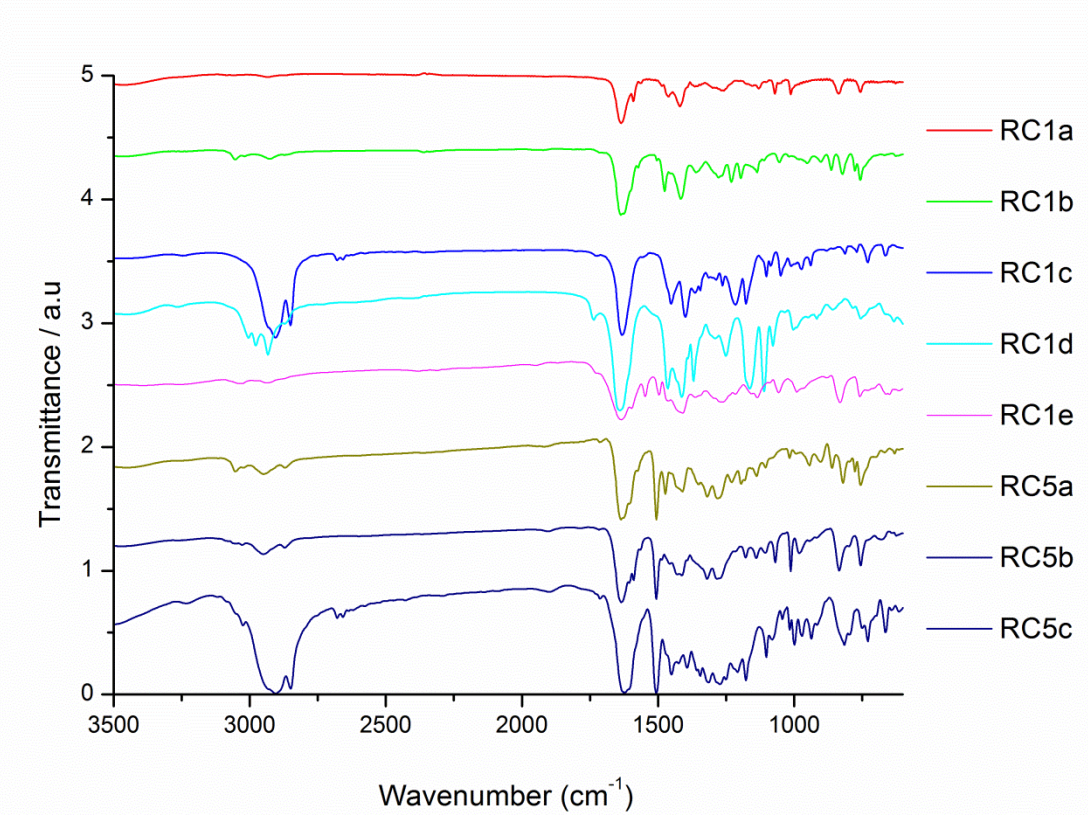

Figure 9: FTIR of functionalised **RC1** and **RC5**. **RC1a** (red), **RC1b** (green), **RC1c** (blue), **RC1d** (cyan), **RC1e** (magenta), **RC5a** (olive), **RC5b** (navy) and **RC5c** (purple).

As signals observed in ^{1}H NMR were so broad, and single crystal data was unavailable for most analogues, MALDI became the primary means of characterisation for these amide-decorated cages. This is analogous to most dendrimers, which also result in broad NMR signals and are, consequently, primarily characterised by mass spectrometry.[9] Molecular ions were apparent for all amide-decorated cages with either sodium or potassium adducts (Table 1).

Amide-decorated cage	Mr Theoretical	Mr Experimental	Assignment
RC1a	3013.19	3036.00	$[M+Na]^+$
RC1b	2667.14	2704.00	$[M+K]^+$
RC1c	2763.90	2786.00	$[M+Na]^+$
RC1d	2605.00	2629.00	$[M+Na]^+$
RC1e	2078.30	2078.30	$[M]^+$
RC5a	3922.40	3947.00	$[M+Na]^+$
RC5b	3576.35	3600.00	$[M+Na]^+$
RC5c	3510.89	3534.00	$[M+Na]^+$

Table 1: MALDI results for **RC1** and **RC5** with bulky acid halides **a–e**.

Materials were screened for porosity, initially with nitrogen, but the addition of these acid halide groups (**a**–**d**) did not yield nitrogen porous materials in the amorphous state for either **RC1** or **RC5** decorated analogues (Table 2). Data for **RC5d** and **e** were not available because reactions were not carried out, hence these are marked as "N/A" in Table 2 and Table 3.

	N_2 SA_{BET} (m^2/g)				
Acid Halide	**a**	**b**	**c**	**d**	**e**
RC1	9	5	8	18	0
RC5	48	0	0	N/A	N/A

Table 2: N_2 sorption analysis of **RC1** and **RC5** functionalised with bulky groups.

Samples were also tested for hydrogen uptake with the possibility of restricted pore sizes inducing selective uptake. However, as with nitrogen sorption analysis, no hydrogen porosity was observed (Table 3).

	H_2 $SA_{Langmuir}$ (m^2/g)				
Acid Halide	**a**	**b**	**c**	**d**	**e**
RC1	0	5	0	141	0
RC5	66	0	0	N/A	N/A

Table 3: H_2 sorption analysis of **RC1** and **RC5** functionalised with bulky groups.

While porosity was not found, **RC1** and **RC5** decorated with **a**, **b**, **d** and **e** still provided an intriguing basis for further possible polymerisation reactions through possession of further functionality (see Chapter 5).

Single crystal structures were obtained for some amide-decorated cages (**RC1a**–**e**) by employing a layering technique with solvent and anti-solvents for each decorated cage (**RC1a** from dichloromethane and methanol, **RC1b** from chloroform and methanol, **RC1c** from chloroform and methanol, **RC1d** from dichloromethane and chloroform and **RC1e** from dichloromethane and pentane). Single crystal structures were collected by Dr. M. Schmidtmann, with single molecules detailed in Figure 10 and their packing shown in Figure 11.

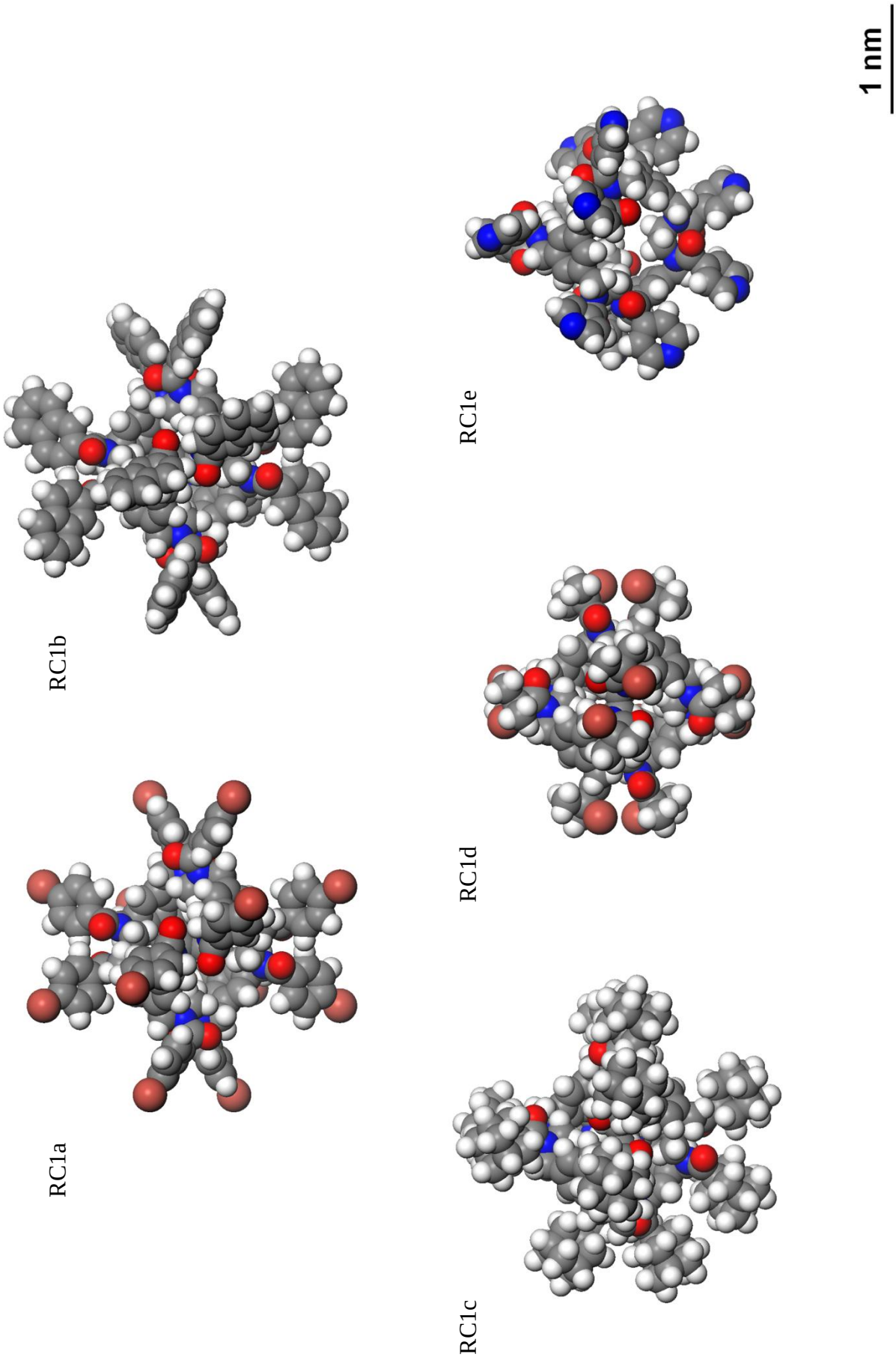

Figure 10: Single molecule crystal X-ray structures for RC1a-e in space filling representation (carbon in grey, hydrogen in white, nitrogen in blue, oxygen in red and bromine in orange).

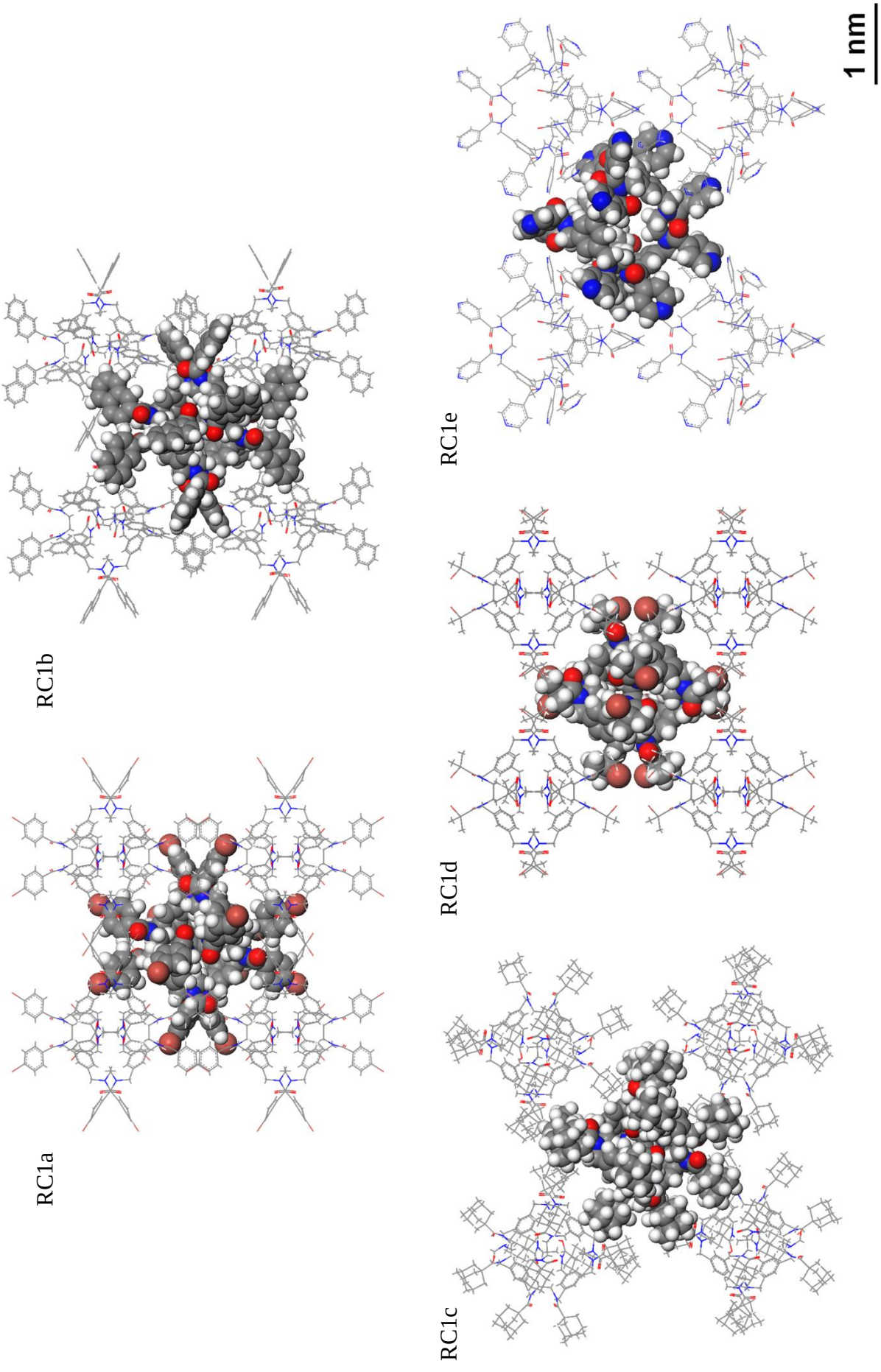

Figure 11: Packing of RC1a-e in space filling representation with neighbouring cages (carbon in grey, hydrogen in white, nitrogen in blue, oxygen in red and bromine in orange).

As with the single crystal structure obtained for **RC1** (Dr. J. T. A. Jones and Dr. M. Schmidtmann, unpublished) all of these crystal structures for decorated **RC1a-d** showed clear inversion of the diamine vertices (Figure 12, seen in red) into the cage molecule. This in turn results in loss of internal pore volume.

Figure 12: Inversion of diamine vertices on reduction of CC1 (yellow) to **RC1** (red). This reduces internal pore volume.

Because no crystal structures were obtained for **RC5** acid halide decorated molecules, a simulation was carried out using Materials Studio of the **RC5** structure by Dan Holden of the University of Liverpool, and compared to the single crystal structure of **CC5**.[5] In this instance, the diamine vertices cannot invert into the cage cavity, instead twisting slightly. The trialdehdye, however, does appear to collapse very slightly into the cage, resulting in some loss of internal pore volume, although this is not as pronounced as seen in **RC1** compared to CC1 (highlighted in Figure 13).

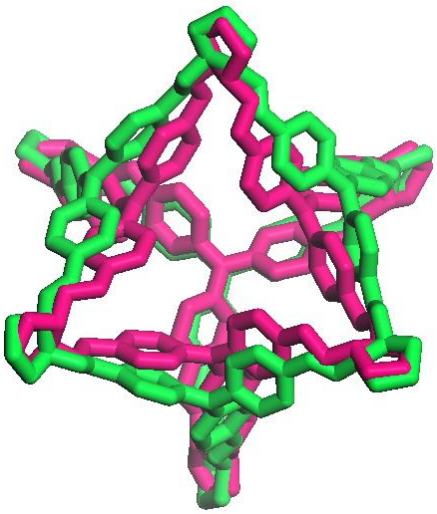

Figure 13: Inversion of diamine vertices on reduction of **CC5** (green) to **RC5** (purple) (decoration omitted for clarity), as determined by molecular simulations (no crystal structure obtainable for this molecule).

4.3 Measuring 'Virtual Porosity'

By taking the single crystal structures measured for **RC1a-e** and removing the solvent computationally from crystal structures using Materials Studio, nitrogen Connolly Surface Area (CSA) of the samples were calculated. This displayed 'virtual' surface areas for the decorated cages,[10] that might be realised should the samples survive desolvation and maintain long range order and crystallinity. Individual cages are coloured differently to distinguish between them while the CSA is shown in light blue (external) or blue (internal) (Figure 14 to Figure 18).

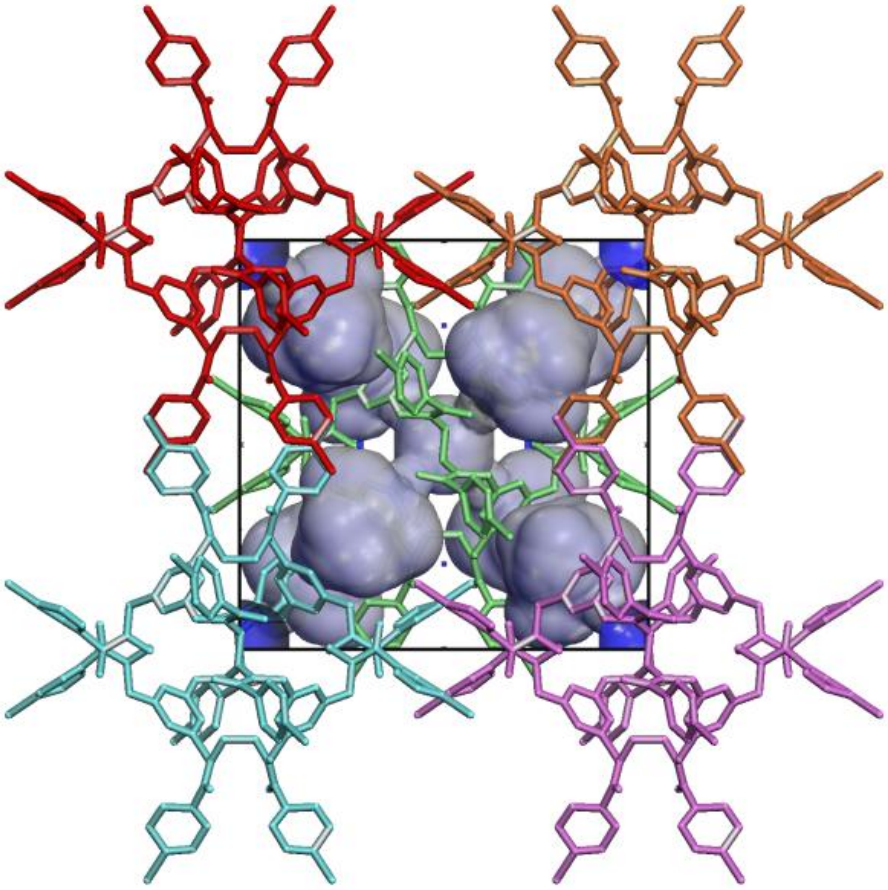

Figure 14: Connolly surface area and packing for **RC1a** with solvent deleted.

RC1a ($C_{132}H_{108}Br_{12}N_{12}O_{12} \cdot 7CHCl_3$) displayed an I23 space group, with two cages per unit cell. There is slight disorder of bromobenzoyl pendant groups throughout the lattice (shown as 0.50:0.50 partial occupancy). The CSA of **RC1a** shows an intrinsic pore from the cage core connected to four extrinsic voids (created by bowl-like pendant groups) in a tetrahedral structure. However, even in an ideal crystal structure with solvent removed, there is insufficient interconnectivity between these tetrahedral void clusters and classical porosity would not be expected.

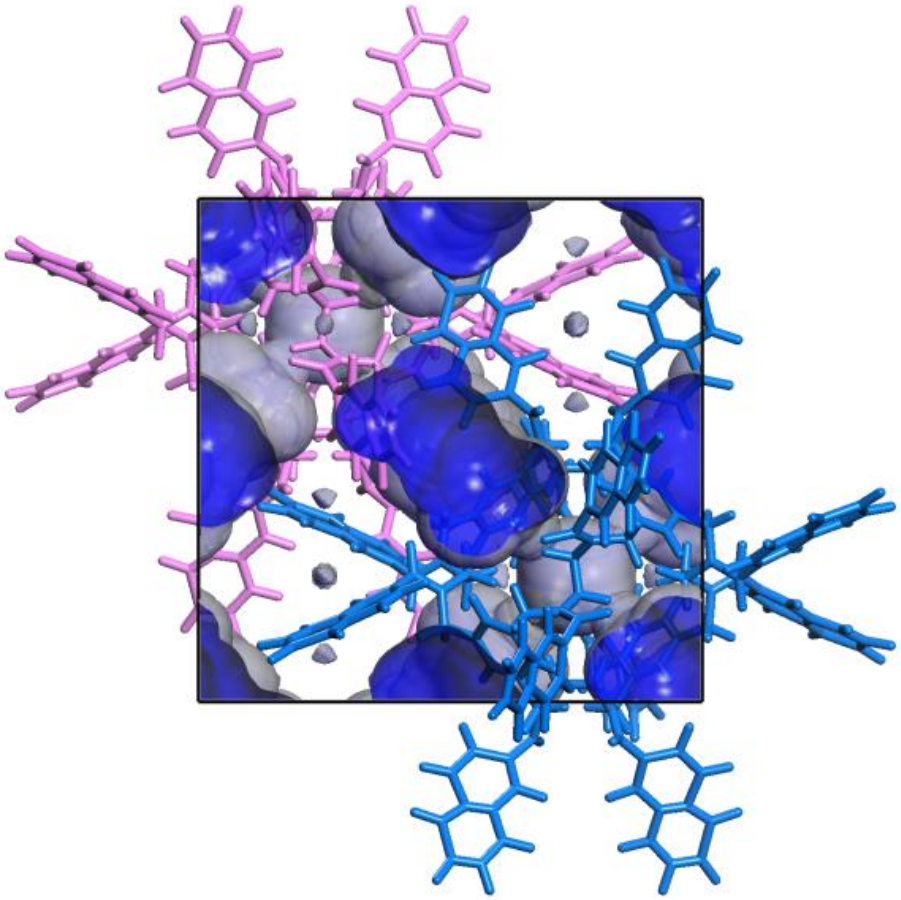

Figure 15: Connolly surface area and packing for **RC1b** with solvent deleted.

RC1b ($C_{180}H_{144}N_{12}O_{12} \cdot 7CHCl_3$) displayed a Pn3 Space group with two cages per unit cell. Again there was disorder of pendant naphthoyl groups (0.637:0.363 partial occupancy). As with **RC1a**, there is an internal pore from the cage core and four extrinsic voids. In this instance, however, the bowls formed by three pendant aromatic groups interlock and pack facing one another, inducing connectivity of extrinsic voids and creating 'virtual' porosity.

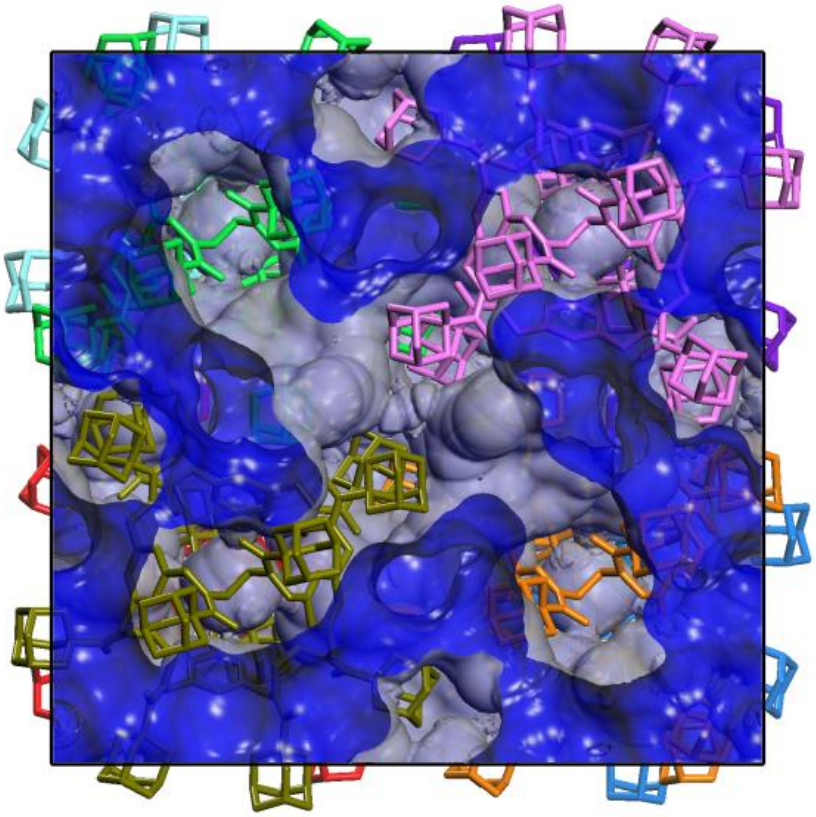

Figure 16: Connolly surface area and packing for **RC1c** with solvent deleted.

RC1c ($C_{180}H_{240}N_{12}O_{12} \cdot 19.5CHCl_3$) displayed a larger I-4 space group with eight cages per unit cell. Disorder this time was apparent on eight vertices in each unit cell (one vertices per cage, 0.75:0.25 partial occupancy) in each unit cell, instead of simple disorder on the pendant groups themselves. When modelling the CSA of **RC1c** using the crystal structure, both small intrinsic pores from the cage core and large extrinsic pores from adamantoyl groups can be observed, while smaller channels are seen, this time interconnecting these voids.

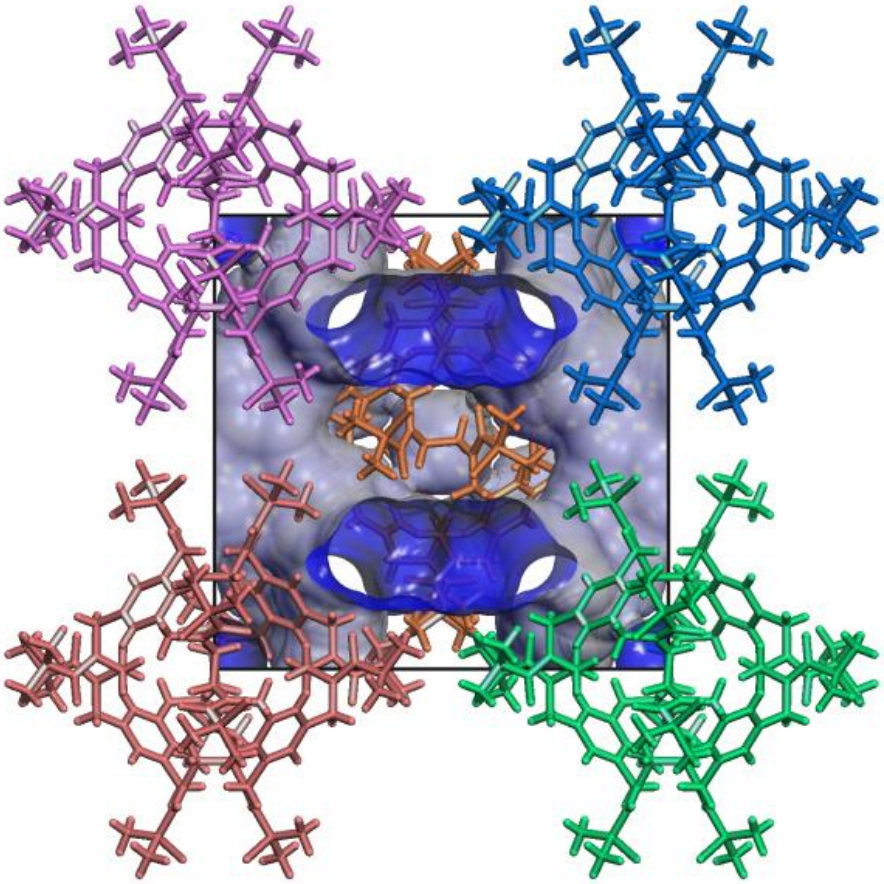

Figure 17: Connolly surface area and packing for **RC1d** with solvent deleted.

RC1d ($C_{96}H_{132}Br_{12}N_{12}O_{12} \cdot 12CHCl_3 \cdot H_2O$) had a P-43n space group with 2 cages per cell. Disorder in this molecule reverted to the pendant groups only, between position of bromo and methyl groups on said pendant groups (0.552:0.448 partial occupancy). The CSA again shows an internal pore, but with much wider open extrinsic voids and a larger distance between each cage.

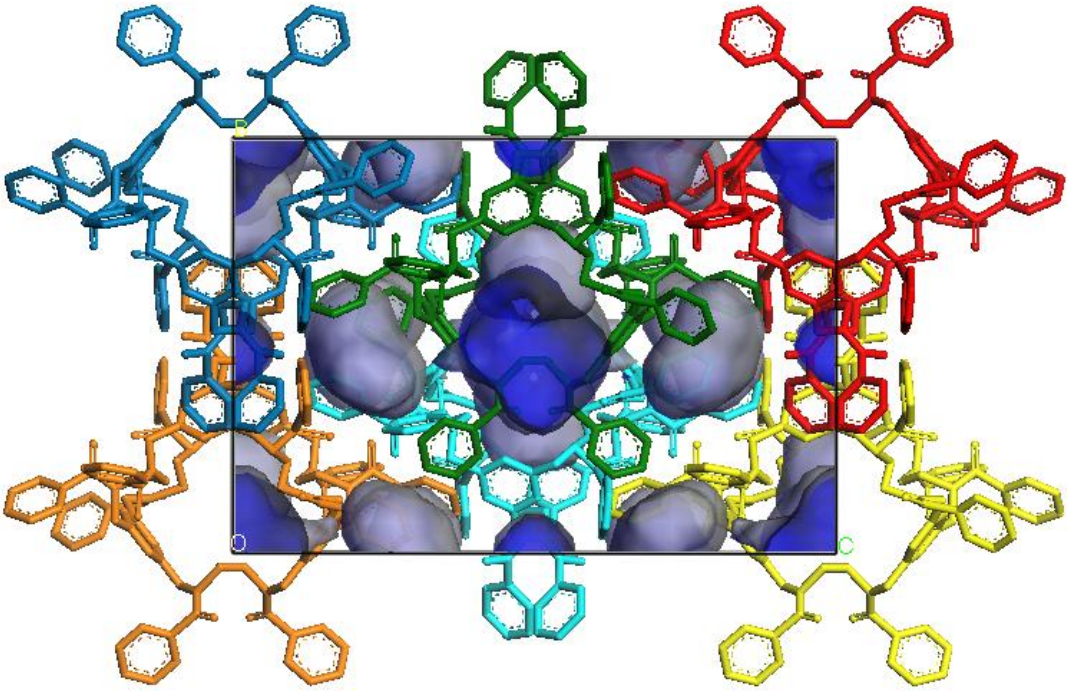

Figure 18: Connolly surface area and packing for **RC1e** with solvent deleted.

RC1e ($C_{120}H_{108}N_{24}O_{12}$) gave rise to an I2/a space group with 6 decorated cages per unit cell. sXRD in this instance was much cruder (with an R value >5). The CSA of **RC1e** shows an intrinsic pore from the cage core and four extrinsic voids (created by bowl-like pendant groups) in a tetrahedral structure. As with **RC1a** however, even in an ideal crystal structure with solvent removed there is insufficient interconnectivity between these tetrahedral void clusters and conventional porosity could not be expected.

The CSA of **RC1b**, **c** and **d** all indicated high levels of virtual porosity (~2000 m^2/g). This highlights the challenge faced in production of discrete porous molecules, where promising and seemingly porous structures can often collapse upon removal of solvent 'propping up' the pores. The high levels of disorder observed even in single crystal X-ray analysis is also perhaps indicative of the level of flexibility in these molecules, which could ultimately be the reasoning for collapse to non porous materials. It is also possible that the amide groups in these cages, unlike in the imine analogues, H-Bond to solvent much more strongly, and hence the solvent is a much less 'innocent partner' in the structure. ^1H NMR is also extremely broad for decorated cages, which also correlates with flexibility in the decorated cages. While

inherently non porous, this new class of amide-decorated cages still show excellent potential as a route for organic functionalisation.

4.4 Recrystallisation: Toward a Porous Polymorph

We hypothesised that a crystalline analogue of these molecules could in fact be more porous[11] (as highlighted in Chapter 3). Thus, all amide-decorated cages were recrystallised on a larger 200 mg scale (using the same solvent systems and layering techniques for which single crystals were grown) in order to measure gas sorption data for crystalline analogues.

However, removal of the crystals from solution after the scaled-up recrystallisation process resulted in most samples rapidly becoming amorphous in air upon removal from solution, as shown by pXRD. Only **RC1b** appeared to retain any crystallinity upon removal from the mother liquor and subsequent drying (Figure 19).

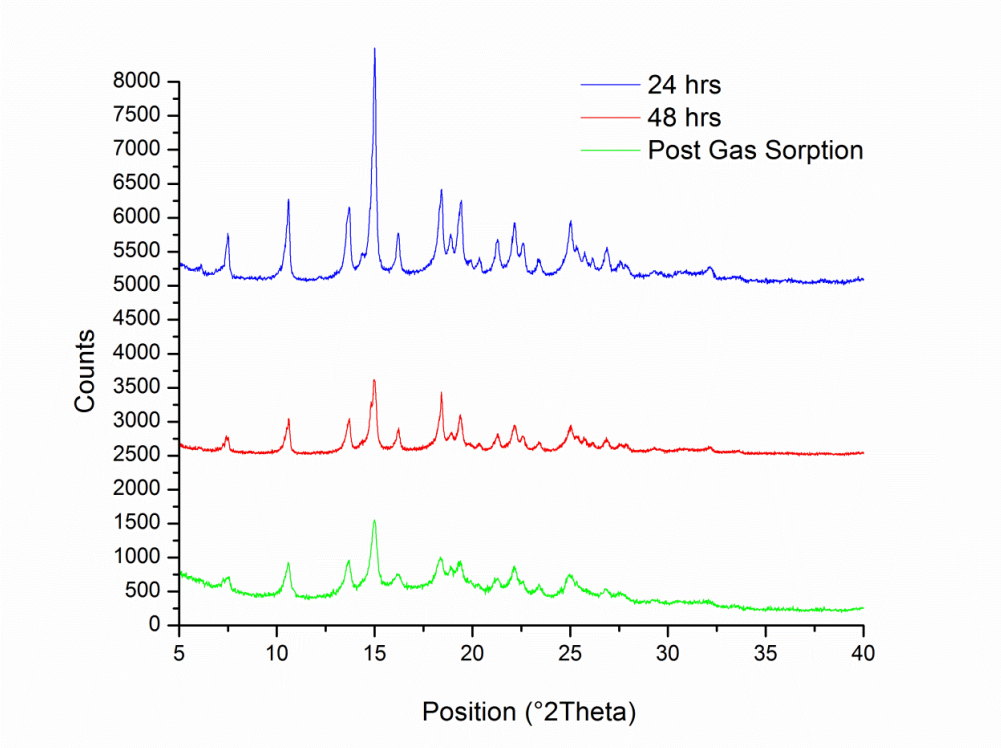

Figure 19: pXRD patterns of **RC1b** after removal from supernatant (24 hrs in blue, 48 hours in red), and post gas sorption (green).

Upon recrystallisation from chloroform and methanol, **RC1b** was still non porous to

N_2 but did appear to adsorb a small amount of H_2 compared to its previous amorphous form (Figure 20, $SA_{Langmuir}$ of 447 m^2/g).

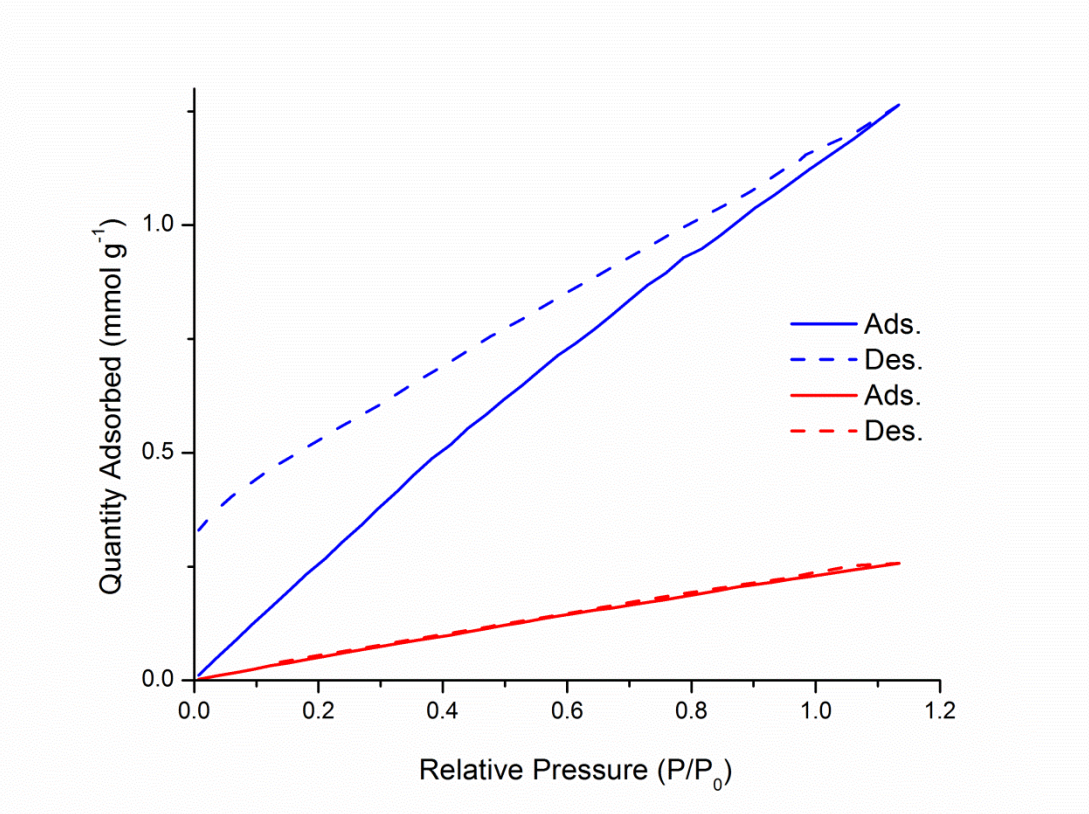

Figure 20: H_2 sorption of amorphous **RC1b** (red) and recrystallised **RC1b** (blue). The partially crystalline form has a limited degree of porosity.

TGA of **RC1b** (Figure 21) indicated no weight change for **RC1b** until ~150 °C, at which point a weight loss occurs. This loss of 23.74 weight % closely corresponds to chloroform being lost from the solvate (measured to be $C_{180}H_{144}N_{12}O_{12} \cdot 7CHCl_3$ by sXRD) with 7 chloroform molecules (835.66 Mr) accounting for 23.85 weight % of total solvate mass (3502.8 Mr). The temperature at which this occurs is notably higher than the normal boiling point of chloroform (61 °C). The decorated cage itself was stable until temperatures of around 350 °C, where degradation begins to occur. Degradation of **RC1b** also appears to be multi-step, with a possible hypothesis being degradation of the inner cage core followed by degradation of the more stable amide pendant groups.

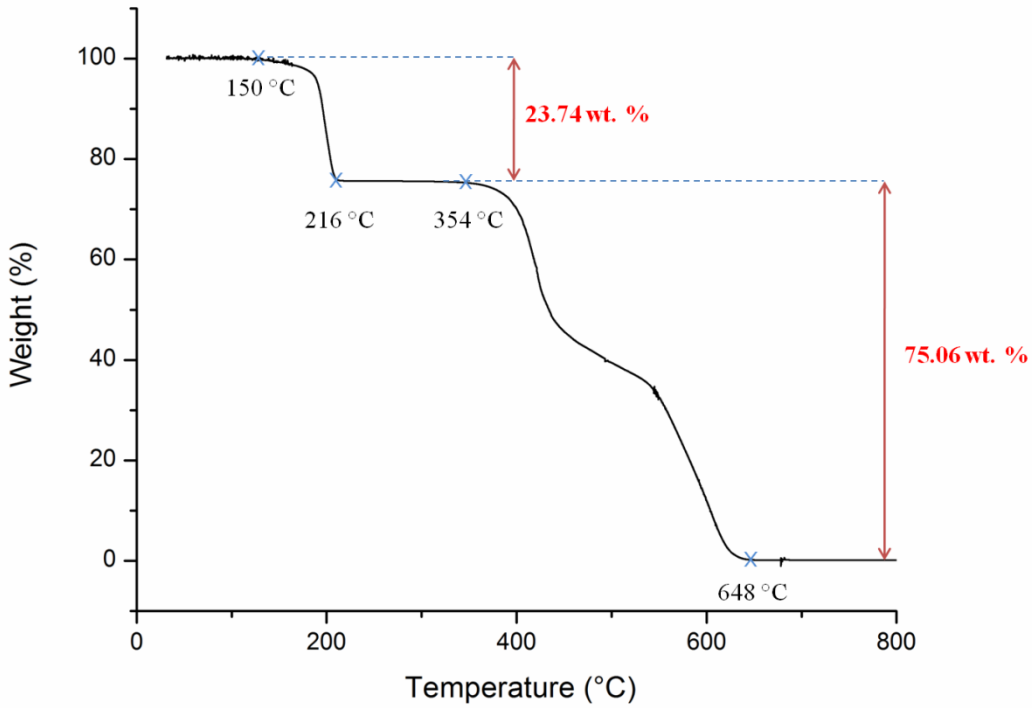

Figure 21: TGA data for **RC1b** after recrystallisation: the first step correlates with solvent loss.

To confirm loss of crystallinity, **RC1b** was heated using TGA to 230 °C and pXRD measured again. As expected, after heating to this elevated temperature and complete removal of solvent, **RC1b** became completely amorphous (Figure 22).

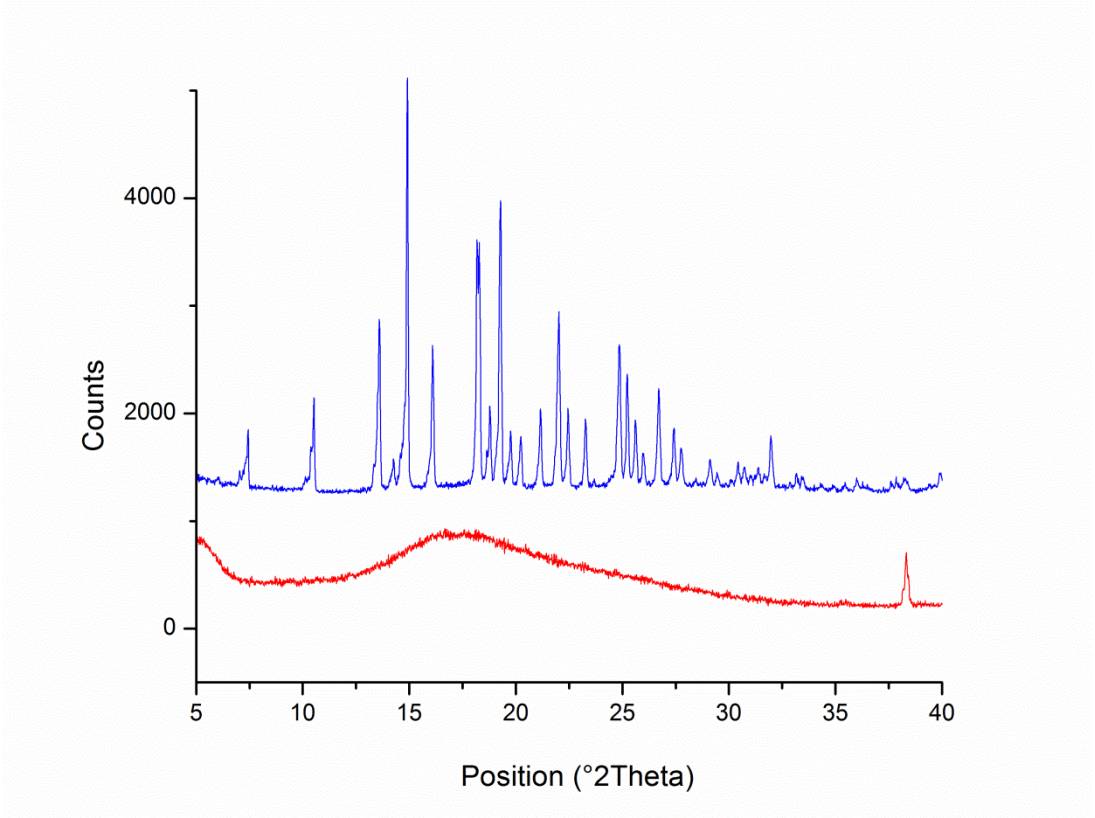

Figure 22: pXRD displaying loss of crystallinity in **RC1b** post desolvation (recrystallised sample in blue and after heating in red).

The crystalline, post gas sorption **RC1b** was submitted for ^{1}H NMR in deuterated dichloromethane to verify that the solvent remaining was chloroform (Figure 23, top). ^{1}H NMR showed remaining chloroform at 7.32 ppm in the crystalline, post gas sorption sample while no such peak was observed from the completely dry amorphous state. More generally, –ArH protons from the naphthalene groups are obvious at 8.04, 7.84, 7.63 and 7.50 ppm. The –ArH from the internal cage is at 7.19 ppm while the –CH_2 nearest to the benzene ring of the internal cage is apparent at 4.90 ppm. Finally, the –CH_2 from the diamine vertices is at 3.78 ppm and is extremely broad. The ratio of chloroform to **RC1b** was also measured in the ^{1}H NMR by taking integrations of the chloroform and –ArH signals, which were approximately 0.56:1 (Figure 24). This closely matches the number of chloroform in the structure (7, 1 H each) compared to –ArH protons (12 per cage) as measured by sXRD.

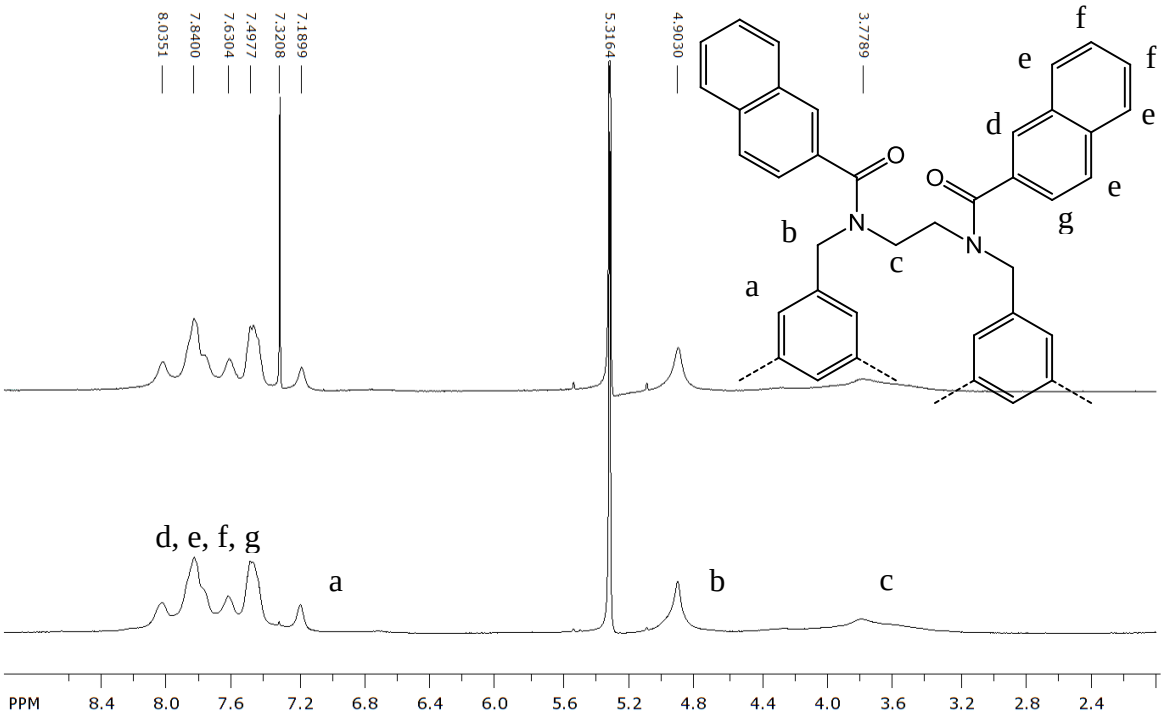

Figure 23: Crystalline (top) and amorphous (bottom) ^{1}H NMR of **RC1b** in δDCM.

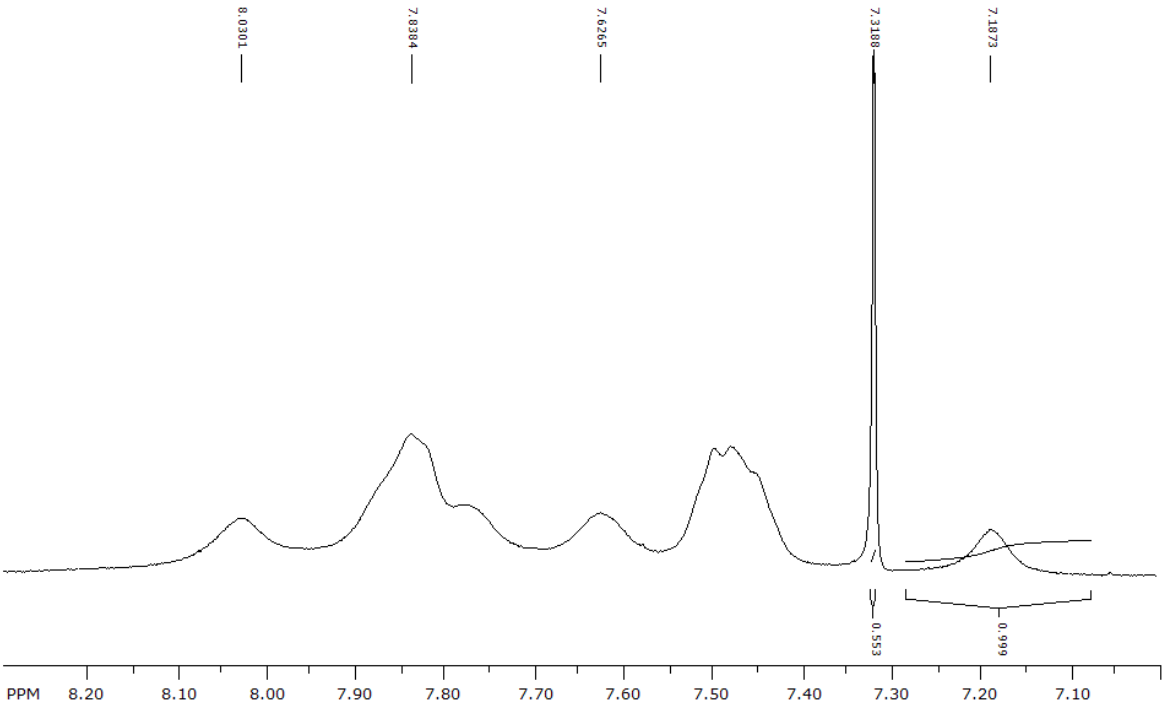

Figure 24: The aromatic region ^{1}H NMR of **RC1b** in δDCM before elevated heating.

SEM (carried out by Dr. T. Hasell) of recrystallised **RC1b** vacuum dried at 120 °C (post gas sorption analysis, still crystalline by pXRD) displayed an interpenetrated rhombohedral morphology (Figure 25).

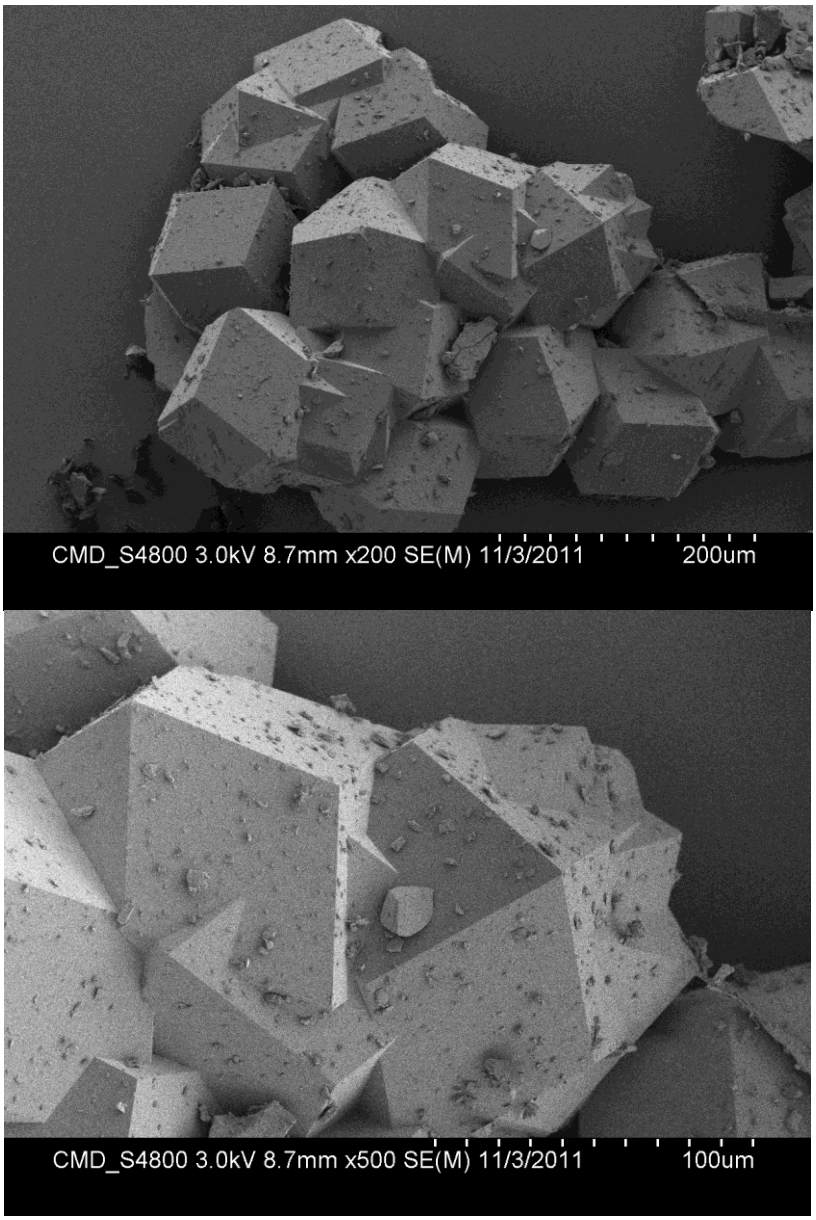

Figure 25: SEM of **RC1b** post gas sorption at 200x magnification (top) and 500x magnification (bottom).

When the same sample was heated by TGA to 230 °C, thus inducing an amorphous state (confirmed by pXRD in Figure 22), the SEM differed greatly. In this case, irregular shapes were observed without any obvious pattern. Sections of the material's surface also appeared to exhibit spherical indentations, possibly created by forced removal of solvent (Figure 26).

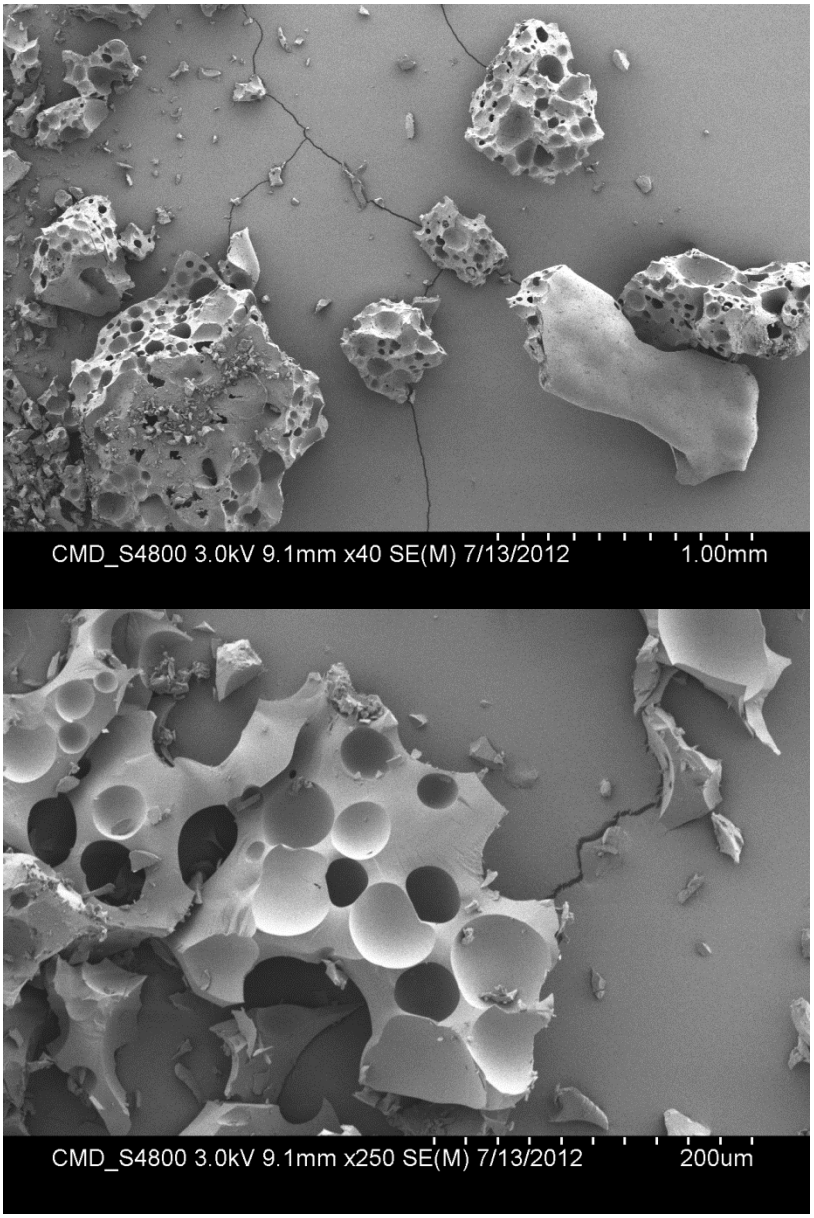

Figure 26: SEM of **RC1b** post heating to 230 °C at 40x magnification (top) and 250x magnification (bottom).

4.5 Functional Groups: Toward Reduced Melting Points

Acid chloride functional aliphatic chains were selected with aspirations of creating disorder, therefore reducing packing efficiency and lowering the lattice energy of the material. In principle, this would make it easier to melt the material while retaining the internal pore of the cage itself, with the aim of creating a 'porous liquid' (Figure 27). This is an intriguing prospect that provides the opportunity to process porous

materials into unusual forms, for controlling absorption/desorption through solid–liquid phase changes, and ultimately for accessing liquid states with well-defined permanent micropores.[12] Giri *et al*. have prepared alkylated organic cages recently,[13] however these have been achieved by condensation of 1,2-diamines with aliphatic chains and 1,3,5-triformylbenzene in a similar fashion to other porous organic cages.[5,8,11] The alkylated organic imine cages prepared by Giri *et al.* have displayed melting points as low as 50 °C (for the octyl cage), though these were mostly (formally) non-porous. A similar isohexyl cage in the same report showed N_2 SA_{BET} of 289 m^2/g, while melting at around 198 °C.

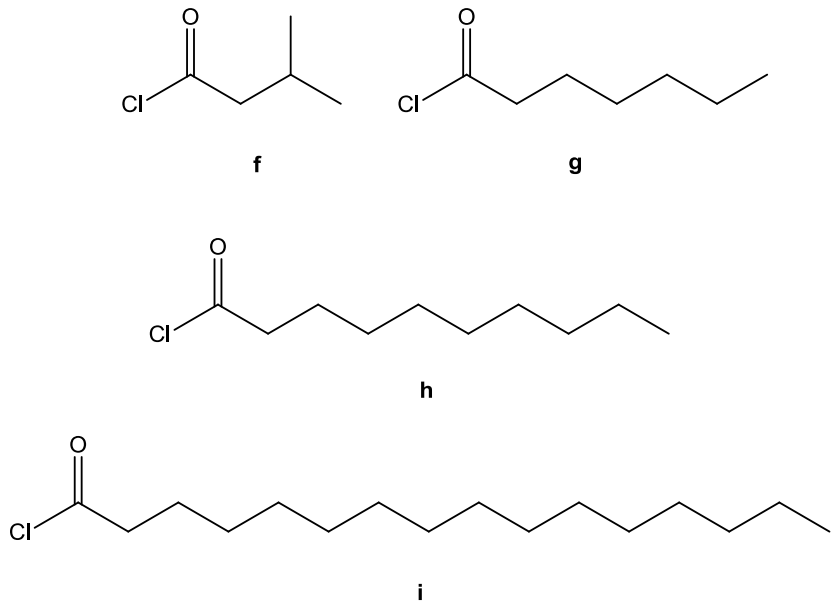

Figure 27: Aliphatic acid chlorides used to target meltable 'porous liquids'.

RC1 and **RC5** did not melt, instead simply decomposing on heating to higher temperatures. Employing identical conditions to those used earlier in this Chapter, however, acid halides **f**–**h** were all successfully added to **RC1** while **f** was added to RC5. Functionalised cages were verified by ^1H and ^{13}C NMR, FT-IR and MALDI. As might be expected with such long, disordered groups, single crystals could not be obtained. Again, signals observed in ^1H NMR were broad, so MALDI became the primary means of characterisation. Molecular ions were apparent for all aliphatic amide-decorated cages with either hydrogen or sodium adducts (Table 4).

Amide-decorated cage	Mr Theorectical	Mr Experimental	Assignment
RC1f	1826.56	1827.80	$[M+H]^+$
RC1g	2163.20	2186.00	$[M+Na]^+$
RC1h	2668.16	2711.00	$[M+Na]^+$
RC1i	3678.07	3699.90	$[M+Na]^+$
RC5f	2735.00	2758.00	$[M+Na]^+$

Table 4: MALDI results for **RC1** and **RC5** modified with aliphatic acid halides **f–h**.

Melting points were successfully reduced to as low as 45 °C (acid chloride **i**), though the effect of melting point reduction appeared to give diminishing returns with increasing aliphatic chain length (Figure 28). The **RC5** analogue with acid halide **f**, however, exhibited a greatly increased melting point (by 130 °C) compared to its **RC1** analogue. Diminishing returns are likely a consequence of reduction in entropy as aliphatic chains get longer, crowding the peripheral space of the amide-decorated cage.

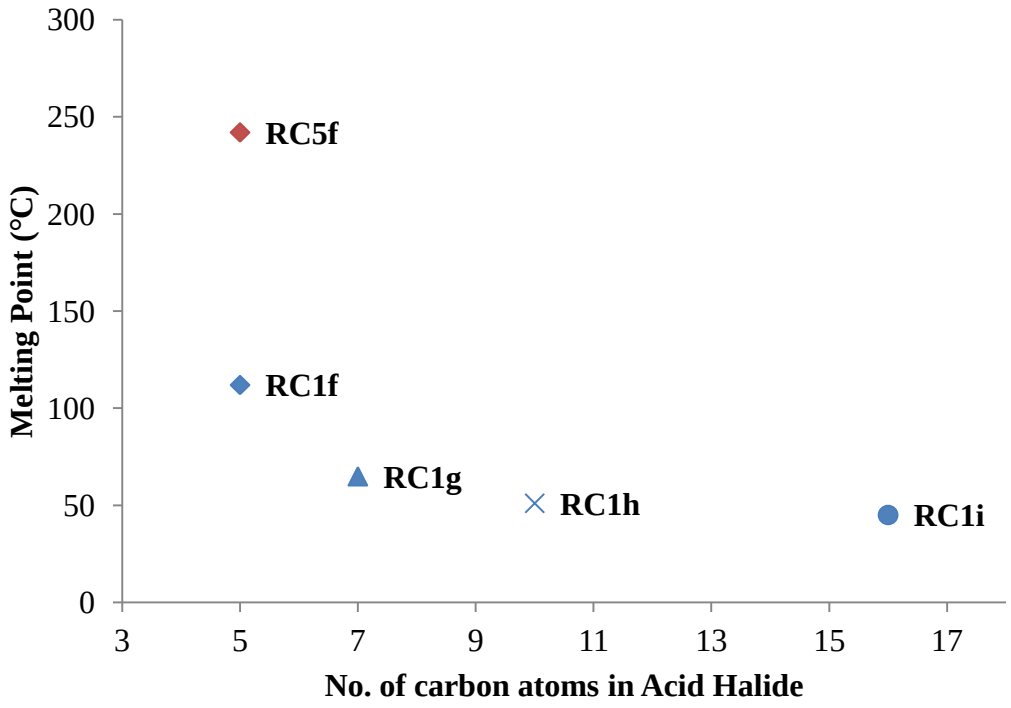

Figure 28: Melting point reduction in **RC1f-i** and **RC5f**.

These aliphatic functionalised **RC1** and **RC5** materials also failed to yield materials porous to nitrogen (Table 5). This finding was initially attributed to possible interpenetration of aliphatic carbon chains, but it is also possibly due to complete collapse of the internal pore as postulated with previous **RC1** and **RC5** decoration. Data for **RC5g**, **h** and **i** was not available as reactions were not carried out, and are therefore described as "N/A".

	N_2 SA_{BET} (m^2/g)			
Acid Halide	**f**	**g**	**h**	**i**
RC1	6	0	1	0
RC5	0	N/A	N/A	N/A

Table 5: N_2 Surface area of cages functionalised with aliphatic groups.

As with bulky amide-decorated cages, samples were screened for hydrogen uptake with the possibility of restricted pore sizes inducing selective uptake: however, as with nitrogen sorption analysis, no porosity to hydrogen was observed (Table 6).

	H_2 $SA_{Langmuir}$ (m^2/g)			
Acid Halide	**f**	**g**	**h**	**i**
RC1	2	0	5	5
RC5	4	N/A	N/A	N/A

Table 6: H_2 Surface area of cages functionalised with aliphatic groups.

4.6 Conclusions

Both **RC1** and **RC5** have been successfully prepared (the former *in situ* and the latter by a two step reaction) and functionalised through simple nucleophilic addition/elimination with acid halides, with single crystal structures being obtained for **RC1a-e**. All amide-decorated cages prepared were shown initially to be amorphous on work-up (Figure 8), with only **RC1b** retaining any long term crystallinity after recrystallisation and removal from solution (Figure 19). All other samples appeared to rapidly become amorphous when exposed to air as the solvent evaporated.

While in the amorphous state, no decorated cages exhibited any porosity to nitrogen or hydrogen. This absence of porosity in cages functionalised with bulky pendant groups (**RC1** and **RC5** with **a-e**) is likely attributed to the initial decrease of the internal pore on reduction, combined with molecules possessing too much flexibility through the removal of the original imine bond present in cages, hence collapsing in upon themselves. Hydrogen bonding of solvent to the more polar amides may also be a factor.

One hypothesis for **RC1b** retaining crystallinity and some limited porosity is that although the structure possesses the same flexible vulnerabilities, it can exhibit strong π-π stacking between pendant naphthoyl groups. Chloroform from this solvate is bound tightly and high above its natural boiling point, only completely leaving the material at around 215 °C (Figure 21), suggesting a robust structure.

Attempts to prepare porous liquids were also made by utilising the same nucleophilic addition/elimination chemistry as used with bulky acid halides (**RC1** and **RC5** with f-i). Aliphatic acid halides were successfully added, with resulting melting points as low as 45 °C achieved (Figure 28). These were in fact lower than those of low-melting point imine cages prepared by Giri *et al*.[13]. Unfortunately however, these aliphatic amide-decorated cages were also non-porous with similar reasoning as for the bulky analogues.

While no porous materials were achieved through reduction and decoration of imine cages, this new class of amide-decorated cages provide a structurally stable and

intriguing basis for further reactions. For example, the efficient addition of 12 organic functionalities to a small organic core is an appealing method to create dendrimers.

4.7 Experimental

Materials. 1,3,5-Triformylbenzene was purchased from Manchester Organics, UK. All other chemicals were purchased from Sigma-Aldrich and used as received.

RC1. Ethylenediamine (1.04 g, 0.0173 mol) was dissolved in methanol (425 mL) in a 2 L round-bottomed flask cooled in an ice bath. 1,3,5-Triformylbenzene (1.875 g, 0.0116 mol) was dissolved in methanol (575 mL) and added dropwise over 24 hours to the ethylene diamine solution using a dropping funnel under a nitrogen atmosphere. During this time, the reaction was stirred continuously at 300 RPM. After this time, sodium borohydride (1.53 g, 0.0403 mol) was added and reaction stirred for a further 12 hours. Water (5 mL) was then added and the reaction stirred for a further 12 hours. The solvent was then removed under vacuum. The resulting white solid was extracted with chloroform (2 x 100 mL) and the remaining white solid removed by filtration. The solvent was then removed with a rotary evaporator (bath at 30 °C) and crude RC1 obtained as white solid in 89 % yield (2.1 g). **RC1** was used without any further purification techniques. ^{1}H NMR ($CDCl_3$, 400 MHz) δ 6.90 (s, 1 H, -ArH), 3.51 (s, 2 H, -$ArCH_2$), 2.48 (s, 2 H, -NCH_3). ^{13}C NMR ($CDCl_3$, 100 MHz) δ 140.0, 128.4, 54.8 ppm. Acc. Mass MS m/z: 817.16 for $C_{48}H_{72}N_{12}$ $[M]^+$, with boron adduct 829.6 for $C_{48}H_{72}N_{12}B[M]^+$.

CC5 (S,S). A 500 mL oven-dried round-bottom flask was cooled to room temperature under a dry nitrogen atmosphere. After tri(4-formylphenyl)amine (742 mg, 2.25 mmol) was charged into the flask, dichloromethane (280 mL) was added. The clear yellow-green solution that was formed was kept for the next step. To another 500 mL oven-dried flask, also cooled to room temperature under N_2, was added (1*S*, 2*S*)-1,2-cyclopentanediamine dihydrocholoride (585 mg, 3.38 mmol), methanol (280 mL), and triethylamine (684 mg, 6.76 mmol). The clear, colourless solution was stirred at room temperature for 5–10 min. This solution was then added

very slowly to the first solution by pouring gently down the side of the flask to form two layers: a colourless layer on the top and a yellow-green layer at the bottom. A cloudy interface appeared between these two layers as the reaction progressed. The resulting suspension was then sealed and kept at room temperature for 7 days. A white solid which adhered to the walls of the flask was observed after 7 days, along with a clear yellow supernatant solution. The white solid was collected by filtration and washed with DCM (3 × 5 mL) to afford pure CC5 (S,S) in 81 % yield (780 mg). ^{1}H NMR (CDCl3, 400 MHz) 7.99 (s, 1H), 7.61 (d, 2H), 7.02 (d, 2H), 3.60 (broad m, 1H), 2.09-2.17 (broad m, 2H), 1.93-1.98 (broad m, 1H). ^{13}C NMR could not be obtained due to extremely poor solubility of CC5 (S,S) resulting in weak spectra. MALDI-TOF MS m/z: 1703 for $C_{114}H_{108}N_{16}$ $[M+H]^+$ and 1726 for $[M+H+Na]^+$.

RC5. CC5 (S,S) (733 mg, 0.43 mmol) was weighed into an oven dried 2 L round-bottomed flask. Chloroform (80 mL) was added to give a cloudy yellow suspension followed by methanol (600 mL) and stirred for 10 minutes under N_2 at 900 RPM. Sodium borohydride (586 mg, 15.50 mmol) was added and the mixture left stirring for 14 hours. Solution had lightened to a paler yellow/less cloudy solution and extra sodium borohydride (586 mg, 15.50 mmol) was added and solution left stirring for a further 4 hours. Solution had again lightened significantly to a cloudy white state and more sodium borohydride was added (586 mg, 15.50 mmol) and left stirring for a further hour. The solution had become clear, indicating complete reduction and chloroform (170 mL) was added, followed by water (150 mL) which induced a white precipitate, followed by stirring for 20 minutes and allowed to settle, giving two distinct layers. Layers were separated using a separating funnel and the aqueous layer extracted 3 times with chloroform (200 mL). Combined organics were dried over $MgSO_4$, filtered and evaporated to dryness to yield RC5 as an off white/yellow powder in 79 % yield (588 mg). ^{1}H NMR (CDCl3, 400 MHz) δ 7.07-7.05 (d, 2 H, -ArH), 6.90-6.88 (d, 2 H, -ArH), 3.71-3.68 and 3.53-3.50 (d, 2 H, -ArCH_2), 2.74 (m, 1 H, -NCH), 1.95 (m, 1 H, -NH), 1.62 (m, 2 H, -$CHCH_2$), 1.32 (m, 1 H, -CH_2CH_3). ^{13}C NMR (CDCl3, 100 MHz) δ 146.7, 134.7, 129.0, 124.1, 64.5, 52.0, 30.9, 21.3 ppm. MALDI-TOF MS m/z 1850.1 for $C_{114}H_{108}N_{16}$ $[M+H]^+$.

RC1a (representative procedure for RC1 functionalisation). Cage1R (200 mg, 0.245 mmol) was dissolved in $CHCl_3$ (20 mL) and added to a 100 mL 2-necked RB flask cooled in an ice bath. Triethylamine (516 µL, 3.702 mmol) was then added and the solution stirred for 15 minutes under N_2. 4-bromobenzoyl chloride (678 mg, 3.084 mmol) was dissolved in $CHCl_3$ (10 mL) and added to the stirring solution slowly by pipette (white gas evolved) and the reaction mixture was left stirring for ~14 hrs. Upon completion, solution was transferred to a separating funnel and extracted with NaOH solution (50 mL, 1 M) followed by extracting the aqueous twice more with $CHCl_3$ (2 x 30 mL). The organics were combined and then extracted once more with H_2O (50 mL), before drying over $MgSO_4$. The solution was then concentrated to dryness using a rotary evaporator to yield an off-white solid (crude yield = 621 mg) and purified using a Biotage Isolera four utilising a silica column with $CHCl_3$/MeOH as solvent. After removal of solvent, **RC1a** was yielded as a white solid in 54 % yield (403 mg). Single crystal data was obtained from a crystal grown in DCM/MeOH. ^{1}H NMR (CD_2Cl_2, 400 MHz) δ 7.54-7.32 (d, 4 H, -BrArH), 6.95 (s, 1 H, -ArH), 4.70 (s, 2 H, -$ArCH_2$), 3.56 (s, 2 H, -NCH_2). ^{13}C NMR ($CDCl_3$, 100 MHz) δ 171.8, 138.1, 134.2, 132.2, 128.3, 125.9, 124.5, 52.3, 39.5 ppm. MALDI-TOF MS m/z = 3036 for $C_{132}H_{108}Br_{12}N_{12}O_{12}Na$ $[M+Na]^+$. CHN Calc. C: 52.62, H: 3.61, N: 5.58; found C: 50.64, H: 4.04, N: 4.70.

RC1b

^{1}H NMR (CD_2Cl_2, 400 MHz) δ 8.04, 7.84, 7.63 and 7.50 (m, 7 H, -Napthalene), 7.19 (s, 1 H, -ArH), 4.90 (s, 2 H, -$ArCH_2$), 3.78 (s, 2 H, -NCH_2). ^{13}C NMR (CD_2Cl_2, 100 MHz) 173.1, 138.8, 133.2, 129.0, 128.8, 128.1, 127.5, 127.1, 126.9, 124.4, 52.4, 39.7 δ ppm. MALDI-TOF MS m/z = 2704 for $C_{180}H_{144}N_{12}O_{12}K$ $[M+K]^+$. CHN Calc. C: 81.06, H: 5.44, N: 6.30; found C: 79.91, H: 5.37 N: 6.23.

RC1c

^{1}H NMR (CDCl3, 400 MHz) δ 7.10 (s, 1 H, -ArH), 5.49 (m, 2 H, -$ArCH_2$), 4.69 (m, 1 H, -NCH_2). $_2$), 4.25 (m, 1 H, -NCH_2), 2.10-1.69 (m, 15 H, -Adamatane). ^{13}C NMR (CDCl3, 100 MHz) δ 177.6, 139.1, 125.1, 50.1, 41.7, 39.5 (2 peaks), 36.7, 28.5 ppm. MALDI-TOF MS m/z = 2786 for $C_{180}H_{240}N_{12}O_{12}Na$ $[M+Na]^+$. CHN Calc. C: 78.22, H: 8.75, N: 6.08; found C: 76.20, H: 8.77, N: 5.93.

RC1d

^{1}H NMR (CD_2Cl_2, 400 MHz) δ 7.16 (s, 1 H, -ArH), 5.74 (m, 2 H, $ArCH_2$), 5.78 (m, 2 H, -NCH_2), 1.97 (s, 6 H, -CCH_3). ^{13}C NMR (CD_2Cl_2, 100 MHz) δ 171.5, 138.3, 125.9, 57.2, 51.3, 39.9, 33.0 ppm. MALDI-TOF MS m/z = 2629 for $C_{96}H_{133}Br_{12}N_{12}O_{12}Na$ $[M+Na+H]^+$. CHN Calc. C: 44.26, H: 5.11, N: 6.45; found C: 44.29, H: 5.06, N: 6.53.

RC1e

^{1}H NMR ($CDCl_3$, 400 MHz) δ 7.71-7.31 (d, 4 H, -C_5H_4N), 6.99 (s, 1 H, -ArH), 4.68 (s, 2 H, -$ArCH_2$), 3.59 (s, 2 H, -NCH_2). ^{13}C NMR ($CDCl_3$, 100 MHz) δ 170.8, 150.9, 142.8, 137.9, 126.1, 51.9, 39.9 ppm. MALDI-TOF MS m/z = 2078 for $C_{120}H_{108}N_{24}O_{12}$, $[M]^+$. CHN Calc. C: 69.35, H: 5.24, N: 16.17; found C: 66.35, H: 5.51, N: 15.11.

RC5a (representative procedure for RC5 functionalisation). Cage5R (150 mg, 0.087 mmol) was dissolved in $CHCl_3$ (20 mL) and added to a 100 mL 2-necked RB flask cooled in an ice bath. Triethylamine (183 µL, 1.313 mmol) was then added and the solution stirred for 15 minutes under N_2. 4-bromobenzoyl chloride (240 mg, 1.095 mmol) was dissolved in $CHCl_3$ (10 mL) and added to the stirring solution slowly by pipette (white gas evolved) and the reaction mixture was left stirring for ~14 hrs. Upon completion, solution was transferred to a separating funnel and extracted with NaOH solution (50 mL, 1 M) followed by extracting the aqueous twice more with $CHCl_3$ (2 x 30 mL). The organics were combined and then extracted once more with H_2O (50 mL), before drying over $MgSO_4$. The solution was then concentrated to dryness using a rotary evaporator to yield an off-white solid (crude yield = 255 mg) and purified twice using a Biotage Isolera four, initially utilising a silica column with $CHCl_3$/MeOH as solvent and then a KP-NH column again with $CHCl_3$/MeOH as solvent. After removal of solvent, **RC5a** was yielded as an off-white solid in 49 % yield (167 mg). ^{1}H NMR ($CDCl_3$, 400 MHz) δ 7.45-7.22 (1 H, -BrArH), 6.94 (s, 1 H, -ArH), 5.36, 4.32 and 3.46 (3 H, -$ArCH_2$, -NCH), 1.89, 1.68 (3 H, -$CHCH_2$, -CH_2CH_3). MALDI-TOF MS m/z = 3947 for $C_{198}H_{168}$ $Br_{12}N_{16}O_{12}Na$ $[M+Na]^+$ .CHN Calc. C: 60.63, H: 4.32, N: 5.71; found C: 59.58, H: 4.18, N: 5.57

RC5b

^{1}H NMR (CDCl3, 400 MHz) δ 7.53-7.44 (7 H, -Napthalene), 6.90 (1 H, -ArH), 5.48,

4.47 and 3.34 (3 H, -$ArCH_2$, -NCH), 1.91, 1.61 (3 H, -$CHCH_2$, -CH_2CH_3). MALDI-TOF MS m/z = 3600 for $C_{246}H_{204}N_{16}O_{12}Na$ $[M+Na]^+$. CHN Calc. C: 82.62, H: 5.75, N: 6.27; found C: 75.85, H: 5.27, N: 5.67

RC5c

^1H NMR (CDCl3, 400 MHz) δ 6.92 (1 H, -ArH), 5.62, 3.64, 3.11 (3 H, -$ArCH_2$, -NCH), 1.96, 1.65, 1.56 (15 H, -Adamantane). (-$CHCH_2$ and -CH_2CH_3 are masked by adamantane signals). MALDI-TOF MS m/z = 3534 for $C_{246}H_{300}N_{16}O_{12}Na$ $[M+Na]^+$. CHN Calc. C: 80.44, H: 8.23, N: 6.10; found C: 71.47, H: 7.38, N: 5.56
^1H NMR (CD_2Cl_2, 400 MHz) δ 7.54-7.32 (d, 4 H, -BrArH), 6.95 (s, 1 H, -ArH), 4.70 (s, 2 H, -$ArCH_2$), 4.70 (s, 2 H, -NCH_2). ^{13}C NMR ($CDCl_3$, 100 MHz) δ 171.8, 138.1, 134.2, 132.2, 128.3, 125.9, 124.5, 52.3, 39.5 ppm.

Additional data for RC1f-i and RC5f

RC1f

^1H NMR ($CDCl_3$, 400 MHz) δ 6.79 (1 H, -ArH), 4.45 (2 H, -$ArCH_2$), 3.34 (2 H, -NCH_2), 2.18 (2 H, -CH_2,$CH(CH_3)_2$)), 1.84 (1 H, -$CH(CH_3)_2$), 0.98 (6 H, -$(CH_3)_2$). ^{13}C NMR ($CDCl_3$, 100 MHz) δ 173.2, 138.3, 124.7, 52.8, 42.1, 26.0, 25.5, 22.8 ppm MALDI-TOF MS m/z = 1827.8 for $C_{108}H_{168}N_{12}O_{12}Na$ $[M+H]^+$. CHN Calc. C: 71.02, H: 9.27, N: 9.20; found C: 69.86, H: 9.16, N: 8.99. Melting point observed at 112 °C by DSC.

RC1g

^1H NMR (CDCl3, 400 MHz) δ 6.81 (1 H, -ArH), 4.63 (2 H, -$ArCH_2$), 3.60 (2 H, -NCH_2), 2.43, 2.30, 2.03, 1.65, 1.30, 0.89 (13 H, -Heptanoyl). ^{13}C NMR (CDCl3, 100 MHz) δ 174.2, 138.7, 125.9, 33.4, 32.9, 31.6, 29.2, 25.6, 25.3, 22.6, 14.1 ppm MALDI-TOF MS m/z = 2163 for $C_{132}H_{216}N_{12}O_{12}$ $[M]^+$ and 2186 for $C_{132}H_{216}N_{12}O_{12}Na$ $[M+Na]^+$. CHN Calc. C: 71.02, H: 9.27, N: 9.20; found C: 69.86, H: 9.16, N: 8.99. Melting point observed at 65 °C by DSC.

RC1h

^1H NMR ($CDCl_3$, 400 MHz) δ 6.70 (1 H, -ArH), 4.57 (2 H, -$ArCH_2$), 3.46 (2 H, -NCH_2), 2.77, 2.35, 2.08, 1.63, 1.27, 0.88 (19 H, -Decanoyl). ^{13}C NMR ($CDCl_3$, 100 MHz) δ 173.9, 138.5, 124.7, 45.8, 33.7, 32.9, 31.9, 29.6, 29.4, 29.2, 25.4, 24.9, 22.7, 14.1 ppm. MALDI-TOF MS m/z = 2688 for $C_{168}H_{288}N_{12}O_{12}$ $[M]^+$ and 2711 for

$C_{168}H_{288}N_{12}O_{12}Na$ $[M+Na]^+$. CHN Calc. C: 75.63, H: 10.88, N: 6.30; found C: 74.91, H: 11.08, N: 6.13. Melting point observed at 51 °C by DSC.

RC1i

^1H NMR ($CDCl_3$, 400 MHz) δ 6.77 (1 H, -ArH), 4.59 (2 H, -$ArCH_2$), 3.26 (2 H, -NCH_2), 2.35, 1.63, 1.26, 0.88 (19 H, -Palmitoyl). ^{13}C NMR ($CDCl_3$, 100 MHz) δ 177.3, 145.6, 101.7, 53.7, 33.8, 31.9, 29.8, 29.69, 29.66, 29.62, 29.5, 29.4, 29.3, 29.1, 27.5, 26.3, 25.3, 24.8, 22.7, 14.1 ppm. MALDI-TOF MS m/z = 3699.9 for $C_{240}H_{432}N_{12}O_{12}Na$ $[M+Na]^+$. CHN Calc. C: 78.37, H: 11.84, N: 4.57; found C: 77.69, H: 12.25, N: 3.65. Melting point observed at 45 °C by DSC.

RC5f

^1H NMR ($CDCl_3$, 400 MHz) δ 6.99 (1 H, -ArH), 5.49, 4.20, 3.37 (3 H, -$ArCH_2$, -NCH), 2.38, 2.19, 1.00 (9 H, -isovaleroyl), 1.94, 1.62 (3 H, -$CHCH_2$, -CH_2CH_3). ^{13}C NMR ($CDCl_3$, 100 MHz) δ 173.0, 146.7, 134.6, 128.2, 124.4, 58.0, 53.7, 43.8, 42.1, 29.2, 25.5, 22.9, 21.6 ppm. MALDI-TOF MS m/z = 2758 for $C_{174}H_{228}N_{16}O_{12}Na$ $[M+Na]^+$. CHN Calc. C: 76.39, H: 8.40, N: 8.19; found C: 68.66, H: 9.13, N: 8.93. Melting point observed at 242 °C by DSC.

Single Crystal Data for RC1a-d

Crystal structures of **RC1a-d** were measured on a Rigaku MicroMax-007 HF rotating anode diffractometer (Mo-Kα radiation, λ = 0.71073Å, Kappa 4 circle goniometer, Rigaku Saturn724+ detector). Empirical absorption corrections using equivalent reflections were performed with the program SADABS[14]; the structures were solved with the program SHELXD[15] and refined using SHELXL[15]. Some of the solvent molecules ($CHCl_3$) in **RC1b** and **RC1c** are heavily disordered but were refined where possible. The largest solvent accessible void after refinement was found for **RC1c** to be ~100 $Å^3$, located in the centres of the cages but no significant electron density was found, solvent accessible voids in **RC1d** are < 25 $Å^3$ and no voids were found in **RC1b**. Therefore we are confident to have located the majority of solvent molecules and the formulas given here are based accordingly on the structure refinements.

Crystal data for **RC1a**: $C_{132}H_{108}Br_{12}N_{12}O_{12} \cdot 7CHCl_3$, formula $C_{139}H_{122}Br_{12}Cl_{14}N_{12}O_{12}$, M = 3607.71 g·mol^{-1}, cubic space group $I23$, a = 19.7269(4)

Å, V = 7676.7(3) Å^3, Z = 2, ρ = 1.561 g·cm^{-3}, μ = 3.434 mm^{-1}, F (000) = 3588. A colourless, rhombohedral crystal (0.20 x 0.20 x 0.12 mm^3) of **RC1a** was measured at 100 K, 37043 reflections (2.45 < Θ < 23.25º) were collected, 2955 reflections unique (R_{int} = 0.0392), 2699 reflections observed ($I > 2\ \sigma(I)$), R_1 = 0.0519 for the observed and R_1 = 0.0560 for all reflections, max/min residual electron density 0.727 and -0.276 e·Å^{-3}, data / restraints / parameters = 2955 / 0 / 211, GOF = 1.109. Each molecule of **RC1a** is located on a special position (23), hence only 1/12th of the cage molecule is crystallographically independent. The bromophenyl group is rotationally disordered by ~30º about an approximate C(O)–C(phenyl) bond in a 1 : 1 ratio. All non H atoms belonging to the cage molecule were refined anisotropically.

Crystal data for **RC1b**: $C_{180}H_{144}N_{12}O_{12} \cdot 7CHCl_3$, formula $C_{187}H_{151}Cl_{21}N_{12}O_{12}$, M = 3502.65 g·mol^{-1}, cubic space group *P*n-3, a = 20.3289(13) Å, V = 8401.2(9) Å^3, Z = 2, ρ = 1.385 g·cm^{-3}, μ = 0.407 mm^{-1}, F (000) = 3620. A colourless, block-shaped crystal (0.10 x 0.10 x 0.05 mm^3) of **RC1b** was measured at 100 K, 52249 reflections (2.45 < Θ < 23.25º) were collected, 2029 reflections unique (R_{int} = 0.0448), 1380 reflections observed ($I > 2\ \sigma(I)$), R_1 = 0.0778 for the observed and R_1 = 0.1049 for all reflections, max/min residual electron density 0.320 and -0.284 e·Å^{-3}, data / restraints / parameters = 2029 / 50 / 241, GOF = 1.121. **7** is located on a special position (23) rendering 1/12th of the cage molecule crystallographically independent.. The one independent naphthyl group is rotationally disordered by ~180º about the C(O)–C(naphthyl) bond in an approximate 2 : 1 ratio. Non H atoms belonging to the cage molecule were refined anisotropically; rigid bond restraints were applied to the anisotropic atomic displacement parameters (ADPs) of the atoms of the disordered part.

Crystal data for **RC1c**: $C_{180}H_{240}N_{12}O_{12} \cdot 19.5CHCl_3$, formula $C_{199.5}H_{259.5}Cl_{58.5}N_{12}O_{12}$, M = 5091.52 g·mol^{-1}, tetragonal space group *I*-4, a = 33.479(3), c = 42.914(5) Å, V = 48100(7) Å^3, Z = 8, ρ = 1.406 g·cm^{-3}, μ = 0.711 mm^{-1}, F (000) = 21048. A colourless, block-shaped crystal (0.30 x 0.25 x 0.12 mm^3) of **RC1c** was measured at 90 K, 291349 reflections (1.55 < Θ < 23.26º) were collected, 34561 reflections unique (R_{int} = 0.0626), 28048 reflections observed ($I > 2\ \sigma(I)$), R_1 = 0.1229 for the observed and R_1 = 0.1410 for all reflections, max/min residual electron density 1.211 and -0.536 e·Å^{-3}, data / restraints / parameters =

34561 / 330 / 2707, GOF = 2.360. One molecule of **RC1c** is crystallographically independent. One of the 6 independent adamantane linker groups is disordered over two sites in an approximate 3 : 1 ratio. Non H atoms belonging to the cage molecule were refined anisotropically, and restraints on connectivity and ADPs were applied to the atoms of the disordered part.

Crystal data for **RC1d**: $C_{96}H_{132}Br_{12}N_{12}O_{12} \cdot 12CHCl_3 \cdot H_2O$, formula $C_{108}H_{146}Br_{12}Cl_{36}N_{12}O_{13}$, M = 4055.49 g·mol^{-1}, cubic space group P-43n, a = 20.3301(7) Å, V = 8402.7(5) Å^3, Z = 2, ρ = 1.603 g·cm^{-3}, μ = 3.485 mm^{-1}, F (000) = 3620. A colourless, trigonal plate shaped crystal (0.12 x 0.12 x 0.05 mm^3) of **RC1d** was measured at 100 K, 110955 reflections ($1.42 < \Theta < 26.35^o$) were collected, 2875 reflections unique (R_{int} = 0.0905), 2490 reflections observed ($I > 2\ \sigma(I)$), R_1 = 0.0446 for the observed R_1 = 0.0560 for all reflections, max/min residual electron density 0.566 and -0.269 e·Å^{-3}, data / restraints / parameters = 2875 / 2 / 147, GOF = 1.049. **RC1d** is located on a special position (23) rendering 1/12th of the cage molecule crystallographically independent. The Br atom and one methyl group of the isobutyl group are disordered over two sites in an approximate 1 : 1 ratio. Non H atoms belonging to the cage molecule were refined anisotropically, and restraints on bond lengths were applied to the atoms of the disordered part.

Single Crystal Data for RC1e

Single crystal X-ray data for **RC1e** was measured on the small molecule single crystal beamline I19, Diamond Light Source, Didcot, UK (λ = 0.6889 Å, CrystalLogic Kappa 3 circle goniometer, Rigaku Saturn724+ detector). An empirical absorption correction using equivalent reflections was performed with the program SADABS; the structure was solved with the program SHELXD (utilising the GROP instruction and a predefined molecular fragment) and refined with SHELXL using the OLEX2 GUI. All non H atoms were refined anisotropically, H atoms were fixed to geometric positions using the riding model. The data are very poor (1.5 Å resolution, data : parameter ~ 3 : 1) and a number of constraints ('AFIX 66' instruction for the benzene and pyridine rings) and restraints (DELU and SIMU instructions in SHELXL) had to be applied in order to keep the model intact. The residual density of the solvent content could not be modelled in any reasonable way, and was masked using the solvent masking routine in OLEX2.

Crystal data for **RC1e**: Formula $C_{120}H_{108}N_{24}O_{12}$, M = 2078.30 g·mol^{-1}, monoclinic space group $I2/a$, a = 23.993(8), b = 18.777(3), c = 27.348(4) Å, β = 90.214(4), V = 12320(5) Å^3, Z = 4, ρ = 1.120 g·cm^{-3}, μ = 0.075 mm^{-3}, F (000) = 4368, crystal size = 0.15 x 0.05 x 0.02 mm^3, T = 100(2) K. 1902 reflections measured (1.28 < Θ < 13.27°), 1902 unique (R_{int} = 0.0000), 1137 observed ($I > 2\sigma(I)$), R_1 = 0.1348 for the observed and R_1 = 0.1725 for all reflections, max/min residual electron density = 0.254 and -0.198 e·Å^{-3}, data / restraints / parameters = 1902 / 711 / 607, GOF = 2.493.

The Connolly surface area (CSA) is generated by rolling a probe molecule across the interface between the probe and the substrate, the interface taken from the contact point of the probe molecule. CSA measurements were obtained in Materials Studio 5.0 (Accelrys) using nitrogen as the probe molecule (radius of 1.82 Å).[16]

4.8 References

(1) Tozawa, T.; Jones, J. T. A.; Swamy, S. I.; Jiang, S.; Adams, D. J.; Shakespeare, S.; Clowes, R.; Bradshaw, D.; Hasell, T.; Chong, S. Y.; Tang, C.; Thompson, S.; Parker, J.; Trewin, A.; Bacsa, J.; Slawin, A. M. Z.; Steiner, A.; Cooper, A. I. *Nat. Mater.* **2009**, *8*, 973.

(2) Hasell, T.; Schmidtmann, M.; Smith, M.; Stone, C.; Cooper, A. I. *Chem. Commun.* **2012**, *48*, 4689.

(3) Mastalerz, M.; Schneider, M. W.; Oppel, I. M.; Presly, O. *Angew. Chem. Int. Ed.* **2011**, *50*, 1046.

(4) Swamy, S. I.; Bacsa, J.; Jones, J. T. A.; Stylianou, K. C.; Steiner, A.; Ritchie, L. K.; Hasell, T.; Gould, J. A.; Laybourn, A.; Khimyak, Y. Z.; Adams, D. J.; Rosseinsky, M. J.; Cooper, A. I. *J. Am. Chem. Soc.* **2010**, *132*, 12773.

(5) Jones, J. T. A.; Hasell, T.; Wu, X.; Bacsa, J.; Jelfs, K. E.; Schmidtmann, M.; Chong, S. Y.; Adams, D. J.; Trewin, A.; Schiffman, F.; Cora, F.; Slater, B.; Steiner, A.; Day, G. M.; Cooper, A. I. *Nature* **2011**, *474*, 367.

(6) Xu, Y.; McLaughlin, M.; Bolton, E. N.; Reamer, R. A. *J. Org. Chem.* **2010**, *75*, 8666.

(7) http://drugmet.rilspace.org/wiki/All_pKa_values accessed March 2012.

(8) Bojdys, M. J.; Briggs, M. E.; Jones, J. T. A.; Adams, D. J.; Chong, S. Y.; Schmidtmann, M.; Cooper, A. I. *J. Am. Chem. Soc.* **2011**, *133*, 16566.

(9) Caminade, A.-M.; Laurent, R.; Majoral, J.-P. *Adv. Drug. Deliver. Rev.* **2005**, *57*, 2130.

(10) Barbour, L. J. *Chem. Commun.* **2006**, 1163.

(11) Hasell, T.; Chong, S. Y.; Jelfs, K. E.; Adams, D. J.; Cooper, A. I. *J. Am. Chem. Soc.* **2011**, *134*, 588.

(12) O'Reilly, N.; Giri, N.; James, S. L. *Chem. Eur. J.* **2007**, *13*, 3020.

(13) Giri, N.; Davidson, C. E.; Melaugh, G.; Del Popolo, M. G.; Jones, J. T. A.; Hasell, T.; Cooper, A. I.; Horton, P. N.; Hursthouse, M. B.; James, S. L. *Chem. Sci.* **2012**, *3*, 2153.

(14) Sheldrick, G. *SHELX-97* **2008**.

(15) Sheldrick, G. *Acta Crystallogr. Sect. A.* **2008**, *64*, 112.

(16) Connolly, M. L. *Science* **1983**, *221*, 709.

Chapter 5
Organic Cage Polymers

Table of Contents

5.0 RC1 and Decorated RC1 as a Monomer in Polymerisation

Earlier in this thesis, the reduction and subsequent decoration of cages was described (Chapter 4). Both reduced cages themselves (containing secondary amine groups) and decorated cages (containing bromine groups and to a lesser extent, arene groups) possessed chemical functionality, giving rise to opportunities for further reactions. As the cages already contained a predefined pore (albeit in an ideal crystalline state), it was hypothesised that the presence of this pore could lead to increased surface areas upon successful polymerisation. There has already been recent progress in this area within the literature, with Jin *et al.* successfully polymerising their [2+3] bromine functionalised cages *via* Sonogashira coupling.[1] This produced materials with low overall gas uptakes, but high selectivity towards CO_2 (213/1 over N_2).[2] Chaikittisilp *et al*. have reported a series of porous networks *via* Sonogashira coupling an 8-armed bromophenyl decorated POSS (BrPh-D4R) with various bi- and tri-functional alkynes with N_2 SA_{BET} between 850-1040 m^2/g.[3] Chaikittisilp *et al*. have also previously utilised the Yamamoto reaction to homo-couple a smaller 8-armed bromophenyl decorated POSS (named BrPh-D4R), yielding a network with N_2 SA_{BET} of 1045 m^2/g.[4]

5.1 RC1 and Bi-Functional Acid Chlorides Toward Porous Polymers

We attempted to utilise the acid chloride addition/elimination reaction (used in the synthesis of functionalised cages as seen in Chapter 4) to create polymers from reduced cages. Four bis-acid chlorides (Figure 1; **1-4**) were chosen, with a selection of flexible (**1** and **2**) and rigid (**3** and **4**) linkers. All linkers were commercially available except **4**, where the carboxylic acid was converted to the acid chloride using a slightly modified preparation from the literature before polymerisation.[5]

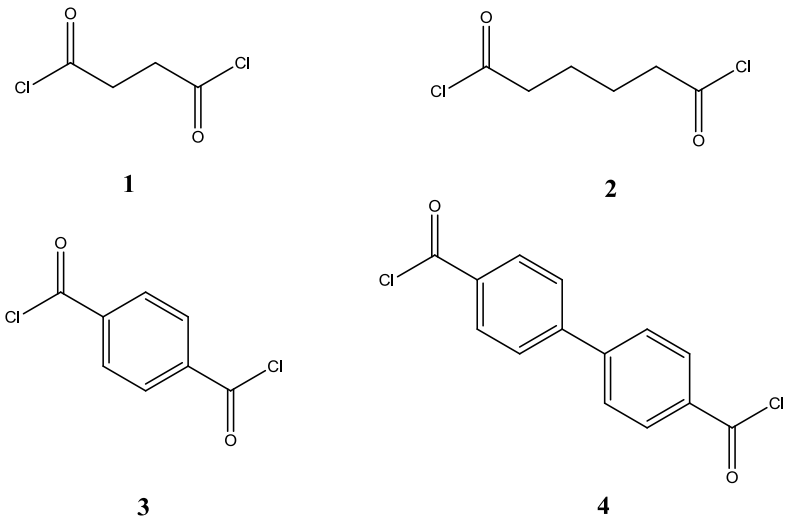

Figure 1: Bis-acid chloride linkers that were reacted with **RC1** to make cage polymer networks.

A 1:6 ratio of **RC1** to bi-functional acid halide was used to balance functional groups, because **RC1** possessed 12 functional amine groups (A12) and each acid chloride has two functional groups (B2) (Figure 2).

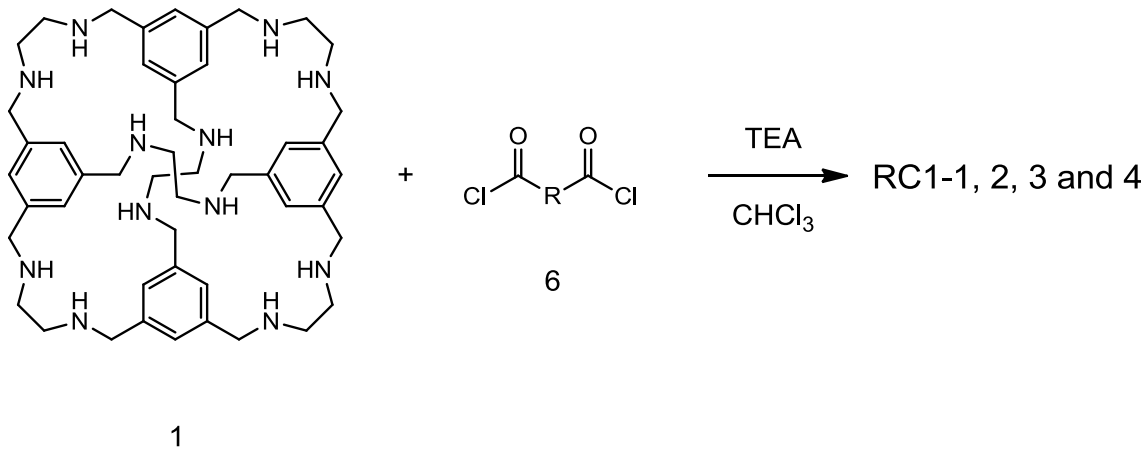

Figure 2: **RC1** and bis-acyl chlorides: general procedure to make cage polymer networks.

Reaction of **RC1** with all four bis-acid chlorides yielded white insoluble polymers almost immediately upon addition of the acid chloride to **RC1** in solution. After stirring overnight, the insoluble precipitates were removed by filtration and washed

thoroughly with chloroform, hydrochloric acid (0.1 M), water, and Soxhlet extracted (with methanol). Yields were 16 %, 45 %, 64 % and 67 % for **RC1-1, 2, 3** and **4** respectively, with higher conversion rates obvious for longer, rigid bis-acid chlorides.

FTIR of the samples all showed a very strong characteristic amide C=O band at ~1650 cm^{-1}, confirming the reaction had indeed occurred. C-N stretches are apparent at ~1250 cm^{-1} while C=C are at 1370 cm^{-1}. **RC1-4** showed multiple C=O stretches, however, suggesting an incomplete reaction and presence of remaining COCl. Alkyl C-H stretches were apparent in all samples at ~2950 cm^{-1}, although they are more prominent in **RC1-1** and **RC1-2** as these contained alkyl carbons in the bisacid chloride. Aromatic C-H bands are visible at ~3000 cm^{-1} (bending) and ~750 cm^{-1} (stretching), with more relative intensity in **RC1-3** and **RC1-4**. There are also broad N-H stretches at ~3350 cm^{-1}, indicating an incomplete reaction (Figure 3, samples offset for clarity).

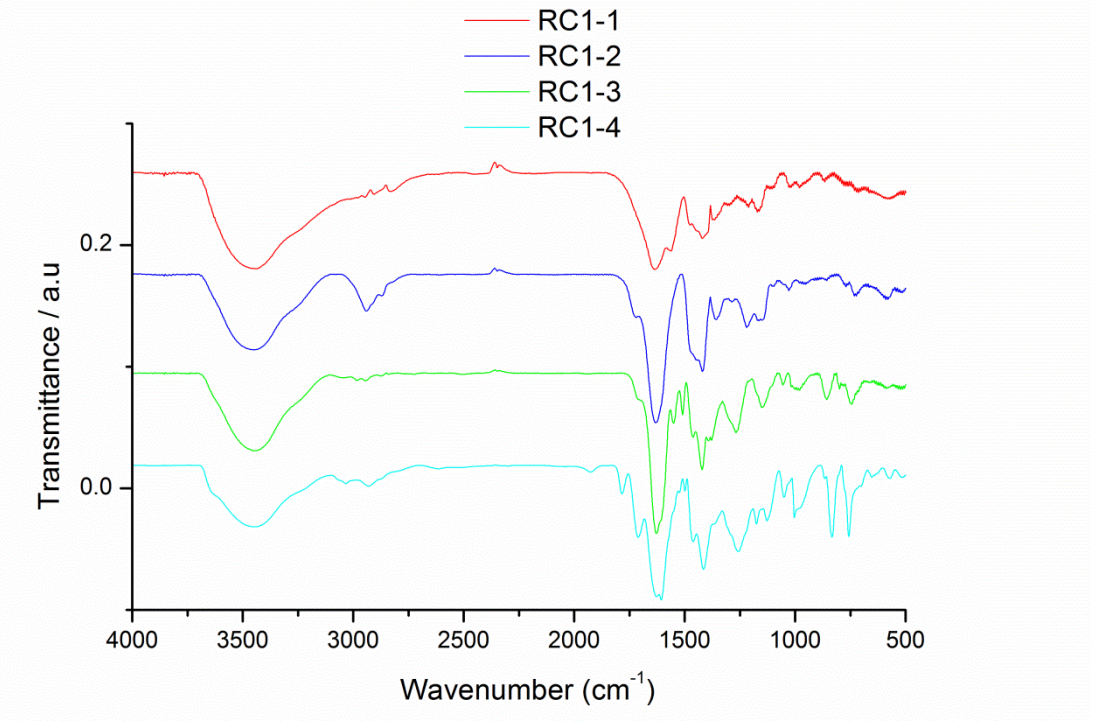

Figure 3: FTIR of **RC1-1**, **2**, **3** and **4**.

CHN theoretical results were calculated based on 100 % reaction of all amine groups. As with other networks (including CMPs)[6,7] CHN was not exact (especially

on carbon percentages). A trend can be observed however of increasing carbon content as higher molecular weight linkers are used (**1** through **4**) whereas nitrogen content is decreased from this same effect (Table 1).

Sample	Theo. C %	Theo. H %	Theo. N %	Exp. C %	Exp. H %	Exp. N %
RC1-1	65.43	7.32	12.72	51.18	6.54	9.60
RC1-2	67.71	8.12	11.28	60.30	7.64	10.12
RC1-3	71.62	6.01	10.44	62.40	5.79	8.36
RC1-4	76.72	5.58	8.13	70.67	5.17	6.53

Table 1: CHN of **RC1-1**, **2**, **3** and **4**.

Of these reactions, only **RC1-3** and **RC1-4** yielded porous materials. Maximum N_2 uptakes of 8.80 and 6.79 mmol/g at 1 bar were observed for **RC1-3** and **RC1-4** respectively. Additionally, maximum H_2 uptakes of 1.86 and 1.96 mmol/g at 1.13 bar were observed for **RC1-3** and **RC1-4** respectively (Table 2).

Sample	N_2 Uptake (mmol/g)*	N_2 SA_{BET} (m^2/g)	H_2 Uptake (mmol/g)**	H_2 $SA_{Langmuir}$ (m^2/g)
RC1-1	0.12	7	0.50	81
RC1-2	0.27	2	0.10	7
RC1-3	8.80	106	1.86	95
RC1-4	6.79	90	1.96	119

Table 2: H_2 and N_2 uptakes and calculated surface areas of **RC1-1**, **2**, **3** and **4**. *N_2 maximum uptake at 1 bar. **H_2 maximum uptake at 1.13 bar.

RC1-3 and **RC1-4** yielded N_2 SA_{BET} of 106 m^2/g and 90 m^2/g, respectively, while both displayed a type II/IV isotherm, with **RC1-4** exhibiting a H4 hysteresis (Figure 5).

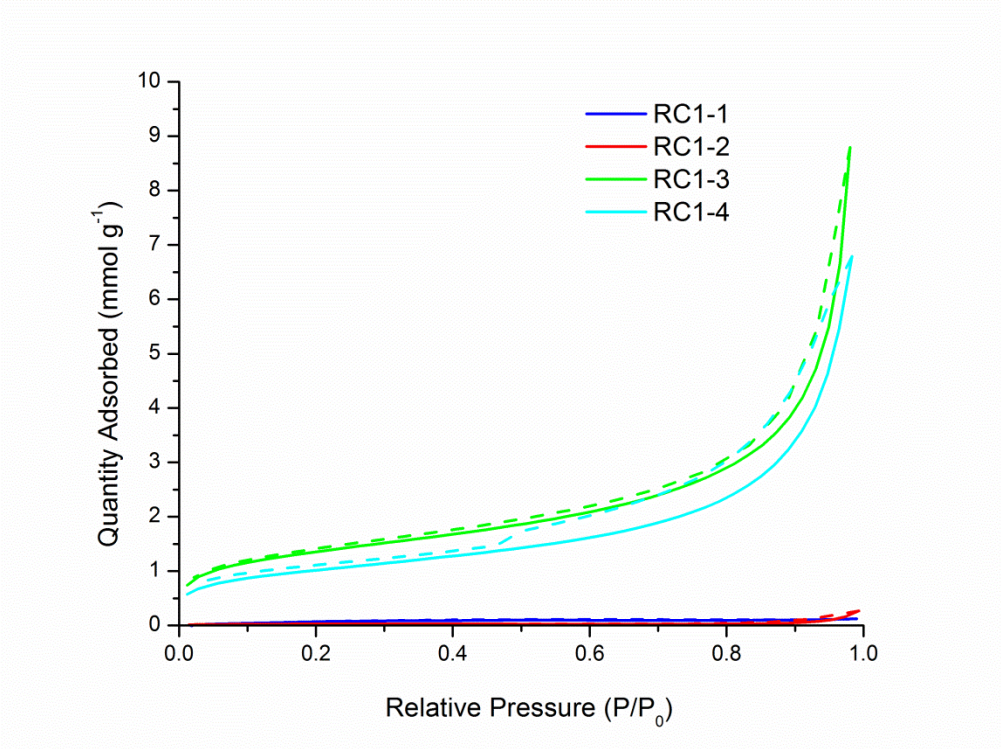

Figure 4: N_2 isotherms for **RC1-1**, **2**, **3** and **4**.

H_2 uptake for **RC1-3** and **RC1-4** was also measured, with both giving rise to Type I isotherms and H_2 $SA_{Langmuir}$ of 95 and 119 m^2/g (Figure 5). Conversely, bis-acid chlorides **RC1-1** and **RC1-2** again yielded non-porous materials. This observation is likely due to **RC1-1** and **RC1-2** containing more flexible bis-acid chloride linkers containing an aliphatic carbon chain. This would result in the polymer collapsing in upon itself. We hypothesise the more rigid bi-functional acid chlorides **RC1-3** and **RC1-4** cannot collapse, thus exhibiting (little) nitrogen and hydrogen uptake. With this logic, it would be reasonable to assume all porosity in **RC1-3** and **RC1-4** is indeed arising from poor packing created by rigid connecting bis-acid chloride struts.

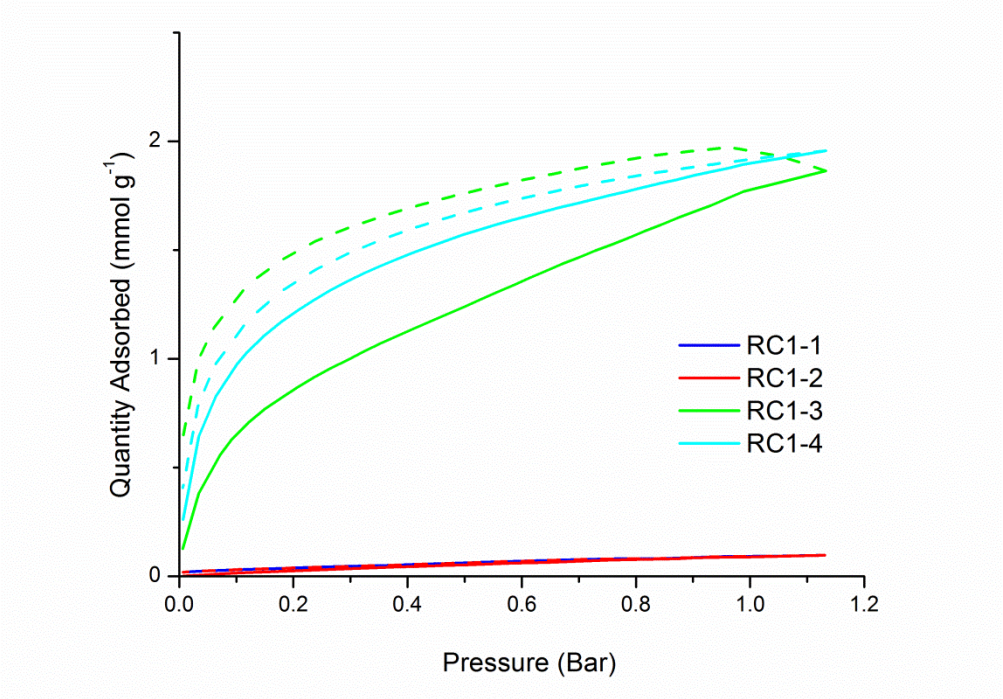

Figure 5: H_2 (bottom) isotherms for **RC1-1, 2, 3** and **4**.

Lack of porosity (**RC1-1** and **RC1-2**) or modest porosity (**RC1-3** and **RC1-4**) could be attributed to incomplete reaction as suggested by low yields and presence of NH bands in FTIR. This is highlighted by the fact the yields are lower for **RC1-1** and **RC1-2**, which are likely to be more affected by steric interactions between cages due to the relative shortness of bis-acid chlorides, thus preventing complete reaction. Longer linkers (**RC1-2**, **RC1-3** and **RC1-4**) gave higher yields, which we hypothesise is due to them allowing two cages to come together and allowing the reaction to proceed further, although still not to completion. It is also likely that this polymeriisation occurs via step-growth polymerisation. As a result, a much smaller amount of RC1 was likely necessary. This reaction is ripe for repeating with a tep-growth approach.

5.2 Functionalised RC1: Toward Polymers

With functionalised reduced cages (**RC1a** and **RC1b** seen in Chapter 4), three separate polymerisation techniques were attempted. Bromobenzene decorated **RC1a** was to be homocoupled *via* Yamamoto coupling[8,9] and used as a monomer in

Sonogashira coupling,[6,7] while naphthalene decorated **RC1b** was hyper cross-linked by Friedel-Crafts alkylation.[10]

5.2.1 Yamamoto Coupling

The bromine functionalised pendant groups in **RC1a** provided an excellent opportunity for C-C coupling polymerisation. Some of the most porous networks to date are synthesised by the Yamamoto reaction, namely PAF-1 and PPN-4 with N_2 SA_{BET} of 5640 m^2/g and 6461 m^2/g, by Ben and Yuan *et al.* respectively.[8,9] Ben *et al.* utilised a nickel(0)-catalyzed Yamamoto-type[11] Ullmann cross-coupling reaction[12] in the production of PAF-1. Unlike other Yamamoto reactions, this example did not utilise lithium, hence aryl halides are not lithiated and do not undergo transmetallation.[13] Lithium was omitted by both Ben and Yuan *et al.* as the aim is towards the creation of porous materials, with additional metals having the possible consequence of blocking pores.

In the Yamamoto reaction, aryl halides coordinate successively to the nickel by oxidative addition and disproportionation. Next, two aromatic rings undergo reductive elimination to form the new C-C bond between the aromatic rings. The excess of ligand ensures that no elemental nickel is formed before the reaction is quenched. The reaction is eventually quenched with concentrated hydrochloric acid, which causes the nickel complex to decompose and therefore terminate the reaction (Figure 6).

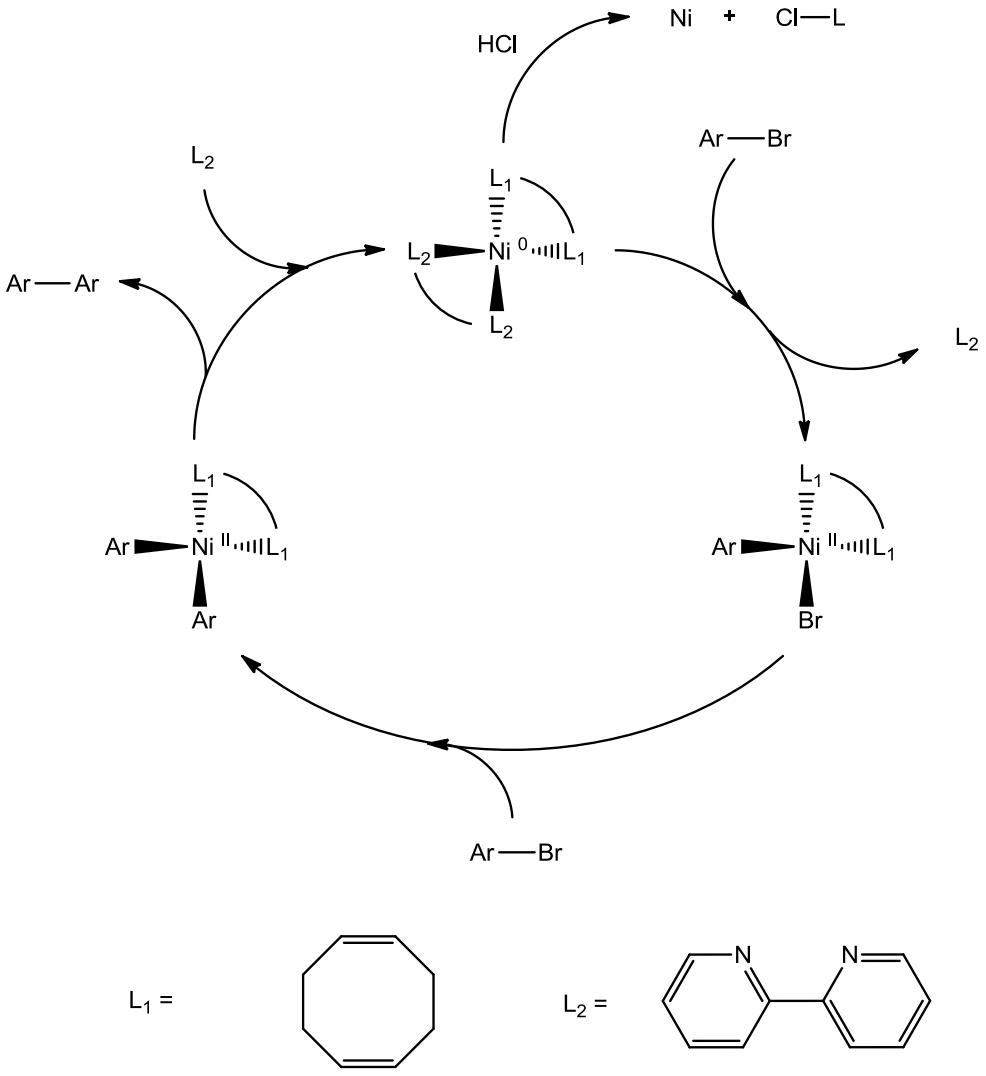

Figure 6: Proposed mechanism of the Yamamoto reaction used here (adapted from references).[13,14]

Using conditions similar to those used in the production of PAF-1, the Yamamoto reaction was employed for homo-polymerisation of the 12-armed bromophenyl decorated cage **RC1a** (Figure 7). The cage aromatic framework (CAF) formed could perhaps be expected to produce a similar structure polymer to **RC1-4** (seen earlier in section 5.1) as it would contain the same repeating unit on coupling of two pendant groups (if all reactive groups were in fact used in both respective polymerisations, and did not couple with another pendant group from the same cage). This 12-armed bromophenyl decorated cage (**RC1a**) contains the highest number of functional groups on a Yamamoto precursor monomer to the best of our knowledge. Chaikittisilp *et al*. have previously utilised the Yamamoto reaction homo-coupling a

smaller 8-armed bromophenyl decorated POSS (named BrPh-D4R), yielding a network with N_2 SA_{BET} of 1045 m^2/g.[4]

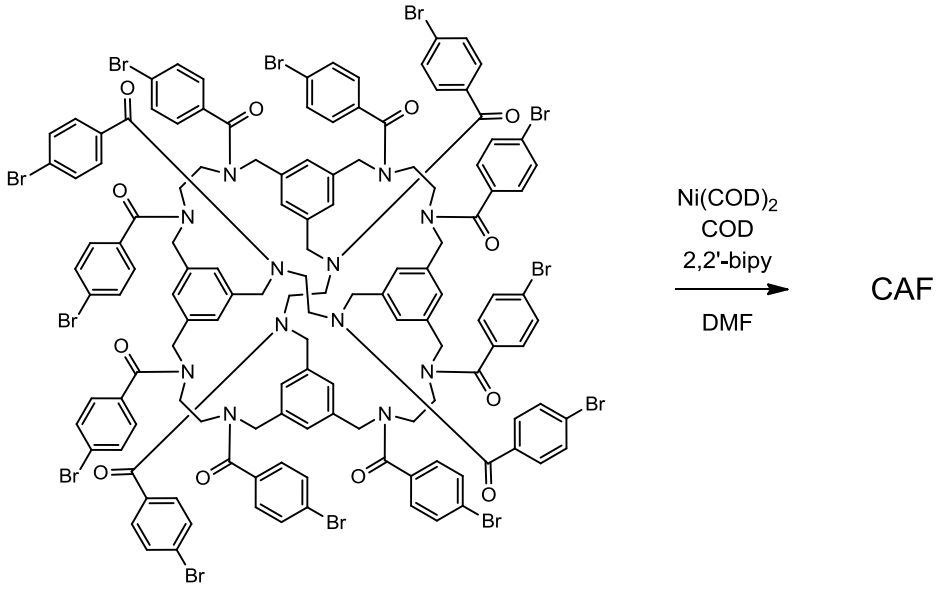

Figure 7: Yamamoto homo-coupling of RC1a towards **CAF-1**.

As with **RC1** and bis-acid chlorides, a white powder was generated after polymerisation and work up. The yield was 140 %, indicating either retention of heavy metal catalyst, or incomplete homo-coupling and thus remaining bromine groups.

FTIR of **CAF-1** contained a very strong characteristic amide C=O band at ~1650 cm^{-1} from the pendant arm on the **RC1a**. C-N are apparent at ~1250 cm^{-1} while C=C are observed at 1370 cm^{-1}. Weak C-Br bands are at 750 cm^{-1}, further suggesting incomplete reaction (Figure 8).

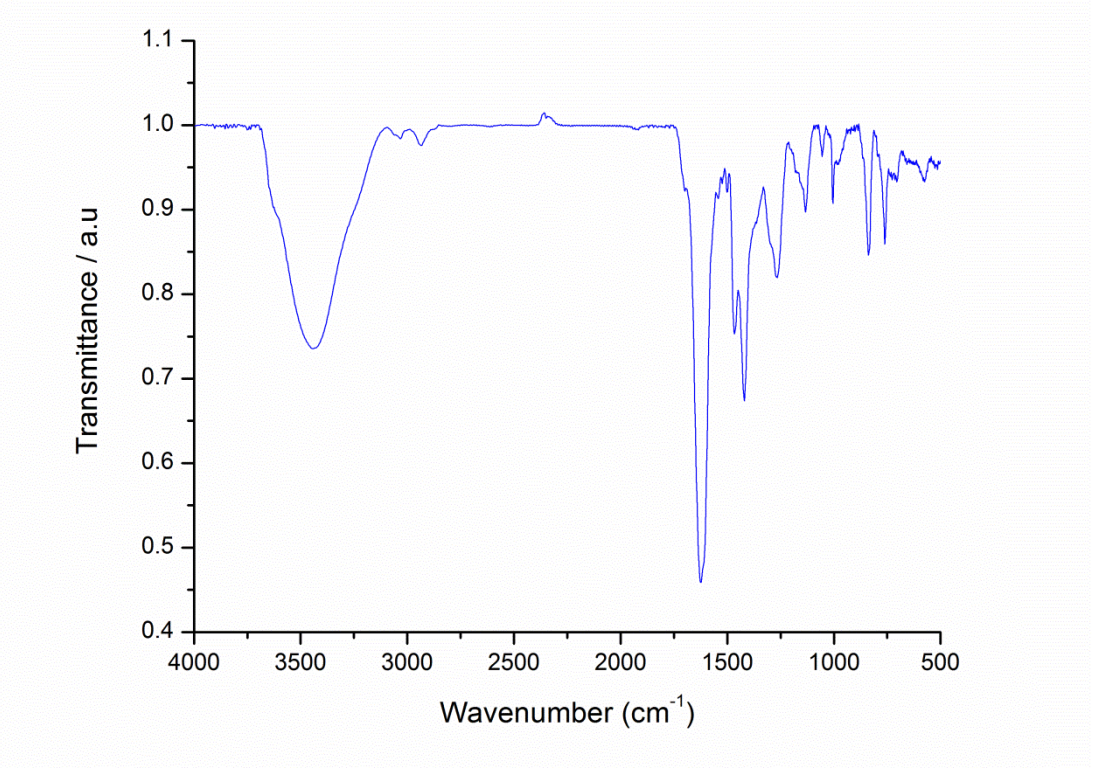

Figure 8: FTIR of **CAF-1**.

CHN analysis as with other networks was inaccurate for carbon, but reasonable for both hydrogen and nitrogen (Table 3). This could be due to incomplete polymerisation, or retention of heavy metal catalyst used in the polymerisation process. Theoretical CHN results were calculated based on 100 % reaction of pendant groups.

Sample	Theo. C %	Theo. H %	Theo. N %	Exp. C %	Exp. H %	Exp. N %
CAF-1	76.72	5.85	8.13	70.03	5.80	7.54

Table 3: CHN analysis for **CAF-1**.

SEM/EDX of **CAF-1** was carried out by Dr. T. Hasell (Figure 9). Intriguingly, and converse to FTIR, EDX analysis indicated very little bromine or nickel within the sample, though small amounts can be seen within the EDX spectrum below. It is likely that a small amount of bromine is in fact present, as nitrogen was also not

detected by EDX, which we know makes up a percentage of the cage material. This is possibly due to these elements being below the detection limit, meaning analysis is qualitative. It is however likely that the majority of bromine has been removed from the **RC1a** sample, as in Yamamoto coupling a stoichiometric amount of Ni catalyst is used,[8,9] which inserts into the aryl bromide bond before removing the bromides by reductive elimination. As the ligand is present in large excess, no elemental Ni is formed before the reaction is terminated.[15-20]

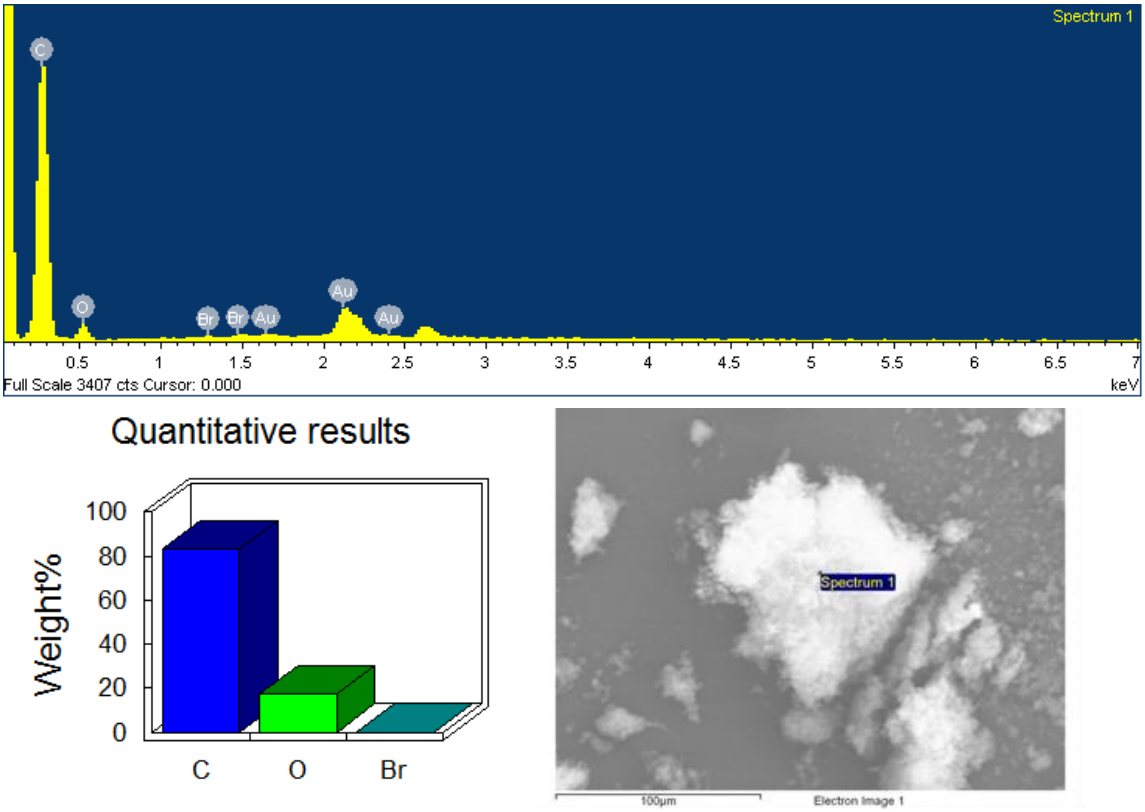

Figure 9: EDX Analysis of **CAF-1**.

When gas sorption data was compared with **RC1-4** however (for which a similar structure was expected), the N_2 uptake was markedly lower. The N_2 SA_{BET} was measured to be 37 m^2/g, giving a maximum uptake of 2.72 mmol/g at 1 bar with a type IV isotherm (Figure 10).

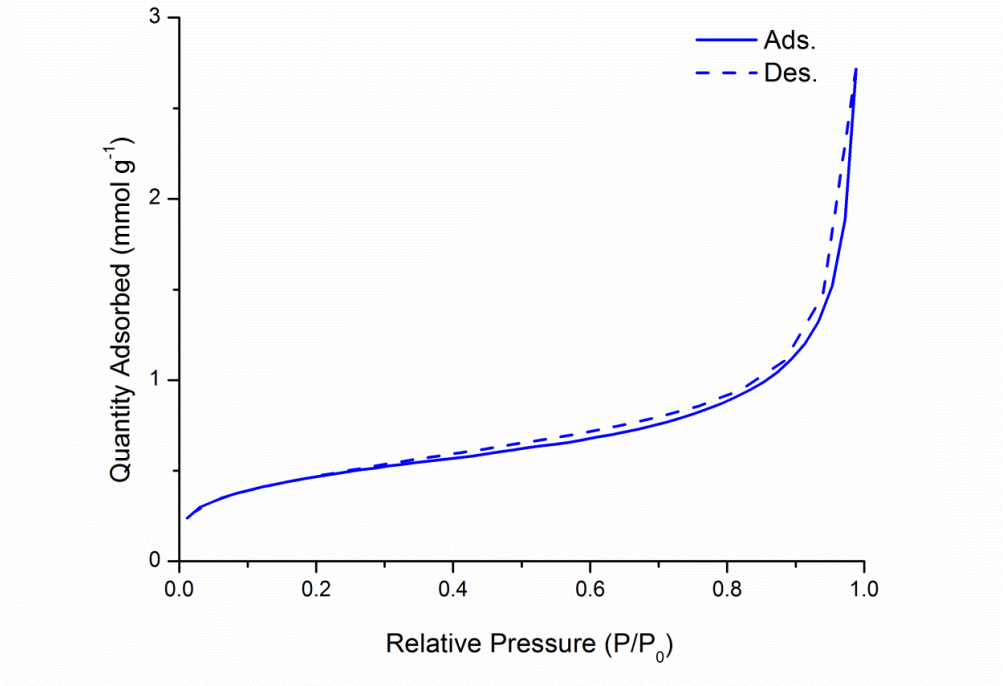

Figure 10: N_2 isotherm for **CAF-1**.

The H_2 uptake was similar to that seen for the **RC1-4** sample (section 5.1) with a maximum uptake of 1.92 mmol/g at 1.13 bar, with a type I isotherm with hysteresis observed (Figure 11).

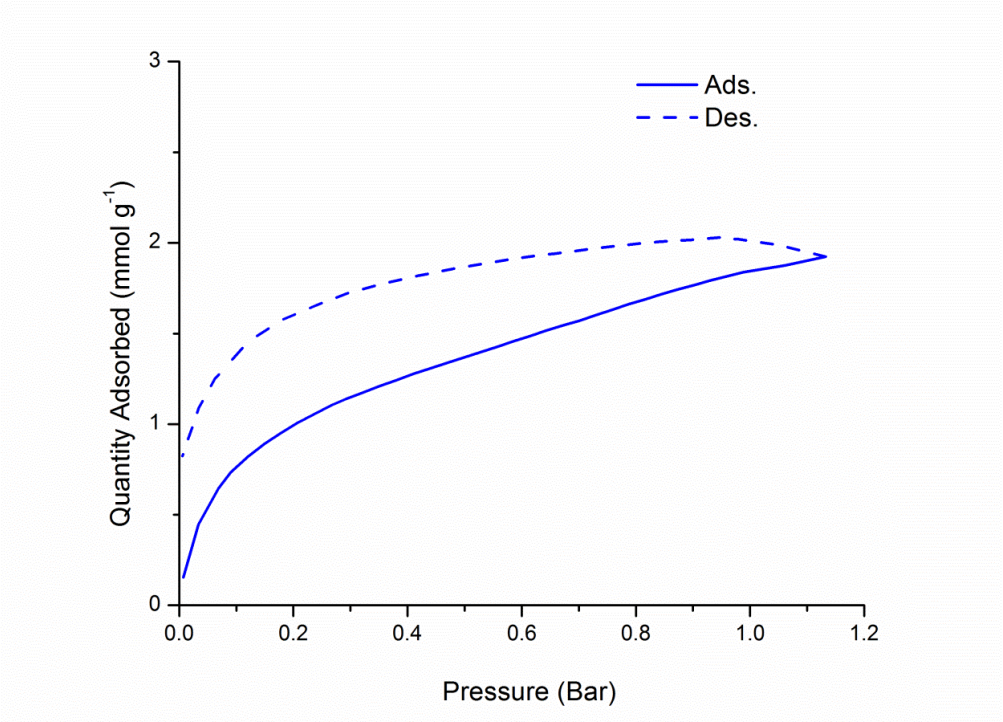

Figure 11: H_2 isotherm for **CAF-1**.

The gas uptake was also much lower in comparison to BrPh-D4R prepared by Chaikittisilp *et al*.[4] We hypothesise that this is due to a much more flexible cage core being present, and overcrowding of the periphery of the cage molecule with bromophenyl arms preventing complete reaction (as suggested by high yield and remaining C-Br bands in FTIR).

5.2.2 Sonogashira Cross-coupling

The Sonogashira cross-coupling[21] reaction has been used to form a number of porous polymer networks (namely CMPs) with N_2 SA_{BET} in excess of 1000 m^2/g.[6,7] The mechanism for Sonogashira cross-coupling involves two cycles; a palladium and a copper cycle.[22] The palladium cycle is based on a fast oxidative addition of R-X to Pd(0) catalyst (where R is: aryl, hetaryl, vinyl and X is: I, Br, Cl, OTf) to give a Pd(II) complex. Next, transmetallation occurs with copper acetylide generated from the copper cycle followed by trans-cis isomerism. The product is finally formed from reductive elimination, while also regenerating the Pd(0) catalyst (Figure 12).

The copper cycle is less well understood. It is believed that the base (generally a tertiary amine, here shown as Et_3N) deprotonates the alkyne forming a copper acetylide. Such tertiary amines however are not usually basic enough to deprotonate the alkyne; therefore it is necessary for a copper ion to complex with the acetylene making the protons more acidic and hence easier to remove and forming the copper acetylide. This continues to react with the palladium intermediate and regenerates the copper halide at the same time.[22]

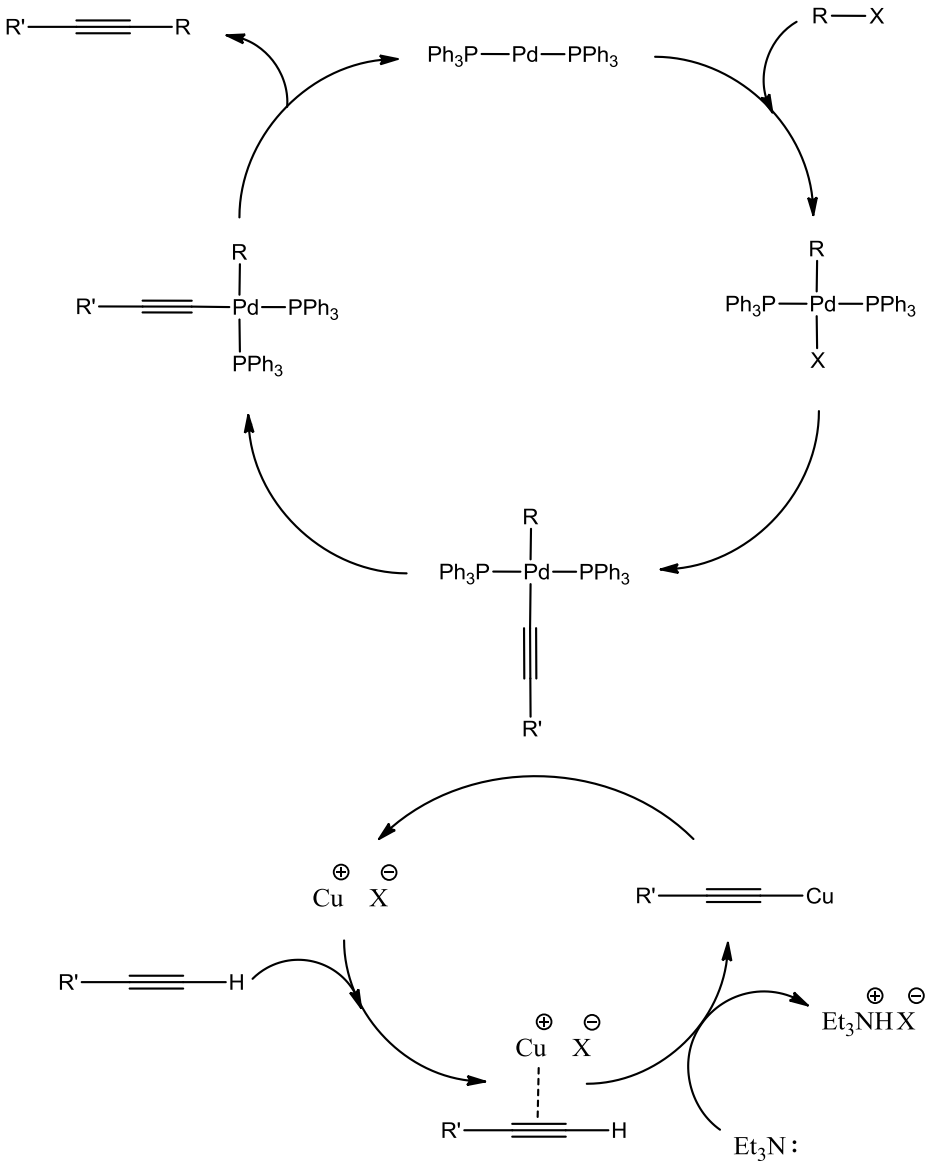

Figure 12: Catalytic cycle of Sonogashira cross-coupling reaction (redrawn from reference).[22]

The use of **RC1a** as a monomer (containing bromophenyl arms) with 1,4-diethynylbenzene in a A12 + B2 reaction was expected to produce an Organic Cage Framework (OCF, to use the terminology of Jin *et al.*)[2] network polymer with the potential to be microporous (Figure 13). In this instance, a 1:25 ratio of **RC1a** to 1,4-diethynylbenzene was used (with an excess of the 1,4-diethynylbenzene linker, replicated from previous CMP preparations in the literature as an excess gave higher surface area networks).[6] Similar attempts have been made in the literature, where a previously discovered [2+3] bromine functionalised cage[1] was linked with various bi-functional diynes using microwave reactors. This produced a network which

exhibited modest overall uptake (CO_2 uptake of 0.23 mmol/g), though was selective of CO_2 over N_2 (213/1) OCFs.[2] Chaikittisilp *et al*. have also reported a series of porous networks *via* Sonogashira-Hagihara cross coupling an 8-armed bromophenyl decorated POSS (BrPh-D4R) with various bi- and tri-functional alkynes with a N_2 SA_{BET} between 850-1040 m^2/g.[3]

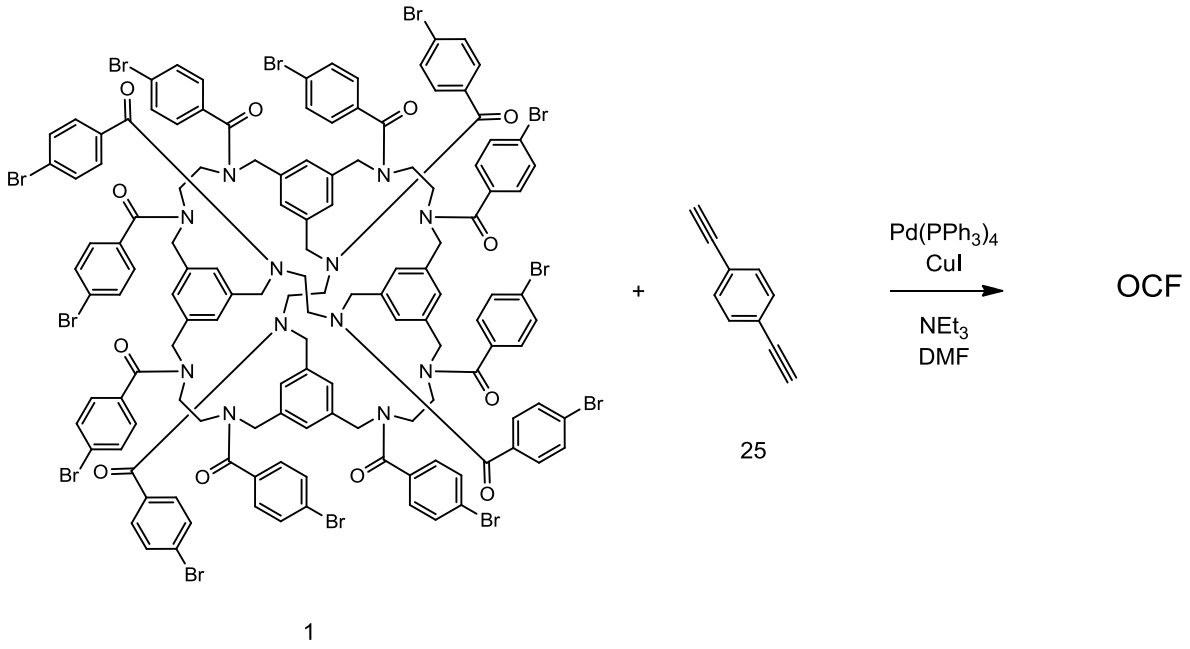

Figure 13: Sonogashira cross-coupling of **RC1a** and 1,4-diethynylbenzene

The reaction yielded a brown insoluble powder similar to those observed for other CMP networks.[6,7] The yield was 132 %, indicating either retention of heavy metal catalyst (Pd or CuI), or incomplete reaction and remaining bromine groups which is consistent with results elsewhere.[7]

FTIR of the **OCF** showed a strong characteristic amide C=O band at ~1650 cm^{-1}, confirming the reaction had indeed occurred. C-N are apparent at ~1250 cm^{-1} while C=C are again visible at 1370 cm^{-1}. Internal acetylenes are apparent at ~2200 cm^{-1} , while the peak at 2100 cm^{-1} and broad peak at ~3300 cm^{-1} suggests the presence of terminal acetylene groups (suggesting incomplete reaction and presence of end groups). C-Br bands are apparent at 750 cm^{-1}, further pointing to an incomplete reaction (Figure 14).

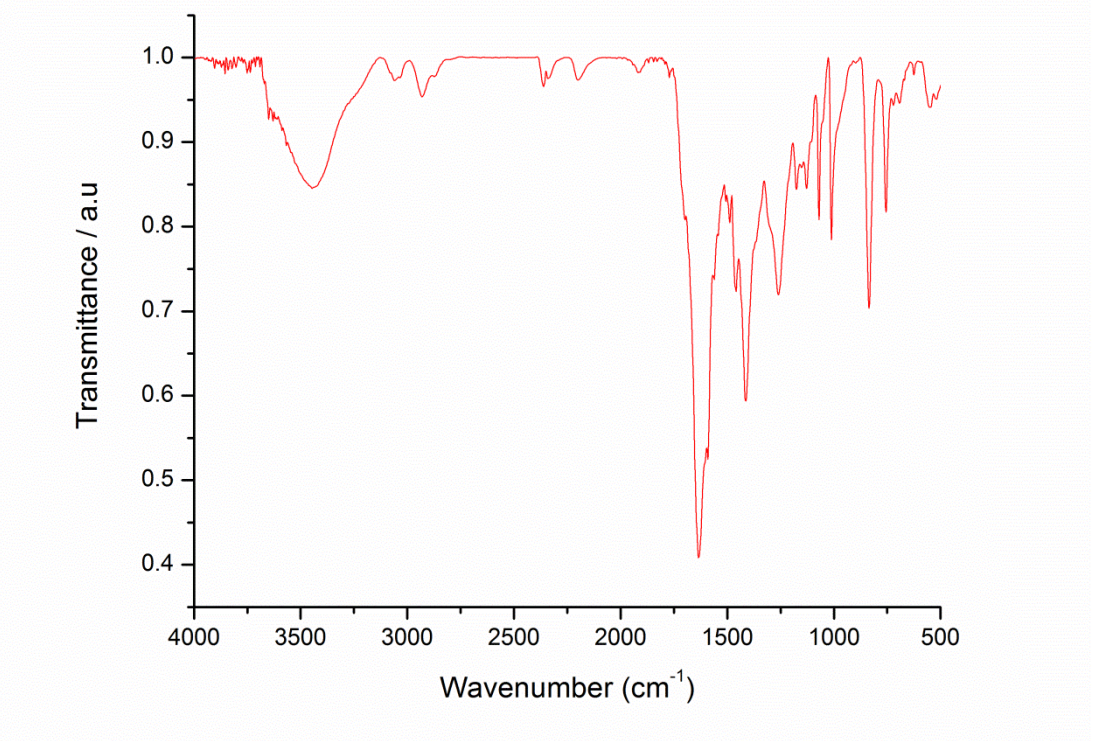

Figure 14: FTIR of the **OCF** formed by Sonogashira cross-coupling of **RC1a** and 1,4-diethynylbenzene.

CHN analysis was again inaccurate, with the largest discrepancy between carbon percentages (Table 4). This could be due to the presence of heavy metals remaining from the Sonogashira coupling reaction (Pd or Cu) or incomplete polymerisation resulting in C-Br end groups, as suggested by FTIR above. CHN results could also be inaccurate due to adsorbed water or gases.[6,7,23] Again theoretical results were based on calculations for 100 % reaction.

Sample	Theo. C %	Theo. H %	Theo. N %	Exp. C %	Exp. H %	Exp. N %
OCF	82.13	5.43	5.81	61.48	3.55	4.07

Table 4: CHN analysis for the **OCF** formed by Sonogashira cross-coupling of **RC1a** and 1,4-diethynylbenzene.

SEM/EDX was collected by Dr. T. Hasell for the **OCF**. EDX analysis this time did indicate the presence of bromine as 6.66 wt. % of the sample, further pointing to an incomplete reaction (Figure 15). Residues of palladium and copper are also present in EDX analysis, which would also contribute to CHN results.

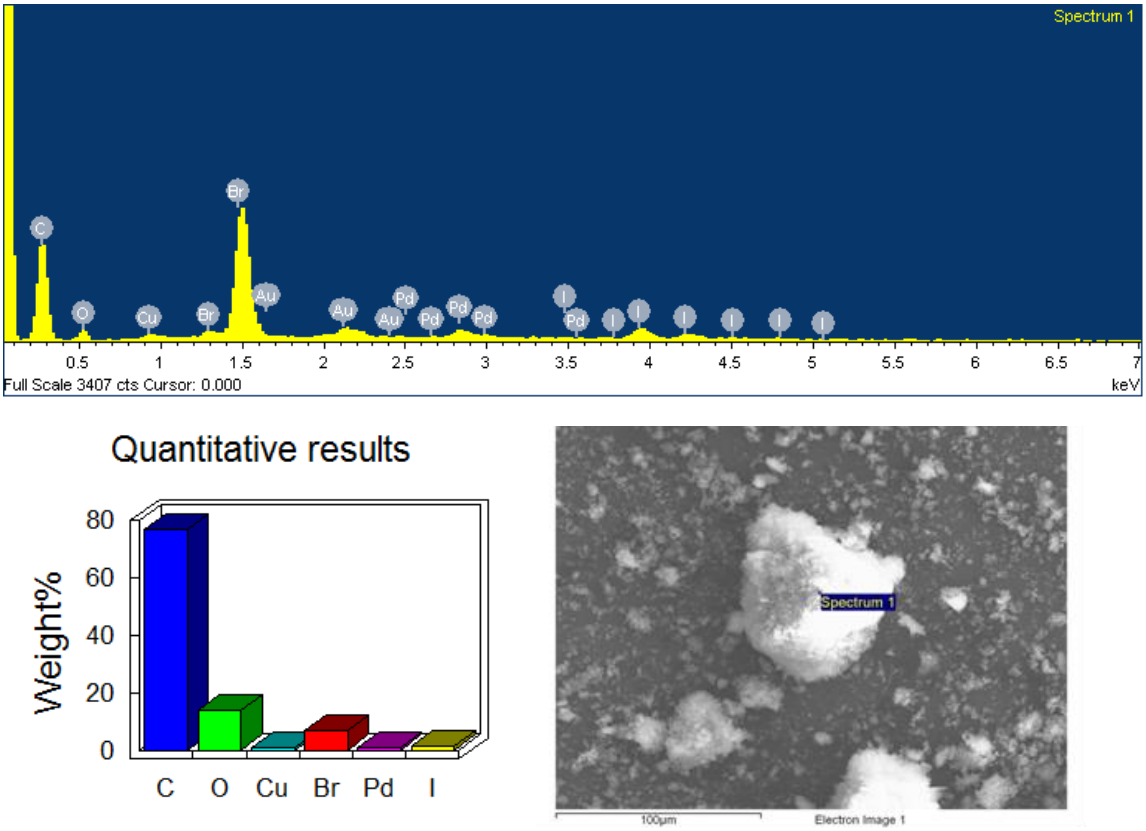

Figure 15: EDX Analysis of **OCF**

This **OCF** was analysed using nitrogen gas at 77 K and showed a type IV isotherm with hysteresis (Figure 16). From the isotherm it was possible to calculate a N_2 SA_{BET} = 150 m^2/g, with a maximum uptake of 6.03 mmol/g at 1 bar (and pore size distribution of 14.9 Å, calculated using a pillared clay model as this has been widely applied previously[7,23,24]). This maximum uptake of N_2 was significantly higher than the polymerized [2+3] bromine cages shown by Jin *et al.*[2]

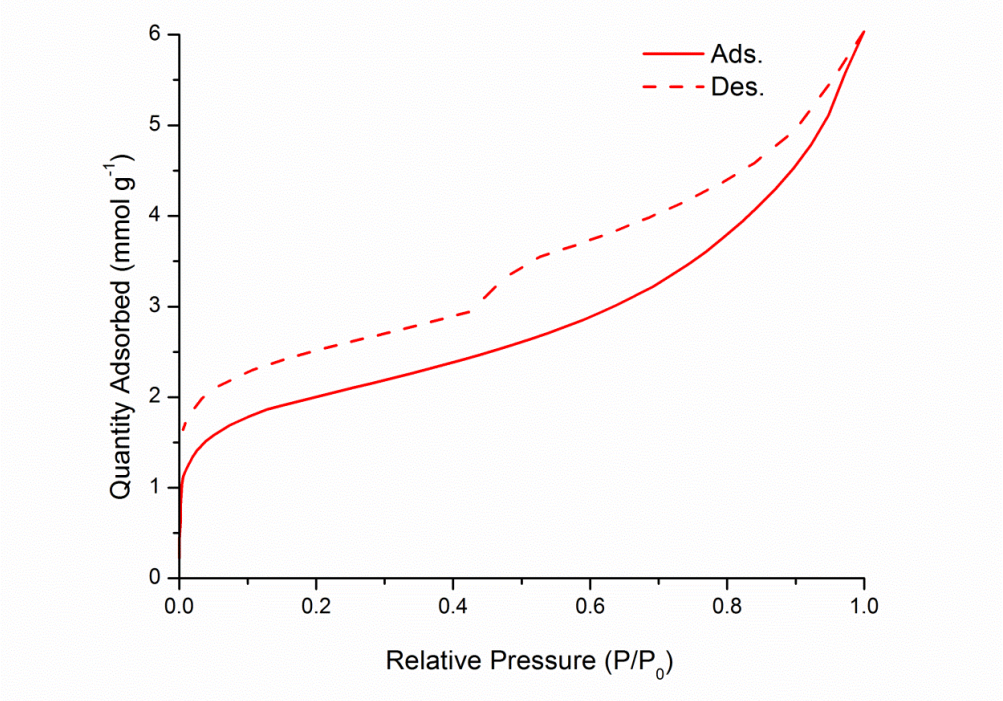

Figure 16: N_2 isotherm for the **OCF**.

The network also showed a maximum H_2 uptake of 1.87 mmol/g at 1.13 bar. (Figure 17)

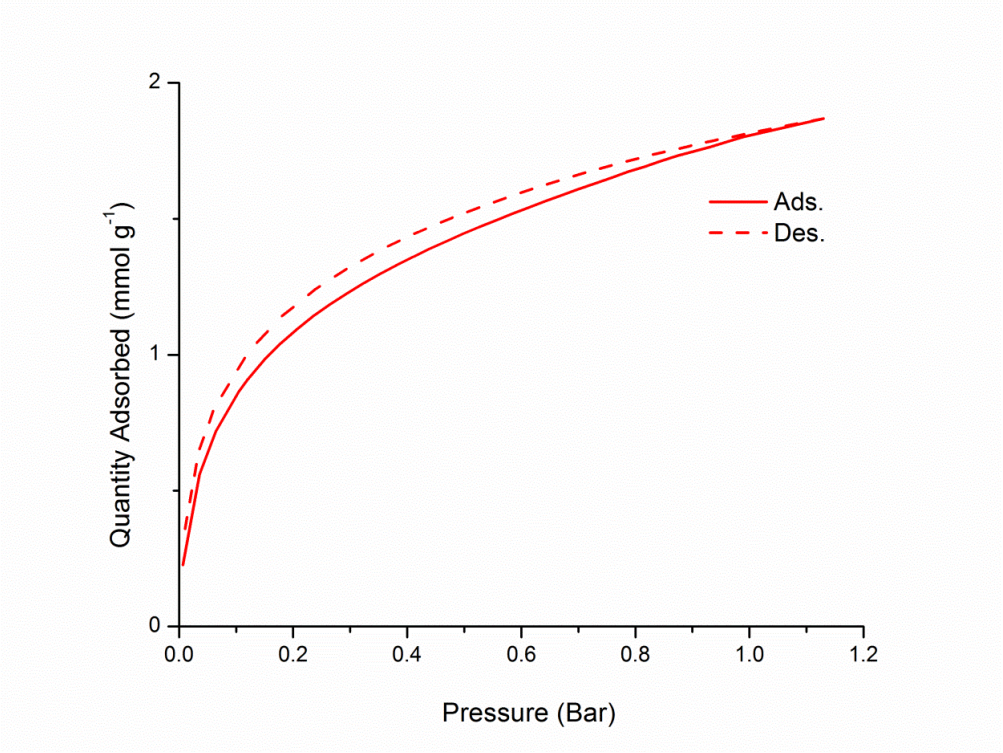

Figure 17: H_2 isotherm for the **OCF**.

As with the **CAF-1** sample, the N_2 SA_{BET} were not comparable to those generated from an 8-armed POSS-centred material.[3] Again, we hypothesise this is due to a much more flexible inner core and overcrowding of the periphery of the cage, preventing complete reaction (as suggested by high yield and remaining C-Br bands in FTIR combined with appearance of bromine in EDX analysis).

5.2.3 Hyper Cross-linked Polymers

Hyper cross-linked polymers (HCPs) are a diverse range of organic polymers created by Friedel-Crafts alkylation reaction with the use of a Lewis acid such as iron(III) chloride.[25-28] Wood *et al.* have reported HCPs with N_2 SA_{BET} surface areas up to 1904 m^2/g at 77 K (BCMP:DCX in 3:1 ratio) and H_2 uptake of 1.69 wt. % at 1.13 bar and 77 K (pDCX).[29] Li *et al.* have recently used a modified version of this technique with use of a small bi-fuctional cross-linker formaldehyde dimethyl acetal (FDA, eliminating the need for chloromethyl groups as seen in previous examples) to produce HCPs from seemingly non-functional monomers (including benzene).[10]

$FeCl_3$ (or sometimes $AlCl_3$) acts as a Lewis Acid in Friedel-Crafts alkylations, removing a halogen leaving group from the alkyl chain, releasing it as a cation for electrophilic addition (to an aromatic ring).[30] Unlike in standard Friedel-Crafts alkylation reactions, however, Li *et al.* do not have an alkyl halide in this instance.[10] This results in methoxy groups being removed from FDA (which are not as electronegative as chloride ions) meaning that while HCl is still evolved, $FeCl_3$ will eventually become "poisoned" with methoxy groups when chloride anions preferentially remove hydrogen to complete addition. Li *et al.* counteracted this by employing an equivalent amount of $FeCl_3$ per benzene ring. The process is then repeated until we see electrophilic addition of the same original molecule on to another aromatic ring, 'knitting' the aromatic rings together (Figure 18).

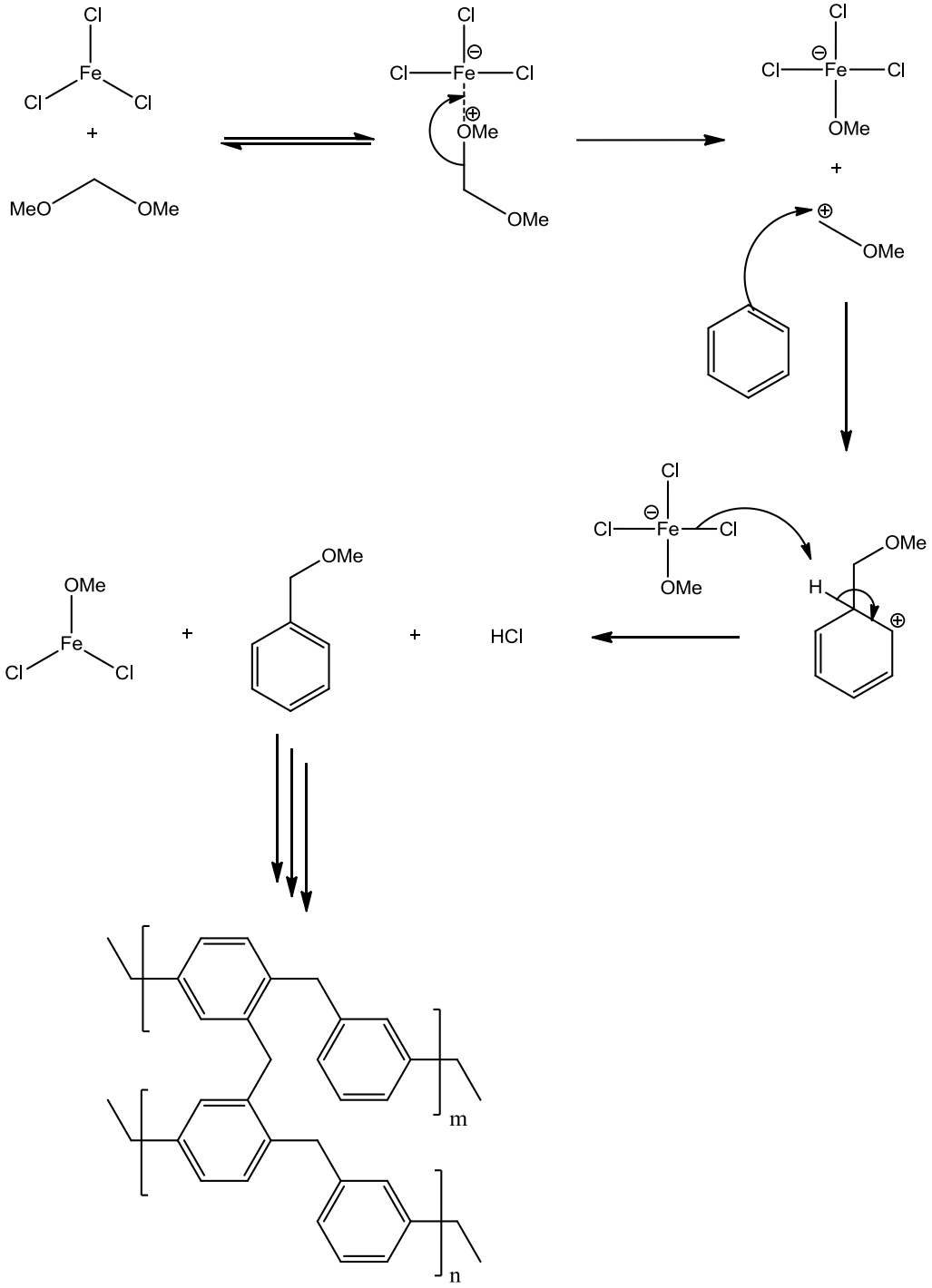

Figure 18: Friedel-Crafts alkylation of benzene (adapted from references).[10,31]

Using **RC1b** as a monomer, we aimed to polymerise the functionalised cage using iron (III) chloride and formaldehyde dimethyl acetal in a similar fashion to that detailed by Li *et al*.[10] The reaction was expected to produce cage hyper-crosslinked polymers (**Cage-HCP**) without the need for halogenated aromatic functional groups

found in other reactions used for the production of porous polymers. These **Cage-HCPs** are linked together by CH_2 bridges between the aromatic groups utilising Friedel-Crafts alkylation (Figure 19).

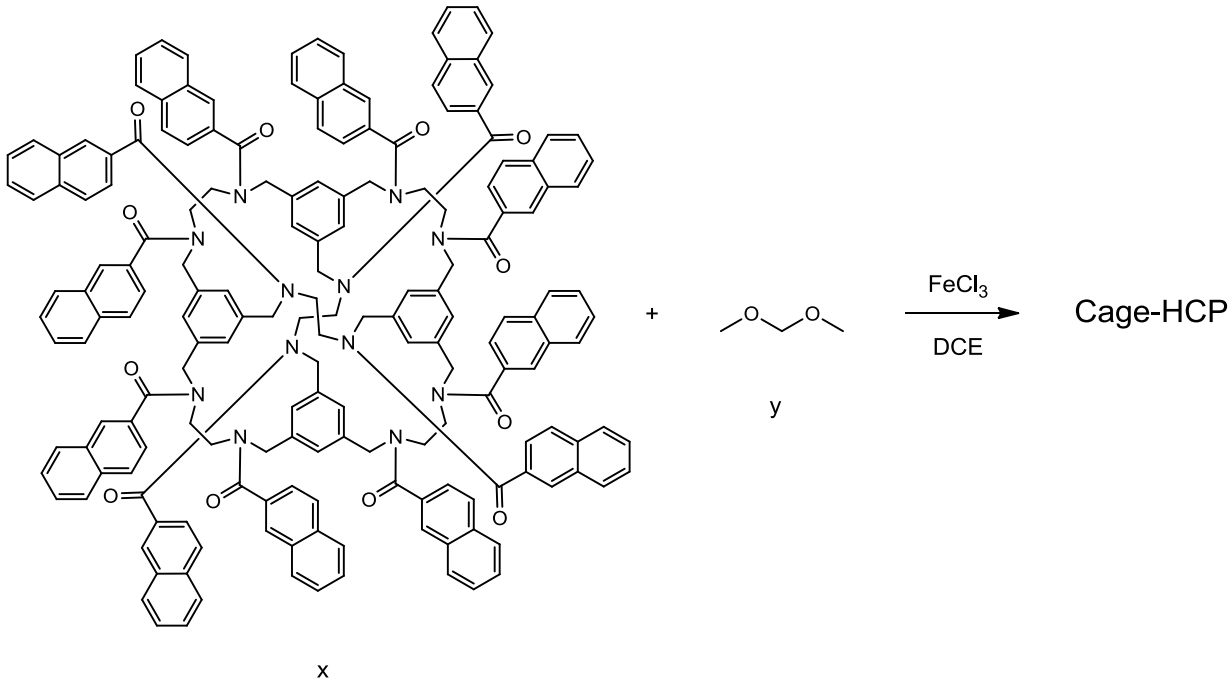

Figure 19: Hyper cross-linking of **RC1b** and FDA by a "knitting" route (x and y are variable).

The reaction was run in parallel three times with increasing varying ratios of monomer, linker and catalyst (1:24:24, 1:48:48 and 1:72:72 respectively, Table 5). Higher ratios were used in comparison with the article by Li *et al.*[10] as naphthoyl groups possessed more C=C bonds and therefore more possibilities for electrophilic addition in Friedel-Crafts alkylation. As each cage possessed 12 pendant groups, ratios of monomer, linker and catalyst could be considered as 1:2:2, 1:4:4 and 1:6:6 in a simplified form. All three reactions returned an insoluble, amorphous brown polymeric network.

Sample	RC1b	FDA	$FeCl_3$	Molar Ratio (RC1b : FDA : $FeCl_3$)
Cage-HCP-1	200 mg (0.075 mmol)	159 uL (1.78 mmol)	292 mg (1.78 mmol)	1 : 24 : 24
Cage-HCP-2	200 mg (0.075 mmol)	318 uL (3.59 mmol)	584 mg (3.59 mmol)	1 : 48 : 48
Cage-HCP-3	200 mg (0.075 mmol)	478 uL (5.40 mmol)	876 mg (5.40 mmol)	1 : 72 : 72

Table 5: Ratio of monomer, cross-linker and catalyst.

FTIR of **Cage-HCP-1, 2** and **3** contained a very strong characteristic amide C=O band at ~1650 cm^{-1} from the pendant arm on the **RC1a**. C-N are apparent at ~1250 cm^{-1} while C=C are at 1370 cm^{-1} (Figure 20).

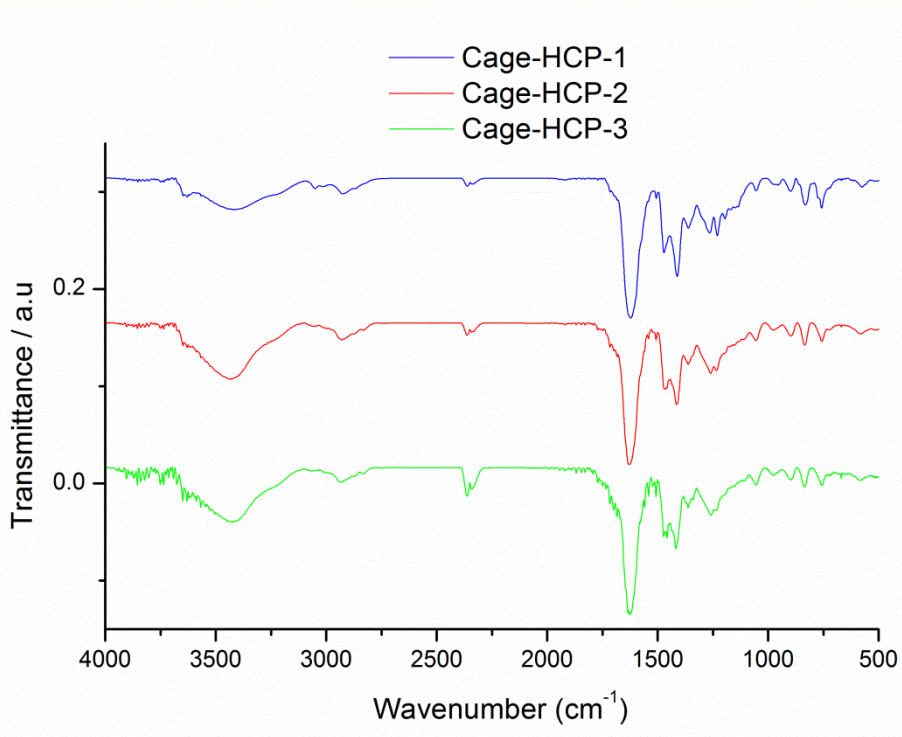

Figure 20: FTIR of **Cage-CHP-1, 2** and **3**.

While not exact, CHN analysis did show the correct trend for percentage of nitrogen in each **Cage-HCP**, with a lower percentage apparent as more FDA cross-linker was

included (while carbon and hydrogen increased, Table 6). CHN results were based on 100 % reaction with respective ratios of FDA cross-linker.

Sample	Theo. C %	Theo. H %	Theo. N %	Exp. C %	Exp. H %	Exp. N %
Cage-HCP-1	81.57	6.44	5.60	73.43	5.05	5.17
Cage-HCP-2	81.98	7.24	5.03	71.85	4.84	4.81
Cage-HCP-3	82.31	7.89	4.57	70.70	4.88	4.72

Table 6: CHN Analysis of **Cage-HCP-1, 2** and **3**.

Unfortunately, all samples appeared non-porous to N_2, with maximum uptakes of 0.37, 0.66 and 0.70 mmol/g for **Cage-HCP-1, 2** and **3** respectively at a maximum pressure of 1 bar. Conversely, reasonable H_2 uptake was observed for both **2** and **3** of around 3.09 mmol/g at a pressure of 1.13 bar, while uptake for **Cage-HCP-1** was markedly less at 0.77 mmol/g (Table 7). This data shows that **RC1b** polymerised by Friedel-Crafts alkylation created a network with selective uptake of H_2 over N_2 (4.5:1 at 1 bar for **Cage-HCP-2** and 4.2:1 at 1 bar for **Cage-HCP-3**).

Sample	N_2 Uptake (mmol/g)*	N_2 SA_{BET} (m^2/g)	H_2 Uptake (mmol/g)**	H_2 $SA_{Langmuir}$ (m^2/g)
Cage-HCP-1	0.37	9	0.77	37
Cage-HCP-2	0.66	12	3.09	194
Cage-HCP-3	0.70	13	3.04	189

Table 7: H_2 and N_2 uptakes and calculated surface areas of **Cage-HCP-4**, **5**, **6** and **7**. *N_2 maximum uptake at 1 bar. **H_2 maximum uptake at 1.13 bar.

Cage-HCP-1, 2 and **3** N_2 isotherms were all type I and essentially non-porous (Figure 21).

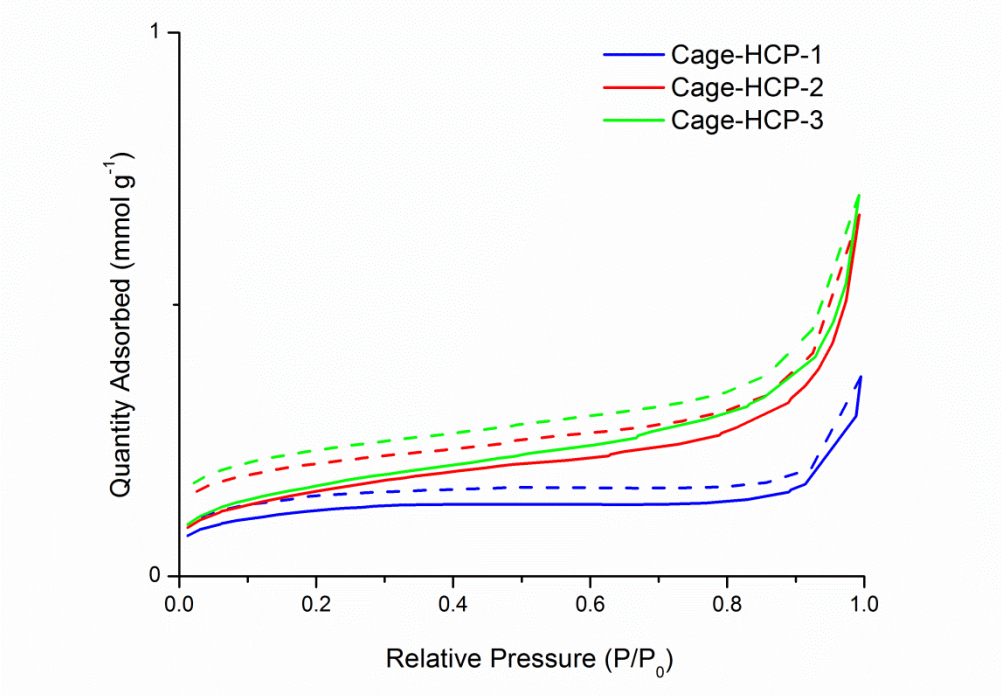

Figure 21: N_2 isotherms for **Cage-HCP-1, 2** and **3**.

Cage-HCP-1, 2 and **3** H_2 isotherms were again all Type I, though this time porosity was observed (Figure 22). The H_2 uptakes measured for **Cage-HCP-2** and **Cage-HCP-3** are higher than that observed in **CAF-1** (1.92 mmol/g) and the **OCF** (1.87 mmol/g). **Cage-HCP-2** and **Cage-HCP-3** were almost identical in uptake, indicating that saturation of FDA and $FeCl_3$ had already been reached in the second reaction.

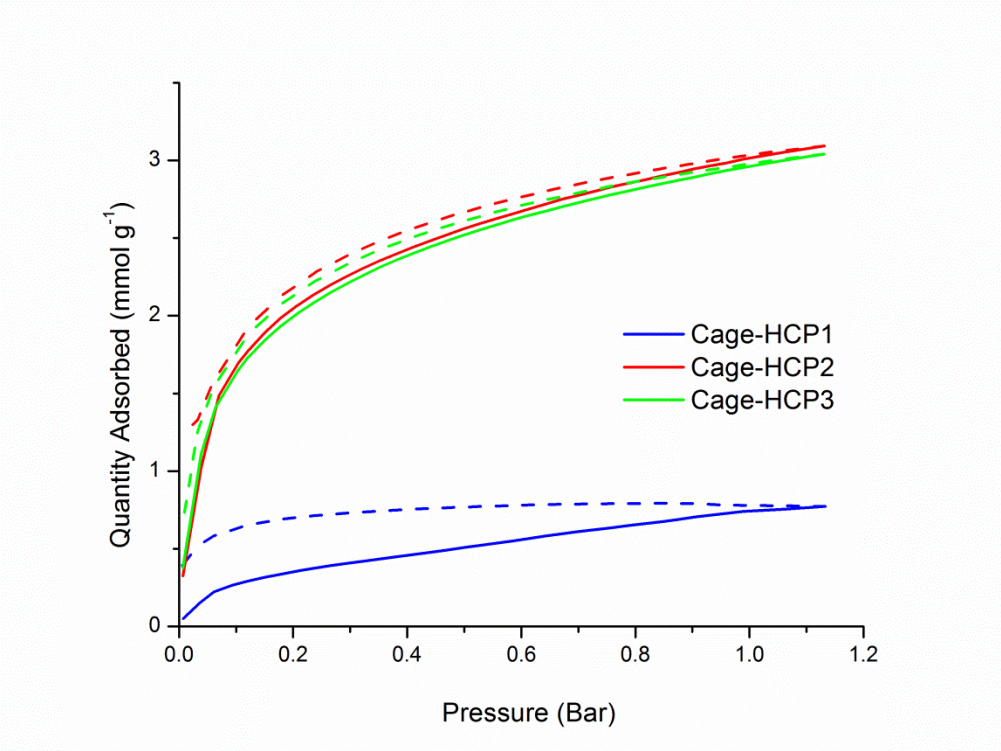

Figure 22: H_2 isotherms for **Cage-HCP-1, 2** and **3**.

The reaction was repeated with the introduction of benzene as a second monomer, in an attempt to increase porosity (Figure 23). Benzene was selected due to previously producing networks with N_2 SA_{BET} up to 1391 m^2/g at 77 K (benzene with three equivalents of FDA)[10].

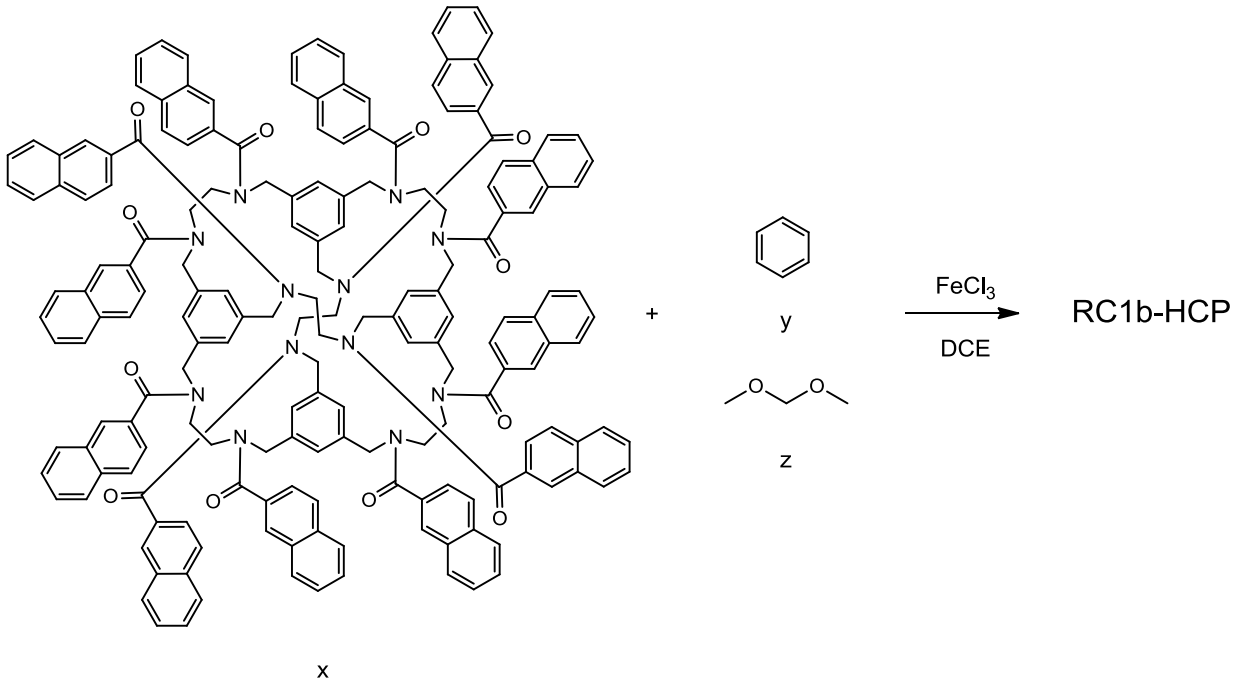

Figure 23: Hyper cross-linking by copolymerisation of **RC1b**, benzene and FDA (x, y and z are variable).

The experiment was run in parallel 4 times, increasing the amount of benzene comonomer while relatively balancing cross-linker and catalyst (Table 8).

Sample	**RC1b**	**Benzene**	**FDA**	**$FeCl_3$**	**Molar Ratio (RC1b : FDA : $FeCl_3$: Benzene)**
Cage-HCP-4	320 mg (0.12 mmol)	32 uL (0.47 mmol)	605 uL (6.84 mmol)	1109 mg (6.84 mmol)	1 : 3.9 : 57 : 57
Cage-HCP-5	240 mg (0.09 mmol)	64 uL (0.94 mmol)	573 uL (6.48 mmol)	1051 mg (6.48 mmol)	1 : 10.4 :72 : 72
Cage-HCP-6	160 mg (0.06 mmol)	96 uL (1.41 mmol)	541 uL (6.12 mmol)	992 mg (6.12 mmol)	1 : 23.4 : 102 : 102
Cage-HCP-7	80 mg (0.03 mmol)	128 uL (1.87 mmol)	510 uL (5.76 mmol)	934 mg (5.76 mmol)	1 : 62.5 :192 : 192

Table 8: Ratios of monomers (**RC1b** and benzene), cross-linker and catalyst.

FTIR of **Cage-HCP-4, 5, 6** and **7** again contained a very strong characteristic amide C=O band at ~1650 cm^{-1} from the pendant arm on the **RC1a**. C-N are apparent at ~1250 cm^{-1} while C=C are at 1370 cm^{-1} (Figure 24).

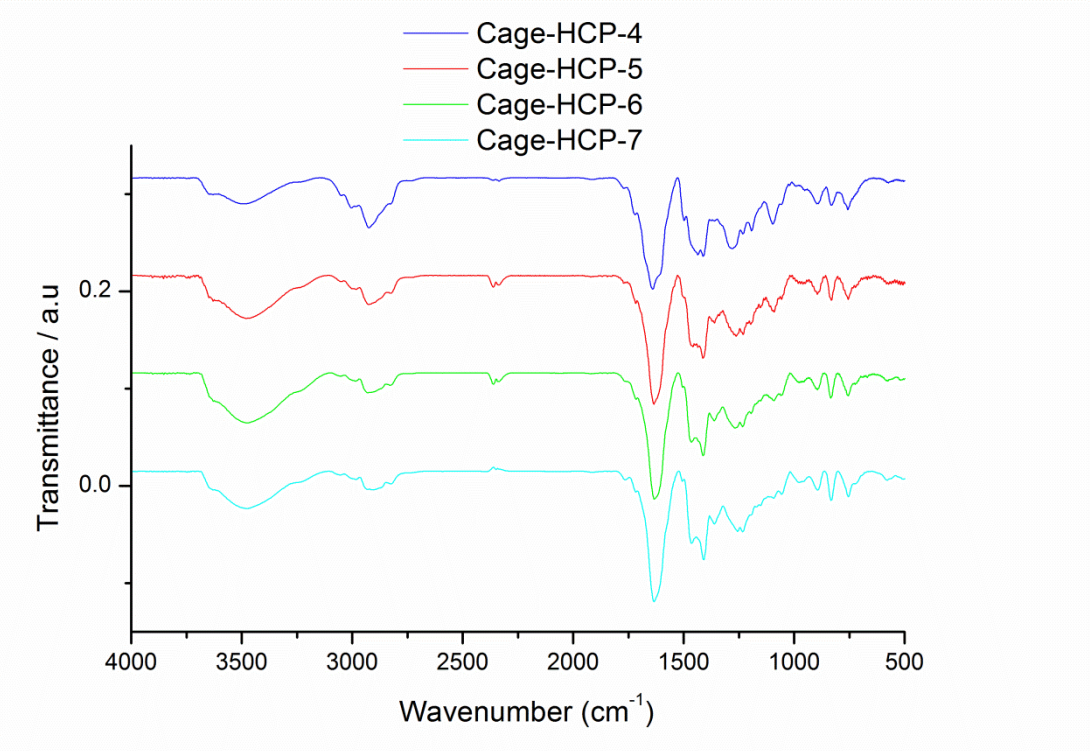

Figure 24: FTIR of **Cage-HCP-4, 5, 6** and **7**.

All four samples were amorphous by pXRD, with presence of **RC1b** in the networks confirmed by detection of nitrogen in CHN analysis. Again, a clear trend can be observed in nitrogen content. As fewer decorated cages are present in the reaction comparatively to benzene, so is the percentage of nitrogen (Table 9). Theoretical CHN analysis percentages were this time calculated based on 100 % complete reaction with regards to ratio of decorated cage, benzene and FDA cross-linker. Networks were all light brown in colour, with a darker brown observed for reactions with a higher relative amount of **RC1b**.

Sample	Theo. C %	Theo. H %	Theo. N %	Exp. C %	Exp. H %	Exp. N %
Cage-HCP-4	82.63	6.00	5.44	74.18	5.38	4.45
Cage-HCP-5	83.75	6.60	4.51	75.75	5.28	3.88
Cage-HCP-6	85.57	7.38	3.29	76.71	5.23	2.97
Cage-HCP-7	87.78	8.33	1.82	80.95	5.25	1.81

Table 9: CHN Analysis of **Cage-HCP-4, 5, 6** and **7**.

On introduction of benzene, all networks produced were porous to both N_2 and H_2. An obvious trend is apparent in both N_2 and H_2 data, with uptake of both hydrogen and nitrogen increasing as the ratio of benzene to **RC1b** is increased (Table 10). The only exception to this trend occurred in nitrogen uptake; where **Cage-HCP-6** interestingly had a lower maximum uptake of nitrogen (14.32 mmol/g) than **Cage-HCP-5** (17.11 mmol/g) but still showed a higher N_2 SA_{BET} (658 m^2/g for **Cage-HCP-6** compared to 554 m^2/g for **Cage-HCP-5**).

Sample	N_2 Uptake (mmol/g)*	N_2 SA_{BET} (m^2/g)	H_2 Uptake (mmol/g)**	H_2 $SA_{Langmuir}$ (m^2/g)
Cage-HCP-4	8.29	324	3.55	216
Cage-HCP-5	17.11	554	4.24	264
Cage-HCP-6	14.32	658	4.67	290
Cage-HCP-7	21.70	954	5.88	395

Table 10: H_2 and N_2 uptakes and calculated surface areas of **Cage-HCP-4, 5, 6** and **7**. *N_2 maximum uptake at 1 bar. **H_2 maximum uptake at 1.13 bar.

The N_2 isotherms were all type II with a H2 hysteresis, with uptake between 8.29 and 21.70 mmol/g (Figure 25).

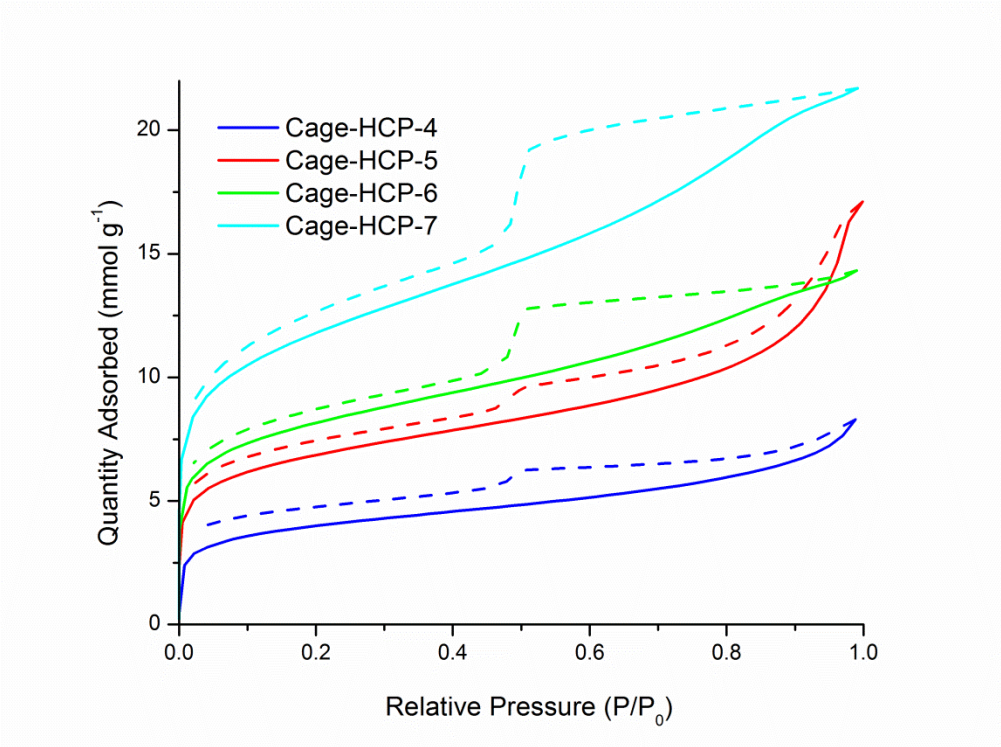

Figure 25: N_2 isotherms for **Cage-HCP-4, 5, 6** and **7**.

The H_2 isotherms were all Type I, with maximum uptake between 3.55 and 5.88 mmol/g at 1.13 bar (Figure 26).

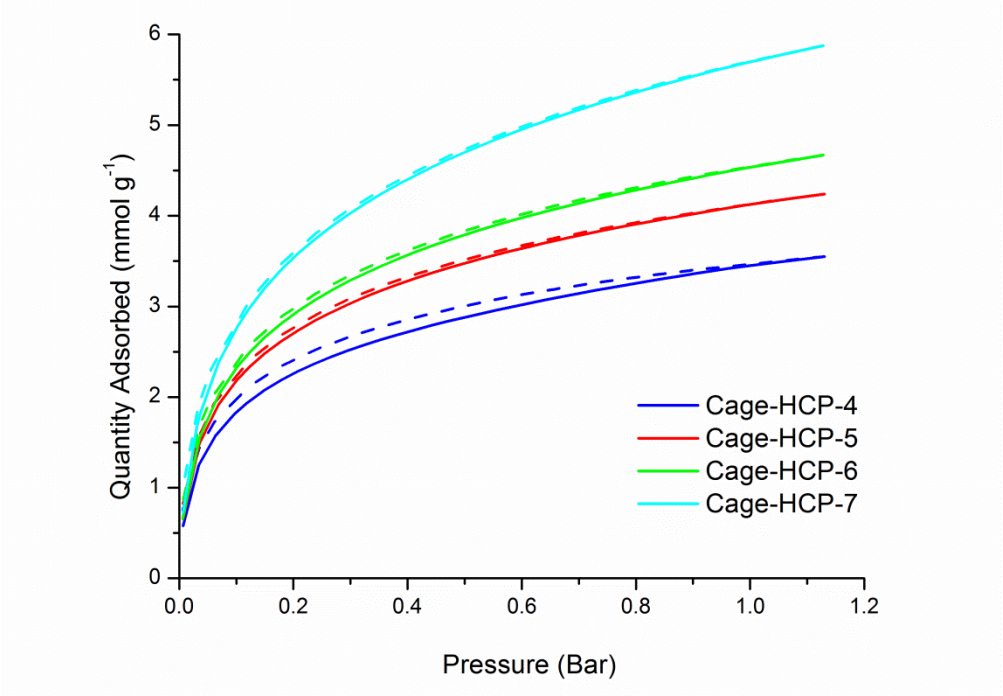

Figure 26: H_2 isotherms for **Cage-HCP-4, 5, 6** and **7**.

PSD for **Cage-CHP-4, 5, 6** and **7** was also calculated, again utilising a pillared clay model. All samples appeared to contain pores of around 10 and 17 Å in diameter (Figure 27).

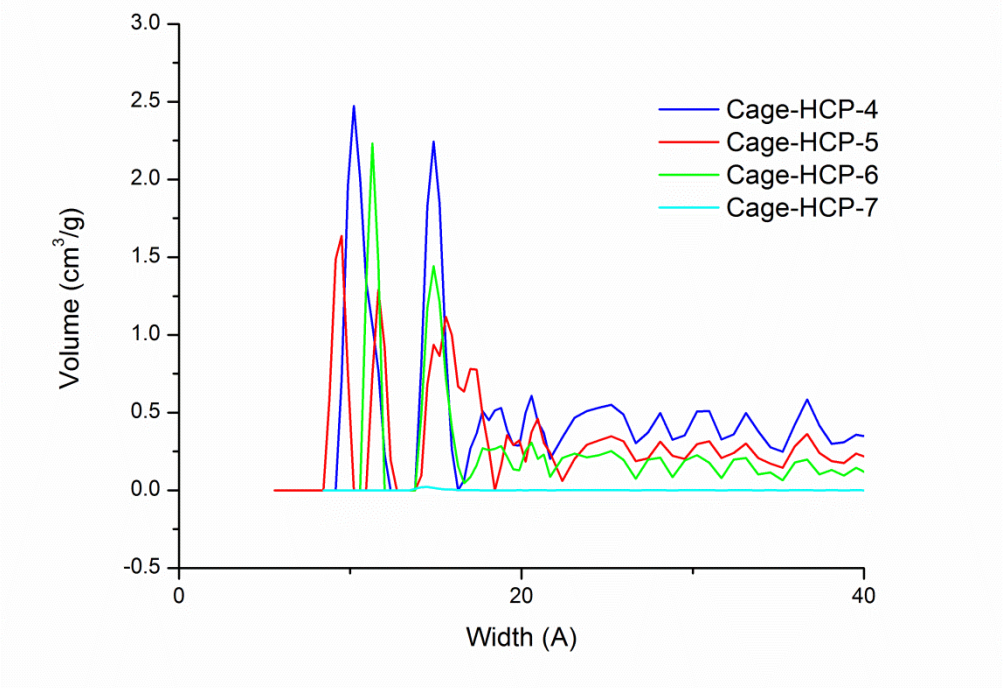

Figure 27: PSD for **Cage-HCP-4, 5, 6** and **7**.

5.3 Conclusions

RC1 was successfully polymerised by step growth polycondensation with a variety of bi-functional acid chlorides to create porous polymers with modest porosity. Nitrogen uptake of up to 8.80 mmol/g and hydrogen uptake of up to 1.96 mmol/g were measured (**RC1-2**, N_2 SA_{BET} = 106 m^2/g) for rigid acid chloride linkers, while flexible linkers returned insoluble non-porous materials. This reaction is ripe for repetition with aa lower amount of **RC1**, as it is likely a step-growth polymerisation and gelating.

The amide-decorated cages **RC1a** and **RC1b** were reacted further to produce cage polymers which were achieved *via* two distinctive methods. Yamamoto homo-coupling of **RC1a** yielded **CAF-1** with N_2 SA_{BET} = 37 m^2/g (maximum N_2 uptake of 2.72 mmol/g at 1 bar and H_2 uptake of 1.92 mmol/g at 1.13 bar). Sonogashira coupling of **RC1a** and 1,4-diethynyl benzene yielded an **OCF** N_2 SA_{BET} = 150 m^2 (maximum uptake of 6.03 mmol/g at 1 bar and H_2 uptake of 1.87 mmol/g at 1.13 bar). Yields and FTIR data combined suggested that the reaction was not reaching completion, with positive yields suggesting retention of heavy atoms (Br) and FTIR including C-Br stretches. This is likely due to overcrowding of the peripheral of the cage molecule with bromophenyl arms preventing reaction completion.

RC1b was successfully polymerised through a 'molecular knitting' approach to yield a **Cage-HCP** with no nitrogen sorption (N_2 SA_{BET} = 12 m^2/g and uptake of 0.66 mmol/g at 1 bar) but with selective H_2 uptake of 4.5:1 (H_2 $SA_{Langmuir}$ = 194 and uptake of 3.09 mmol/g) (4.5:1). When the same reaction was repeated with the introduction of benzene as a comonomer, networks with N_2 SA_{BET} between 324-954 m^2/g (maximum uptake between 8.29 and 21.70 mmol/g at 1 bar) were achieved. H_2 $SA_{Langmuir}$ between 216-395 m^2/g (maximum uptake between 3.55 and 5.88 mmol/g at 1.13 bar) were also observed on inclusion of benzene as a second monomer.

5.3 Experimental

Materials. All chemicals were purchased from Sigma-Aldrich and used as received.

Biphenyl-4,4'-dicarbonoyl chloride: Biphenyl-4,4'-dicarboxylic acid (500 mg, 2.064 mmol) was suspended in dichloromethane (30 mL, anhydrous) in a 250 mL round bottom flask equipped with a stirrer bar, $CaCl_2$ drying tube and a reflux condenser. Thionyl chloride (1.5 mL, 20.642 mmol) and DMF (400 µL, 5.166 mmol) were added to the white suspension and left stirring for 1 hour at room temperature. The reaction was then heated at reflux (oil bath 60 °C) for 4 hours where a homogenous solution developed. After another hour at reflux, reaction was removed from heat and allowed to cool to room temperature before concentrating the yellow solution to dryness yielding a white precipitate. Toluene (100 mL, anhydrous) was added and evaporated to dryness once more before drying on high vacuum to yield biphenyl-4,4'-dicarbonoyl chloride in 94 % yield (541 mg). ^{1}H NMR ($CDCl_3$, 400 MHz) δ 8.28-8.26 (d, 2 H, -ArH), 7.81-7.79 (d, 2 H, -ArH).^{13}C NMR ($CDCl_3$, 100 MHz) δ 168.0, 145.8, 133.2, 132.0, 128.0 ppm.

Synthesis of Cage-bisacyl chlorides

RC1-4 (representative procedure): RC1 (200 mg, 0.245 mmol) was dissolved in $CHCl_3$ (20 mL) and added to a 100 mL 2-necked round bottom flask cooled in an ice bath. Triethylamine (246 µL, 1.762 mmol) was then added and the solution stirred for 15 minutes under N_2. Biphenyl-4,4'-dicarbonoyl chloride (430 mg, 1.542 mmol) was dissolved in $CHCl_3$ (10 mL) and added to the stirring solution slowly by pipette (white gas evolved and white precipitate formed) and the reaction mixture was left stirring for ~14 hrs. Reaction mixture was filtered under reduced pressure, washed with chloroform (30 mL), HCl (30 ml, 0.1 M) and water (30 mL). The crude was finally purified by soxhlet extraction with methanol for 24 hours to yield a **RC1-4** as a white powder (339 mg) in 64 % yield. CHN Calc. C: 76.72, H: 5.58, N: 8.13; found C: 70.67, H: 5.17, N: 6.53. IR (KBr pellet, ν) 3446 (m), 3025 (w), 2890 (w), 1784 (w), 1710 (m), 1627 (s), 1606 (s), 1461 (m), 1415 (m), 1257 (m), 1174 (w), 1128 (w), 1004 (w), 833 (m), 757 (m) cm^{-1}.

RC1-1

51 mg in 16 % yield. CHN Calc. C: 64.43, H: 7.32, N: 12.72; found C: 51.18, H: 6.54, N: 9.60. IR (KBr pellet, ν) 3456 (s), 3436 (s), 2956 (w), 2922 (w), 2850 (w), 2823 (w), 1633 (s), 1560 (m), 1475(m), 1421 (m), 1263 (w), 1172 (w), 1163 (w) cm^{-1}.

RC1-2

163 mg in 45 % yield. CHN Calc. C: 67.71, H: 8.12, N: 11.28; found C: 60.30, H: 7.64, N: 10.12. IR (KBr pellet, ν) 3469 (m), 3448 (m), 2941 (w), 1720 (w), 1633 (s), 1440 (m), 1419 (m), 1355 (w), 1218 (w), 1170 (w), 1161 (w) cm^{-1}.

RC1-3

298 mg in 67 % yield. CHN Calc. C: 71.62, H: 6.01, N: 10.44; found C: 62.40, H: 5.79, N: 8.36. IR (KBr pellet, ν) 3444 (m), 2940 (w), 2920 (w), 1627 (s), 1550 (w), 1510 (w), 1461 (m), 1421 (m), 1390 (w), 1379 (w), 1269 (w), 1151 (w) cm^{-1}.

Synthesis of CAF-1

CAF-1: Using a glove bag, $Ni(COD)_2$ (714 mg, 2.594 mmol) and 2,2'-bipyridyl (405 mg, 2.594 mmol) were weighed into an oven dried 100 mL 2-necked round bottom flask equipped with a stirrer bar. Anhydrous DMF (60 mL) was added to give a black/purple slurry and 1,5-cyclooctadiene (325 µL, 2.638 mmol) added. The solution was heated at 80 °C with stirring under N_2 for 1 hr. **RC1a** (500 mg, 0.166 mmol) was added *via* side-neck with some DMF (~2 mL) washing, before leaving the reaction stirring. After 3 days, the reaction was removed from heat and allowed to cool to room temperature before adding HCl (15 mL, 36 %) to the black/purple solution and left stirring for a further hour, during which time the solution paled to a grey and finally green colour. The mixture was filtered under reduced pressure and washed with water (100 mL), chloroform (100 mL), THF (100 mL) and water (100 mL) once more to yield a white powder. The crude was purified by soxhlet extraction with chloroform for 24 hrs before drying in a vacuum oven to yield **CAF-1** as an off-white solid (478 mg) in 140 % yield. CHN Calc. C: 76.72, H: 5.85, N: 8.13; found C: 70.03, H: 5.80, N: 7.54. IR (KBr pellet, ν) 3444 (m), 3057 (w), 3031 (w), 2935 (w), 1699 (w), 1627 (s), 1541 (w), 1498 (w), 1463 (m), 1417 (m), 1375 (w), 1363 (w), 1265 (w), 1132 (w), 835 (w), 759 (w) cm^{-1}.

Synthesis of OCF

OCF: RC1a (282 mg, 0.094 mmol) and 1,4-diethynylbenzene (106 mg, 0.842 mmol) were weighed into a 100 mL 2-necked round bottom flask equipped with a stirrer bar and backfilled with N_2 three times. DMF (1.5 mL) and triethylamine (1.5 mL) were added and the solution heated to 100 °C internally with stirring. $Pd(PPh_3)_4$

(50 mg, 0.004 mmol) and CuI (16 mg, 0.008 mmol) were weighed into a sample vial and suspended in DMF (1.5 mL) before adding to stirring solution of **RC1a** and 1,4-diethynylbenzene. A brown precipitate formed almost immediately and the reaction was left stirring overnight. The reaction was removed from heat and allowed to cool to RT and DMF (20 mL) was added before filtering under reduced pressure. The flask was washed twice more with DMF (2x 20 mL) and washed over filter cake before purification by soxhlet extractor with MeOH for 24 hours to yield **OCF** as a brown powder (346 mg) in 132 % yield. CHN Calc. C: 82.13, H: 5.43, N: 5.81; found C: 61.48, H: 3.55, N: 4.07. IR (KBr pellet, ν) 3446 (w), 3050 (w), 2802 (w), 2206 (w), 1699 (w), 1635 (s), 1519 (m), 1560 (w), 1542 (w), 1488 (w), 1458 (w), 1413 (m), 1261 (w), 1176 (w), 1154 (w), 1128 (w), 1070 (w), 1012 (w), 835 (m), 756 (w) cm^{-1}.

Synthesis of Cage-HCP

Cage-HCP-1 (representative procedure): RC1b (200 mg, 0.075 mmol) was added into a 50 mL 2-necked round bottom flask equipped with a stirrer bar followed by dichloroethane (5 mL). Formaldehyde dimethyl acetal (159 uL, 1.788 mmol) was added by pipette and reaction mixture stirred at 400 RPM under N_2. Iron (III) chloride (292 mg, 1.788 mmol) was added to the clear solution giving a brown colour. Temperature was set to 80 °C internally and left stirring for 24 hrs. Reaction was removed from heat and allowed to cool to room temperature, before addition of methanol (20 mL) and filtration of reaction slurry under reduced pressure. Light brown precipitate was afforded which was further washed with methanol (20 mL) before purification by soxhlet extraction overnight. The precipitate was slurried in chloroform (50 mL), filtered and dried under vacuum to yield **Cage-HCP-1**as a light brown powder (117 mg) in 52 % yield. CHN Calc. C: 81.57, H: 6.44, N: 5.60; found C: 73.43, H: 5.05, N: 5.17. (KBr pellet, ν) 3409 (w), 3040 (w), 2925 (w), 1622 (s), 1471 (m), 1411 (m), 1361 (w), 1265 (w), 1230 (w), 1195 (w), 1170 (w), 1149 (w), 1136 (w), 861 (w), 757 (w) cm^{-1}.

Cage-HCP-2

189 mg in 77 % yield. CHN Calc. C: 81.98, H: 7.24, N: 5.03; found C: 71.85, H: 4.85, N: 4.81. (KBr pellet, ν) 3435 (w), 2948 (w), 2826 (w), 1627 (s), 1465 (m), 1459 (m), 1413 (m), 1361 (w), 1259 (w), 1234 (w), 849 (w), 752 (w) cm^{-1}.

Cage-HCP-3

192 mg in 71 % yield. CHN Calc. C: 82.31, H: 7.89, N: 4.57; found C: 70.70, H: 4.88, N: 4.72. (KBr pellet, ν) 3421(w), 2945 (w), 2828 (w), 1635 (s), 1625 (s), 1577 (m), 1560 (m), 1473 (m), 1465 (m), 1458 (m), 1448 (w), 1436 (w), 1417 (w), 1370 (w), 1340 (w), 1259 (w), 1236 (w), 866 (w), 751 (w) cm^{-1}.

Cage-HCP-4

396 mg in 96 % yield. CHN Calc. C: 82.63, H: 6.00, N: 5.44; found C: 74.18, H: 5.38, N: 4.45. (KBr pellet, ν) 3625 (w), 3489 (w), 3003 (w), 2923 (m), 2827 (w), 1720 (w), 1639 (s), 1498 (w), 1436 (m), 1411 (m), 1280 (m), 1232 (w), 1193 (w), 1095 (w), 896 (w), 829 (w), 757 (w) cm^{-1}.

Cage-HCP-5

327 mg in 93 % yield. CHN Calc. C: 83.75, H: 6.60, N: 4.51; found C: 75.75, H: 5.28, N: 3.88. (KBr pellet, ν) 3629 (w), 3479 (w), 2995 (w), 2925 (m), 2820 (w), 1716 (w), 1635 (s), 1491 (m), 1432 (m), 1413 (m), 1371 (w), 1272 (m), 1263 (m), 1206 (w), 1099 (w), 822 (w), 755 (w) cm^{-1}.

Cage-HCP-6

317 mg in 108 % yield. CHN Calc. C: 85.57, H: 7.38, N: 3.29; found C: 76.71, H: 5.23, N: 2.97. (KBr pellet, ν) 3627 (w), 3477 (w), 3001 (w), 2920 (w), 2831 (w), 1716 (w), 1633 (s), 1463 (m), 1411 (m), 1361 (w), 1265 (w), 1234 (w), 1195 (w), 1094 (w), 835 (w), 759 (w) cm^{-1}.

Cage-HCP-7

244 mg in 104% yield. CHN Calc. C: 87.78, H: 8.33, N: 1.82; found C: 80.95, H: 5.25, N: 1.81. (KBr pellet, ν) 3631 (w), 3481 (w), 3005 (w), 2924 (w), 2836 (w), 1716 (w), 1635 (s), 1463 (m), 1409 (m), 1361 (w), 1255 (w), 1232 (w), 1195 (w), 1056 (w), 833 (w), 754 (w) cm^{-1}.

5.4 References

(1) Jin, Y.; Voss, B. A.; Jin, A.; Long, H.; Noble, R. D.; Zhang, W. *J. Am. Chem. Soc.* **2011**, *133*, 6650.

(2) Jin, Y.; Voss, B. A.; McCaffrey, R.; Baggett, C. T.; Noble, R. D.; Zhang, W. *Chem. Sci.* **2012**, *3*, 874.

(3) Chaikittisilp, W.; Sugawara, A.; Shimojima, A.; Okubo, T. *Chem. Eur. J.* **2010**, *16*, 6006.

(4) Chaikittisilp, W.; Sugawara, A.; Shimojima, A.; Okubo, T. *Chem. Mater.* **2010**, *22*, 4841.

(5) Pryor, K. E.; Shipps Jr, G. W.; Skyler, D. A.; Rebek Jr, J. *Tetrahedron* **1998**, *54*, 4107.

(6) Jiang, J.-X.; Su, F.; Trewin, A.; Wood, C. D.; Campbell, N. L.; Niu, H.; Dickinson, C.; Ganin, A. Y.; Rosseinsky, M. J.; Khimyak, Y. Z.; Cooper, A. I. *Angew. Chem. Int. Ed.* **2007**, *46*, 8574.

(7) Dawson, R.; Laybourn, A.; Khimyak, Y. Z.; Adams, D. J.; Cooper, A. I. *Macromolecules* **2010**, *43*, 8524.

(8) Ben, T.; Ren, H.; Ma, S.; Cao, D.; Lan, J.; Jing, X.; Wang, W.; Xu, J.; Deng, F.; Simmons, J. M.; Qiu, S.; Zhu, G. *Angew. Chem. Int. Ed.* **2009**, *48*, 9457.

(9) Yuan, D.; Lu, W.; Zhao, D.; Zhou, H.-C. *Adv. Mater.* **2011**, *23*, 3723.

(10) Li, B.; Gong, R.; Wang, W.; Huang, X.; Zhang, W.; Li, H.; Hu, C.; Tan, B. *Macromolecules* **2011**, *44*, 2410.

(11) Yamamoto, T. *Bull. Chem. Soc. Jpn.* **1999**, *72*, 621.

(12) Zhou, G.; Baumgarten, M.; Müllen, K. *J. Am. Chem. Soc.* **2007**, *129*, 12211.

(13) Jhaveri, S. B.; Carter, K. R. *Chem. Eur. J.* **2008**, *14*, 6845.

(14) Zhang, Z.-B.; Fujiki, M.; Tang, H.-Z.; Motonaga, M.; Torimitsu, K. *Macromolecules* **2002**, *35*, 1988.

(15) Kim, Y.-J.; Sato, R.; Maruyama, T.; Osakada, K.; Yamamoto, T. *J. Chem. Soc., Dalton Trans.* **1994**, 943.

(16) Yamamoto, T.; Abla, M. *J. Organomet. Chem.* **1997**, *535*, 209.

(17) Yamamoto, T.; Maruyama, T.; Zhou, Z.-H.; Ito, T.; Fukuda, T.; Yoneda, Y.; Begum, F.; Ikeda, T.; Sasaki, S. *J. Am. Chem. Soc.* **1994**, *116*, 4832.

(18) Yamamoto, T.; Wakabayashi, S.; Osakada, K. *J. Organomet. Chem.* **1992**, *428*, 223.

(19) Zhou, Z.-h.; Yamamoto, T. *J. Organomet. Chem.* **1991**, *414*, 119.

(20) Murakami, Y.; Yamamoto, T. *Inorg. Chem.* **1997**, *36*, 5682.

(21) Sonogashira, K.; Tohda, Y.; Hagihara, N. *Tetrahedron Lett.* **1975**, *16*, 4467.

(22) Chinchilla, R.; Nájera, C. *Chem. Rev.* **2007**, *107*, 874.

(23) Dawson, R.; Cooper, A. I.; Adams, D. J. *Prog. Polym. Sci.* **2012**, *37*, 530.

(24) Dawson, R.; Stockel, E.; Holst, J. R.; Adams, D. J.; Cooper, A. I. *Energy Environ. Sci.* **2011**, *4*, 4239.

(25) Lee, J.-Y.; Wood, C. D.; Bradshaw, D.; Rosseinsky, M. J.; Cooper, A. I. *Chem. Commun.* **2006**, 2670.

(26) Germain, J.; Hradil, J.; Fréchet, J. M. J.; Svec, F. *Chem. Mater.* **2006**, *18*, 4430.

(27) Ahn, J.-H.; Jang, J.-E.; Oh, C.-G.; Ihm, S.-K.; Cortez, J.; Sherrington, D. C. *Macromolecules* **2005**, *39*, 627.

(28) Fontanals, N.; Manesiotis, P.; Sherrington, D. C.; Cormack, P. A. G. *Adv. Mater.* **2008**, *20*, 1298.

(29) Wood, C. D.; Tan, B.; Trewin, A.; Niu, H.; Bradshaw, D.; Rosseinsky, M. J.; Khimyak, Y. Z.; Campbell, N. L.; Kirk, R.; Stöckel, E.; Cooper, A. I. *Chem. Mater.* **2007**, *19*, 2034.

(30) Clayden, J.; Greeves, N.; Warren, S.; Wothers, P. *Organic Chemistry*; Oxford University Press, 2001, 22, 553.

Chapter 6
Conclusions and Future Work

Table of Contents

6.0 Conclusions

6.0.1 New Porous Organic Cages

A new porous organic cage was successfully prepared, highlighting the importance of work-up techniques and displaying interesting properties related directly to polymorphism. The cage showed switchable porosity depending on work-up conditions, as seen with CC1, with selective H_2 uptake when amorphous and both N_2 and H_2 uptake when crystalline.[1] This is the opposite of other related studies for a porous organic cage (CC3) where surface area rose upon total amorphisation.[2] Maximum N_2 uptake of 13.53 mmol/g at 1 bar (N_2 SA_{BET} = 946 m²/g) and H_2 uptake of 7.73 mmol/g at 1.13 bar (H_2 $SA_{Langmuir}$ = 479 m²/g) was observed for the cage in its **CC12$^{\gamma}$** polymorph.

The method of recrystallisation was also shown to be extremely important. Slow diffusion of **CC12** in DCM with dioxane using a vial-in-vial technique yielded crystalline (and porous) **CC12$^{\gamma}$**. When the same solvent system was used in a high-throughput polymorphism study, utilising layering of directing solvent (dioxane) on top of a **CC12** solution (DCM), an amorphous (and non-porous) material was afforded.

CC12 was also successfully reduced to give a secondary amine. This cage was also catenated, as with the previous examples CC1, CC2, and CC4.[3] This is likely due to the relatively low steric bulk of the diamine compared to other cages which cannot catenate, such as CC3 which comprises bulky cyclohexane groups on its vertices, thus preventing interpenetration of cages.

Experimentation with length of diamine showed an influence on the size of cage produced, with an even number of carbons in the diamine (2, 4) resulting in [4+6] cages and an odd number of carbons in the diamine (3, 5) resulting in [2+3] cages. Diamines with larger carbon numbers, (6, 7), however, resulted in the formation of both [2+3] and [4+6] cages, suggesting that the two stoichiometries have similar formation energies. This is currently being investigated by Dr. K. E. Jelfs by computational approaches.

6.0.2 Reduction and Functionalisation of Organic Cages

Although porous organic cages were successfully reduced (**RC1** and **RC5**) and fully decorated to create a new class of amide-decorated cages, the ultimate goal of enhancing porosity was not achieved. All decorated cages were amorphous originally, and with the exception of **RC1b** were unable to retain crystallinity after recrystallisation. **RC1b**, however, retained chloroform in its solvate to around 150 °C, but still showed limited gas uptake.

Other properties, such as melting point, were lowered to as low as 45 °C through addition of aliphatic acid chlorides. These melting points were in fact lower than those of imine cages prepared by Giri *et al*.[4] Unfortunately, these aliphatic amide-decorated cages were also non-porous. We hypothesise that this results from increased flexibility in the cage core on removal of the more rigid imine bond by reduction to the secondary amine, causing the cage to collapse in upon itself on removal of solvent. It is also possible that the amide groups in these cages, unlike in the imine analogues, hydrogen bond to solvent much more strongly, and hence the solvent is a much less 'innocent partner' in the structure. However, these decorated cages do provide a basis for further reactions through addition of increased functionality.

Although no porous materials were achieved through reduction and decoration of imine cages, this new class of amide-decorated cages provide a structurally stable and intriguing basis for further reactions from the possession of increased functionality (highlighted in Chapter 5). For example, the efficient addition of 12 organic functionalities to a small organic core is an appealing method to create dendrimers.

6.0.3 Cage Polymers

Reduced (**RC1**) and functionalised cages (**RC1a** and **b**) were used in different polymerisation reactions to create various microporous polymer networks. **RC1** was initially mixed with various bi-functional acid chlorides to yield porous polymers with N_2 uptake of up to 8.88 mmol/g and H_2 uptake of up to 1.96 mmol/g (at 1 and 1.13 bar respectively).

RC1a was homo-coupled (Yamamoto coupling[5]) and used as a monomer in Sonogashira coupling[6] with 1,4-diethynylbenzene to yield microporous polymers. **RC1a** homo-coupled by Yamomoto conditions showed N_2 uptake of 2.72 mmol/g and H_2 uptake of 1.92 mmol/g (at 1 and 1.13 bar respectively), while **RC1a** was polymerised *via* Sonogashira conditions and exhibited N_2 uptake of 6.03 mmol/g and H_2 uptake of 1.87 mmol/g (also at 1 and 1.13 bar respectively).

RC1b was hyper cross-linked utilising a small bi-fuctional cross-linker formaldehyde dimethyl acetal (FDA)[7] to produce selectively porous microporous polymers with H_2 uptake of 3.09 mmol/g and N_2 uptake of only 0.66 mmol/g, thus exhibiting selective H_2 uptake of 4.5:1 at 1 bar. When the same reaction was repeated with the introduction of benzene as a comonomer, networks with N_2 SA_{BET} between 324-954 m^2/g (maximum uptake between 8.29 and 21.70 mmol/g at 1 bar) were achieved. H_2 $SA_{Langmuir}$ between 216-395 m^2/g (maximum uptake between 3.55 and 5.88 mmol/g at 1.13 bar) were also observed on inclusion of benzene as a second monomer.

6.0.4 Summary

In this thesis, I have successfully produced a new porous organic cage with high N_2 SA_{BET} of 946 m^2/g. This ranks among the most porous molecular organic crystals to date. In producing this cage, I have highlighted the importance of polymorphism and work-up conditions. The effect on cage structure and porosity has also been emphasised, with polymorphism differing drastically for **CC12** in comparison with analogous CC2. The length of the diamine also had a large effect on influencing the production of either [2+3] or [4+6] cages.

While I did not induce high levels of porosity by functionalising cages, I have opened up a new class of easily-prepared functional materials for alternative uses, such as polymerisation. These materials possess 12 functional arms, higher than that of competing POSS materials (which only possess 8)[8,9] or similar functional cages prepared by other groups.[10]

Finally, I have prepared modestly nitrogen and hydrogen porous molecules, which exhibit higher total uptake than related materials produced by other groups, such as the OCFs prepared by Jin *et al.*[10]

6.1 Future Work

While completing the work in this thesis, there were a plethora of opportunities and ideas to open up future research possibilities. I briefly summarise some of the more promising ones here.

6.1.1 Further Polymorphism Studies

Polymorphism in these cage crystals clearly has a huge impact upon their physical properties, as already highlighted by Jones *et al.*[1] and again here in this thesis. While CC3 becomes more porous on amorphisation,[2] **CC12** behaves in the opposite manner and only exhibits N_2 porosity in the crystalline state. We have tried to rationalise this by hypothesising that the cyclohexane diamine vertex in CC3 is too large to interpenetrate with a neighbouring cage window, so that upon amorphisation it will not result in extreme close packing and interpenetration of cages. **CC12** meanwhile possesses smaller dimethyl groups which we believe can interpenetrate, and pack closely in an amorphous state, thus blocking pores. This is ripe for study *via* molecular simulations.

6.1.2 Functionalisation with Bulkier Groups to Generate Porosity

While the addition of bulky groups to **RC1** and **RC5** did not result in permanently crystalline or porous materials, it is still feasible that addition of more bulky groups would induce porosity. We could continue to target this through two methods: the first being the addition of bulkier groups than previously investigated. However, this route has already been tentatively explored, and it is problematic because of issues connected with solubility of starting materials (e.g., using anthracene- and pyrene-functionalised acid chlorides). The second possible route is to utilise functionality on **RC1a** to couple on mono-functional alkynes with solubilising groups *via* Sonogashira coupling to systematically bulk out the amide-decorated cages in separate steps.

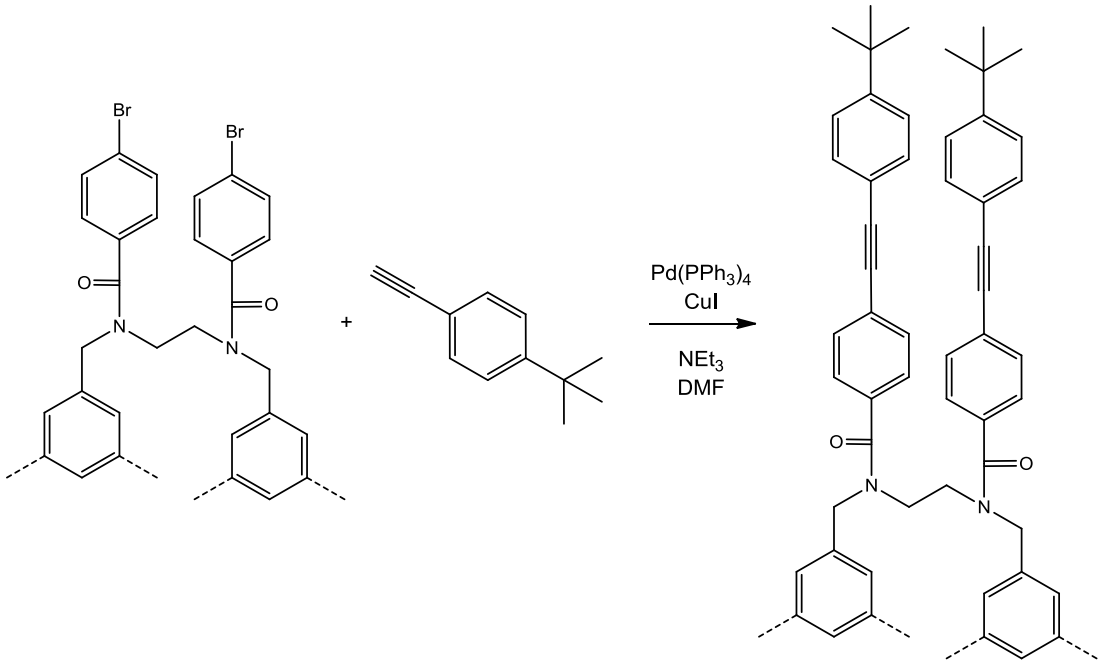

Figure 1: Bulking of **RC1a** *via* Sonogashira reaction with t-butylphenylacetylene.

6.1.3 Functionalisation: Towards MOF Linkers

MOFs are perhaps the most studied of all microporous materials in recent times, and one example exists already in the literature where **RC1** was employed as a Zn MOF linker.[11] Many MOFs consist of multi functional carboxylic acids,[12] which we believe we could readily fashion by conversion of **RC1a** from –Br to –COOH functionality by successive lithiation and addition of CO_2,[13] thus creating another prospective MOF linker (Figure 2).

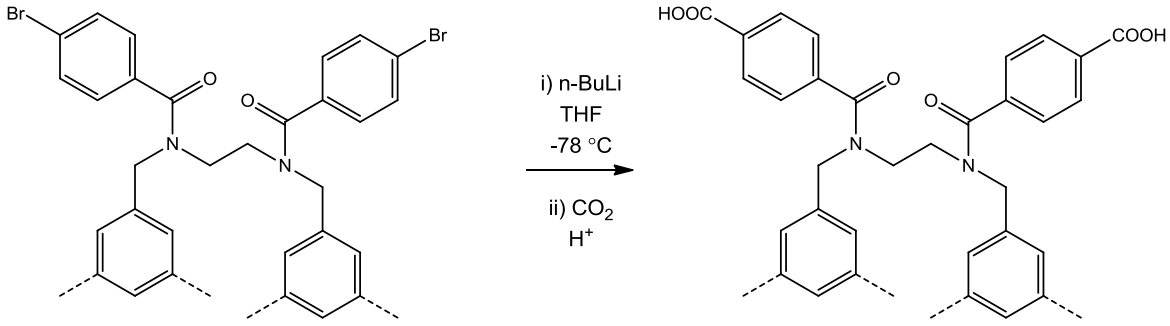

Figure 2: Possible conversion of **RC1a** to a carboxylic acid by altering conditions from reference.

MOFs have also been prepared from pyridine ligands.[14] As such, attempts have already been successful towards preparing a decorated cage for use as a MOF linker prepared from reduced CC1 and isonicotinoyl chloride hydrochloride (**RC1e**, as seen in Chapter 4) (Figure 3). This material could readily be tested as a possible MOF linker in the future.

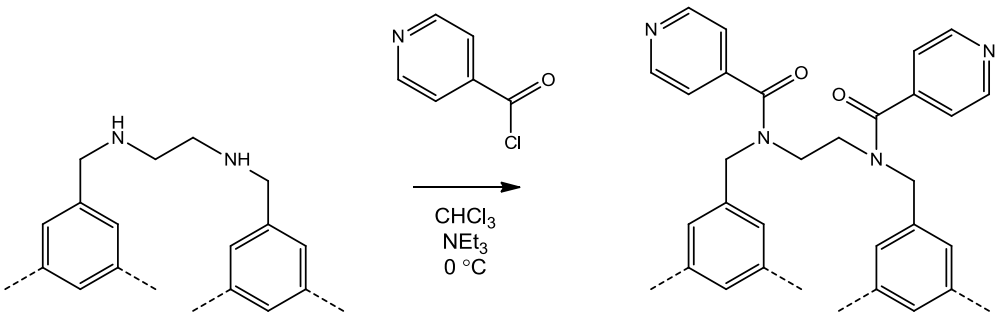

Figure 3: Preparation of **RC1e**.

Hybrid cages have also been prepared from pyridine linkers and platinum, which we could also attempt to emulate with a pyridine decorated cage.[15]

6.1.4 Cage Star Polymers

RC1d presented an opportunity for use as an amide initiator (as seen with other amide initiators in the literature[16]) to create a star polymer *via* ATRP (atom transfer radical polymerisation), with some tentative experiments already made with styrene as a monomer, due to solubility in the bulk (Figure 4).

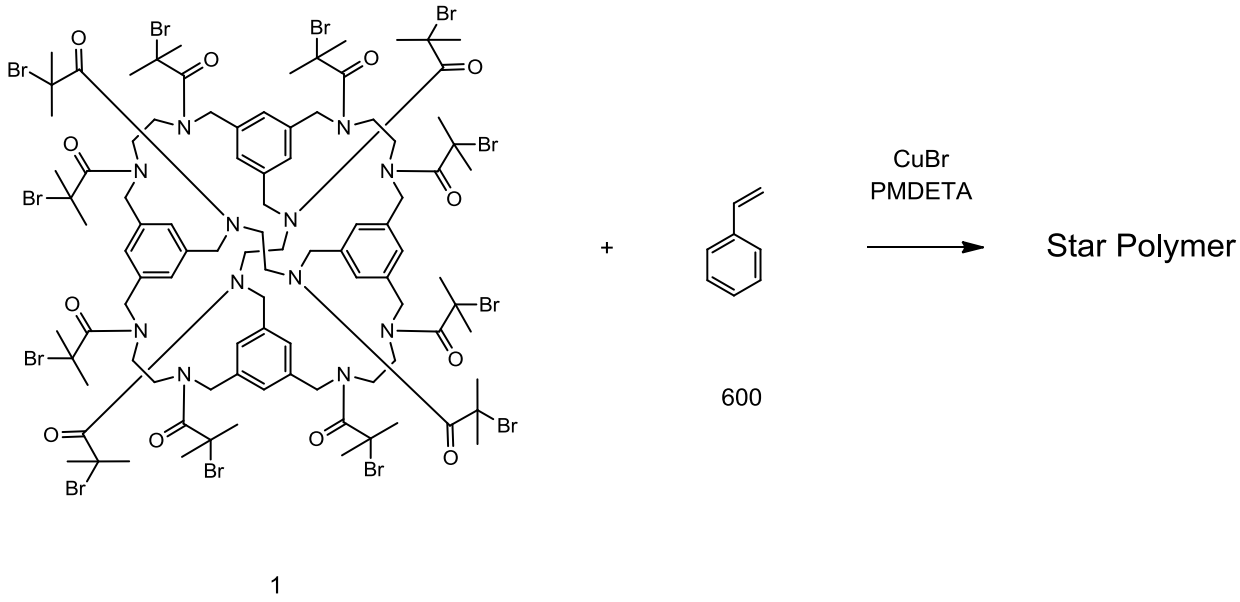

Figure 4: Preparation of a cage star polymer.

A star with molecular weight ≈ 75,000 g/mol (chain length of 50 monomers) and polydispersity index of 1.35 was observed. Attempts were made to further verify that the styrene arms were of uniform chain length by hydrolysing the amide bonds and re-running GPC. Unfortunately, GPC of the polymer after attempted hydrolysis showed no differences. This finding is likely due to the extremely hydrophobic nature of the styrene chain, thus rendering the amide bond 'unreachable' by aqueous media and hence harder to hydrolyse. This work merits further investigation, with possibilities for pH responsive star polymers depending on the monomer choice.

6.2 References

(1) Jones, J. T. A.; Holden, D.; Mitra, T.; Hasell, T.; Adams, D. J.; Jelfs, K. E.; Trewin, A.; Willock, D. J.; Day, G. M.; Bacsa, J.; Steiner, A.; Cooper, A. I. *Angew. Chem. Int. Ed.* **2011**, *50*, 749.

(2) Hasell, T.; Chong, S. Y.; Jelfs, K. E.; Adams, D. J.; Cooper, A. I. *J. Am. Chem. Soc.* **2011**, *134*, 588.

(3) Hasell, T.; Wu, X.; Jones, J. T. A.; Bacsa, J.; Steiner, A.; Mitra, T.; Trewin, A.; Adams, D. J.; Cooper, A. I. *Nat. Chem.* **2010**, *2*, 750.

(4) Giri, N.; Davidson, C. E.; Melaugh, G.; Del Popolo, M. G.; Jones, J. T. A.; Hasell, T.; Cooper, A. I.; Horton, P. N.; Hursthouse, M. B.; James, S. L. *Chem. Sci.* **2012**, *3*, 2153.

(5) Ben, T.; Ren, H.; Ma, S.; Cao, D.; Lan, J.; Jing, X.; Wang, W.; Xu, J.; Deng, F.; Simmons, J. M.; Qiu, S.; Zhu, G. *Angew. Chem. Int. Ed.* **2009**, *48*, 9457.

(6) Chinchilla, R.; Nájera, C. *Chem. Rev.* **2007**, *107*, 874.

(7) Li, B.; Gong, R.; Wang, W.; Huang, X.; Zhang, W.; Li, H.; Hu, C.; Tan, B. *Macromolecules* **2011**, *44*, 2410.

(8) Chaikittisilp, W.; Sugawara, A.; Shimojima, A.; Okubo, T. *Chem. Eur. J.* **2010**, *16*, 6006.

(9) Chaikittisilp, W.; Sugawara, A.; Shimojima, A.; Okubo, T. *Chem. Mater.* **2010**, *22*, 4841.

(10) Jin, Y.; Voss, B. A.; Jin, A.; Long, H.; Noble, R. D.; Zhang, W. *J. Am. Chem. Soc.* **2011**, *133*, 6650.

(11) Swamy, S. I.; Bacsa, J.; Jones, J. T. A.; Stylianou, K. C.; Steiner, A.; Ritchie, L. K.; Hasell, T.; Gould, J. A.; Laybourn, A.; Khimyak, Y. Z.; Adams, D. J.; Rosseinsky, M. J.; Cooper, A. I. *J. Am. Chem. Soc.* **2010**, *132*, 12773.

(12) Furukawa, H.; Ko, N.; Go, Y. B.; Aratani, N.; Choi, S. B.; Choi, E.; Yazaydin, A. Ö.; Snurr, R. Q.; O'Keeffe, M.; Kim, J.; Yaghi, O. M. *Science* **2010**, *329*, 424.

(13) Alame, M.; Jahjah, M.; Berthod, M.; Lemaire, M.; Meille, V.; de Bellefon, C. *J. Mol. Catal. A: Chem.* **2007**, *268*, 205.

(14) Klein, N.; Senkovska, I.; Baburin, I. A.; Grünker, R.; Stoeck, U.; Schlichtenmayer, M.; Streppel, B.; Mueller, U.; Leoni, S.; Hirscher, M.; Kaskel, S. *Chem. Eur. J.* **2011**, *17*, 13007.

(15) Yoshizawa, M.; Fujita, M. *Bull. Chem. Soc. Jpn.* **2010**, *41*, 609.

(16) Adams, D. J.; Young, I. *J. Polym. Sci., Part A: Polym. Chem.* **2008**, *46*, 6082.

(1) Jones, J. T. A.; Holden, D.; Mitra, T.; Hasell, T.; Adams, D. J.; Jelfs, K. E.; Trewin, A.; Willock, D. J.; Day, G. M.; Bacsa, J.; Steiner, A.; Cooper, A. I. *Angew. Chem. Int. Ed.* **2011**, *50*, 749.

(2) Hasell, T.; Chong, S. Y.; Jelfs, K. E.; Adams, D. J.; Cooper, A. I. *J. Am. Chem. Soc.* **2011**, *134*, 588.

(3) Hasell, T.; Wu, X.; Jones, J. T. A.; Bacsa, J.; Steiner, A.; Mitra, T.; Trewin, A.; Adams, D. J.; Cooper, A. I. *Nat. Chem.* **2010**, *2*, 750.

(4) Giri, N.; Davidson, C. E.; Melaugh, G.; Del Popolo, M. G.; Jones, J. T. A.; Hasell, T.; Cooper, A. I.; Horton, P. N.; Hursthouse, M. B.; James, S. L. *Chem. Sci.* **2012**.

(5) Ben, T.; Ren, H.; Ma, S.; Cao, D.; Lan, J.; Jing, X.; Wang, W.; Xu, J.; Deng, F.; Simmons, J. M.; Qiu, S.; Zhu, G. *Angew. Chem. Int. Ed.* **2009**, *48*, 9457.

(6) Chinchilla, R.; Nájera, C. *Chem. Rev.* **2007**, *107*, 874.

(7) Li, B.; Gong, R.; Wang, W.; Huang, X.; Zhang, W.; Li, H.; Hu, C.; Tan, B. *Macromolecules* **2011**, *44*, 2410.

(8) Chaikittisilp, W.; Sugawara, A.; Shimojima, A.; Okubo, T. *Chem. Eur. J.* **2010**, *16*, 6006.

(9) Chaikittisilp, W.; Sugawara, A.; Shimojima, A.; Okubo, T. *Chem. Mater.* **2010**, *22*, 4841.

(10) Jin, Y.; Voss, B. A.; Jin, A.; Long, H.; Noble, R. D.; Zhang, W. *J. Am. Chem. Soc.* **2011**, *133*, 6650.

(11) Swamy, S. I.; Bacsa, J.; Jones, J. T. A.; Stylianou, K. C.; Steiner, A.; Ritchie, L. K.; Hasell, T.; Gould, J. A.; Laybourn, A.; Khimyak, Y. Z.; Adams, D. J.; Rosseinsky, M. J.; Cooper, A. I. *J. Am. Chem. Soc.* **2010**, *132*, 12773.

(12) Furukawa, H.; Ko, N.; Go, Y. B.; Aratani, N.; Choi, S. B.; Choi, E.; Yazaydin, A. Ö.; Snurr, R. Q.; O'Keeffe, M.; Kim, J.; Yaghi, O. M. *Science* **2010**, *329*, 424.

(13) Alame, M.; Jahjah, M.; Berthod, M.; Lemaire, M.; Meille, V.; de Bellefon, C. *J. Mol. Catal. A: Chem.* **2007**, *268*, 205.

(14) Klein, N.; Senkovska, I.; Baburin, I. A.; Grünker, R.; Stoeck, U.; Schlichtenmayer, M.; Streppel, B.; Mueller, U.; Leoni, S.; Hirscher, M.; Kaskel, S. *Chem. Eur. J.* **2011**, *17*, 13007.

(15) Yoshizawa, M.; Fujita, M. *ChemInform* **2010**, *41*, no.

(16) Adams, D. J.; Young, I. *J. Polym. Sci., Part A: Polym. Chem.* **2008**, *46*, 6082.